INAUGURAL – DISSERTATION

zur Erlangung der Doktorwürde

der

Naturwissenschaftlich-Mathematischen Gesamtfakultät

der

Ruprecht-Karls-Universität Heidelberg

vorgelegt von

Diplom-Geologe Manuel Sehrt

aus Seeheim-Jugenheim

Tag der mündlichen Prüfung: 02. Juli 2014

Variscan to Neogene long-term landscape evolution at the Moroccan passive continental margin (Tarfaya Basin and western Anti-Atlas)

Gutachter: apl. Prof. Dr. Ulrich A. Glasmacher
Prof. Dr. Peter A. Kukla

ACKNOWLEDGEMENT

My very special thanks go to my supervisor apl. Prof. Dr. Ulrich A. Glasmacher, who sparked my interest in thermochronology and made my PhD project possible. Of course, I would particularly like to thank also Prof. Dr. Peter A. Kukla from Aachen, who agreed to write an expertise for the present PhD thesis.

I would like to thank my colleagues Axel Wenke, Dr. Victoria Sachse, Dr. Björn Heise and Dr. Martin Wipf for the nice time during sampling campaigns in Morocco and the interesting, interdisciplinary discussions. Further, I am grateful to Dr. Rainer Zühlke for planning and organizing the sampling campaigns.

I gratefully acknowledge the financial support of RWE-Dea AG and logistic support by ONHYM. In particular, my sincere thanks go to Oliver Kluth, Dr. Torge Schümann, Haddou Jabour, Dr. Lahcen Boutib and Dr. Salim Lahsini for the Atlantic Margin Project management, their support during various visits in Rabat, Morocco and their assistance during the field campaigns.

I am also grateful to Prof. Dr. Daniel Stockli for supporting me while doing (U-Th-Sm)/He analyses in Lawrence, Kansas.

Furthermore, I would like to thank the whole staff of apl. Prof. Dr. Glasmacher's Research Group 'ThermoArchaeo' at the University of Heidelberg, namely Margit Brückner and Dr. Friederike Bauer. Of course, I am particularly grateful to my friend and former roommate Dr. René Grobe for long and profound discussions concerning thermochronological and other questions of meaning.

My special thanks go to my dear parents and siblings for their love, unconditional support and encouragement during my PhD study. Last but not least I owe thanks all those, in particular Rebecca, who continuously believed in me and supported my PhD study in any possible way.

Thank you very much!

ABSTRACT

The present study introduces the first comprehensive thermochronological research at the southern Moroccan passive continental margin. The established low-temperature thermochronological methods apatite and zircon fission-track (AFT, ZFT) as well as apatite and zircon (U-Th-Sm)/He (AHe, ZHe) dating combined with time-temperature (t-T) path modelling have been applied to resolve the long-term landscape evolution of the Tarfaya Basin and western Anti-Atlas. The Tarfaya Basin is the northern part of the Tarfaya-Laâyoune-Dakhla Basin that extends over 1000 km along the Moroccan Central Atlantic margin. The basin is characterised by vast subsidence since Mid-Triassic times, whereby up to 12 km of Mesozoic to Cenozoic sedimentary rocks have been accumulated. In the northeast, the basin is bounded by an ENE-trending Palaeozoic fold belt, the Anti-Atlas. The mountain belt consists of numerous widespread Precambrian basement inliers surrounded by a thick Palaeozoic sedimentary succession that is folded during the Variscan orogeny. Due to massive surface uplift and exhumation since the Upper Carboniferous–Lower Permian, the Anti-Atlas reaches elevations of more than 3300 m and therefore, constitutes a potential source area for the surrounding basins. The study intends to analyse and interpret thermochronological data to constrain the pattern and history of subsidence and exhumation at the southern Moroccan passive continental margin.

The **main research objective** was focused on the thermal, subsidence and exhumation history of the Tarfaya Basin in order to better comprehend the hydrocarbon generation in time and space. To determine the t-T development, thermochronological analyses were performed on 66 outcrop and well samples from Mesozoic–Cenozoic sedimentary rocks. The results reveal a continuous subsidence phase in the offshore Tarfaya Basin from Mid-Triassic onward to recent times. In contrast, AHe and AFT data as well as thermal modelling point to a basin inversion in the northeastern onshore basin starting in the Palaeogene at 65–50 Ma. The rock uplift and exhumation period resulted in the erosion of a 1.2–1.6 km thick Cretaceous–Palaeogene sedimentary pile at an average rate of 0.025 mm/a corresponding with peak Atlasian surface uplift in the Cenozoic. Detrital AFT ages from 92 (±16) to 237 (±35) Ma of the Upper Cretaceous–Neogene succession indicate no heating above 60 °C confirming immature to early mature Cenomanian to Campanian and Eocene source rocks in the onshore Tarfaya Basin.

The **second objective** dealt with the thermal, subsidence and exhumation history of the western Anti-Atlas mountain belt. Thermochronological data of 34 Precambrian–Lower Carboniferous samples propose a common geological evolution of the western Anti-Atlas. ZFT ages from 287 (±23) to 331 (±24) Ma point to a main exhumation in the Upper Carboniferous–Lower Permian related to the Variscan folding and post-folding erosion. The rock uplift and exhumation phase lasted up to the Lower Cretaceous, whereby 9 km of Precambrian–Palaeozoic overburden has been eroded at an average rate of 0.046 mm/a. In the late Lower Cretaceous to Upper Cretaceous, the western Anti-Atlas underwent a minor subsidence phase in accordance with the widespread transgression across the North African continent in the Cenomanian–Turonian. AHe ages between 49 (±3) and 89 (±5) Ma as well as t-T path modelling indicate the final exhumation period starting in the Upper Cretaceous, contemporaneously with the earliest record of surface uplift in the Atlas system during Senonian (90–65 Ma). The exhumation process and erosion of the 1.5–2.5 km thick Cretaceous

overburden continued until present time at an average rate of 0.045 mm/a. Except for a hiatus in the Upper Cretaceous, the extensive denudation events in the western Anti-Atlas suggest a continuous clastic sediment flux to the Tarfaya Basin from Triassic to recent times.

The third objective considered the establishment of a correlation between subsidence history of the Tarfaya Basin and exhumation history of the western Anti-Atlas. Hence, a provenance analysis of the Cretaceous to Neogene sedimentary succession has been performed. Thermochronological data suggest a continuous sediment transport from the western Anti-Atlas to the Tarfaya Basin from Lower Cretaceous onward to present time. Furthermore, due to Precambrian ZHe and ZFT single grain ages, a concurrent sediment input from a cratonic area, i.e. the Reguibat Shield, occurred. During the early Upper Cretaceous, the influx from various source areas into the Tarfaya Basin decreased. In the Neogene, the sediment input from the cratonic area reduced and an influx emerged from the High Atlas probably by a coastal longitudinal flow, i.e. the Canary Current. Finally, the northeastern onshore Tarfaya Basin delivered clastic material to the offshore and southern onshore basin in the Neogene.

ZUSAMMENFASSUNG

Die vorliegende Studie stellt die erste umfassende thermochronologische Forschungsarbeit am südlichen marokkanischen passiven Kontinentalrand dar. Zur Auflösung der langzeitlichen Landschaftsentwicklung des Tarfaya Beckens und des westlichen Anti-Atlas wurden die bewährten niedrig-Temperatur thermochronologischen Methoden, Apatit- und Zirkon-(U-Th-Sm)/He (AHe, ZHe) sowie Apatit- und Zirkon-Spaltspurdatierung (AFT, ZFT) in Kombination mit Zeit-Temperatur (t-T) Modellierungen angewandt. Das Tarfaya Becken stellt den nördlichen Abschnitt des Tarfaya-Laâyoune-Dakhla Beckens dar, welches sich über 1000 km entlang des marokkanischen zentralatlantischen Randes erstreckt. Das Becken ist seit der Mitteltrias bis in die Gegenwart von enormer Versenkung geprägt, wobei bis zu 12 km an mesozoisch–känozoischen Sedimentgesteinen abgelagert wurden. Im Nordosten ist das Becken von einem ENE-verlaufenden paläozoischen Faltengürtel, dem Anti-Atlas, begrenzt. Der Gebirgsgürtel besteht aus zahlreichen großflächigen präkambrischen Grundgebirgsfenstern, die von einer mächtigen, verfalteten, paläozoischen sedimentären Abfolge umgeben sind. Aufgrund von gewaltiger Heraushebung und Exhumierung seit dem Oberkarbon–Unterperm erreicht der Anti-Atlas Höhen von mehr als 3300 m und stellt daher ein potentielles Liefergebiet für die umgebenden Becken dar. Die Studie befasste sich mit der Analyse und Interpretation thermochronologischer Daten, um die Versenkungs- und Exhumierungsgeschichte des südlichen marokkanischen passiven Kontinentalrandes nachzuzeichnen.

Der **Forschungsschwerpunkt** richtete sich auf die thermische, Subsidenz- und Exhumierungsgeschichte des Tarfaya Beckens zum besseren Verständnis der Kohlenwasserstoffbildung in Zeit und Raum. Zur Bestimmung der t-T Entwicklung wurden thermochronologische Analysen an 66 mesozoisch–känozoischen, sedimentären Aufschluss- und Bohrproben durchgeführt. Die Ergebnisse zeigen eine kontinuierliche Versenkungsphase in dem offshore Tarfaya Becken seit der Mitteltrias bis in die heutige Zeit. Im Gegensatz dazu deuten AHe und AFT Daten ebenso wie thermische Modellierungen auf eine Beckeninversion im nordöstlichen onshore Becken im Paläogen vor 65–50 Ma hin. Die Anhebungs- und Exhumierungsphase, welche mit der Heraushebung des Atlas Gebirgsgürtels korreliert, führte zur Erosion einer 1.2–1.6 km mächtigen, kretazisch–paläogenen Abfolge bei einer durchschnittlichen Rate von 0.025 mm/a. Detritische AFT Alter von 92 (±16) bis 237 (±35) Ma schließen eine Aufheizung der oberkretazisch–neogenen Schichten über 60 °C aus. Diese Feststellung bekräftigt frühreifes bis unreifes organisches Material in den Muttergesteinen des Cenomanium–Campanium und Eozän in dem onshore Tarfaya Becken.

Die **zweite Fragestellung** beschäftigte sich mit der thermischen, Subsidenz- und Exhumierungsgeschichte des westlichen Anti-Atlas Gebirgsgürtels. Thermochronologische Daten von 34 Proben des Präkambriums bis Unterkarbons deuten auf eine einheitliche geologische Entwicklung des westlichen Anti-Atlas hin. ZFT Alter von 287 (±23) bis 331 (±24) Ma weisen auf eine bedeutende Exhumierung im Oberkarbon–Unterperm, verbunden mit der variszischen Faltung und anschließenden Erosion, hin. Die Anhebungs- und Exhumierungsphase dauerte bis in die Oberkreide an, wobei 9 km an präkambrischer–paläozoischer Überlagerung bei einer durchschnittlichen Rate von 0.046 mm/a erodiert wurden. In der späten Unterkreide bis Oberkreide erlebte der westliche Anti-Atlas eine geringfügige Versenkungsphase, die in Übereinstimmung mit der ausgedehnten Transgression über dem nordafrikanischen Kontinent während des Cenomanium–Turonium ist. Sowohl

AHe Alter von 49 (±3) bis 89 (±5) Ma als auch t-T Modellierungen zeigen, dass die abschließende Exhumierung in der Oberkreide, zeitgleich mit den frühesten Anzeichen einer Heraushebung des Atlasgebietes im Senonium (90–65 Ma), begann. Der Exhumierungsprozess und die Erosion der 1.5–2.5 km mächtigen Kreideüberlagerung setzten sich, bei einer Rate von 0.045 mm/a, bis in die heutige Zeit fort. Mit Ausnahme einer Unterbrechung in der Oberkreide, lassen die umfassenden Denudationsereignisse im westlichen Anti-Atlas einen kontinuierlichen klastischen Sedimenteintrag in das Tarfaya Becken seit der Trias bis in die heutige Zeit vermuten.

Das **dritte Forschungsziel** bestand darin, eine Korrelation zwischen der Subsidenzgeschichte des Tarfaya Beckens und der Exhumierungsgeschichte des westlichen Anti-Atlas herzustellen. Demzufolge wurde eine Herkunftsanalyse der kretazisch–neogenen, sedimentären Abfolge durchgeführt. Thermochronologische Daten verdeutlichen einen kontinuierlichen Sedimenttransport aus dem westlichen Anti-Atlas ins Tarfaya Becken seit der Unterkreide bis zum gegenwärtigen Zeitpunkt. Basierend auf ZHe und ZFT Einzelkornaltern, ereignete sich parallel ein Sedimenteintrag aus einem kratonischen Gebiet, i.e. dem Reguibat Schild. Während der frühen Oberkreide verringerte sich der Zustrom aus den unterschiedlichen Liefergebieten ins Tarfaya Becken. Im Neogen reduzierte sich der Sedimenteintrag aus dem kratonischen Liefergebiet und ein Zustrom aus dem Hohen Atlas möglicherweise durch eine Küstenlängsströmung, i.e. dem Kanarenstrom, trat auf. Zusätzlich lieferte das nordöstliche onshore Tarfaya Becken klastisches Material in das offshore und südliche onshore Becken im Neogen.

Keywords: low-temperature thermochronology, long-term landscape evolution, Moroccan passive continental margin, western Anti-Atlas mountain belt, Tarfaya Basin, subsidence and exhumation history, hydrocarbon generation, apatite and zircon fission-track, apatite and zircon (U-Th-Sm)/He analysis, time-temperature path modelling, HeFTy, provenance analysis, detrital thermochronology

TABLE OF CONTENTS

LIST OF FIGURES

LIST OF TABLES

1

INTRODUCTION

The present study was part of a comprehensive project for hydrocarbon exploration at the Moroccan passive continental margin. For a long time, Morocco is subject of numerous research programmes and exploration studies. In Morocco, source rocks are well known occurring mainly in the Silurian, Jurassic, Cretaceous and Eocene strata (Macgregor, 1996; Morabet et al., 1998). According to the large number of Mesozoic to Cenozoic basins at the Central Atlantic margin, a promising hydrocarbon potential is suggested. Productive oil and gas fields exist in the Essaouira Basin, Rharb Basin and Pre-Rif Basin (Jabour et al., 2000; Macgregor, 1996).

The Atlantic Margin Project dealt with the hydrocarbon potential of the Tarfaya Basin, the southernmost Moroccan basin. Oil shows appear in the offshore wells Cap Juby-1, MO-2 and MO-8 probably sourced from Upper Triassic or Jurassic carbonate layers (Davison, 2005; Jabour et al., 2000; Macgregor and Moody, 1998; Morabet et al., 1998; ONAREP, 2002, 2003). The vast majority of Mesozoic–Cenozoic source rocks in the Tarfaya Basin derive from two stratigraphic intervals, the Upper Cretaceous (particularly Cenomanian–Turonian) and Eocene. However, no oil and gas production exist in the Tarfaya Basin due to mainly immature source rocks. Therefore, the Atlantic Margin Project has been carried out in order to unravel the hydrocarbon generation in the basin by biostratigraphic, geochemical, source rock, basin development and source-to-sink analyses.

The present thesis investigated the long-term landscape evolution of the Moroccan passive continental margin assessed by low-temperature thermochronology (LTT). Due to the lack of thermochronometric data, the time-temperature (t-T) development of the Tarfaya Basin is so far poorly understood and constrained. The determination of the thermal history in the Tarfaya Basin is essential for a detailed explanation of the hydrocarbon generation in time and space. To improve the understanding of the processes involved, the established and sensitive LTT methods apatite and zircon (U-Th-Sm)/He dating (AHe, ZHe) as well as apatite and zircon fission-track dating (AFT, ZFT) were performed. LTT techniques have been applied successfully to unravel rates of exhumation in a variety of tectonic scenarios, such as active orogens and passive margins (Bishop, 2007; Gunnell et al., 2009; Reiners and Brandon, 2006). Based on the AHe, AFT and ZHe data, designated samples were modelled with the 2-D numerical modelling software 'HeFTy' to determine thermal histories of the Tarfaya Basin and the western Anti-Atlas (Ketcham, 2005; Ketcham et al., 2007a, b; Ketcham et al., 2009).

Applying the aforementioned thermochronological methods, the current research study intends to resolve the following three key objectives:

(A) The main research goal dealt with the t-T development of the Tarfaya Basin, especially of the pre-Palaeogene sediments, in order to better comprehend the hydrocarbon generation in time and space (Fig. 1.1).

(B) Furthermore, the study was focused on Palaeogene to Neogene sedimentary rocks. Due to their low thermal imprint below the partial annealing zone and partial retention zone, Cenozoic sedimentary rocks indicate the t-T evolution of the source area, so-called provenance (Fig. 1.1).

(C) The third objective was the determination of the thermal, subsidence and exhumation history of potential source areas. Consequently, the research interest was concentrated additionally on the northeastern continental source region, the Anti-Atlas mountain belt (Fig. 1.1).

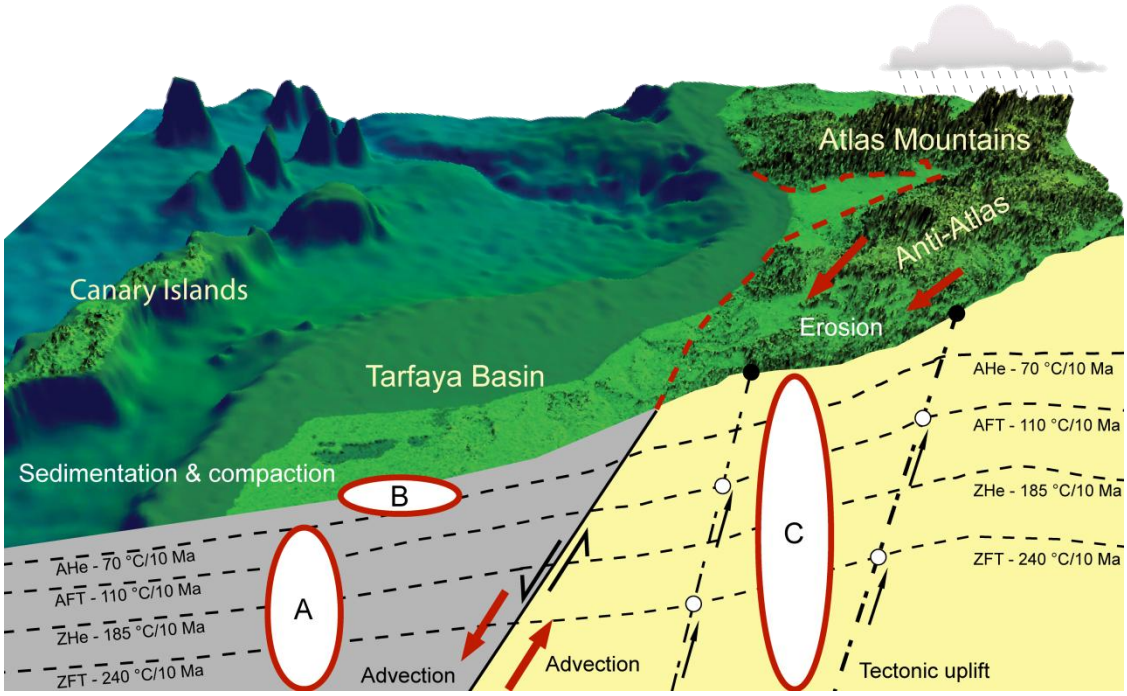

Fig. 1.1: Thermal and tectonic processes at the Atlantic margin of Morocco including key objectives of the present study. The represented thermochronological analyses (AHe, AFT, ZHe and ZFT) were performed in the project. Rocks in the subsurface (white circles) are exhumed and sampled at the surface (filled circles). (A) Thermal, subsidence and exhumation history of the Tarfaya Basin. (B) Provenance analysis of Cenozoic sedimentary rocks. (C) Thermal, subsidence and exhumation history of the Anti-Atlas mountain belt (modified after Bauer et al., 2010; Ehlers and Farley, 2003).

2

GEOLOGICAL SETTING

Contents

2.1 Overview

Morocco is located in a particular region, the northwestern edge of the large African continent, and is bounded by the Central Atlantic passive continental margin in the west and an active plate collision zone, the Alpine belt, in the north (Fig. 2.1). The geographic position of Morocco explains the varied landform with a wide range of outcropping terranes from Archean to Cenozoic age as well as different tectonic systems of sedimentary basins up to metamorphic fold belts. The topography of Morocco shows two contrary domains, (1) the southern area consisting mainly of lowlands with gentle topography and (2) the Atlas mountain belt to the north dominating by a rugged topography with high mountain ranges as well as rhomboid plateaus and basins (Fig. 2.1).

In northern Morocco, the Rif mountains, the western continuation of the Kabylian- Tellian belt (Maghrebides) extends along the Mediterranean coast (Alboran Sea) till the Strait of Gibraltar. South of the coastal region, elevated plateaus, the Mesetas occur, followed by the Atlas mountain belt that forms the northern boundary to the lower Sahara region. The High Atlas exhibit huge elevations with more than 4000 m a.s.l. including the highest peak of North Africa, the 4165 m high Jebel Toubkal. The Middle Atlas, a limb of the Atlas system, stretches perpendicular through the Meseta and reaches elevations of about 3000 m a.s.l. The elevation decreases continuously westward from the Middle Atlas towards the Meseta, the Atlantic coastal basins and finally to the Atlantic abyssal plain. At the northern sub-Sahara boundary, south of the High Atlas, a vast mountain belt, the Anti-Atlas (AA) is situated reaching up to 2700 m a.s.l. in the Jebel Sarhro Mountains and 3300 m a.s.l. in the recent Jebel Siroua volcano. South of the Anti-Atlas, the elevation decreases to less than 400 m a.s.l. in the Tindouf Basin and 200 m a.s.l. in the Tarfaya Basin (TB).

The geographic and geological characteristics

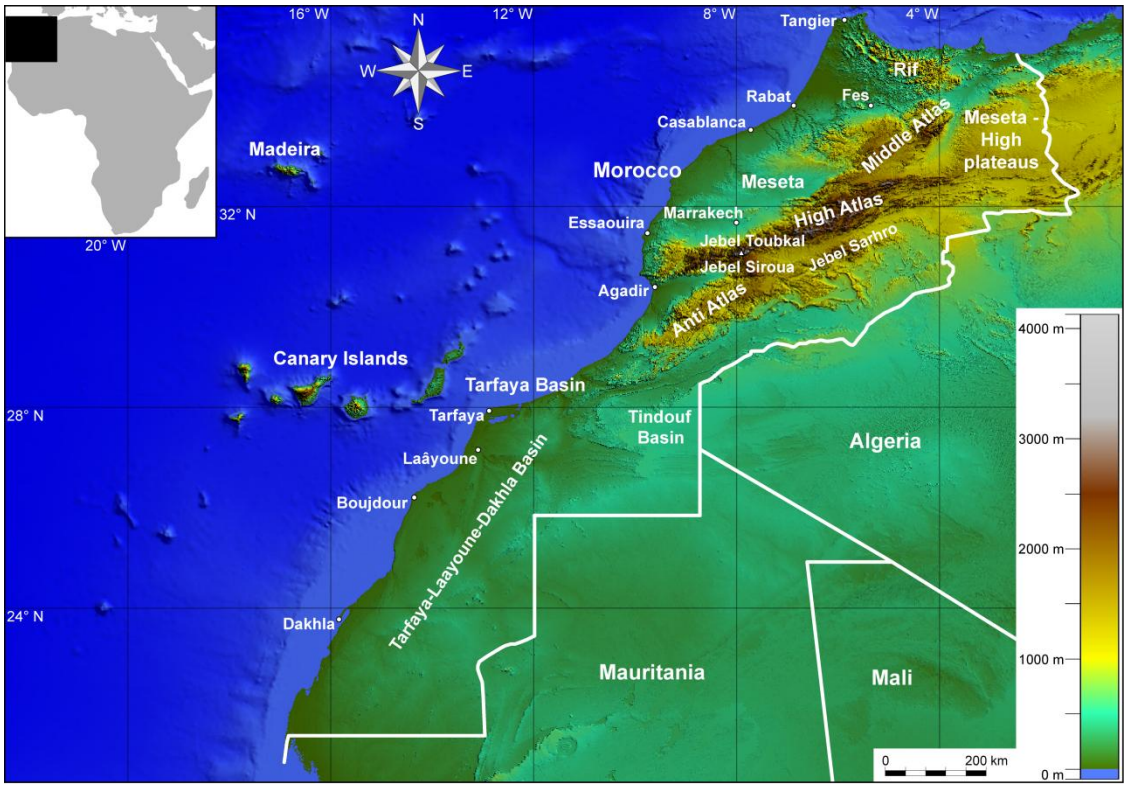

Fig. 2.1: Overview of the Moroccan regions. Digital elevation model (DEM) derived from Aster GDEM.

of Morocco are due to the specific position at the northwestern edge of Africa during the plate tectonic Wilson-Cycle. The Mesozoic–Cenozoic cycle started with the Pangaea break-up, continued with the opening of the Central Atlantic as well as the Alpine Tethys Ocean and ended with the closure of the Tethys Ocean and the formation of the Alpine mountain range (Michard et al., 2008a).

2.2 Central Atlantic passive continental margin

The NW African Central Atlantic passive continental margin extends from the northern top of Morocco up to the Guinea fault zone in the south. Similarities in the stratigraphy appear along the entire NW African margin. The Moroccan Central Atlantic passive continental margin stretches over nearly 3000 km from Tangier to Lagouira in the south representing one of the oldest continental margins conjugate to the Nova Scotia margin in North America. Except for the offshore area around the Rif and Atlas mountains, the complete margin reveals a broad homogeneity in the geodynamic evolution.

Numerous Mesozoic to Cenozoic extensional basins are located along the two conjugate margins of Morocco and North America (Withjack et al., 2012). On- and offshore basins at the Moroccan passive continental margin are from north to south the Pre-Rif and Rharb Basins, Doukkala Basin, Essaouira Basin, Souss Basin, Tarfaya Basin and Tarfaya-Laâyoune-Dakhla Basin (Davison, 2005; Hafid et al., 2008; Zühlke et al., 2004) (Fig. 2.2). Based on the key position at the Central Atlantic Ocean and the promising hydrocarbon potential, the Moroccan margin is subject of numerous research programmes and exploration studies.

The opening of the Central Atlantic Ocean and consequently, the development of the Central Atlantic passive continental margin is connected with two different tectonic stages, a rifting and a drifting episode. The onset of continental rifting at the future Moroccan margin occurred in the Upper Permian before 260 Ma (Hafid et al., 2008; Zühlke et al., 2004) (Fig. 2.3). In the Tarfaya-Laâyoune segment, the rifting possibly started in Mid-Triassic times (Ellouz et al., 2003). The rifting propagated from E to W and from S to N with a NW-SE extension direction, oblique to the ENE–WSW trend of the Atlas Mountains (Beauchamp et al., 1999; Le Roy and Piqué, 2001). Thereby, a system of NE–SW striking syn-rift normal faults, graben and half-graben connected to E–W striking transfer faults emerged on top of the Variscan continental crust (Frizon de Lamotte et al., 2009; Hafid et al., 2008). Except for the Atlantic and Atlas basins, the rifting yielded an enormous erosion in western Morocco and consequently, the extensive exposure of Palaeozoic and Precambrian rocks (Michard et al., 2008a).

The initial sedimentation during the rifting consisted of Triassic red marine and fluviatile fine-grained clastic rocks accompanied by volcanic intercalations (Brown, 1980; Le Roy and Piqué, 2001). In the Upper Triassic (210–200 Ma), the formation of evaporite basins started at both sides of the Central Atlantic rift (Fig. 2.3). Broad diapiric salt basins developed with a thickness of up to 1500 m in the offshore area, whereby sedimentation rates of about 1 mm/a have been reached (Davison, 2005). The halokinesis of the syn-rift salt greatly influenced the evolution of the continental slope and the abyssal plain (Hafid et al., 2008) (Fig. 2.3). Simultaneously, a high magmatic activity took place at the Central Atlantic rift. This brief event at 200 (± 1) Ma is characterised by voluminous basaltic magmatism and termed as Central Atlantic Magmatic Province (CAMP) (Hames et al., 2003; McHone, 2000; Olsen et al., 2003; Wilson, 1997). The CAMP consists of dikes, sills, subaerial lavas, pyroclastics and plutons at both sides of the entire

Central Atlantic rift in a 6000 km long, N–S trending zone and has been dated to 197–203 Ma in Morocco (Fietchner et al., 1992; Knight et al., 2004; Marzoli et al., 2004; Sahabi et al., 2004; Sebai et al., 1991; Verati et al., 2007) and 198–203 in the USA (Hames et al., 2000). Whereas the origin of the CAMP is not precisely clarified, suggested theories are an asymmetric, subhorizontal plume (McHone, 2000) or multiple source origin. During CAMP, no distinct rock uplift phase occurred, since the evaporites appear within and above the basalt. The Central Atlantic rifting stage lasted until the Hettangian-Sinemurian (200–190 Ma) (Zühlke et al., 2004), while Gouiza et al. (2010) assumed a two-phase rifting stage up to 175 Ma confirmed by numerical modelling at a Doukkala–High Atlas transect.

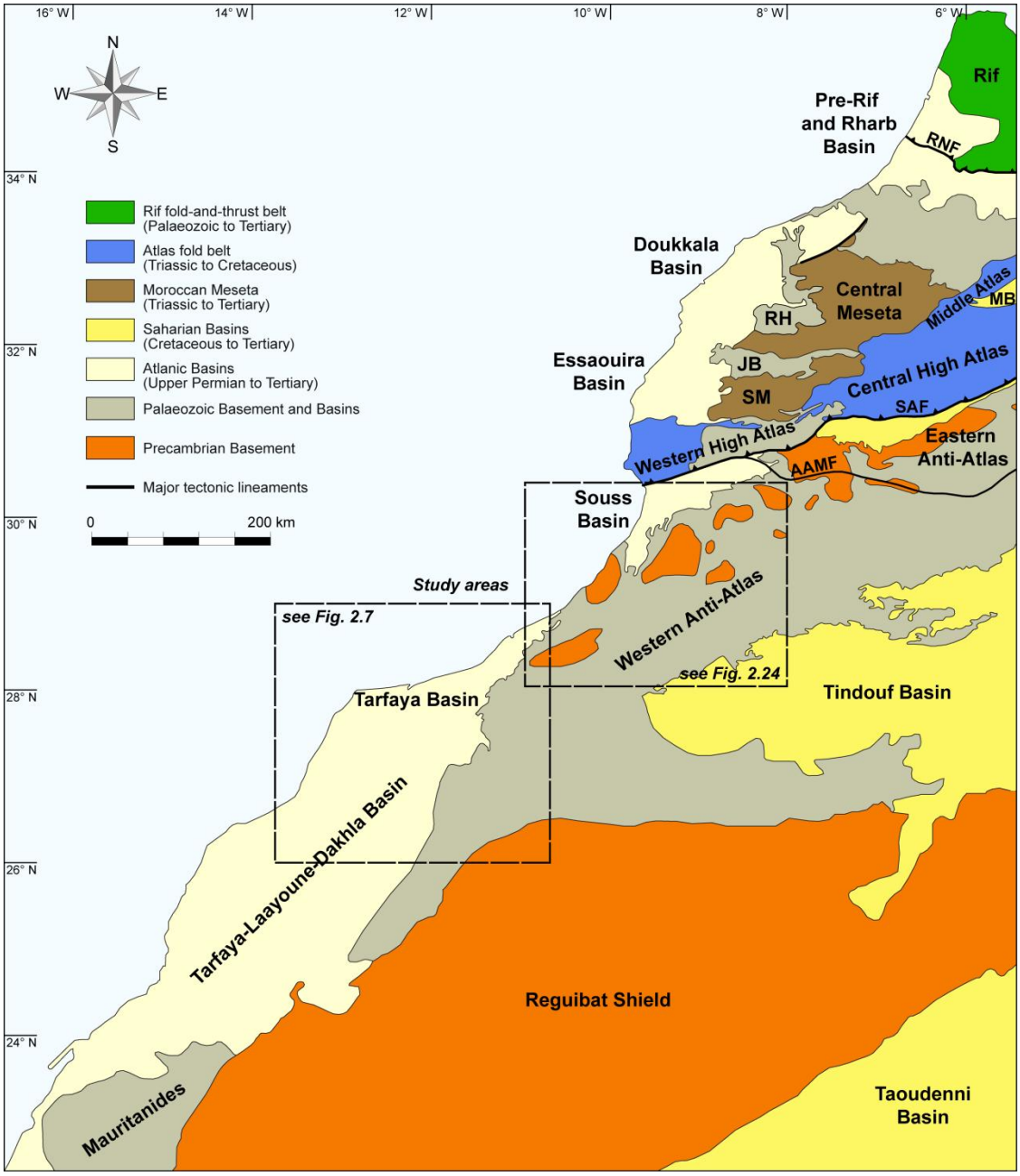

Fig. 2.2: Overview of the main tectono-sedimentary units of western Morocco including Atlantic Basins and study areas (Fig. 2.7 and Fig. 2.24). MB: Missour Basin; SM: Southern Meseta; JB: Jebilet; RH: Rehamna; RNF: Rif Nappe Front; SAF: South Atlas Fault; AAMF: Anti-Atlas Major Fault (modified from Zühlke et al., 2004).

During the initial phase of drifting in the Lower Jurassic, the opening of the Central Atlantic at the Moroccan margin and the Ligurian Tethys began, which were connected by a transform fault system (Fig. 2.4). The ocean spreading started in the southern part between Western Sahara–Mauritania and the Baltimore Canyon (Davison, 2005). The oldest oceanic crust in the Central Atlantic is of Sinemurian to Late Pliensbachian age (195–184 Ma) (Le Roy et al., 1998; Sahabi et al., 2004; Steiner et al., 1998; Zühlke et al., 2004). Previous models suggested a later onset of sea-floor spreading in Toarcian to Bajocian times (178–169 Ma) (Klitgord and Schouten, 1986). During the early drift stage (185–145 Ma), the Central Atlantic spreading half-rate was approximately 19 mm/a (Klitgord and Schouten, 1986) (Fig. 2.3). The onset of drifting caused a major transgression coupled with high subsidence rates that were compensated by thick terrigenous clastic sequences as well as the establishment of a carbonate platform extending over 6000 km from Portugal to Guinea-Bissau. The Jurassic carbonate platform overlapping Triassic sediments and Variscan basement is considered as a post-rift sequence of a Triassic aborted rift (Jansa, 1981; Piqué and Laville, 1996). The

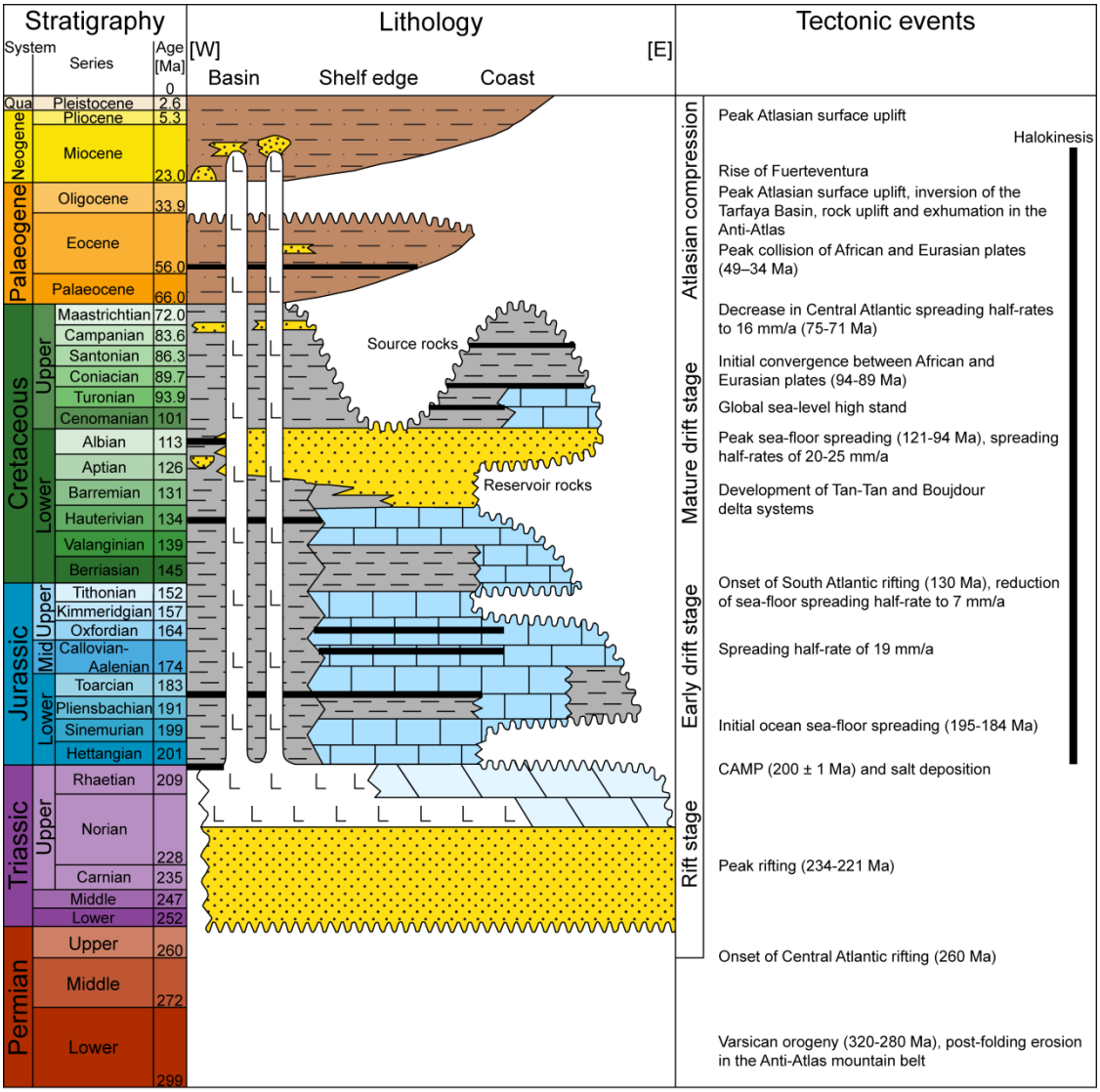

Fig. 2.3: Summary of chrono- and lithostratigraphic features along the Moroccan passive continental margin (modified from Davison, 2005). Tectonic events are taken from Zühlke (2004).

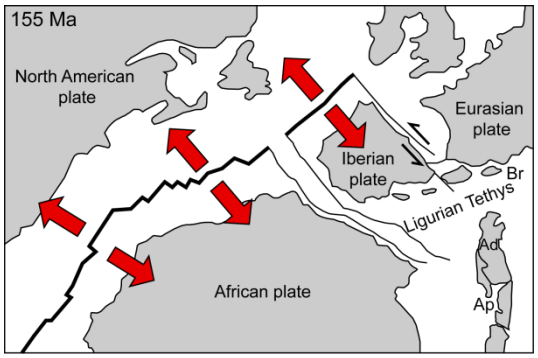

Fig. 2.4: Schematic relative motion of the African, North American and Iberian platein the Upper Jurassic. Ad: Adria; Ap: Apulia; Br: Briançonnais (according to Grobe, 2011; Rosenbaum et al., 2002).

Moroccan passive continental margin was dominated by open marine transgressive conditions till the sea level fall in the Berriasian, whereby the carbonate deposition terminated (Hafid et al., 2008). During the early post-rift period in the Upper Jurassic–Lower Cretaceous, a main stage of erosion took place in the Central Atlantic that yielded a widespread exposure between the Western Meseta and the Anti-Atlas. In the Lower Cretaceous, huge amounts of sediments were deposited in the basins along the entire NW African passive continental margin (Davison, 2005) (Fig. 2.5).

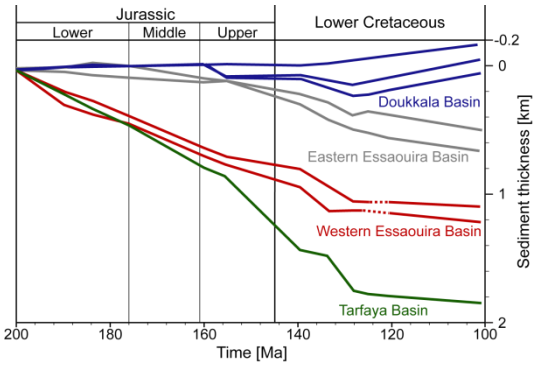

Fig. 2.5: Subsidence curves for different wellsin the Doukkala and Essaouira Basin as well as the Puerto Cansado-1 well in the Tarfaya Basin (according to Le Roy and Piqué, 2001).

The sea level fall lasted until Hauterivian and enabled in large areas the formation of prograde delta systems, unconformably overlying the carbonate platform (Davison, 2005; Hafid et al., 2008; Ranke et al., 1982; von Rad and Wissmann, 1982). A steady rising sea level led to the deposition of a thick Aptian–Albian succession composed of shallow marine, lagoonal and intertidal sediments represented by shales, sandstones and shelly limestones (El Khatib et al., 1995). The high sea level in the Upper Cretaceous–Eocene flooded the majority of Morocco and effected the deposition of marly limestones. Between Palaeocene and Eocene, marine clastic sediments were deposited at the Moroccan passive continental margin overlain by continental clastics of Oligocene age (Davison, 2005).

Since the onset of drifting in the Lower Jurassic, multiple changes in the drift direction emerged due to the opening of the South Atlantic, the rotation and collision of Iberia, the Tethys closure and most comprehensive to the collision of Africa and Iberia during the Rif-Betic orogeny in the Oligocene–Miocene (Michard et al., 2008a). In the Upper Cretaceous (90 Ma), the opening of the South Atlantic Ocean terminated the parallel movement of Africa and southern Eurasia yielding a convergence of the continents (Rosenbaum et al., 2002) (Fig. 2.3). The convergent motion of the African and Eurasian plates resulted in Pyrenees–Alps and Maghrebides–Atlas crustal shortening events that led to the closure of the Tethys Ocean and the formation of the Atlas mountain belt (Michard et al., 2008a). The onset of compressive deformation and related surface uplift in the Atlas system occurred as early as the Senonian, whereby the timing of the inversion is still a matter of debate (Beauchamp et al., 1999; Ellouz et al., 2003; Frizon de Lamotte et al., 2009; Laville et al., 1995). The main inversion of the Mesozoic extensional rift system took place during two distinct stages, (1) in the Middle to Upper Eocene and (2) in the Pliocene–Quaternary, separated by a period of subsidence in the

Oligocene–Miocene (Beauchamp et al., 1999; Beauchamp et al., 1996; Frizon de Lamotte et al., 2000; Frizon de Lamotte et al., 2008; Froitzheim et al., 1988; Giese and Jacobshagen, 1992) (Fig. 2.3, Fig. 2.6). In the Ouarzazate Basin, the onset of continental sedimentation in the Middle Eocene corresponds to the earliest record of Atlas surface uplift (Tesón et al., 2010). The Oligocene–Miocene subsidence episode is attested with the deposition of thick continental molasses unconformably overlain the Atlas system (Frizon de Lamotte et al., 2000). The second phase of compressive deformation and associated surface uplift and relief building in the Atlas system started after the molasse deposition and is still active at present (Frizon de Lamotte et al., 2009). In the compressional tectonic stages, the Atlas belt underwent a NW–SE shortening including the deformation of Neogene continental deposits (Ait Brahim et al., 2002; Morel et al., 2000). The surface uplift of the Atlas belt results from both lithospheric thinning and moderate crustal shortening yielding the rugged topography in the Atlas mountain belt (Babault et al., 2008; Frizon de Lamotte et al., 2009; Missenard et al., 2006; Teixell et al., 2005; Zeyen et al., 2005). The Atlas Mountains constitutes the southernmost edge of the Alpine deformation that is mainly limited to areas north of the South Atlas Fault (SAF). In southern Morocco, e.g. the Anti-Atlas, the Mesozoic–Cenozoic deformation is negligible (Frizon de Lamotte et al., 2000; Helg et al., 2004).

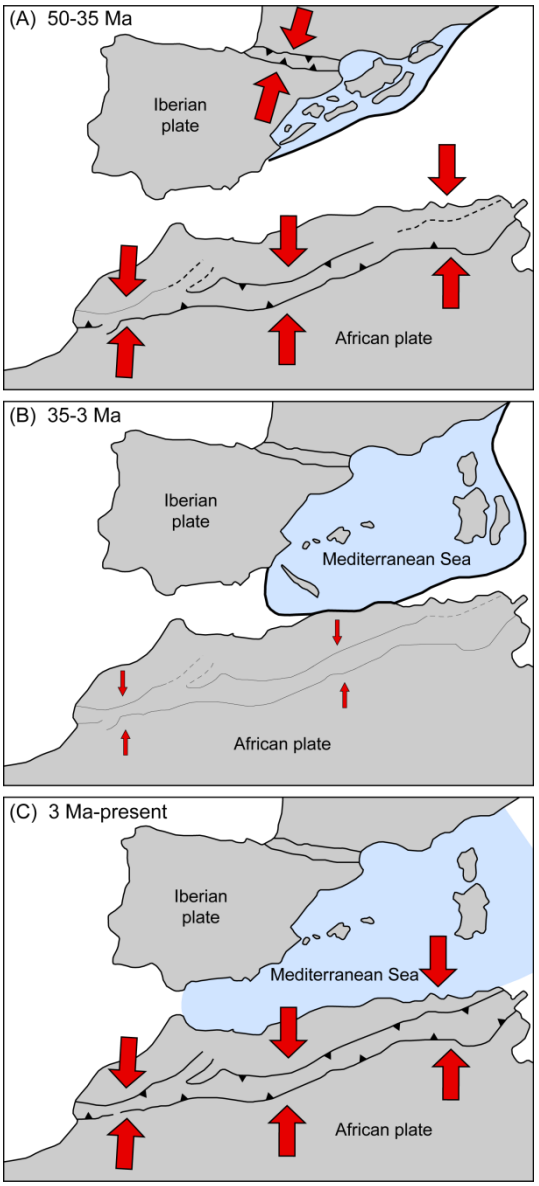

Fig. 2.6: Schematic kinematic scenario of the Maghreb and West Mediterranean since the Eocene. (A) First inversion of the Atlas Basin. (B) Subsidence stage in the Atlas system. (C) Second inversion of the Atlas system (modified from Frizon de Lamotte et al., 2009).

2.3 Tarfaya-Laâyoune-Dakhla Basin – Tarfaya Basin

2.3.1 Overview

The Tarfaya-Laâyoune-Dakhla Basin extends over 1000 km along the western Saharan margin from the Mauritanian border to the Canary Islands in the north. The basin is bounded by the Mauritanides thrust belt (Adrar Souttouf, Dhoul, Zemmour) and Precambrian Reguibat Arch in the SE–E, the Palaeozoic fold belt of the Anti-Atlas in the NE and the East Canary Ridge in the NW (Hafid et al., 2008) (Fig. 2.2, Fig. 2.7). The Tarfaya Basin (TB) is the northern continuation of the Tarfaya-Laâyoune-Dakhla Basin and stretches from Daora to Ifni along the western margin of the Sahara (Davison, 2005). The topography of the TB is dominated by lowlands with elevations of less than 200 m (Fig. 2.8, 2.9 and Fig. 2.10).

2.3.2 Triassic to Neogene subsidence and uplift history

Subsidence analyses have been carried out from different areas of the Tarfaya-Laâyoune-Dakhla Basin indicating vast subsidence since the onset of rifting. The subsidence rates

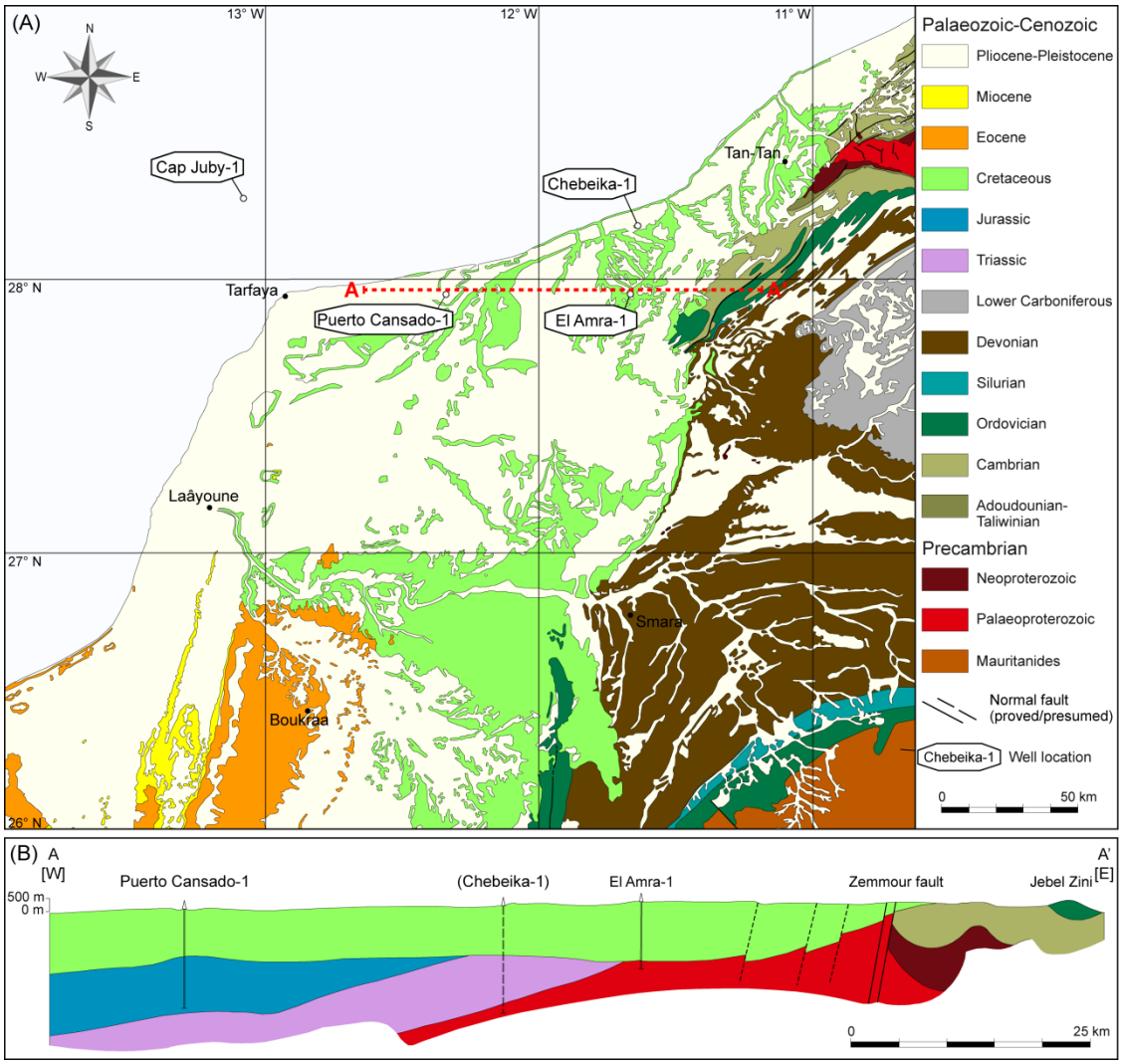

Fig. 2.7: (A) Geological map from the study area of the Tarfaya-Laâyoune-Dakhla Basin. Red dashed line is a cross section (A–A'). (B) Cross section across the northern Tarfaya-Laâyoune-Dakhla Basin (according to Choubert et al., 1966; Ministére de l'Energie et des Mines, 1985).

Fig. 2.8: View from Gor el Berd, close to Smara into the flat topography of the Tarfaya Basin (MA-61, MA-62).

Fig. 2.9: View from Labtaina al Talliya at Oued Saguia el-Hamra into the flat, desertic, sabkha-like landscape of the Tarfaya Basin (MA-69, MA-70).

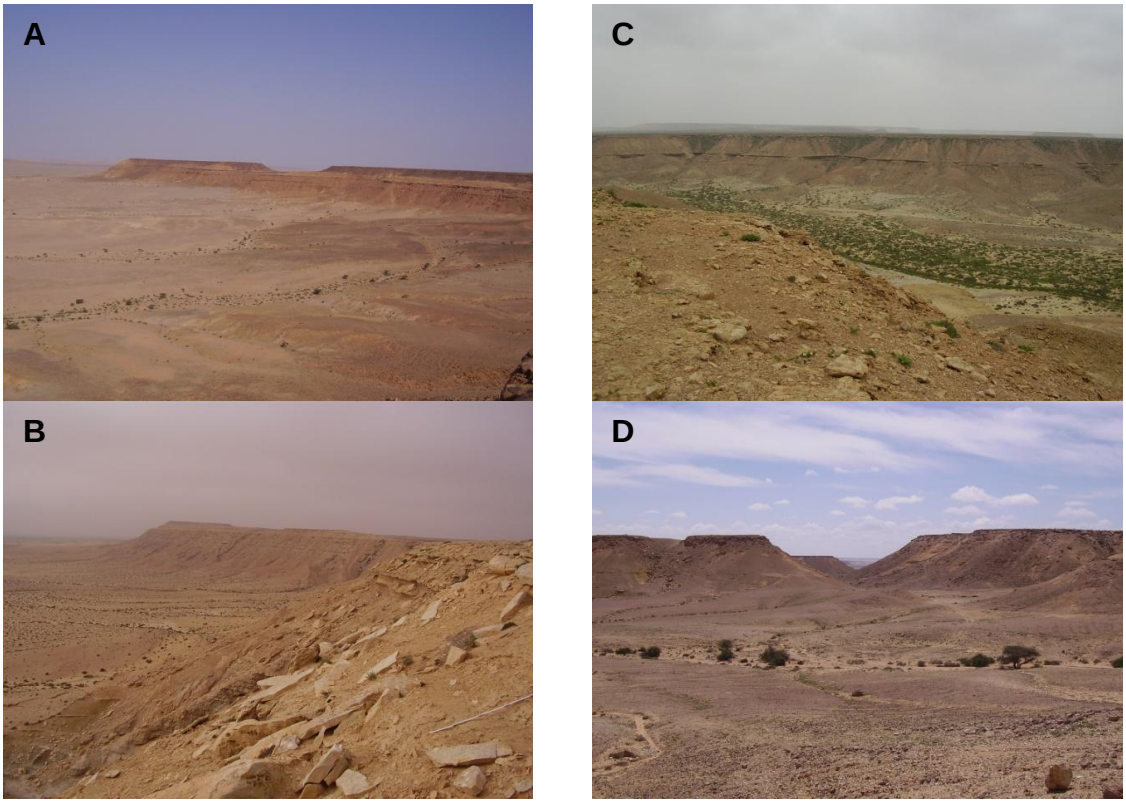

Fig. 2.10: Typical flat, desertic landscape with sabkha-like slopes. (A) View from Gor El Berd, close to Smara (MA-61, MA-62). (B) View from Sabkha La´cal, close to Akhfennir. (C) View from El Ouatia at the Oued Chebeika (MA-73, MA-74). (D) View from Labtaina al Talliya at Oued Saguia el-Hamra (MA-69, MA-70).

presented below have been determined by von Rad and Einsele (1980) in the Boujdour area and Wenke et al. (2013) in the Tan-Tan, Cap Juby and Laâyoune area. In Triassic times, subsidence is strongly dependent on locality with peak subsidence rates of about 250 m/Ma at the outer shelf of the Tan-Tan area (Fig. 2.11). During the early drift stage, subsidence rates reached maximum values of 120 m/Ma in the Boujdour area, 150 m/Ma in the Cap Juby area and 200 m/Ma in the Laâyoune area (Fig. 2.11). The entire basin was affected by massive subsidence with rates of 50–140 m/Ma during the delta formation in the early Lower Cretaceous (Fig. 2.11). Afterwards, the subsidence decreased gradually to < 25 m/Ma in the Upper Cretaceous. The Palaeogene and Neogene is characterised by a diverse subsidence/uplift history. In the Maastrichtian to Lower Oligocene, the peak Atlasian deformation and surface uplift strongly affected the northeastern onshore TB resulting in flexural rock uplift and erosion of the Meso- to Cenozoic succession down to the Lower Cretaceous (Choubert et al., 1966; Wenke et al., 2011, 2013). Besides, von Rad and Einsele (1980) postulated a rock uplift in the Neogene, contemporaneously to the Canary volcanism. A brief subsidence episode is documented in the Early Miocene (~190 m/Ma in the Laâyoune area). Thereafter, the subsidence curves reveal Neogene rock uplift in the entire basin with maximum rates of 80 m/Ma, excluding a subsidence phase in the Laâyoune area during Pliocene–Pleistocene (Fig. 2.11). The Atlasian orogeny is reflected in the Tarfaya-Laâyoune-Dakhla Basin by an increasing periodic influx of detrital material into the offshore part of the basin from Upper Cretaceous onward (Hafid et al., 2008; Wenke et al., 2011, 2013).

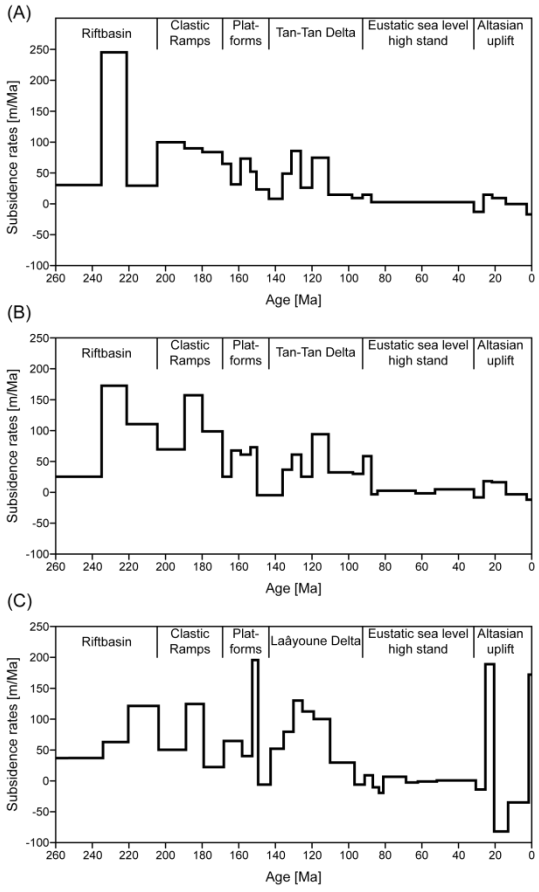

Fig. 2.11: Permian to present day quantitative subsidence history at the outer shelf of the (A) Tan-Tan area, (B) Cap Juby area and (C) Laâyoune area (Wenke et al., 2013).

2.3.3 Structural features

The Tarfaya-Laâyoune-Dakhla Basin is characterised by depressions and block tilting in the SW and in the N by syn-rift graben, half-graben, horsts and W-dipping normal faults overlain by virtually undeformed Jurassic to Cretaceous formations, which form a slightly westward dipping monocline (Abou Ali et al., 2005; El Khatib et al., 1995; Hafid et al., 2008). Main faults in the basin are the Tarfaya transfer fault and the Tiznit fault (Le Roy and Piqué, 2001). In the E of the Tarfaya Basin, the basement is cut by several faults that are believed to represent the reactivated Variscan, E-directed Zemmour thrust separating Anti-Atlas and Tindouf Basin to the east (Choubert et al., 1966; Le Roy and Piqué, 2001) (Fig. 2.7).

2.3.4 Lithologies

The basement of the Tarfaya-Laâyoune-Dakhla Basin consists of Precambrian rocks from the West African Craton (WAC) as well as Pan-

African belt and in the south of Palaeozoic rocks from the Mauritanides unconformably overlain by Meso- to Cenozoic sediments. The thickness of the sedimentary succession exceeds 12 km in the northern onshore basin and decreases southwards to approximately 1 km in Ad Dakhla (Kolonic et al., 2002).

Upper Triassic–Lower Jurassic syn-rift deposits of the Tarfaya Basin were found only in the subsurface (Hafid et al., 2008). The succession is composed of red conglomerates and sandstones, thin bedded red shales and carbonates, evaporites and volcanics (Ranke et al., 1982). The sedimentary succession was deposited under continental to restricted marine conditions and reach a thickness of up to 3 km in the Chebeika-1 well and 5 km in the offshore basin (El Khatib et al., 1995; Heyman, 1989; Le Roy and Piqué, 2001). Upper Triassic evaporites exist only offshore and form the southern extremity of the Moroccan salt basin (Hafid et al., 2008). In the Chebeika-1 well, doleritic basalt lava flows from the CAMP are interbedded in the Triassic succession.

In the Middle–Upper Jurassic, the basin is dominated by the westward progradation of a carbonate platform (El Khatib et al., 1995; Ranke et al., 1982). The thickness varies between 600 m in the Puerto Cansado-1 well and 1700 m in the Amseiquir-1 well, whereby the carbonates only appear in the northern segment of the basin. The maximum transgression occurred in the Oxfordian–Kimmeridgian, while the carbonate platform prevailed up to the Tithonian (Hafid et al., 2008). The carbonates and lagoonal shales of the Jurassic succession provide good source rocks, e.g. in the Cap-Juby area (Davison, 2005; Jabour et al., 2000; Morabet et al., 1998).

The transgression is followed by an important regression from Tithonian to Hauterivian and resulted in the deposition of a 1–4 km thick continental to transitional sequence consisting of predominantly fine-grained clastic sediments that unconformably overlies the carbonate platform (Hafid et al., 2008; Ranke et al., 1982; von Rad and Wissmann, 1982) (Fig. 2.12, Fig. 2.13 and Fig. 2.14).

Fig. 2.12: (A) Albian succession at the mouth of Oued Chebeika. A shallowing upward trend with anoxic, marine sediments at the base, covered by oxic siliciclastics is exposed. (B) Fine-grained sandstone (MA-72).

Fig. 2.13: Aptian–Albian red bed sandstone at Oued Saguia el-Hamra (MA-65).

Fig. 2.14: Lower Cretaceous outcrop from the Tarfaya Basin. The picture is taken from Abteh close to Oued Chebeika (MA-75).

In the Tarfaya-Laâyoune-Dakhla Basin, the sea level fall led to the formation of the prograding

Tan-Tan and Boujdour delta systems (Davison, 2005; Ranke et al., 1982; von Rad and Wissmann, 1982). Several authors proposed that the Tindouf Basin, Reguibat Shield, Mauritanides and the Anti-Atlas constitute source areas for the clastic sediment material of the Lower Cretaceous delta systems (Ali, 2012; Ali et al., 2014; Davison, 2005; Jarvis et al., 1999; Ranke et al., 1982).

A marine transgression began in the Upper Albian and lasted until the Turonian–Lower Coniacian including peaks in the Albian/ Cenomanian, Cenomanian/Turonian and Santonian/Campanian (Kolonic et al., 2002; Kuhnt et al., 2001; Kuhnt et al., 2005). During Albian to Lower Cenomanian, the Tarfaya Basin is characterised by shallow marine to lagoonal sedimentation composed of thinly bedded black marls, claystones, siltstones and dolomitic limestones (Einsele and Wiedmann, 1982; El Khatib et al., 1995; Wiedmann et al., 1982) (Fig. 2.15). The succession of the transgressive Upper Cenomanian–Coniacian consists of deeper-water shales and limestones and is overlain by shallow water oyster shell beds of the Santonian (Davison, 2005) (Fig. 2.16). At the Cenomanian/Turonian boundary appear organic-rich black shales that were deposited during the C/T anoxic event caused by an shelf upwelling along the Atlantic coast (Kolonic et al., 2005; Kuhnt et al., 2001; Kuhnt et al., 2005; Lüning et al., 2004) (Fig. 2.17). The Upper Cretaceous biogenic, marine sediments reach a maximum thickness of 800–1000 m (Kolonic et al., 2002; Kuhnt et al., 2001; Kuhnt et al., 2005; Leine, 1986; Ranke et al., 1982). Sedimentation rates during the Cenomanian–Turonian exceeded 0.001 mm/a for deep areas to approximately 0.005–0.020 mm/a on the continental shelf at the TB (Herbin et al., 1986; Kolonic et al., 2002; Nzoussi-Mbassani et al., 2003; Nzoussi-Mbassani et al., 2005).

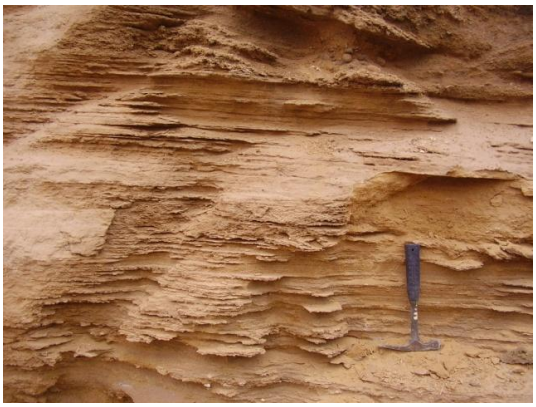

Fig. 2.15: Cenomanian–Turonian silt- to sandstone at the Oued Ma Fatma (MA-79).

Fig. 2.16: Cross stratified Coniacian sandstone overlain by bioturbatic siltstone at Labtaina al Talliya (MA-69, MA-70).

Fig. 2.17: Turonian black shales, covered by Senonian, Miocene and Pliocene–Quaternary siliciclastics at the Oued Ma Fatma (modified after Wenke et al., 2011).

The Palaeocene–Eocene is characterised by thin marine siliceous chalk layers as well as sandy and marly sediments unconformably overlying the Upper Cretaceous (El Khatib et al., 1995) (Fig. 2.18). At the shelf edge an erosional unconformity truncates the Palaeocene, Upper Cretaceous and partially the

Lower Cretaceous. The erosion probably took place in Santonian to Palaeocene times based on the rock uplift of the hinterland and slope reequilibration (Jarvis et al., 1999). The 300 m thick Oligocene continental sandstones and conglomerates occur only in the southern basin due to erosion during a regressive period in the northern part (Davison, 2005). The Palaeogene reaches a maximum thickness of 1 km in the centre of the onshore Tarfaya-Laâyoune-Dakhla Basin and decreases seawards to 200 m (Ranke et al., 1982). The Miocene is dominated by sandy limestones and oyster beds and is exposed onshore only in the western part of the basin (Davison, 2005; Ranke et al., 1982) (Fig. 2.19, Fig. 2.20). The largely thin Miocene succession thickens westwards beyond the shelf edge up to 1000 m (Hafid et al., 2008).

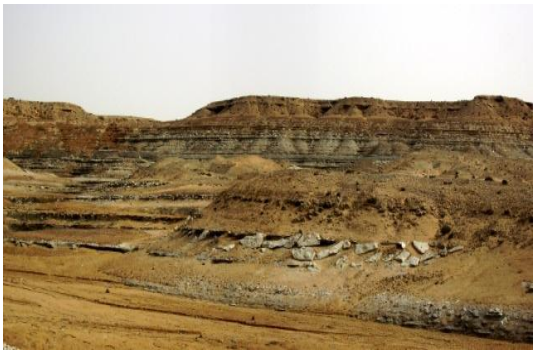

Fig. 2.18: Eocene black shales at the coastline north of Lemsid (MA-57, MA-58).

Fig. 2.19: Miocene fine-grained sandstone at the Sabkha Matmarfag (MA-54, MA-55).

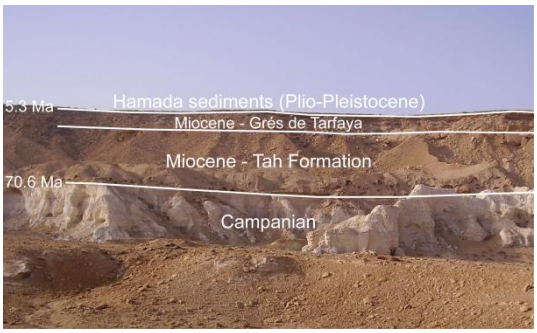

Fig. 2.20: Campanian shales, overlain by Miocene and Plio-Pleistocene siliciclastics at the Sabkha Tah (MA-53).

2.3.5 Hydrocarbon potential of Morocco – Tarfaya Basin

Morocco is for a long time subject of numerous research programmes and exploration studies. Based on the large number of Mesozoic to Cenozoic basins at the Atlantic margin, a promising hydrocarbon potential is suggested. Therefore, the exploration interest in Morocco is focused on the Atlantic margin and several companies drilled exploratory wells (MO-1 to MO-8, Cap Juby-1, El Amra-1 etc.) in the on- and offshore Tarfaya-Laâyoune-Dakhla Basin since the mid-1950s (El Mostaine, 1991; Jarvis et al., 1999; Leine, 1986).

The hydrocarbon potential of Morocco derive from only a few key source rock intervals, the Silurian, Upper Cretaceous and Eocene, whereby the majority of the Silurian petroleum systems are now extinct (Boote et al., 1998; Macgregor, 1996) (Fig. 2.21). Further source rock intervals has been detected in the Devonian, Triassic and Jurassic (Macgregor, 1998) (Fig. 2.21). Despite considerable exploration effort, no large discoveries have been made due to the absence of mature source rocks. Many Moroccan basins contain overmature Palaeozoic and immature Upper Cretaceous/Eocene source rocks (Macgregor, 1996). However, noteworthy oil shows in the Moroccan basins emphasize the possible economic relevance of petroleum systems along the NW African passive continental margin. In the offshore wells Cap Juby-1, MO-2

and MO-8 of the Tarfaya Basin, oil shows appear probably sourced from Upper Triassic, Toarcian or Middle Jurassic intra-shelf carbonate layers (Davison, 2005; Jabour et al., 2000; Macgregor and Moody, 1998; Morabet et al., 1998; ONAREP, 2002, 2003). Productive oil fields exist since the 1970s in the Essaouira Basin, where the source rocks are shales of Oxfordian age (Broughton and Trepanier, 1993; Jabour et al., 2000; Macgregor, 1996). Furthermore oil and gas producing fields are situated in the Rharb and Pre-Rif Basin at the northern Moroccan Atlantic margin.

In the Tarfaya-Laâyoune-Dakhla Basin, several source rocks occur in the Jurassic, Cretaceous and Cenozoic sedimentary units. Wenke et al. (2011) identified 13 potential source rock and 11 reservoir units. In the Jurassic, potential source rocks are Toarcian black shales, Callovian and Upper Oxfordian carbonates of the inner and outer shelf areas (Wenke et al., 2011). The Tan-Tan well shows 60 m of Lower Jurassic source rocks matured during the Lower Cretaceous (Davison, 2005). Based on the burial depth, the Lower Jurassic unit is probably post-mature for hydrocarbon generation in large parts of the basin (Jarvis et al., 1999). Indications for kerogen type-III source rocks of Berriasian and Valanginian age were found in well MO-07 (Ellouz et al., 1998). Evidences for the presence of Upper Hauterivian source rocks are known from the Cap Juby area. Furthermore, certain layers of the Aptian–Albian have source rock potential (Cool et al., 2008; Morabet et al., 1998; Tissot et al., 1980). Sachse et al. (2011) did not found high quality source rocks in the Lower Cretaceous, but indications of petroleum impregnation are existing. However, the vast majority of Mesozoic–Cenozoic source rocks in the Tarfaya Basin derive from two stratigraphic intervals, the Upper Cretaceous (particularly Cenomanian–Turonian) and Eocene (Fig. 2.22, Fig. 2.23). Numerous studies are dealing with the Cenomanian–Turonian organic carbon rich black shales formed during the C/T anoxic event (Kolonic et al., 2002; Kolonic et al., 2005; Kuhnt et al., 2001; Kuhnt et al., 2009; Kuhnt et al., 2005; Lüning et al., 2004). High quality petroleum source rocks with high C_{org} content and hydrogen index (HI) values were found in Cenomanian, Turonian, Coniacian and Eocene samples of the onshore TB (Sachse, 2011; Sachse et al., 2011; Sachse et al., 2012). The source rocks of the Cenomanian–Turonian exist onshore and reach a maximum thickness of 50 m, with varying TOC content between 6 and 20 % (Einsele and Wiedmann, 1982; Herbin et al., 1986; Kuhnt et al., 1990; Sachse et al., 2011; Sachse et al., 2012; Wiedmann et al., 1982). Coniacian as well as Eocene samples of the onshore TB reached C_{org} content of up to 9 %, Santonian samples of up to 13 % (Sachse et al., 2011; Sachse et al., 2012). TOC content from Albian to Campanian black shales of the offshore TB reach maximum values of 12 % (Cool et al., 2008). Vitrinite reflectance data of Cenomanian, Turonian,

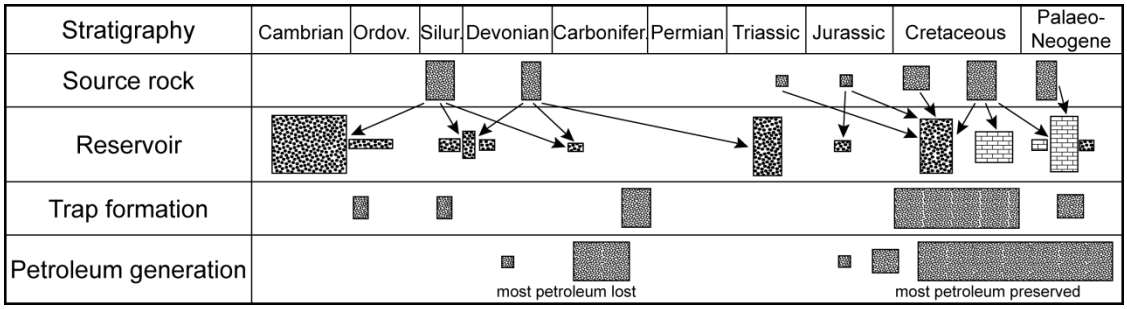

Fig. 2.21: Composite petroleum systems of Morocco. Boxes are sized according to the relative importance of the various reservoirs, source rocks and events (modified after Macgregor, 1998).

Fig. 2.22: Turonian black shales at Oued Ma Fatma.

Fig. 2.23: Eocene black shales at the coastline north of Lemsid.

Coniacian and Santonian samples from the TB range between 0.3 and 0.4 %, Campanian samples showed VR_r values of 0.4–0.7 % and Eocene samples of 0.5 %, indicating immature to early mature organic matter (Sachse et al., 2014; Sachse et al., 2011; Sachse et al., 2012).

The main reservoirs of the Tarfaya-Laâyoune-Dakhla Basin are Triassic–Jurassic deepwater clastic sediments, Jurassic talus slope deposits, Lower Cretaceous basin-floor sandstones and turbidite sands in the deep water fans of the Boujdour and Tan-Tan Deltas as well as Palaeocene to Oligocene turbidite sandstones (Jarvis et al., 1999; Macgregor and Moody, 1998; Ranke et al., 1982; von Rad and Sarti, 1986; Wenke et al., 2013) (Fig. 2.21).

The generation of structural traps in the TB is dominated by the principal mechanism of the halokinesis (Jarvis et al., 1999). Due to the salt movement in the Jurassic salt flank and drape anticline, traps are common in the TB (Jarvis et al., 1999). The main traps are carbonate build-ups (Macgregor and Moody, 1998). Furthermore, main exploration targets are sporadic roll-over structures of the Albian generated along listric faults and Maastrichtian carbonate reservoirs (Heyman, 1989; Jabour et al., 2000; Morabet et al., 1998).

2.4 Anti-Atlas

2.4.1 Overview

The ENE-trending Anti-Atlas (AA) mountain belt extends from the Atlantic Ocean over 500 km into the Moroccan interior and shows a rugged topography achieving elevations up to 3300 m a.s.l. and a plateau height of 1800 m a.s.l. (Fig. 2.1, Fig. 2.2, Fig. 2.24 and Fig. 2.27). In the north, the mountain belt is bounded by a reactivated Variscan fault system, the South Atlas Fault (SAF) that separates the High Atlas

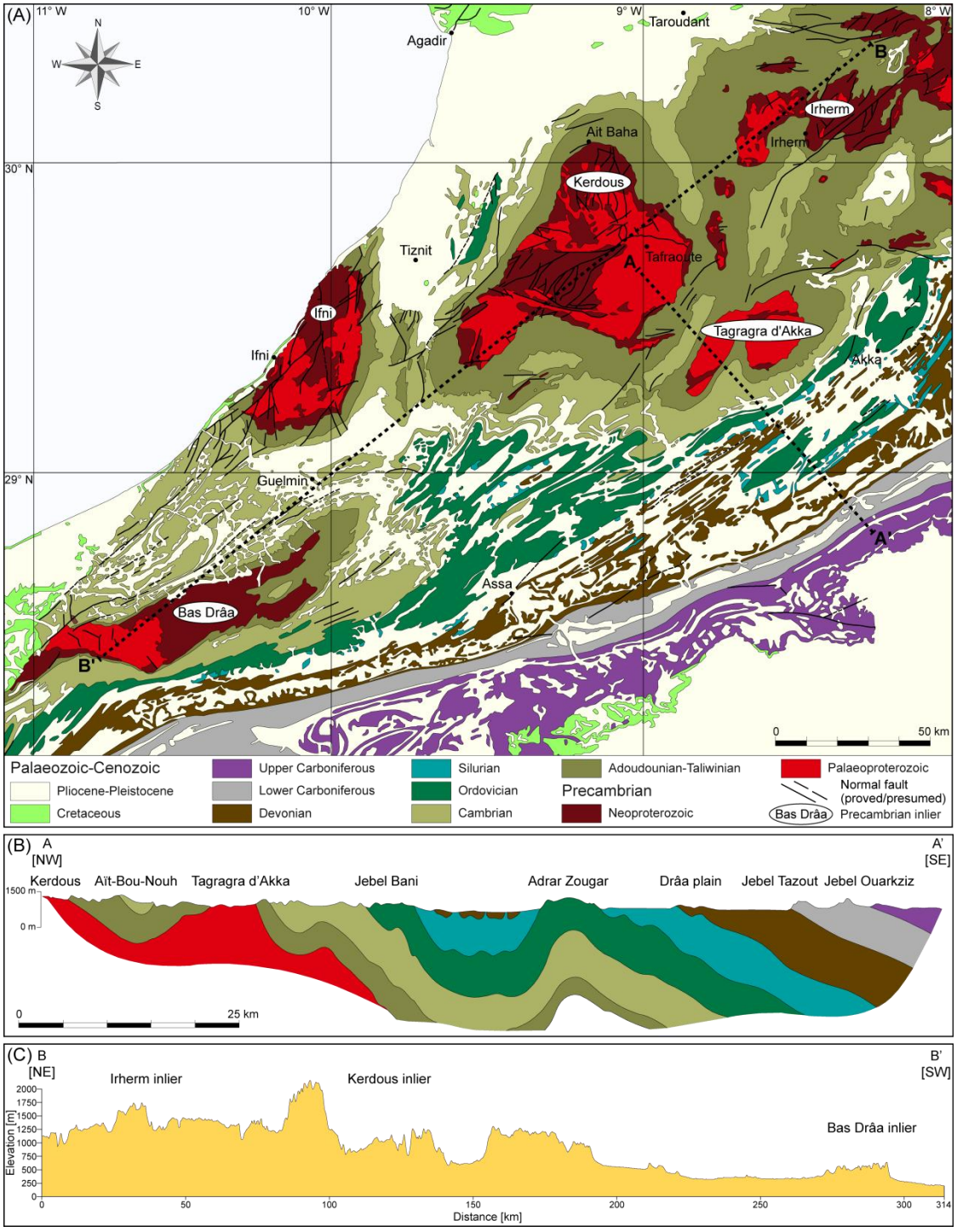

Fig. 2.24: (A) Geological map from the study area of the western Anti-Atlas. Black dashed lines are geological (A–A') and topographic (B–B') cross sections. (B) Geological cross section across the western Anti-Atlas (according to Michard, 1976; Ministére de l'Energie et des Mines, 1985). (C) Topographic cross section.

(HA) and Anti-Atlas (Fig. 2.2). The AA is divided at the Anti-Atlas Major Fault (AAMF) in an eastern and western part (EAA, WAA), characterised by slightly contrasting lithostratigraphic columns (Fig. 2.2). Due to the Eburnean basement, the metacratonic western Anti-Atlas

Fig. 2.25: Folded Precambrian to Cambrian of the western Anti-Atlas. The picture is taken close to Irherm.

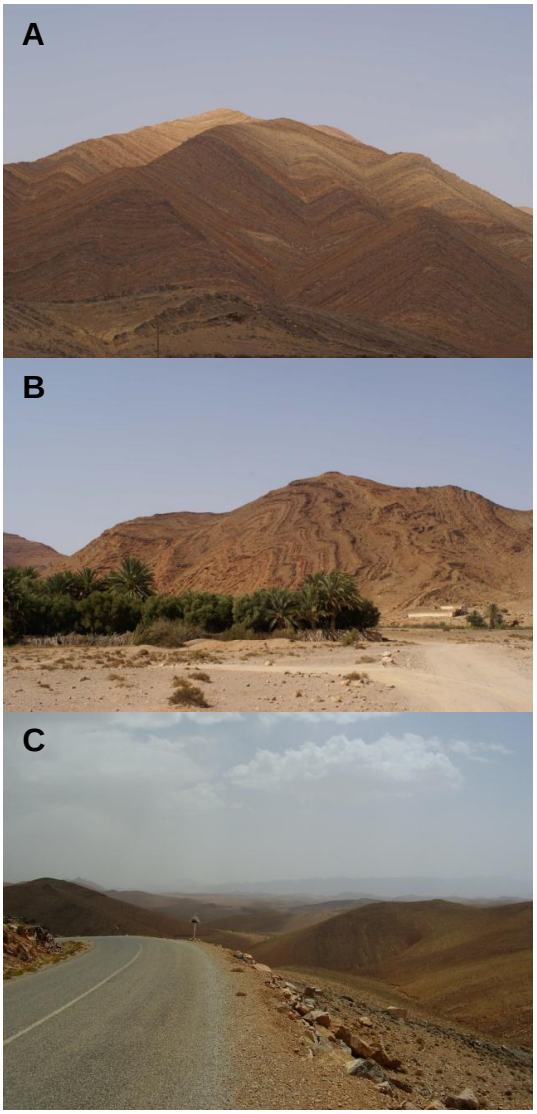

Fig. 2.26: Folded Precambrian to Cambrian of the western Anti-Atlas. (A) Picture is taken close to Irherm. (B) View from the Bas Drâa inlier. (C) Picture is taken at the eastern Kerdous inlier, close to Tafraoute.

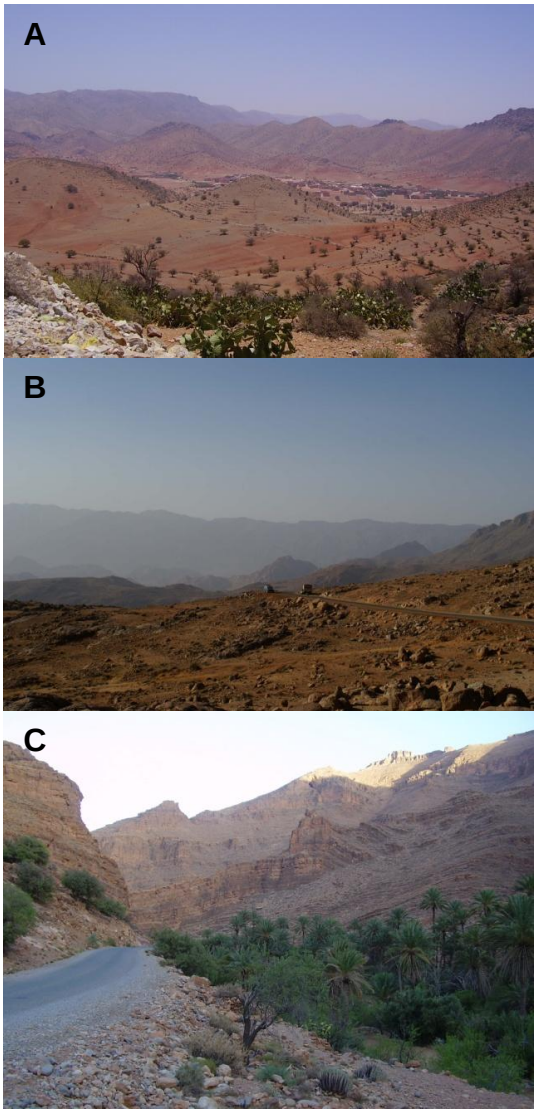

Fig. 2.27: Landscape from the western Anti-Atlas. (A) Typical rugged topography of the western Anti-Atlas. Picture is taken from a small village between Tanalt and Tarcouate in the western Kerdous inlier. (B) Rough, desertlike landscape between Tafraoute and Âït Mansour. (C) Deeply incised canyon and oasis of Âït Mansour, formed by the Oued Sidi Mansour.

marks the northern rim of the West African Craton (WAC), whereas Palaeoproterozoic exposures are lacking east of the AAMF (Gasquet et al., 2008) (Fig. 2.24). The AA forms the southern Phanerozoic foreland of two intracontinental mountain belts, (1) the Late Palaeozoic North African Variscides and (2) the Cenozoic Atlas belt and consists of numerous widespread Precambrian basement inliers surrounded by a thick Palaeozoic sedimentary succession that are folded during the Alleghenian–Variscan orogeny (Burkhard et al., 2006; Frizon de Lamotte et al., 2000; Hoepffner et al., 2006; Hoepffner et al., 2005; Pique and Michard, 1989) (Fig. 2.2, Fig. 2.24, Fig. 2.25 and Fig. 2.26). The inliers are structural culminations of the Variscan fold belt and form a large NE–SW trending anticline (Helg et al., 2004; Michard et al., 2008b) (Fig. 2.2, Fig. 2.24). The anticline could arise from buckling and thermal doming caused by a baby plume (Fullea et al., 2010) or the controversial flow of Canary mantle plume material (Berger et al., 2010; Duggen et al., 2009).

2.4.2 West African Craton – Pan-African belt

The West African Craton (WAC) extends over millions of square kilometres in the Sahara Desert from the Ivory Coast in the south across Mali and Mauritania and is bounded by the Anti-Atlas mountain belt as well as the Algerian Ougarta in the north. The crystalline basement crops out in the Precambrian inliers of the WAA and the Reguibat Shield, whereas it is overlain by a thick layer of virtually undeformed sediments in the Tindouf Basin and large parts of the Anti-Atlas (Fig. 2.24). The WAC formed at the amalgamation of three Archean terranes during the Eburnean orogeny (2.1–2.0 Ga). It is suggested that the Eburnean orogeny represents a major tectonic impulse of crustal growth connected with the emergence of the hypothetical supercontinent Columbia (Bertrand and Jardim de Sá, 1990; Rodgers and Santosh, 2002).

In the Neoproterozoic, the WAC was mainly affected by the Pan-African event, whereby Proto-Gondwana emerged, followed by a collision event of Proto-Gondwana, Proto-Laurasia and Congo Craton enabling the establishment of the hypothetical supercontinent Pannotia (Dalziel, 1997). The Pan-African belt surrounding the WAC formed in two main phases between 750–660 Ma and 630–560 Ma (Gasquet et al., 2008; Michard et al., 2008a). In Morocco, the belt is only exposed with low-P-metamorphic units in the Precambrian inliers of the AA. Subduction and collision processes are well described with obduced ophiolites and island arcs in the Siroua and Bou Azzer inliers (Saquaque et al., 1989; Thomas et al., 2002).

In the Late Ediacaran–Lower Cambrian, the Anti-Atlas area was affected by post-Pan-African extensional tectonics with the formation of numerous widespread graben and half-graben structures (Algouti et al., 2001; Benssaou and Hamoumi, 2003; Burkhard et al., 2006; Pique et al., 1999). Tholeiitic–alkaline volcanism in the Lower Cambrian points to an intracontinental setting (Burkhard et al., 2006). The rifting was active until Lower Carboniferous and resulted in the vast subsidence of the Anti-Atlas Basin and the WAC (Burkhard et al., 2006; Michard et al., 2008b). Until the end of this phase up to 12 km of mainly shallow marine fine-grained clastic deposits accumulated in the northern WAC and the former Pan-African belt (Burkhard et al., 2006; Helg et al., 2004; Michard et al., 2008b) (Fig. 2.28). The delivery area of the huge clastic sedimentation could be the widespread Hoggar Shield that was affected by magmatism and rock uplift since the Cambrian (Michard et al., 2008a).

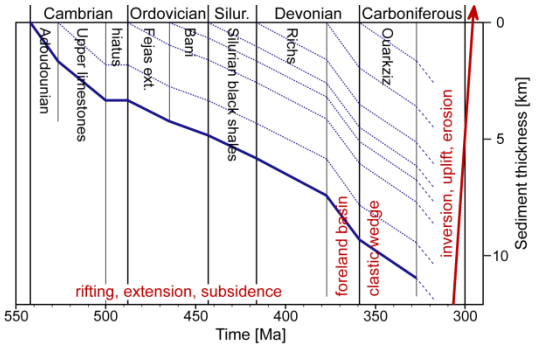

Fig. 2.28: Sediment accumulation curve for the western Anti-Atlas between Guelmin and Foum El Hassan. The recent sediment thickness is compiled from a variety of stratigraphic literature data regarding the western Anti-Atlas. Relevant formation names and events are displayed at the top and bottom of the chart (according to Burkhard et al., 2006).

2.4.3 Variscan to Neogene uplift and exhumation history

The rock uplift and exhumation of the Precambrian basement and the erosion of the Palaeozoic cover is mainly related to three major tectonic episodes: (1) the Variscan orogeny in the Upper Carboniferous–Lower Permian, (2) exhumation in the Triassic–Jurassic, as the AA formed the denudation shoulder of the Central Atlantic rift and (3) in the Upper Eocene–Pleistocene linked to the surface uplift of the Atlas belt (Burkhard et al., 2006; Gasquet et al., 2008; Helg et al., 2004).

The Variscan compression with a main shortening direction of NW–SE yielded intense inversion and folding of the Palaeozoic Anti-Atlas Basin (Burkhard et al., 2006). The folding is dominated by upright detachment folds, whereas thrusting structures are lacking except for the westernmost AA along the Atlantic coastline (Belfoul et al., 2001; Helg et al., 2004). K-Ar and zircon fission-track data from the western Anti-Atlas (WAA) confirm rock uplift and exhumation of the Precambrian basement in the Upper Carboniferous associated with the Variscan folding and post-folding erosion (Bonhomme and Hassenforder, 1985; Margoum, 2001; Sebti et al., 2009; Soulaimani and Piqué, 2004). The post-folding erosion of the WAA correlates with northwestern source areas of the detrital input in the Jebel Reounia sandstones (Upper Namurian) of the Tindouf Basin, suggesting that the rock uplift and erosion of the western Anti-Atlas has been started as early as ~320 Ma (Cavaroc et al., 1976; Michard et al., 2008b; Sebti et al., 2009). The Mauritanides orogen dated at 330–310 Ma as well as the western Meseta domain show also ages of Variscan folding (Hoepffner et al., 2006; Lecorche et al., 1991; Michard et al., 2008a).

Based on the lack of Meso–Cenozoic successions in the AA, the post-Variscan tectonics is difficult of explanation. The AA was affected by vertical movements in the Upper Permian–Lower Triassic caused by the Central Atlantic and Tethys rifting (El Arabi et al., 2006; Knight et al., 2004). Various authors supposed the last significant rock uplift in the AA during Triassic rifting and Lower to Middle Jurassic transtensional tectonic processes related to sedimentation in the High Atlas system and offshore (El Arabi et al., 2006; Hafid et al., 2008; Laville et al., 2004). Therefore, the AA is suggested as the denudation shoulder of the Central Atlantic rift, but even a connection with the Atlas rift is feasible (El Harfi et al., 2006; Malusà et al., 2007).

In contrast to the Tindouf Basin, Tarfaya-Laâyoune-Dakhla Basin, Meseta and High Atlas, Cretaceous to Middle Eocene deposits are lacking in the Anti-Atlas as well as the northern part of the Middle Atlas. Choubert (1948) proposed a 200 km wide E–W seaway in Cenomanian–Turonian times at the present High Atlas, southern Middle Atlas and Western Meseta between two elevated areas, the Anti-Atlas in the south and the northern Middle Atlas. This interpretation is disputable since the Cenomanian–Turonian series of the High Atlas, Meseta and Middle Atlas are devoid of any coastal facies suggesting the proximity of a shoreline northward or southward (Charrière

et al., 2009; Frizon de Lamotte et al., 2008). Hence, a flooding of the entire northern Morocco, including the AA area during Cenomanian–Turonian is more probable (Michard et al., 2008b). Zouhri et al. (2008) postulated that the Anti-Atlas was covered by shallow marine Cenomanian–Turonian carbonates eroded during Senonian–Cenozoic times. The erosion phase is documented in the Tindouf Basin, where the Cretaceous series are truncated by the Miocene–Pliocene molasses (Frizon de Lamotte et al., 2009). Preserved Cretaceous–Palaeogene deposits reach 1–2 km in the Atlantic basins and the Meseta, which is probably a minimum value because of post-deposition Atlasian denudation (Hafid et al., 2008; Hafid et al., 2006; Mustaphi et al., 1997; Saddiqi et al., 2009; Zühlke et al., 2004). Therefore, a Cretaceous–Eocene sedimentary pile of 1.5 km is thus realistic for the western Anti-Atlas (Ruiz et al., 2011). If the entire Moroccan territory was overlain by Cretaceous deposits, the northern Middle Atlas, the Anti-Atlas and the Reguibat Shield look like wide anticlines with intermediate synclines in the Meseta, High Atlas and the Tindouf Basin originated by a lithosphere folding referable to N–S compression consistent with the Africa–Eurasia convergence (Frizon de Lamotte et al., 2009; Teixell et al., 2003).

Whereas high elevations in the Atlas mountain belt are due to Cenozoic crustal shortening during the convergence of Africa and Eurasia, the Anti-Atlas is considered to have undergone minor Alpine deformation (Frizon de Lamotte et al., 2004; Frizon de Lamotte et al., 2000; Helg et al., 2004; Missenard et al., 2006; Teixell et al., 2005) even though Neogene transpressional faulting is documented in its eastern segment (Malusà et al., 2007). Ruiz et al. (2011) and Burkhard et al. (2006) proposed that the present-day topography of the western AA is the result of a recent slight exhumation and erosion starting in the Oligocene (30 Ma). Altogether, the Anti-Atlas mountain belt is a key natural laboratory as it is possibly the southernmost expression of the Alpine deformation.

2.4.4 Lithologies

The Precambrian basement inliers of the Anti-Atlas mountain belt consist of a large variety of magmatic, metamorphic and sedimentary rocks. The oldest rocks are Palaeoproterozoic low- to medium-grade metasedimentary series and intrusive granitoids assigned to the Eburnean orogeny (2 Ga) (Ait Malek et al., 1998; Gasquet et al., 2008; Soulaimani and Piqué, 2004; Walsh et al., 2002) (Fig. 2.29).

Fig. 2.29: Precambrian granite (2 Ga). (A) Granite outcrop at Âït Mansour (MA-13). (B) Hand specimen of the rose porphyric granite at Tarcouate (MA-17).

U-Pb ages of zircons from granitoids of the Irherm, Bas Drâa, Kerdous and Tagragra de Tata inliers range between 2.0 and 2.1 Ga (Ait Malek et al., 1998; Walsh et al., 2002). Microgranites and pegmatites of the Kerdous and Tagragra de Tata inliers have been dated at 1.8 Ga (Gasquet et al., 2004). Subsequently, in the

Tonian–Cryogenian the deposition of a sedimentary cover of quartzites and limestones occurred (Lkest/Taghdout Group) that were deformed and recrystallized during the Pan-African orogeny (685–660 Ma) (Gasquet et al., 2008; Sebti et al., 2009). Between 610 and 550 Ma several granitoid generations intruded in the Pan-African mountain belt (Fig. 2.30, Fig. 2.31). The Neoproterozoic magmatism is confirmed by U-Pb data from the Bas Drâa and Kerdous inliers ranging from 560 to 583 Ma (Ait Malek et al., 1998). The youngest units of the Precambrian inliers are slightly deformed late- and post-orogen volcano-sedimentary series (Anezi and Ouarzazate/ Tanalt Group) dated at 550–570 by U-Pb geochronology that unconformably overlie the Eburnean and Pan-African sequences (Sebti et al., 2009; Soulaimani et al., 2004; Thomas et al., 2002). The Anezi formation is characterised by alluvial fans, fluvial deposits, volcanic rocks and granitoids with a thickness of up to 2000 m, while the Ouarzazate/Tanalt Group consist of breccias, conglomerates and volcanic rocks with a maximum thickness of 800 m (Soulaimani and Piqué, 2004).

Fig. 2.30: Precambrian diabase (600 Ma) at Khmes aït Oufka (MA-09).

Fig. 2.31: Precambrian granite (600 Ma) at Tarsouale (MA-12). (A) Mafic xenoliths (Gabbro) in granite. (B) Hand specimen of the porphyric granite.

The Precambrian basement is conformably overlain by Upper Ediacaran–Lower Cambrian (Adoudounian) carbonates and siltstones, followed by Cambrian to Ordovician siliciclastic series, Silurian shales and Devonian carbonates, sandstones and shales, folded during the Variscan orogeny (Burkhard et al., 2006; Sebti et al., 2009; Soulaimani and Burkhard, 2008; Soulaimani et al., 2004). The Palaeozoic succession was primarily deposited under shallow marine conditions. During Middle Cambrian–Upper Silurian times, the sedimentation was dominated by a detrital input, followed by Upper Silurian–Devonian carbonate deposition and a renewed increase in detrital input during Lower Carboniferous times (Burkhard et al., 2006; Michard et al., 1982; Pique and Michard, 1989; Wendt, 1985). The Palaeozoic succession reaches a thickness of at least 10 km in the westernmost Anti-Atlas near Tiznit, a thickness of 8–10 km in the central AA and decreases to approximately 6 km in the easternmost AA (Burkhard et al., 2006; Faik et al., 2001; Michard et al., 2008b; Michard et al., 2010; Ruiz et al., 2008).

2.5 Thermochronological data of Morocco

Low-temperature thermochronological data are quite scarce in northwest Africa as well as the Central Atlantic passive margin. In Morocco, only a few data from the Central and Marrakech High Atlas, the western Meseta and the Anti-Atlas are published (Fig. 2.32).

Whereas thermochronological data of the Tarfaya-Laâyoune-Dakhla Basin are still lacking, Ruiz et al. (2011) presented apatite and zircon (U-Th-Sm)/He ages (AHe and ZHe) as well as apatite fission-track ages (AFT) of Precambrian rocks from the westernmost basement inliers Kerdous, Ifni and Irherm of the Anti-Atlas (Fig. 2.24, Fig. 2.32). In this study, AFT ages of the Kerdous inlier range between 143 (±11) and 173 (±23) Ma, whereas AFT ages from the Ifni inlier are slightly younger varying from 121 (±8) to 141 (±9) Ma. AHe ages from the Irherm inlier cover a range between 58 (±1) and 148 (±2) Ma and ZHe ages of the same samples from 193 (±15) to 248 (±20) Ma. To determine the post-Variscan rock uplift history of the WAA, Sebti et al. (2009) performed zircon fission-track (ZFT) analyses on Precambrian granites and schists of the Kerdous and Ifni inliers. The ZFT ages range between 319 (±32) and 358 (±31) Ma in the Kerdous inlier and from 327 (±37) to 338 (±35) Ma in the Ifni inlier. These data are consistent with K-Ar ages (white micas, biotite) varying between 291 (±7) and 357 (±9) Ma of the Kerdous inlier and the Lakhssas Plateau (Bonhomme and Hassenforder, 1985; Margoum, 2001; Soulaimani and Piqué, 2004). Thermochronological data indicate a common geological evolution in the western Anti-Atlas with a burial of 7–9 km of the Precambrian inliers in the Carboniferous (Ruiz et al., 2011; Sebti et al., 2009). K-Ar and ZFT ages are assigned to the Variscan folding, followed by rapid exhumation and cooling related to the post-folding erosion. The t-T modelling

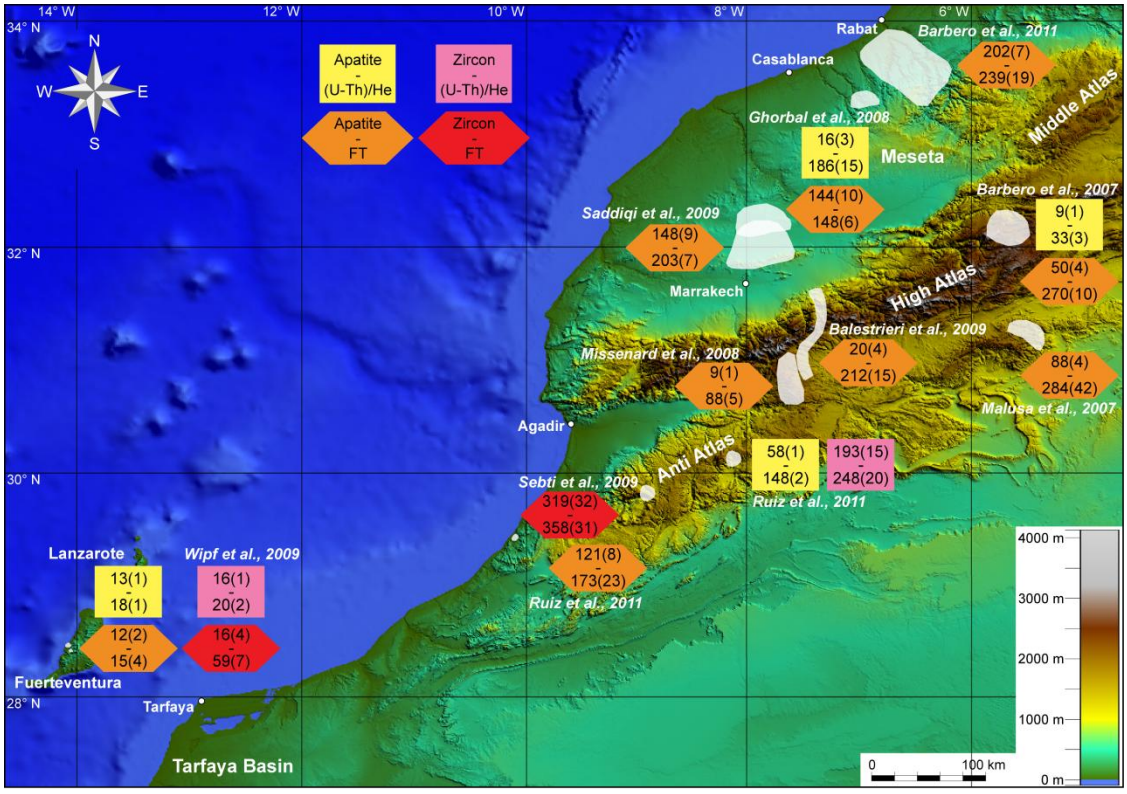

Fig. 2.32: Overview of the published low-temperature thermochronological data from Morocco. White transparent areas are sampling areas of the respective study. Digital elevation model (DEM) derived from Aster GDEM.

performed by Ruiz et al. (2011) shows a slow cooling in the Upper Triassic to Lower Cretaceous. Based on the overall Cenomanian–Turonian transgression across North Africa, the models reveal a subsidence phase during Cretaceous–Eocene followed by a final cooling from 30 Ma until recent times (Frizon de Lamotte et al., 2009; Guiraud et al., 2005; Ruiz et al., 2011). In the eastern Anti-Atlas, AFT ages cover a range between 88 (±4) and 284 (±42) Ma (Malusà et al., 2007). The Variscan units have been buried beneath 3 km overburden before the Mesozoic. Thermal models point to a very slow Mesozoic–Palaeogene cooling and a fast Neogene exhumation between Upper Miocene–Pliocene (Malusà et al., 2007).

Furthermore, thermochronological analyses have been carried out in the High Atlas and the Moroccan Meseta. Barbero et al. (2011) presented AFT ages from the western Meseta ranging between 202 (±7) and 239 (±18) Ma, whereas Ghorbal et al. (2008) published a younger AFT age of 148 (±6) Ma from the same Precambrian granitic body. In the southwestern Meseta, AFT ages vary between 144 (±10) and 153 (±18) Ma in the Rehamna Massif and from 186 (±5) to 203 (±7) Ma in the Jebilet Massif (Ghorbal et al., 2008; Saddiqi et al., 2009). AHe data of the western and southwestern Mesta reveal a vast spread from 16 (±3) to 186 (±15) Ma (Ghorbal et al., 2008). The t-T modelling shows a heating phase from Upper Triassic to Lower Jurassic simultaneously to the main stage of Central Atlantic rifting and the associated major subsidence in the High Atlas, Middle Atlas and the Atlantic rift (Barbero et al., 2011; Ghorbal et al., 2008; Lancelot and Winterer, 1981; Saddiqi et al., 2009). Ghorbal et al. (2008) emphasized that the subsidence affected an area stretching from the Atlantic margin to the Atlas. Subsequently, a cooling event between Upper Jurassic–Lower Cretaceous occurred (Ghorbal et al., 2008; Saddiqi et al., 2009). Similar to the WAA, the western Meseta underwent a phase of burial during Upper Cretaceous–Eocene with a maximum depth of 1–2 km (Barbero et al., 2011; Ghorbal et al., 2008; Saddiqi et al., 2009). Ghorbal et al. (2008) suggested that the subsidence involved a larger area from the northern Atlas belt to the Rif mountains. Published AFT data from the Central and Marrakech High Atlas show a very large spread between 9 (±1) and 270 (±10) Ma (Balestrieri et al., 2009; Barbero et al., 2007; Missenard et al., 2008). AHe ages from the Central High Atlas cover a range from 9 (±1) to 33 (±3) Ma (Barbero et al., 2007). Thermal modelling suggests that the main surface uplift and major denudation event in the Central and Marrakech High Atlas results from thermal doming as well as crustal shortening coupled with the Africa–Eurasia convergence in the Lower to Middle Miocene (Balestrieri et al., 2009; Barbero et al., 2007; Missenard et al., 2008).

Wipf et al. (2010) presented thermochronological data of Lower Cretaceous sedimentary and Neogene magmatic rocks from Fuerteventura, Canary Islands. In this study, AHe, AFT and ZHe ages are in the same order of magnitude varying between 12 (±2) and 20 (±2) Ma, whereas ZFT ages are obviously older ranging from 16 (±4) to 59 (±7) Ma. AHe, AFT, ZHe as well as several ZFT data are referred to a Lower Miocene magmatic event and a subsequent rapid cooling with rates of 50–70 °C/Ma. ZFT ages of Lower Cretaceous sediments indicate a reheating event in the Eocene linked with the initial island formation stage. This event started with a slow cooling from 50 to 20 Ma, followed by a rapid cooling at 20 Ma related to the Miocene magmatic phase.

2.6 Crustal and lithospheric thickness, geothermal gradients and heat flow densities of Morocco

Recent works, based on geophysical modelling of gravity, geoid, topography and heat flow data confirmed the existence of a thinned lithosphere under the Anti-Atlas, the High Atlas and Middle Atlas (Frizon de Lamotte et al., 2004; Missenard et al., 2006; Teixell et al., 2005; Zeyen et al., 2005). In the WAC, the lithosphere attains a thickness of 250 km, whereas the metacratonic areas at the border of the WAC reveal a thickness of 130–150 km (Michard et al., 2008a). Geophysical models show that the lithosphere–asthenosphere boundary (LAB) is situated at ~110–130 km depth below the western Anti-Atlas (Fullea et al., 2010; Ruiz et al., 2011). The lithosphere thins down to 60–80 km in a NE-oriented corridor underneath the central and eastern Anti-Atlas, High Atlas and Middle Atlas (Frizon de Lamotte et al., 2004; Fullea et al., 2010; Missenard et al., 2006; Teixell et al., 2005; Zeyen et al., 2005). This assumption provides an explanation for the high present-day topography of the Atlas belt. The average crustal thickness of the AA mountain belt reaches approximate values of 30–35 km (Frizon de Lamotte et al., 2004; Michard et al., 2008a).

Since Morocco exhibit a large variety of geological formations due to its geographical position, an enormous spread in the geothermal gradient and heat flow density (HFD) can be observed. The geothermal gradient ranges between approximately 12 and 50 °C/km (Rimi, 1990, 2000; Zarhloule et al., 2005) (Tab. 2.1). The maximum values of 30–50 °C/km und 70–110 mW/m^2 (HFD) are reached in northeastern Morocco (Rimi, 1990, 2000, 2001; Rimi and Lucazeau, 1987) (Fig. 2.33, Tab. 2.1). The southern Central Atlantic margin, the Rif mountains and the Middle Atlas constitute the Moroccan regions with the highest crustal temperatures, whereas the Anti-Atlas show the lowest temperatures indicating no significant thermal or tectonic reactivation since the Precambrian (Rimi, 1999). Geothermal gradients and heat flow densities of Moroccan regions are presented in Figure 2.33 and Table 2.1.

The geothermal gradient along the Atlantic margin varies between 23–34 °C/km, whereas the Tarfaya-Laâyoune-Dakhla Basin reveals a slightly lower gradient of 20–30 °C/km (Rimi, 1990). The appreciable increase of the

Table 2.1: Geothermal gradients and heat flow densities of Moroccan regions (Rimi, 1990, 1999, 2000, 2001; Rimi et al., 1998; Rimi and Lucazeau, 1987; Zarhloule et al., 2005)

Locality		Geothermal Gradient [°C/km]	Heat flow [mW/m^2]
Northeastern Morocco		30–50	70–110
Southwestern Rif		20–34	50–90
Meseta		16–24	60–65
High plateaus		16–30	60
Atlantic margin		23–34	65–85
Tarfaya-Laâyoune-Dakhla Basin		20-30	60-90
Wells:	Chebeika-1		54
	Puerto Cansado-1		78
	Cap Juby-1		87
Anti-Atlas		12–16, 20–25	36–40
Wells:	Oum Doul-1		83
	Adrar Zougar-1		85
Tindouf Basin		20–34	70–100

gradient offshore towards the Canary Islands can be explained by the intensive hot spot volcanism (Rimi, 2001; Zarhloule et al., 2005) (Fig. 2.33). In the Tindouf Basin, a large spread in the gradient of 20–34 °C/km was determined (Rimi, 1990). Geothermal gradients as well as heat flow densities at Precambrian shields are in general substantially lower compared to other continental areas. In the southern WAC, the gradient ranges between 10 and 15 °C/km, while the HFD is about 37 (±8) mW/m^2 (Brigaud et al., 1985). Comparable with the WAC and further metacratonic areas, the AA mountain belt shows a very low gradient of 12–16 °C/km (Rimi, 1990). In contrast, Ruiz et al. (2011) and Zarhloule et al. (2005) recommended a geothermal gradient of 20–25 °C/km for the western Anti-Atlas based on the lithosphere thickness (Fig. 2.33, Tab. 2.1). Except for the AA, southern Morocco is characterized by high heat flow densities. In the Tarfaya-Laâyoune-Dakhla Basin, the HFD varies between 60–100 mW/m^2 due to numerous well data ranging from 54 to 88 mW/m^2 (Rimi, 1990, 1999, 2000). An E–W trending heat flow density anomaly with a mean value of 80–100 mW/m^2 extends from the Canary Islands across the Tindouf Basin to the southern Algerian Sahara (Lucazeau et al., 1988; Rimi, 1990). Consistent with data from the WAC, the average HFD of the Anti-Atlas reveal a considerably lower value of 36–40 mW/m^2 (Rimi, 1999; Rimi and Lucazeau, 1987).

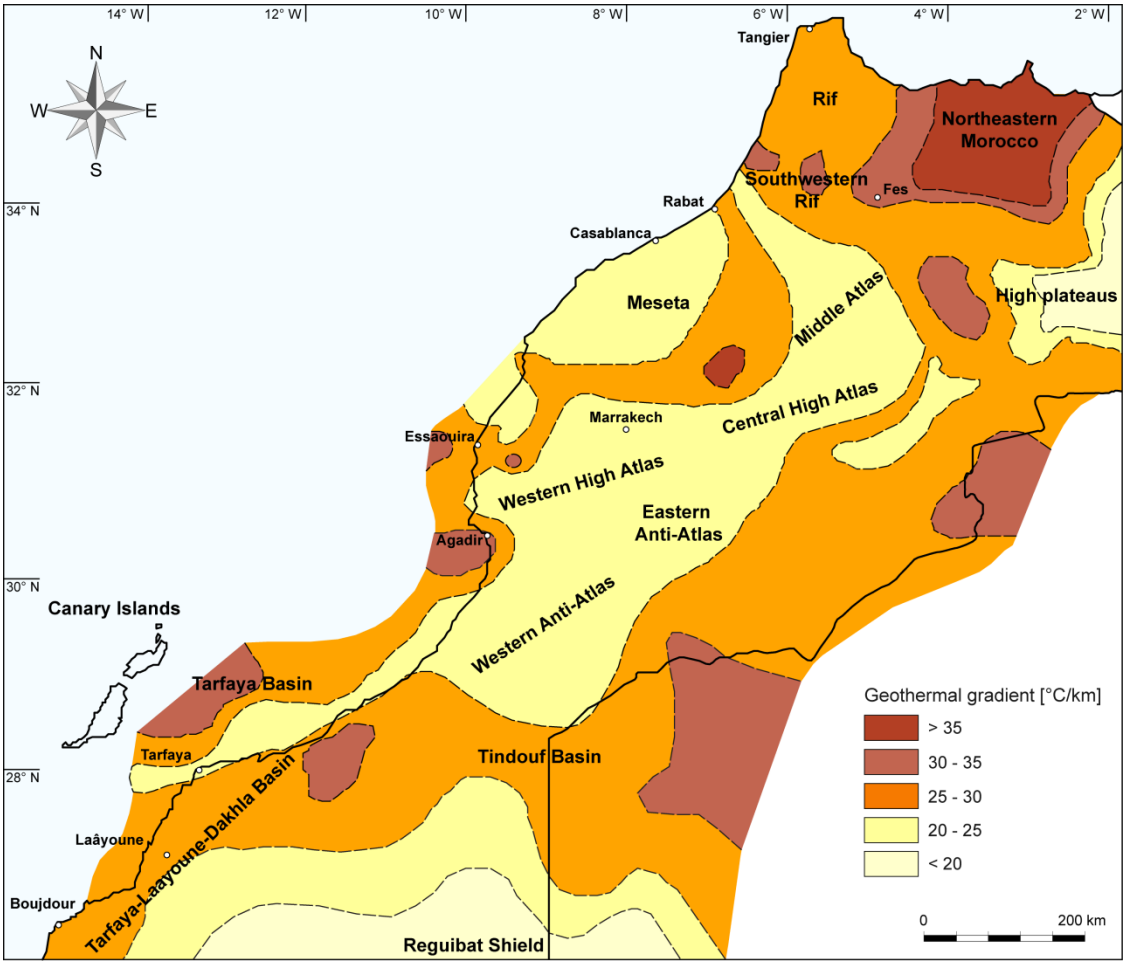

Fig. 2.33: Geothermal gradient map of Morocco (modified from Zarhloule et al., 2005).

3

METHODOLOGY

Contents

3.1 Low-temperature thermochronology

Thermochronological methods, such as (U-Th-Sm)/He and fission-track (FT) dating, are based on the production of an isotope or radiation damage, respectively, resulting from nuclear decay, and the subsequent, thermally controlled retention of these decay products. Reiners and Brandon (2006) described that these thermal sensitivity of thermochronometers and thereof revealed ages provide information about the cooling history of the rock, rather than the crystallization ages of its minerals.

As other radiometric dating methods, low-temperature thermochronology is subject to the general decay equation (1), describing the decay of natural radiogenic mother isotopes (N) to measurable decay products (daughter isotopes or radiation damages) (D).

$$D = D_0 + N(e^{\lambda t} - 1) \qquad (1)$$

t: *Age of the sample*
D: *Quantity of daughter products*
D_0: *Quantity of daughter isotope in the original composition*
N: *Quantity of mother isotope*
λ: *Decay constant*

Based on the assumption that radiogenic mother isotopes disintegrate to stable daughter products, the sample age, where the radiometric system is thermodynamically closed, can be calculated by the general age equation (2).

$$t = \frac{1}{\lambda} ln\left(1 + \frac{D}{N}\right) \qquad (2)$$

Substitution of D with the density of spontaneous fission-tracks $\rho_s=\lambda_f/\lambda_d N(e^{\lambda dt}-1)$ and N with the density of induced fission-tracks $\rho_i=^{238}NI\sigma\phi$ yields the age equation of fission-track dating (Galbraith and Laslett, 1993; Hurford and Green, 1982; Wagner and Van den Haute, 1992) (3).

$$t = \frac{1}{\lambda_\alpha} ln\left[1 + \frac{\lambda_\alpha \rho_s Q G I \sigma \phi}{\lambda_f \rho_i}\right] \qquad (3)$$

t: *Age of the sample*
ρ_s: *Density of spontaneous fission-tracks*
ρ_i: *Density of induced fission-tracks*
λ_α: *Decay constant for α-emission of ^{238}U, $1.55125 \times 10^{-10} a^{-1}$ (Jaffey et al., 1971)*
λ_f: *Spontaneous fission decay constant of ^{238}U, $\sim 8.5 \times 10^{-17} a^{-1}$ (Wagner and Van den Haute, 1992)*
λ_d: *Total decay constant of ^{238}U, $\lambda_f + \lambda_\alpha$*
I: *Isotopic ratio $^{235}U/\ ^{238}U$, 7.2527×10^{-3} (Cowan and Adler, 1976)*
σ: *Thermal neutron fission cross section for ^{235}U, 580.2×10^{-24} cm^2 (Hanna et al., 1969)*
ϕ: *Thermal neutron fluence*
Q: *Procedure factor for etching conditions and individual counting of the operator*
G: *Geometry factor (0.5 for the external detector method)*

The basic foundation of the (U-Th-Sm)/He technique is the accumulation of ^{4}He due to the α-decay of ^{238}U, ^{235}U, ^{232}Th, their daughter products and ^{147}Sm. The decay equation is (Farley, 2002) (4):

$$^4He = 8\ ^{238}U\left(e^{\lambda_{238} t} - 1\right) + 7\left(\frac{^{235}U}{137.88}\right)\left(e^{\lambda_{235} t} - 1\right) + 6\ ^{232}Th\left(e^{\lambda_{232} t} - 1\right) + {}^{147}Sm\left(e^{\lambda_{147} t} - 1\right) \qquad (4)$$

t: *Accumulation time or He age*
λ: *Decay constant ($\lambda_{238} = 1.551 \times 10^{-10} a^{-1}$, $\lambda_{235} = 9.849 \times 10^{-10} a^{-1}$, $\lambda_{232} = 4.948 \times 10^{-11} a^{-1}$, $\lambda_{147} = 6.54 \times 10^{-12} a^{-1}$) (Farley, 2002; Lugmair and Marti, 1978)*

3.1.1 Fission-track thermochronology

Apatite (AFT) and zircon fission-track thermochronology (ZFT) is based on the spontaneous fission of ^{238}U, during which the heavy fragments of this fission create chemically etchable linear defects in the crystals (Wagner, 1972) (Fig. 3.1).

Fission-tracks are metastable in relation to time and temperature. The annealing of spontaneous fission-tracks is governed by temperature and the time the apatite and zircon grains have been kept at a certain temperature.

In apatite, the fission-tracks anneal completely at temperatures above 110 °C/10 Ma. The isotherm is referred to as the closure temperature (T_c) of the system, based on the concept of other geochronological techniques where the mineral becomes "closed" to the diffusion of the daughter product below a certain temperature (Dodson, 1973; Dodson, 1979; Ravenhurst and Donelick, 1992). Below 110 °C/10 Ma fission-tracks in apatite partially anneal up to 60 °C/10 Ma, where the annealing is virtually zero. Consequently, the AFT system is sensitive to the temperature range between 110–60 °C/10 Ma, called the partial annealing zone (PAZ) (Gleadow and Fitzgerald, 1987).

Information on the thermal history of apatite is stored in two archives: the etch pit areal density at an artificially polished internal surface and the length distribution of horizontal confined tracks (Lisker et al., 2009; Wagner and Van den Haute, 1992).

The temperature sensitive annealing of fission-tracks in apatite is kinetically constrained by two important effects: (1) the chemical composition of the apatite (i.e. Cl/F-ratio) and (2) the crystallographic orientation of the tracks. Both kinetic parameters are routinely determined.

Whereas fluorine rich apatites totally anneal at 90–110 °C/10 Ma, chlorine rich apatites anneal between 110 °C/10 Ma and 150 °C/10 Ma. Besides electron microprobe measurements of the chemical composition, the etch pit diameter (D_{par}) has been shown as an alternate parameter that represents the chlorine and fluorine content of individual apatite crystals, with Cl-rich apatites showing larger etch pits than fluorapatite (Barbarand et al., 2003; Donelick, 1993, 1995; Sobel and Seward, 2010). In the thermal modelling software 'HeFTy', D_{par} can be used as a kinetic parameter (Ketcham, 2005; Ketcham et al., 2007a, b; Ketcham et al., 2009).

Furthermore, the crystallographic orientation affects the annealing, as tracks parallel to the c-axis anneal slower than tracks orthogonal to

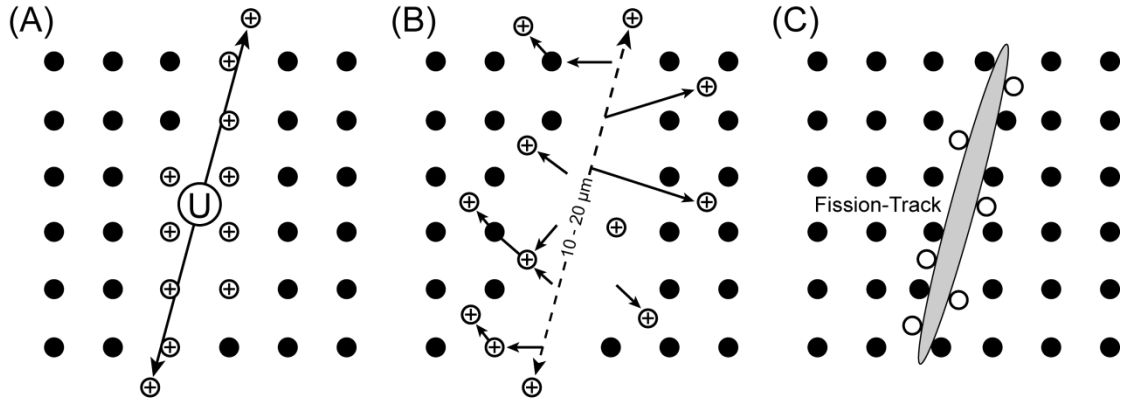

Fig. 3.1: Schematic illustration of fission-track formation according to the 'ion explosion spike' theory of Fleischer et al. (1975). (A) Ionisation of the lattice atoms by the moving charged particle. (B) Positive charged ions repel each other, creating a cylindrical zone of disordered structure. (C) Formed fission-track (redrafted after Dickin, 2005; Ravenhurst and Donelick, 1992; Wagner and Van den Haute, 1992).

the c-axis (Donelick et al., 1999; Green, 1981, 1988; Green and Durrani, 1977; Laslett et al., 1984). This anisotropy increases with annealing (Donelick et al., 1999; Green, 1981; Laslett et al., 1984). The database on crystallographic effects of annealing in apatite are integrated in recent annealing models (Donelick, 1991; Donelick et al., 1999; Donelick et al., 1990; Ketcham, 2003; Ketcham et al., 2007a, b; Ketcham et al., 1999). In this study, the confined fission-track lengths were corrected for their crystallographic orientation by applying the computer code 'HeFTy' to the data set (Ketcham et al., 2007a).

In zircon, beside temperature the annealing kinetics is controlled by the degree of metamictisation which can be determined by Raman spectroscopy. Metamictisation is caused by interaction of the alpha particle and the alpha-recoil nucleus with the crystal lattice of zircon (Geisler et al., 2001; Nasdala, 2009; Vance, 1975; Zhang et al., 2008; Zhang et al., 2009). The alpha-particle creates point defects and the alpha recoil nucleus creates large areas of amorphisation, mostly nest-shaped. The amount of alpha-particle and alpha-recoil nucleus within the crystal lattice of zircon is a function of the uranium and thorium content. Alpha-particle and alpha-recoil nucleus anneal at a higher temperature than fission-tracks in zircon (Nasdala et al., 2004; Nasdala et al., 2001). Therefore, the total annealing temperature of zircon decrease from 330 °C/10 Ma to 190 °C/10 Ma with increasing metamictisation (Garver, 2002; Garver and Kamp, 2002; Rahn et al., 2004; Reiners and Brandon, 2006). Various other authors discussed the partial annealing zone of fission tracks in zircon as ranging between ~300 °C/10 Ma and 200 °C/10 Ma (Brix et al., 2002; Garver, 2002; Hasebe et al., 2003; Rahn et al., 2004; Reiners and Brandon, 2006; Tagami et al., 1996; Yamada et al., 2003; Yamada et al., 2007; Yamada et al., 1995). The interpretation of the ZFT ages will consider the uranium concentration as a broad indicator for the possible temperature the samples have experienced. Nevertheless, for a full description of the metamictisation, the Th-content has also to be taken under consideration.

3.1.2 (U-Th-Sm)/He thermochronology

The (U-Th-Sm)/He thermochronology of apatite (AHe) and zircon (ZHe) is based on the accumulation of ^{4}He due to the α-decay of ^{238}U, ^{235}U, ^{232}Th, their daughter products and ^{147}Sm. Related to mineral specific diffusion parameters and the duration of a certain temperature, apatite and zircon are characterized by a closure temperature (T_c) and a partial retention zone (PRZ) at a specific holding time.

The closure temperature of mineral grains is dependent on the activation energy (E), a geometric factor for the crystal form (A), the thermal diffusivity (D_0), the length of the average diffusion pathway from the interior to the surface of the grain (a) and the cooling rate at closure temperature (Dodson, 1973). The crystal size itself represents the effective diffusion domain in apatites, with larger crystals having a higher closure temperature (Farley, 2000; Reiners and Farley, 2001).

In apatite, the T_c is ~70 °C/1 Ma for a simple monotonic cooling rate of 10 °C/1 Ma and a subgrain domain size of > 60 µm and the partial retention zone (PRZ) ranges from 40 °C/1 Ma to 70 °C/1 Ma (Farley, 2000; Farley et al., 1996; Wolf et al., 1998; Wolf et al., 1996).

In zircon grains with an effective radius of 60 µm and a cooling rate of 10 °C/1 Ma, the He diffusion data yield closure temperatures of 171–196 °C, with an average of 183 °C/1 Ma (Reiners et al., 2002; Reiners et al., 2004).

Various complicating factors in the (U-Th-Sm)/He thermochronology may cause false cooling ages and a large variety in the single grain aliquot ages of a sample.

Since α-particles travel approximately 25 µm in

apatite and 20 µm in zircon after being emitted with high kinetic energy during the decay of U and Th, α-particles may be ejected out of a crystal or injected into a crystal from decay in surrounding grains. Therefore, an α-ejection (F_t) correction is needed for the compensation of the lost or gained helium fraction (Farley, 2000; Farley et al., 1996; Wolf et al., 1996). This correction factor strongly depends on grain size and shape, but includes high, generally unknown errors, which are believed to be as high as 20 %.

Current studies deal with the recently introduced correction for radiation damage (Flowers et al., 2009; Flowers et al., 2007; Shuster and Farley, 2009; Shuster et al., 2006). The ^{4}He diffusion in apatite is impeded by radiation-induced damage to the crystal structure (Shuster et al., 2006). Their model predict that the effective ^{4}He closure temperature of apatite will vary with cooling rate and effective U concentration [5], but may differ from the commonly assumed T_c of ~70 °C by up to ±15 °C (Shuster and Farley, 2009; Shuster et al., 2006; Spiegel et al., 2009).

$$eU = [U] + 0.235[Th] + 0.0053[Sm] \quad (5)$$

The eU factor characterizes the dependency of ^{4}He-diffusion on the amount of accumulated crystal defects created by the movements of the fission products and the alpha-recoil nucleus in the crystal lattice.

In apatite, radiation damage leads to increased cooling ages (Shuster and Farley, 2009; Shuster et al., 2006). According to Reiners et al. (2004) and Reiners (2005) the influence of radiation damage on ZHe ages is minor as long as U concentrations are less than ~1000 ppm. At higher U concentrations, a rapid decrease in the He ages is observable.

Depending on the amount of radiation damage and cooling history of the hosting rock, the He diffusivity of a zircon can either be decreased, as He is trapped, resulting in a positive correlation with the eU content or the He diffusivity can increase as numerous traps are connected, resulting in a negative correlation (Guenthner and Reiners, 2010). Such an inverse correlation can be seen by plotting the ZHe age as a function of eU (Reiners, 2005). If such a negative correlation trend is envisaged in the data, the low-eU zircons are the most reliable ones to give a meaningful ZHe cooling age.

Beside radiation damage, older apatite ages are believed to be caused by U-/Th-rich inclusions or fluid inclusions that might not completely dissolved during sample digestion, zonation, variation in grain size or related to slow cooling through the PRZ (Fitzgerald et al., 2006; Reiners and Farley, 2001). To avoid these factors only appropriate crystals (inclusion- and crack-free with accurate grain size) were selected. Based on old AHe ages, Fitzgerald et al. (2006) recommended the calculation of a weighted mean age and the determination of a 'most representative age'.

In the present study, the youngest AHe aliquot ages and the ZHe ages with the lowest eU concentration were used for further interpretation and discussion.

3.2 Sampling strategy

Two field campaigns were carried out within this project. In June–July 2008 started the first field campaign with the sampling of six wells in the ONHYM facilities, followed by a field trip in the western Anti-Atlas mountain belt and the northern Tarfaya Basin (Fig. 3.2). The second field trip in March 2009 was focused on the Tarfaya–Laâyoune Basin between Tan-Tan in the north, Boujdour in the south and Smara in the east (Fig. 3.2).

In total, 100 samples were collected and prepared for thermochronological analyses, composed of 34 samples from the Anti-Atlas and 66 samples from the Tarfaya Basin.

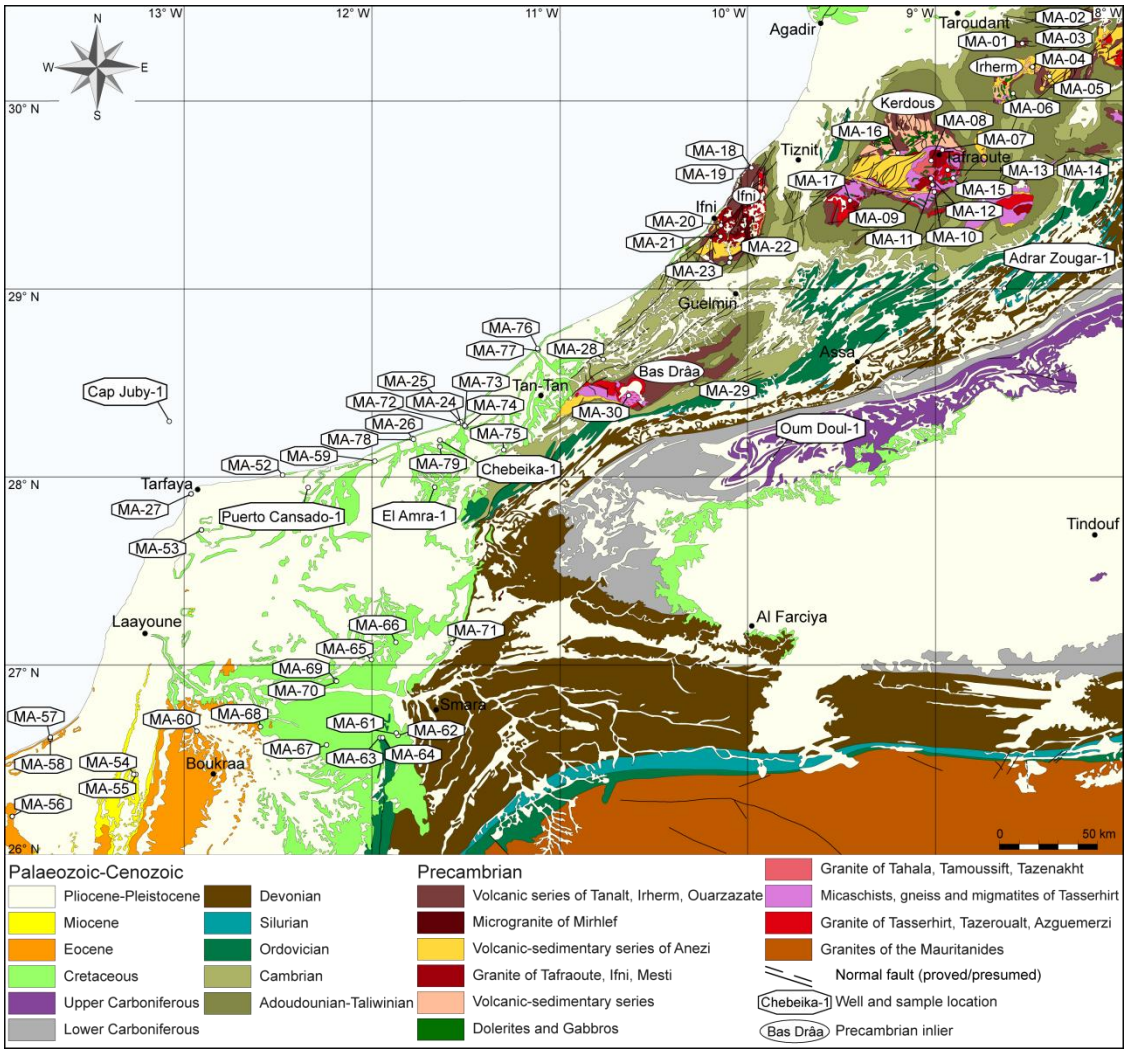

Fig. 3.2: Geological map of the western Anti-Atlas and Tarfaya Basin with sample and well locations.

To determine the thermal and exhumation history of potential source areas for the Tarfaya Basin, Precambrian inliers from the western Anti-Atlas were sampled (Fig. 3.2). The landscape of the Anti-Atlas mountain belt is characterized by a complex topography with a large distribution of elevations of up to approximately 2000 m above sea level in the study area. Therefore, 23 samples were taken from various elevations between 60 and 1885 m a.s.l. (Tab. 4.20). Samples were collected from different Precambrian lithologies (2000–550 Ma), including mainly magmatic rocks like granite, rhyolite, gabbro and diabase as well as siliciclastic metasedimentary rocks of the four westernmost basement inliers Irherm, Kerdous, Ifni and Bas Drâa (Fig. 3.2, Tab. 4.20).

The wells Oum Doul-1 and Adrar Zougar-1, located in the southwestern Anti-Atlas at the boundary to the Tindouf Basin, have been drilled in Precambrian to Palaeozoic metasedimentary rocks (Fig. 3.2, Fig. 3.3). Whenever drill cuttings were available, samples were taken from medium- to coarse-grained siliciclastic sediments over the entire drilling profile. The five samples from the Oum Doul-1 well are of Devonian to Lower Carboniferous age (Fig. 3.3, Tab. 4.21). In the Adrar Zougar-1 well, six samples were collected from the Precambrian to Middle Ordovician succession (Fig. 3.3, Tab. 4.21).

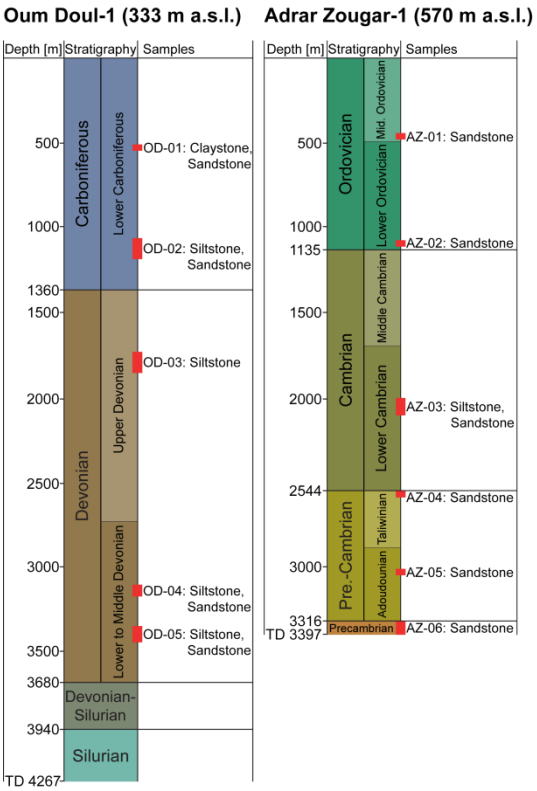

Fig. 3.3: Schematic stratigraphic profile from wells Oum Doul-1 and Adrar Zougar-1 of the western Anti-Atlas with sample positions.

In the Tarfaya Basin, 35 outcrop samples were taken for the determination of the time–temperature development and Provenance analysis (Fig. 3.2). Due to the flat topography of the Tarfaya Basin with elevations of less than 400 m a.s.l., an elevation-dependent sampling strategy could be neglected. The outcrop samples were collected from sandstones and conglomerates ranging between Lower Cretaceous and Pleistocene age and from siliciclastic metasedimentary rocks of Lower Ordovician age (Fig. 3.2, Tab. 4.1).

The three sampled onshore wells El Amra-1, Chebeika-1 and Puerto Cansado-1, situated in the northern Tarfaya Basin, have been drilled in the Mesozoic succession and the Precambrian basement (Fig. 3.2, Fig. 3.4 and Fig. 3.5). The offshore well Cap Juby-1 contains the Mesozoic to Cenozoic succession (Fig. 3.5). Whenever drill cores or cuttings were available samples were taken from medium- to coarse-grained siliciclastic sediments over the entire drilling profile (Fig. 3.5). 26 samples from the four wells are sandstones, siltstones and conglomerates of Triassic to Lower Cretaceous age and two samples of Miocene age (Fig. 3.5, Tab. 4.2). Furthermore two samples were taken from siliciclastic metasedimentary rocks of the Precambrian basement. In the Chebeika-1 well, one sample was collected from a diabase of the CAMP intruded in the Triassic succession.

Fig. 3.4: Drill core and cutting boxes from wells Cap Juby-1, Puerto Cansado-1 and Chebeika-1, ONHYM facilities, Rabat.

3.3 Sample processing - preparation

Sample processing followed the standard heavy mineral separation techniques (Grist and Ravenhurst, 1992a, b; Stockli, 2005).

To avoid any contamination and due to the drilling fluids in the cuttings, all samples were washed and subsequently dried in an oven with a maximum temperature of 30 °C. Outcrop samples of about 3 kg were crushed with a rock splitter. Additionally, a hand specimen was stored. Further crushing of the outcrop samples as well drill core samples were performed by a jaw crusher. After crushing, samples were sieved and particles < 300 µm were separated for the shaking table (Wilfley table). Particles > 300 µm of outcrop and drill core samples as well as drill cuttings were further processed with a roller mill

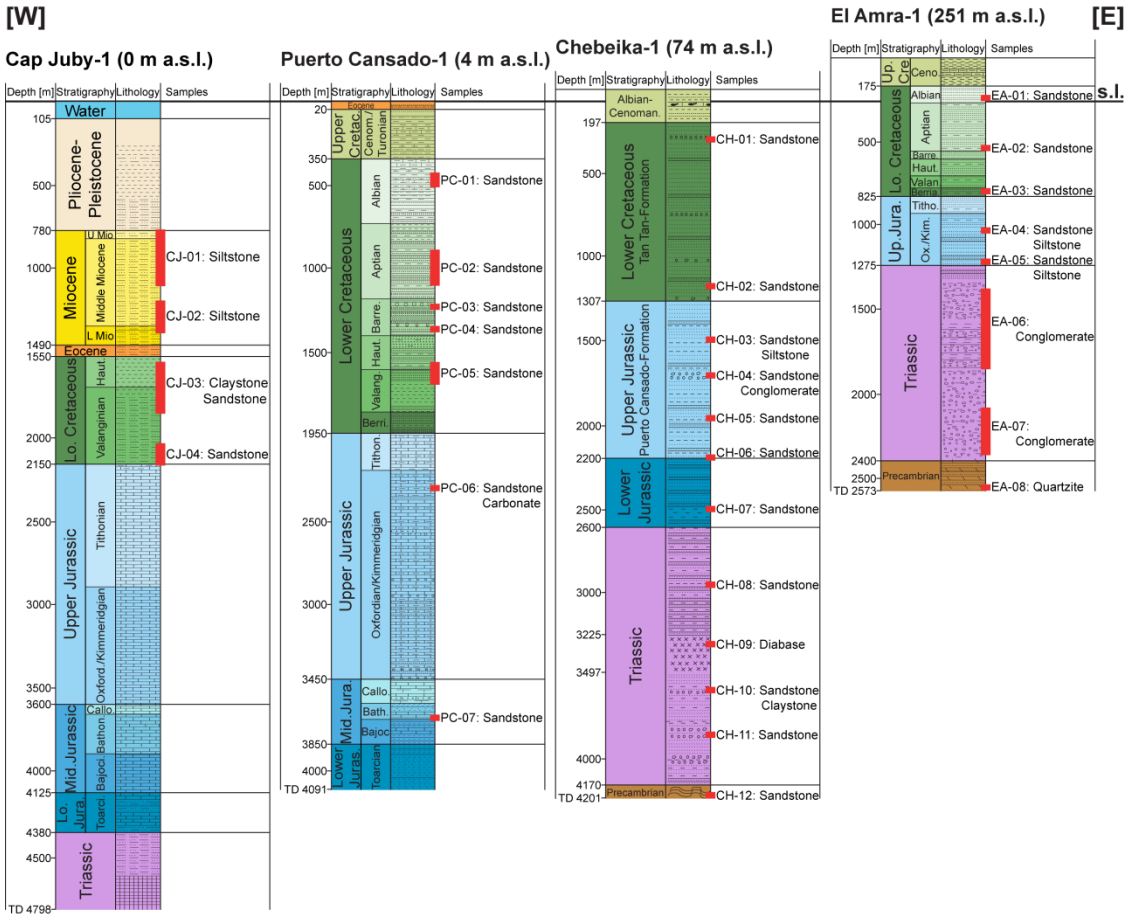

Fig. 3.5: Schematic geological profile from wells Cap Juby-1, Puerto Cansado-1, Chebeika-1 and El Amra-1 of the Tarfaya Basin (W–E) with sample positions. Stratigraphy after Wenke et al. (2011).

aiming at the reduction of the grain size to < 300 µm. After every crushing cycle, the samples were sieved and particles < 300 µm went to the shaking table. This procedure was repeated until more than 90 % of the sample material was < 300 µm. The separation with the shaking table was followed by sieving of the heavy fraction through 63 µm. Consequently, a sample fraction with grain sizes between 63 µm and 300 µm was obtained for further processing.

Heavy mineral separation was performed to receive apatite and zircon concentrates. The first step was the heavy liquid separation by LST Fastfloat (80 % sodium polytungstate) with a density of 2.8 kg/m^3 in a heavy liquid centrifuge, followed by the separation with a manual magnet and Frantz magnetic separator. Finally, the non-magnetic fraction was processed by methylene iodide with a density of 3.3 kg/m^3 and a solution of methylene iodide and acetone with a density of 3.2 kg/m^3 in a centrifuge or separating funnel depending on the sample quantity. In several zircon fractions an aqua regia digestion was carried out to eliminate non-magnetic heavy minerals, e.g. pyrite.

3.3.1 Fission-track processing and data acquisition

The mounts necessary for the fission-track analysis were prepared by standard preparation techniques (Glasmacher et al., 1998; Grist and Ravenhurst, 1992a, b).

Apatite grains were embedded in epoxy resin and afterwards dried for at least 48 hours. The grain mounts were cut, grinded and polished to reveal a smooth internal mineral surface.

For observation under the optical microscope, an etching procedure was carried out to make the fission-tracks visible. Sobel and Seward (2010) emphasized that D_{par} values are influenced by etching conditions and therefore a controlled etching is essential for further use of D_{par} as a kinetic parameter in thermal models like 'HeFTy'. Apatite mounts were etched in 5.5 M HNO_3 for 20 (±1) s at 20 (±1) °C (thermalized water bath) and covered in close contact by U–free micas as external detectors. The mounts were packed into an aluminium tube together with three glass neutron dosimeter (CN5) of known uranium content at the top, middle and bottom of the batch and Durango apatite samples as internal age standards.

Zircon grains were embedded in Teflon on a hotplate at 315 °C. Subsequently the grain mounts were grinded and polished to reveal a smooth internal mineral surface. A controlled etching process were performed after standards given by Gleadow et al. (1976) and Garver (2003). The etchant was a KOH:NaOH eutectic melt mixed at a ratio of 7:5. Zircon mounts were etched in an oven at 200 (±5) °C for 3.5–8 h and afterwards also covered in close contact by U–free micas as external detectors. The mounts were packed into an aluminium tube together with three glass neutron dosimeter (CN1) of known uranium content at the top, middle and bottom of the batch and Fish Canyon Tuff zircon samples as internal age standards.

Apatite and zircon batches were irradiated at the research reactor FRM II in Garching, Germany with a fluence of 1 x 10^{16} or 1 x 10^{15} thermal neutrons/cm^2, except for one apatite batch irradiated at the research reactor Triga in Mainz, Germany. After irradiation detection micas were etched in 48 % HF for 20 (±1) min at 20 (±1) °C. Based on water release into the horizontal confined fission-tracks as a result of irradiation, sample mounts have been cleaned with 99.9 % ethanol in an ultrasonic bath and dried for 10 min at 90 °C. Finally grain mount and detection mica are attached side by side to a glass slide for further processing under the optical microscope.

Area densities (tracks/cm^2) of spontaneous and induced tracks, confined track lengths and c-axis oriented etch pit diameters (D_{par}) (Donelick, 1993, 1995) were determined at the Heidelberg fission-track laboratory of the Thermochronology and Archaeometry Research Group. The applied system consists of an Leitz® 'Aristomet' optical microscope equipped with an Autoscan® 'AS3000i' 3-axis microscope stage, a high-resolution Peltier-cooled colour CCD camera 'ColorView III' (5 megapixel) of Olympus® and a Windows® based computer system with two Samsung® 244T monitors. Movement along each axis is monitored by an external laser scale sensor 'BL 55 RE' of Sony®. These sensors guarantee a deviation of less than 500 nm along 4–5 cm of movement. The entire setup is operated with the Autoscan® software Trakscan®, which also calculates the track densities. Applying the largest possible resolution, each pixel is equivalent to less than 250 nm in size. Fission tracks were counted using 100x (apatite) and 160x (zircon) dry objectives. Confined length and etch pit size were measured by a 160x dry objective using the Autoscan® computer code 'EasyLength®'.

Fission-track ages were determined using external detector method (Fleischer et al., 1965) combined with the ζ-method described by Hurford and Green (1982, 1983) and Wagner and van den Haute (1992). The ζ-values of 333.4 (±17.9) and 334.6 (±15.8) for apatite and 140.8 (±5.9) for zircon were obtained by counting Durango apatite and Fish Canyon Tuff zircon age standards. All ages and 1σ errors were calculated with the computer code 'TRACKKEY' (Dunkl, 2002). The fission-track data are presented after the recommen-

dation of Hurford (1990) and reported as central ages according to Galbraith and Laslett (1993).

In samples with a large spread in the single grain age distribution, age populations were determined by using the computer code 'Popshare' (Dunkl and Székely, 2002).

3.3.2 (U-Th-Sm)/He processing and data acquisition

(U-Th-Sm)/He analysis was performed on suitable single grains of apatite and zircon. The heavy mineral concentrates obtained from separation process were screened and at least three appropriate grains selected for AHe and ZHe dating. As the α-ejection correction factor strongly depends on grain size and shape only euhedral grains with a minimum size of 60 µm in width and a maximum length of 300 µm are used for dating in order to minimise the uncertainties. Apatite and zircon were known to occasionally produce a relatively large scatter in ages obtained on crystals from one sample that is generally believed to be caused either by cracks, mineral or fluid inclusions or by zoning of uranium and thorium concentration within a single crystal. Therefore, only crystals free of inclusions and cracks were selected, requiring a careful and time-intensive picking process. The apatite and zircon concentrates were searched under a binocular and suitable mineral grains were handpicked, using fine tweezers. Before packing in U-free Pt foil tubes, the crystal sizes of the grains were measured (Mitchell and Reiners, 2003).

The apatite analysis as well as the zircon analysis of well samples was performed at the (U-Th-Sm)/He Laboratory of the Department of Geology, University of Kansas, Lawrence, USA. The handpicking of apatite and zircon grains and screening for inclusions were carried out using a Nikon SMZ-U stereomicroscope with rotating stage and cross-polarization. All grains were digitally photographed using a Nikon digital ColorView® camera. AnalySIS® imaging software was used for the morphometrical measurement of each grain before loading into Pt tubes (Fig. 3.6).

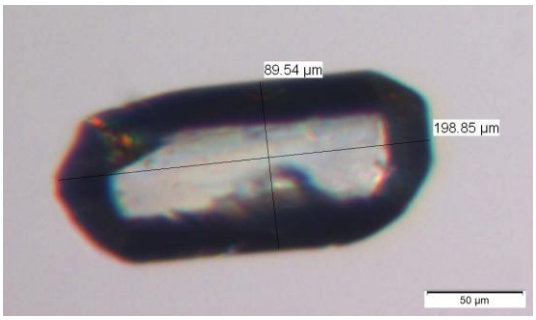

Fig. 3.6: Apatite grain with shape dimensions photographed with the Nikon digital ColorView® camera at the (U-Th-Sm)/He Laboratory of the Department of Geology, University of Kansas.

Subsequently, the morphometric values were imported into a LabView programme to calculate the α-ejection correction factor. The apatite procedure generally follows that of House et al. (2000), ideal for single-crystal analysis. The radiogenic ^{4}He was extracted in an ultrahigh vacuum chamber through heating with Nd-YAG lasers. The aliquots were heated for 10 minutes at 1300 °C and subsequently reheated to ensure complete degassing. The released gas was measured and quantified with a Balzers Prisma QMS-200 quadrupole mass spectrometer. After complete degassing, grains were recovered and dissolved for U, Th and Sm determination. The apatite aliquots were spiked with known amounts of tracer-isotopes (^{230}Th, ^{235}U, ^{149}Sm) and dissolved in 30 % HNO_3 for 1 h at 90 °C. The zircon grains were dissolved by using a standard U-Pb double pressure-vessel digestion procedure (HF, HNO_3 and HCl) for a total of four days. In order to minimize effects caused by undetected mineral inclusions some apatite grains were processed like zircon to ensure complete digestions as described in Vermeesch et al. (2007). ^{147}Sm was determined in order to

constrain the potentially significant radiogenic ^{4}He input by this isotope. After dissolution, spiked aliquot solutions were analyzed for U, Th, and Sm using a Fisons/VG PlasmaQuad II Inductively Coupled Plasma Mass Spectrometer (ICP-MS) as described by Stockli et al. (2003) and Wipf (2006). All quantities were measured on a single crystal, to eliminate uncertainties that arise from grain to grain heterogeneities (Ehlers and Farley, 2003; Farley and Stockli, 2002). Reported errors are 6 % for apatite and 8 % for zircon based on the respective reproducibility of the Durango and Fish Canyon Tuff age standards.

The zircon analysis of outcrop samples was performed at the Arizona Radiogenic Helium Dating Laboratory of the Department of Geosciences, University of Arizona, Tucson, USA. The handpicking of zircon grains and screening for inclusions were carried out at the Heidelberg fission-track laboratory of the Thermochronology and Archaeometry Research Group by using an Olympus SZX16® stereomicroscope with a rotating stage. All grains were digitally photographed with an Olympus XC50® digital 'ColorView' (5 megapixel) camera. Olympus Stream® imaging software was used to measure shape dimensions of each grain before loading into Pt tubes (Fig. 3.7).

At the Radiogenic Helium Dating Laboratory the radiogenic ^{4}He was extracted by in vacuo heating for 20 min at 1250–1400 °C with an Nd-YAG laser, followed by cryogenic purification and quantification of the amount of released He with a Balzers quadrupole mass spectrometer (QMS). Subsequently, grains were recovered and dissolved in Teflon microvials in Parr bombs with HF, HNO_3 and HCl to remove fluoride salts. After dissolution, spiked aliquot solutions were analyzed for U and Th content on a high-resolution Element2 ICP-MS. Based on the reproducibility of standards an estimated uncertainty of less than 3 % (1σ) has been proposed (Mitchell and Reiners, 2003).

The obtained AHe and ZHe raw data were corrected for alpha ejection using the method of Farley (1996) and Farley et al. (2002).

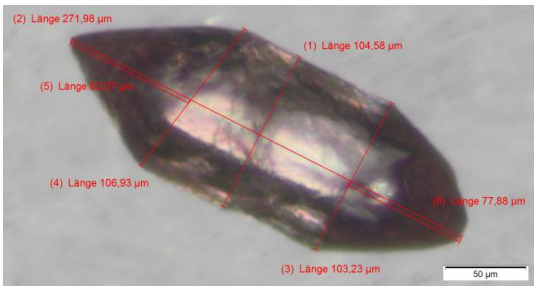

Fig. 3.7: Zircon grain with shape dimensions photographed with the Olympus XC50® digital 'ColorView' camera at the Heidelberg fission-track laboratory.

3.4 Time-temperature path modelling

The thermal history can be achieved by a modelling procedure that combines the annealing kinetics of fission-tracks in apatite and the He-diffusion behaviour of apatite and zircon with the determined apatite fission-track data set (single grain ages, confined fission-track length distribution, D_{par}®), apatite and zircon (U-Th-Sm)/He data sets and the time-temperature (t-T) coordinates from the known geological evolution of the area. The computer code 'HeFTy' v. 1.7.4 (Ketcham, 2005; Ketcham et al., 2007a, b; Ketcham et al., 2009) used for modelling tests the geological heating and cooling constraints against the thermochronological data in order to determine a best-fit t-T evolution. The primary goal of the program is to define envelopes of good and acceptable results in t-T space that contain all paths passing baseline statistical criteria and being conformed to the user-entered geological constraints. A good fit corresponds to a merit value of 0.50 or higher (goodness of fit, GOF ≥ 50 %) and an acceptable fit corresponds to a merit value of 0.05 or higher (GOF ≥ 5 %).

The modelling process was started with the forward approach, considering information from geological evolution of the study area and the thermochronological data set. In this study AFT ages were combined with AHe and ZHe data whenever available. Based on the best forward model, the inverse modelling was initiated. Along this t-T path geologically constrained time-temperature boxes were entered in the program by using the time-scales of Gradstein (2004). The modelling procedure was initiated with wide open boxes that were continuously minimized during the modelling process to find the best solution. The computer code generates in the Monte Carlo approach at least 10000 single t-T paths, displaying only those that best approximate the measured data. The amount of needed model runs to find the best possible solution is dependent on the existed degrees of freedom. In simple AFT or combined AFT+AHe+ZHe modelling 50000 model runs were performed, whereas in simple AHe or ZHe modelling 30000 model runs were sufficient to find the best solution.

Several apatite He-diffusion models are given by 'HeFTy' software (Farley, 2000; Flowers et al., 2009; Shuster et al., 2006; Wolf et al., 1996), while each model was tested to find the best fit model. In the present study the He-diffusion models for apatite of Farley (2000) and Shuster et al. (2006) and for zircon of Reiners et al. (2004) with α-ejection correction after Farley et al. (1996) were used to model the thermal history (Fig. 3.8). The applied annealing model of fission-tracks in apatite is described by Ketcham et al. (2007a) (Fig. 3.8).

3.5 Thermochronology in sedimentary basins

Sedimentary basins represent some of the best natural laboratories for studying and constraining geological processes. The determination of the sedimentation, burial, erosion and inversion history combined with various analytical and modelling techniques enables to evaluate hydrocarbon generation in time and space. Thermochronological methods, especially apatite fission-track and apatite (U-Th-Sm)/He dating, play an increasingly important role in the evaluation of these processes. In combination with further burial and thermal history analysis, thermochronometers provide important constraints on the timing and duration of heating/cooling events that can be used to evaluate hydrocarbon systems. In contrast to vitrinite reflectance data, thermochronology can determine temperatures and its timing. Combined with maximum palaeotemperature techniques, thermochronology provide some of the best indicators for magnitude and timing of basin inversion in sedimentary basins (Green et al., 1995; Hill et al., 1995).

As the apatite annealing temperature range of 60–110 °C/10 Ma corresponds with liquid hydrocarbon generation temperatures, AFT dating is particularly important for basin analysis and hydrocarbon exploration.

In a well with currently maximum temperatures at any depth, the shallowest/coolest samples should have relatively old AFT ages, due to detrital ages that are at least as old as the depositional age (Armstrong, 2005; Naeser, 1979) (Fig. 3.9a). A considerable scatter in the detrital AFT single grain age distribution in the shallow section is based on the variation in source regions with different exhumation histories. AFT ages can either decrease or increase down section in the upper part of the well (Fig. 3.9a). Based on the apatite PAZ, below 60 °C the AFT ages decrease continuously down section up to 110 °C, where the AFT ages are virtually zero depending on the apatite chemistry (Fig. 3.9a). An inversion after maximum burial yields an

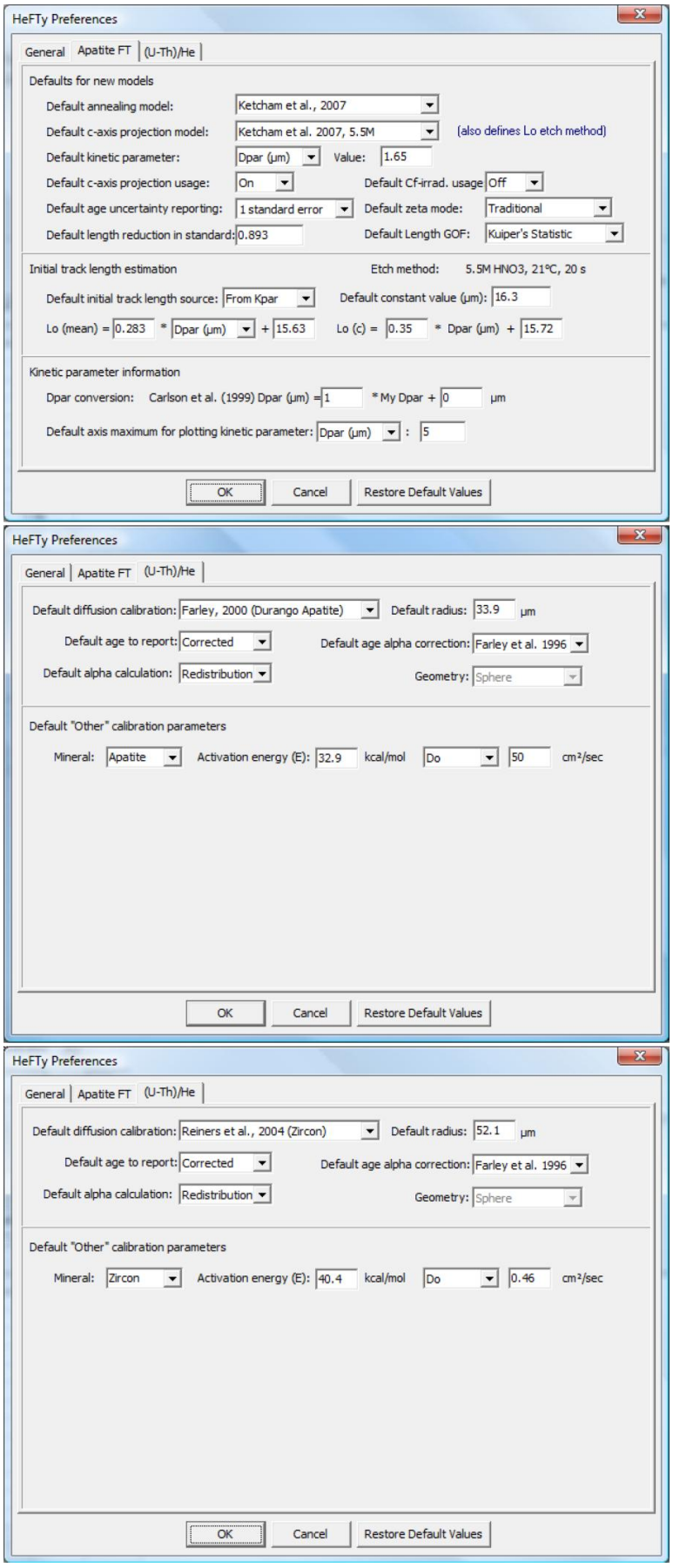

Fig. 3.8: HeFTy preferences for time-temperature modelling (radius from sample MA-12).

uplifted PAZ and total annealing zone (Fig. 3.9b). In the inverted zones the accumulation of fission-tracks results in increasing ages and generates a fossil PAZ and fossil total annealing zone (Armstrong, 2005; Fitzgerald and Gleadow, 1990; Naeser, 1979) (Fig. 3.9b). Due to the fact that most wells are too shallow a fossil and modern PAZ occur rarely together. Except that temperatures (PRZ: 40–70 °C/1 Ma) are lower, in a well with currently maximum temperatures the general structure of the AHe age profile is similar to the AFT profile with detrital He ages above the PRZ that can reveal a considerable scatter based on variations in source regions (Fig. 3.9a). An inversion after maximum burial generates an AHe age profile similar to the AFT profile (Fig. 3.9b). The exhumation of the section forms a fossil PRZ and a new PRZ as helium accumulates. An example study in the Ottway Basin of Australia showed decreasing AHe ages from wells of 75 Ma at the surface to virtually zero at depths with a temperature of approximately 80 °C (House et al., 1999).

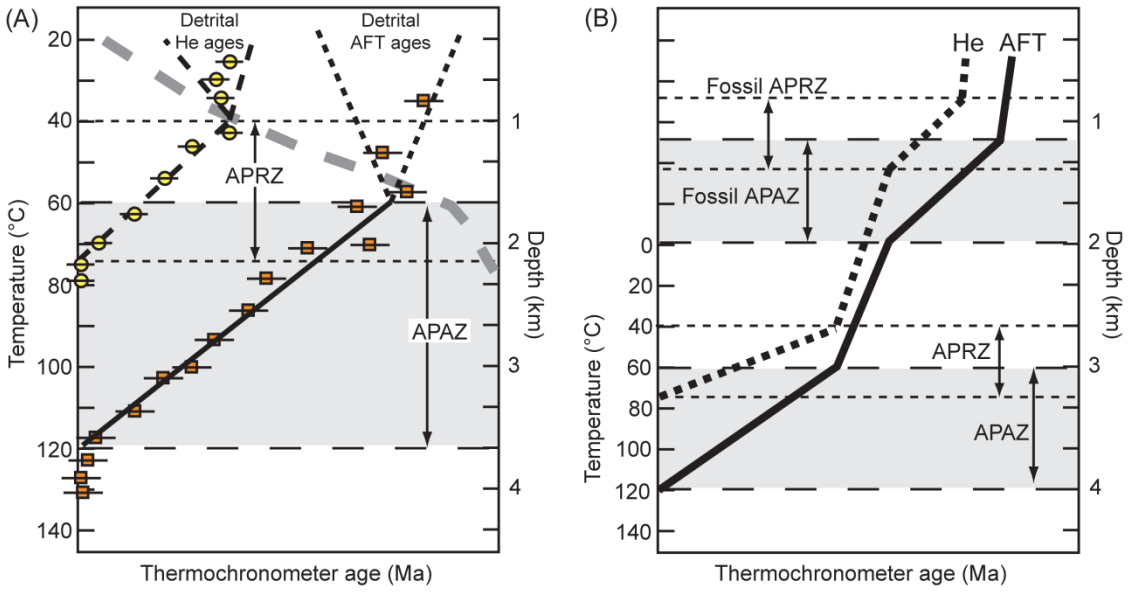

Fig. 3.9: Low-temperature thermochronometer versus temperature profiles in a well. (A) Scenario without uplift and exhumation. AFT ages (filled squares) are all older than AHe ages (filled circles). APAZ: apatite partial annealing zone; APRZ: apatite partial retention zone. (B) Scenario with rock uplift toward surface resulting in a fossil APAZ and APRZ (Armstrong, 2005; Naeser, 1979).

4

RESULTS

Contents

4.1 Tarfaya Basin

28 Cretaceous to Cenozoic and two Lower Ordovician outcrop samples as well as 29 Meso- to Cenozoic and two Precambrian samples from wells Chebeika-1, El Amra-1, Puerto Cansado-1 and Cap Juby-1 have been collected and prepared for low-temperature thermochronology. Every sample that contained apatite grains were processed for apatite fission-track analysis. Whenever suitable grains were available in the well samples, apatite (U-Th-Sm)/He dating were carried out. Furthermore, apatite and zircon (U-Th-Sm)/He as well as zircon fission-track analysis were performed on designated outcrop samples. The complete thermochronological data set as well as location and description of the samples from the Tarfaya Basin are presented in Tables 4.1 and 4.2.

Table 4.1: All thermochronological data from outcrop samples of the Tarfaya Basin and sample location with description

Sample	Coordinates (WGS84)		Elevation	Lith.	Stratigraphic age	Apatite	Error	Apatite	Error	Zircon	Error	Zircon	Error
	N Latitude	W Longitude	[m a.s.l.]			(U-Th-Sm)/He	± 1σ	FT	± 1σ	(U-Th-Sm)/He	± 1σ	FT	± 1σ
	DD°MM'SS.S"	DD°MM'SS.S"				[Ma]	[Ma]	[Ma]	[Ma]	[Ma]	[Ma]	[Ma]	[Ma]
MA-18	29°38'42"	9°58'49"	150	sdst	Lo Cretaceous	no ap.	-	176.2	19.6	n.d.	-	n.d.	-
MA-19	29°38'42"	9°58'49"	150	congl	Lo Cretaceous	63.5	3.8	180.7	13.7	n.d.	-	n.d.	-
MA-24	28°17'13"	11°31'25"	0	sdst	Albian	72.6	4.4	172.2	12.1	184.7	3.0	503.0	48.3
MA-25	28°17'34"	11°31'28"	0	sdst	Albian	no ap.	-	no ap.	-	n.d.	-	n.d.	-
MA-26	28°12'10"	11°46'54"	2	sdst	Turonian	no ap.	-	216.3	18.0	n.d.	-	n.d.	-
MA-27	27°54'36"	12°57'46"	0	sdst, carb	Lower Pliocene	no ap.	-	142.5	16.2	n.d.	-	n.d.	-
MA-28	28°37'16"	10°46'38"	344	sdst, carb	Pleistocene	no ap.	-	no ap.	-	n.d.	-	n.d.	-
MA-52	28°00'17"	12°28'51"	25	sdst	Mio-Pliocene	no ap.	-	237.2	34.8	n.d.	-	n.d.	-
MA-53	27°43'34"	12°54'26"	34	sdst	Miocene	n.d.	-	145.3	14.5	n.d.	-	404.3	29.3
MA-54	26°25'22"	13°15'44"	148	sdst	Miocene	no ap.	-	104.4	17.4	811.5	13.8	461.3	46.7
MA-56	26°12'05"	13°54'36"	105	congl	Mio-Pliocene	n.d.	-	182.9	14.8	n.d.	-	n.d.	-
MA-57	26°36'32"	13°42'29"	50	sdst, carb	Eocene	no ap.	-	no ap.	-	n.d.	-	n.d.	-
MA-58	26°36'33"	13°42'25"	61	sdst	Pliocene	n.d.	-	141.7	35.0	n.d.	-	n.d.	-
MA-59	28°04'48"	11°59'01"	80	sdst	Pliocene	n.d.	-	91.6	16.2	n.d.	-	n.d.	-
MA-60	26°39'44"	12°56'19"	101	sdst	Eocene	no ap.	-	no ap.	-	n.d.	-	n.d.	-
MA-61	26°37'42"	11°52'47"	332	congl	Lo Cretaceous	n.d.	-	186.8	14.2	n.d.	-	n.d.	-
MA-63	26°37'31"	11°58'15"	321	brec	Lower Ordovician	no ap.	-	no ap.	-	n.d.	-	n.d.	-
MA-64	26°37'31"	11°58'15"	321	quart	Lower Ordovician	no ap.	-	no ap.	-	n.d.	-	n.d.	-
MA-65	27°01'46"	12°00'38"	281	sdst	Lo Cretaceous	no ap.	-	no ap.	-	n.d.	-	n.d.	-
MA-66	27°07'18"	11°52'46"	351	sdst, slst	Lo Cretaceous	no ap.	-	no ap.	-	n.d.	-	n.d.	-
MA-67	26°34'41"	12°14'47"	263	sdst	Cenoman-Turon	n.d.	-	220.4	18.0	n.d.	-	n.d.	-
MA-68	26°40'41"	12°35'22"	226	sdst	Eocene	no ap.	-	no ap.	-	n.d.	-	n.d.	-
MA-69	26°55'11"	12°12'01"	165	sdst	Coniacian	n.d.	-	141.1	11.6	n.d.	-	n.d.	-
MA-70	26°55'08"	12°12'01"	184	sdst	Coniacian	no ap.	-	206.4	16.6	n.d.	-	n.d.	-
MA-71	27°07'07"	11°34'36"	226	congl	Lo Cretaceous	no ap.	-	no ap.	-	n.d.	-	n.d.	-
MA-72	28°17'37"	11°32'37"	12	sdst	Albian	n.d.	-	170.5	14.7	n.d.	-	n.d.	-
MA-75	28°08'29"	11°18'18"	147	sdst	Lo Cretaceous	no ap.	-	199.3	17.6	n.d.	-	n.d.	-
MA-77	28°40'37"	11°07'21"	25	sdst	Lo Cretaceous	n.d.	-	185.3	14.3	1195.0	17.1	585.0	58.3
MA-78	28°12'15"	11°46'58"	17	sdst	Campanian	n.d.	-	174.9	12.1	n.d.	-	452.3	40.7
MA-79	28°09'33"	11°38'20"	147	sdst	Cenoman-Turon	no ap.	-	no ap.	-	n.d.	-	n.d.	-

Elevation in meter above sea level; Lith.: Lithology; sdst: sandstone; congl: conglomerate; carb: carbonate; brec: breccia; Lo Cretaceous: Lower Cretaceous; Cenoman-Turon: Cenomanian-Turonian; no ap.: no apatite; n.d.: not determined.

Table 4.2: All thermochronological data from wells of the Tarfaya Basin (Chebeika-1, El Amra-1, Puerto Cansado-1 and Cap Juby-1) and sample location with description

Sample	Depth [m b.s.]	Recent T [°C]	Lithology	Stratigraphic age	Apatite (U-Th-Sm)/He [Ma]	Error ± 1σ [Ma]	Apatite FT [Ma]	Error ± 1σ [Ma]
Chebeika-1								
CH-01	301 - 304	28	sdst	Lower Cretaceous	no ap.	-	143.0	11.8
CH-02	1213 - 1214.50	50	sdst	Lower Cretaceous	no ap.	-	131.8	32.1
CH-03	1456.50 - 1458.50	56	sdst, slst	Upper Jurassic	14.0	0.8	119.9	10.5
CH-04	1696.50 - 1698.50	63	sdst, congl	Upper Jurassic	15.1	0.9	98.1	15.8
CH-05	1961 - 1964	69	sdst	Upper Jurassic	1.3	0.1	114.4	24.1
CH-06	2194 - 2196	75	sdst	Upper Jurassic	2.5	0.1	69.0	7.0
CH-07	2489 - 2490	82	sdst	Lower Jurassic	0.0	0.0	68.9	6.3
CH-08	2959.50 - 2961	94	sdst	Triassic	0.0	0.0	38.4	3.8
CH-09	3265 - 3267	102	dia	Triassic	0.0	0.0	20.6	4.3
CH-10	3646 - 3648	111	sdst, clyst	Triassic	0.0	0.0	8.5	2.3
CH-11	3839 - 3844	116	sdst	Triassic	0.0	0.0	8.7	1.8
CH-12	4188 - 4191	125	sdst	Precambrian	0.0	0.0	0.0	0.0
El Amra-1								
EA-01	215 - 218	25	sdst	Albian	no ap.	-	111.0	12.1
EA-02	530 - 535	33	sdst	Aptian	140.3	8.4	146.7	11.5
EA-03	789 - 792	40	sdst	Berriasian	no ap.	-	no ap.	-
EA-04	1013 - 1016	45	sdst, slst	Oxfordian–Kimmeridgian	no ap.	-	no ap.	-
EA-05	1234 - 1238	51	sdst, slst	Oxfordian–Kimmeridgian	no ap.	-	117.2	16.1
EA-06	1390 - 1865	61	congl	Triassic	no ap.	-	75.7	13.7
EA-07	2114 - 2362	76	congl	Lower Triassic	11.4	0.7	71.2	12.9
EA-08	2572.80 - 2574.20	84	quart	Precambrian	no ap.	-	no ap.	-
Puerto Cansado-1								
PC-01	433.50 - 499.50	32	sdst	Albian	34.0	2.0	117.8	10.9
PC-02	890 - 1095.80	45	sdst	Aptian	18.0	1.1	128.6	11.0
PC-03	1284 - 1286	53	sdst	Barremian	no ap.	-	117.3	10.5
PC-04	1357 - 1360	54	sdst	Barremian	15.9	2.2	120.2	11.1
PC-05	1555 - 1674	60	sdst	Hauterivian	18.8	1.1	64.5	5.0
PC-06	2296.50 - 2297.50	78	sdst, carb	Tithonian	3.5	0.2	48.7	4.5
PC-07	3668 - 3669.80	112	sdst	Bathonian	0.0	0.0	12.8	3.1
Cap Juby-1								
CJ-01	780 - 1100	48	slst	Upper Miocene	9.1	0.5	67.3	12.8
CJ-02	1200 - 1370	58	slst	Middle Miocene	6.2	0.4	92.8	11.9
CJ-03	1560 - 1850	71	sdst, clyst	Valanginian	0.8	0.0	110.8	40.5
CJ-04	2040 - 2180	83	sdst	Valanginian	1.1	0.1	no ap.	-

Depth in meter below surface; sdst: sandstone; slst: siltstone; congl: conglomerate; dia: diabase; clyst: claystone; quart: quartzite; carb: carbonate; no ap.: no apatite.

4.1.1 Chebeika-1

4.1.1.1 Apatite (U-Th-Sm)/He ages

Four samples from well Chebeika-1 with two and three, respectively single grain aliquots have been analysed by apatite (U-Th-Sm)/He dating. Two samples contained no suitable apatite grains for AHe processing. Raw AHe ages cover a range from 1.0 (±0.1) to 71.4 (±4.3) Ma (Tab. 4.3). α-ejection correction after Farley et al. (1996) was applied to all grains resulting in ages between 1.3 (±0.1) and 88.8 (±5.3) Ma (Tab. 4.3). Since the youngest AHe age of the aliquots is generally considered to reveal the most accurate date of cooling, the youngest single grain age of every sample was used for further interpretation and discussion. These α-ejection corrected single grain ages range from 15.1 (±0.9) Ma at a depth of 1696.50–1698.50 m to 1.3 (±0.1) Ma at a depth of 1961–1964 m (Fig. 4.2, Tab. 4.3). Based on the AHe ages of 1.3 (±0.1) and 2.5 (±0.1) Ma from samples CH-05 and CH-06 and the increment of the current temperature with increasing depth, the AHe ages of samples CH-07 to CH-12 have been set at 0.0 Ma. The ages decrease almost continuously with increasing depth (Fig. 4.2). All single grain aliquot ages are significantly younger than the corresponding sedimentation age of the sampled rock and younger as the apatite fission-track age.

All samples show no clear positive correlation between single grain age and effective Uranium concentration (eU = [U] + 0.235 [Th] + 0.0053 [Sm]; e.g. Shuster et al., 2006; Spiegel et al., 2009) (Fig. 4.1).

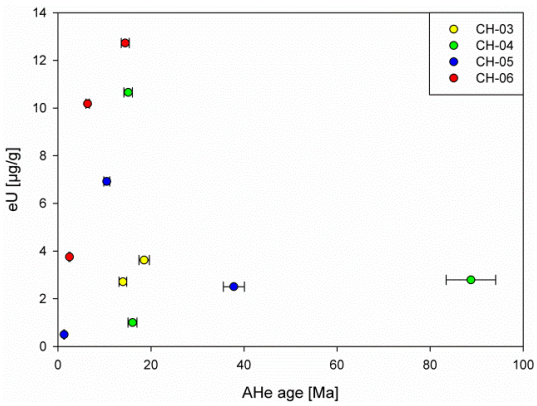

Fig. 4.1: AHe single grain ages (1σ error) from well Chebeika-1 plotted against eU.

In samples from the Chebeika-1 well, no correlation between equivalent grain radius and AHe age distribution has been determined (Reiners and Farley, 2001) (Fig. 4.3).

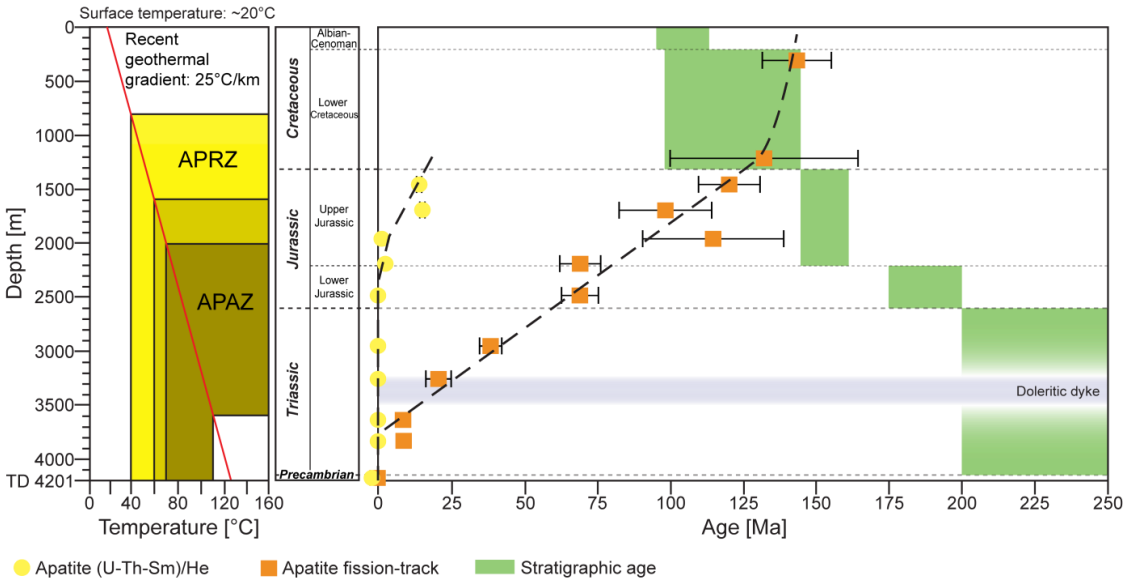

Fig. 4.2: Thermochronometric age (1σ error) – depth distribution of the Chebeika-1 well. On the left side the recent temperature distribution as well as a schematic stratigraphic profile is displayed.

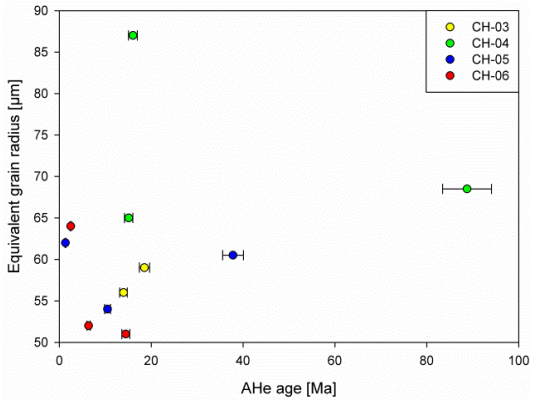

Fig. 4.3: AHe single grain ages (1σ error) from well Chebeika-1 plotted against equivalent grain radius.

4.1.1.2 Apatite fission-track ages

In the Chebeika-1 well, twelve samples have been determined by apatite fission-track analysis. The apatite fission-track central ages range from 143.0 (±11.8) Ma at a depth of 301–304 m to 0.0 Ma at a depth of 4188–4191 m (Fig. 4.2, Tab. 4.4). Sample CH-12, with an age of 0.0 Ma, indicates a complete annealing and therefore a current temperature of more than 110 °C in 4188–4191 m depth. Except for sample CH-05, the AFT ages decrease continuously from the top to the bottom of the well (Fig. 4.2). The scatter is due to the very low amount of apatite single grains in samples CH-04 and CH-05. Whereas in sample CH-04 an age of 98.1 (±15.8) Ma was determined by five grains, in sample CH-06 only six grains was analysed resulting in an AFT age of 114.4 (±24.1) Ma. The ages of the Triassic and Jurassic samples are younger than the respective sedimentation or intrusive age of the sampled rock. In contrast the Lower Cretaceous samples reveal similar AFT and sedimentation ages. The single grain age distributions of eleven samples fulfilled the requirement of the χ^2-test indicating a homogenous distribution with respect to the 1σ error of the single grain ages (Galbraith, 1981). Whereas the test is passed when $\chi^2 > 5$ %, the samples reached values between 45 and 100 %. Sample CH-11 barely failed the requirement of the χ^2-test with a value of 4 %.

4.1.1.3 Etch pit size and track length distribution

Etch pit size (D_{par}) and confined spontaneous fission-track lengths were measured in every sample. A total of 685 D_{par} values were determined for all apatite grains (Tab. 4.5). The mean D_{par} values for each sample reveal a range between 1.3 (±0.2) and 1.7 (±0.3) µm. The narrow D_{par} distribution indicates a very homogenous chemical composition concerning the fluorine and chlorine content of the apatites. Five samples show a negative skewness ranging from -0.120 to -1.490, while the other samples exhibit a positive skewness between 0.073 and 1.218. The skewness is a factor of symmetry of the D_{par} value distribution. A large skewness value indicates a larger variation in the etch pit size. The largest etch pit size as well as the largest spread ranging between 1.0 (±0.1) and 2.7 (±0.1) was measured in sample CH-06. No positive correlation between single grain ages and D_{par} values has been detected.

Confined spontaneous fission-track lengths were detected in only five of twelve samples. A total of 34 track lengths were measured (Tab. 4.5). The obtained mean track lengths range from 9.1 (±1.1) to 11.4 (±1.7) µm. The track length distributions of the samples show no significant skewness ranging between -0.566 and -0.271. The largest track length of 14.6 (±0.1) µm and the smallest of 6.9 (±0.1) µm were measured in sample CH-01. After correcting of the confined track lengths for their crystallographic orientation by the computer code 'HeFTy', the mean confined fission-track lengths changed to a distribution between 11.8 (±0.8) and 13.2 (±1.1) µm (Ketcham et al., 2007a). The skewness of the c-axis corrected track length distributions range from -0.397 to 0.416. The largest track length after c-axis correction of 15.2 (±0.1) µm and the smallest of 10.2 (±0.1) µm was determined in sample CH-01.

Table 4.3: Apatite (U-Th-Sm)/He data from well Chebeika-1 of the Tarfaya Basin

Sample	Recent T [°C]	Mass [µg]	Radius [µm]	U [µg/g]	Th [µg/g]	Sm [µg/g]	eU [µg/g]	Th/U	^{4}He [nmol/g]	F_t	Raw age [Ma]	Error ± 1σ [Ma]	Corr. age [Ma]	Error ± 1σ [Ma]
CH-03.1	**56**	**4.8**	**56.0**	**1**	**8**	**9**	**3**	**9.9**	**0.15**	**0.728**	**10.2**	**0.6**	**14.0**	**0.8**
CH-03.3	56	5.7	59.0	2	8	18	4	4.6	0.28	0.750	13.9	0.8	18.5	1.1
CH-04.1	63	11.4	68.5	2	2	33	3	0.9	1.19	0.805	71.4	4.3	88.8	5.3
CH-04.2	**63**	**8.5**	**65.0**	**6**	**22**	**63**	**11**	**3.9**	**0.71**	**0.777**	**11.7**	**0.7**	**15.1**	**0.9**
CH-04.3	63	24.5	87.0	<1	3	26	1	5.6	0.10	0.840	13.5	0.8	16.0	1.0
CH-05.1	69	3.6	54.0	3	18	9	7	6.2	0.28	0.711	7.5	0.4	10.5	0.6
CH-05.2	69	6.0	60.5	1	8	18	3	13.5	0.41	0.750	28.4	1.7	37.8	2.3
CH-05.3	**69**	**5.2**	**62.0**	**<1**	**1**	**<1**	**<1**	**-58.2**	**0.00**	**0.735**	**1.0**	**0.1**	**1.3**	**0.1**
CH-06.1	75	3.9	52.0	7	12	21	10	1.7	0.26	0.725	4.6	0.3	6.4	0.4
CH-06.2	75	3.6	51.0	12	5	20	13	0.4	0.73	0.727	10.5	0.6	14.5	0.9
CH-06.3	**75**	**7.6**	**64.0**	**2**	**7**	**8**	**4**	**3.1**	**0.04**	**0.767**	**1.9**	**0.1**	**2.5**	**0.1**

eU = [U] + 0.235 [Th] + 0.0053 [Sm] (concentrations in weight %); F_t: α-ejection correction factor; raw ages are corrected after Farley et al. (1996); radius calculated according to Shuster et al. (2006) and Ketcham (2009). Data in bold: youngest apatite (U-Th-Sm)/He grain of each sample discussed in the text.

Table 4.4: Apatite fission-track data from well Chebeika-1 of the Tarfaya Basin

Sample	Recent T [°C]	n	U (std) [µg/g]	Sp. Tracks ρ_s	Sp. Tracks N_s	Ind. Tracks ρ_i	Ind. Tracks N_i	$P(\chi^2)$ [%]	Central age [Ma]	Error ± 1σ [Ma]
CH-01	28	20	13.5 (11.3)	6.370	400	11.291	709	99.9	143.0	11.8
CH-02	50	3	6.6 (5.6)	3.512	27	6.763	52	86.3	131.8	32.1
CH-03	56	20	18.3 (8.3)	9.869	311	20.944	660	97.0	119.9	10.5
CH-04	63	6	9.84 (7.1)	3.624	60	9.424	156	85.2	98.1	15.8
CH-05	69	5	12.28 (7.7)	4.839	35	10.784	78	89.4	114.4	24.1
CH-06	75	17	20.3 (17.9)	5.661	171	21.021	635	97.8	69.0	7.0
CH-07	82	18	22.0 (13.9)	6.465	237	24.059	882	94.7	68.9	6.3
CH-08	94	20	23.1 (15.7)	3.820	174	25.577	1165	89.4	38.4	3.8
CH-09	102	20	7.09 (3.3)	0.769	40	8.630	449	44.8	20.6	4.3
CH-10	111	11	15.27 (9.6)	0.673	15	20.418	455	81.1	8.5	2.3
CH-11	116	20	29.3 (19.3)	0.964	48	29.389	1463	4.0	8.7	1.8
CH-12	125	2	3.63 (1.0)	0.000	0	4.185	18	100.0	0.0	0.0

U (std): Uranium concentration and standard deviation; n: number of counted apatite grains; ρ_s: density of spontaneous tracks (10^5 tr/cm^2); N_s: number of spontaneous tracks; ρ_i: density of induced tracks (10^5 tr/cm^2); N_i: number of induced tracks; $P(\chi^2)$: probability that single grains are consistent and belong to the same population. Test is passed if $P(\chi^2) > 5$ % (Galbraith, 1981). Nd = 13338 tracks counted on CN5 dosimeter glass. Central ages are calculated using a ζ-value of 333.36 ± 17.89. Samples were irradiated at the FRM II reactor facility in Garching, Germany with a fluence of 1×10^{16} neutrons/cm^2.

Table 4.5: Confined fission-track length data from well Chebeika-1 of the Tarfaya Basin

Sample	n CT	CT mean [µm]	CT std [µm]	CT skew	CT min [µm]	CT max [µm]	L_c mean [µm]	L_c std [µm]	L_c skew	L_c min [µm]	L_c max [µm]	n D_{par}	D_{par} mean [µm]	D_{par} std [µm]	D_{par} skew	D_{par} min [µm]	D_{par} max [µm]
CH-01	27	11.4	1.7	-0.566	6.9	14.6	13.2	1.1	-0.397	10.2	15.2	113	1.7	0.2	0.447	1.1	2.5
CH-02	n.da.*	-	-	-	-	-	-	-	-	-	-	15	1.7	0.2	-1.490	1.3	1.8
CH-03	2	9.6	0.6	0.000	9.2	10.0	11.8	0.8	0.000	11.2	12.3	98	1.5	0.2	0.552	1.1	2.1
CH-04	n.da.	-	-	-	-	-	-	-	-	-	-	30	1.5	0.2	-0.120	1.0	1.8
CH-05	n.da.	-	-	-	-	-	-	-	-	-	-	25	1.6	0.3	1.218	1.3	2.2
CH-06	3	9.1	1.1	-0.271	8.0	10.2	11.9	0.5	0.416	11.4	12.5	81	1.6	0.4	1.167	1.0	2.7
CH-07	1	9.4	-	-	9.4	9.4	12.6	-	-	12.6	12.6	89	1.6	0.3	-0.527	1.0	2.2
CH-08	1	11.0	-	-	11.0	11.0	13.2	-	-	13.2	13.2	84	1.7	0.3	-0.382	0.9	2.4
CH-09	n.da.	-	-	-	-	-	-	-	-	-	-	57	1.5	0.2	0.073	1.1	1.9
CH-10	n.da.	-	-	-	-	-	-	-	-	-	-	41	1.3	0.2	-0.123	0.9	1.8
CH-11	n.da.	-	-	-	-	-	-	-	-	-	-	51	1.5	0.2	0.371	1.1	2.0
CH-12	n.da.	-	-	-	-	-	-	-	-	-	-	1	1.2	-	-	1.2	1.2

n: number of measured individual confined tracks (CT) and etch pit diameter (D_{par}); CT mean: mean confined track length; L_c mean: mean track length after c-axis correction; D_{par} mean: mean etch pit diameter; std: standard deviation; skew: skewness of distribution relative to the mean value; min: minimum single values; max: maximum single values; n.da.: no data.

4.1.2 El Amra-1

4.1.2.1 Apatite (U-Th-Sm)/He ages

Two samples from well El Amra-1 with two and three, respectively single grain aliquots have been analysed by apatite (U-Th-Sm)/He dating. Three samples contained no apatite grains and three samples no suitable grains for AHe processing. Raw AHe ages cover a range from 8.5 (±0.5) to 145.8 (±8.7) Ma (Tab. 4.6). α-ejection correction after Farley et al. (1996) was applied to all grains resulting in ages between 11.4 (±0.7) and 185.4 (±11.1) Ma (Tab. 4.6). The youngest α-ejection corrected single grain age of each sample range from 140.3 (±8.4) Ma at a depth of 530–535 m to 11.4 (±0.7) Ma at a depth of 2114–2362 m (Fig. 4.5, Tab. 4.6). The ages decrease almost continuously with increasing depth (Fig. 4.5). Whereas the AHe age of sample EA-07 is significantly younger than the corresponding sedimentation age of the sampled rock and younger than the apatite fission-track age, sample EA-02 reveal an age older than the depositional age and equal to the AFT age. The age is probably caused by uranium and thorium rich inclusions that might not have been completely dissolved during sample digestion.

In samples from the El Amra-1 well, no clear correlation between single grain age and effective Uranium concentration has been determined (Fig. 4.4).

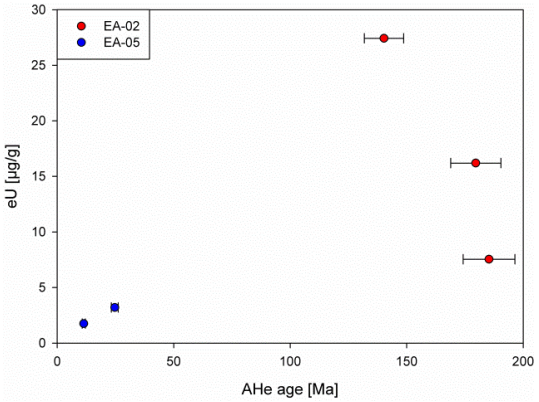

Fig. 4.4: AHe single grain ages (1σ error) from well El Amra-1 plotted against eU.

The samples show no correlation between equivalent grain radius and AHe age distribution (Fig. 4.6).

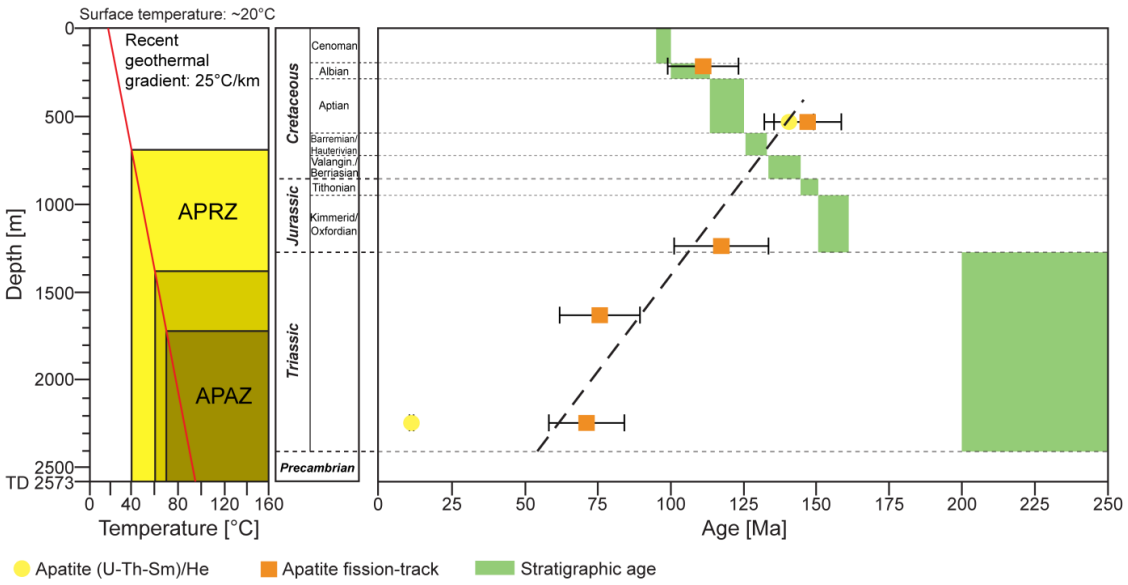

Fig. 4.5: Thermochronometric age (1σ error) – depth distribution of the El Amra-1 well. On the left side the recent temperature distribution as well as a schematic stratigraphic profile according to Wenke et al. (2011) is displayed.

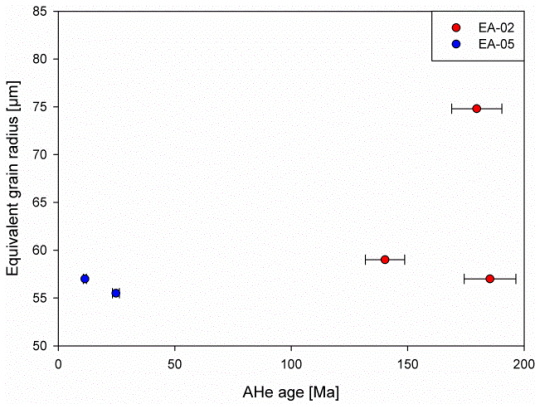

Fig. 4.6: AHe single grain ages (1σ error) from well El Amra-1 plotted against equivalent grain radius.

4.1.2.2 Apatite fission-track ages

Five of eight samples from well El Amra-1 have been determined by the apatite fission-track method. Three samples contained no apatite grains. The AFT central ages vary between 146.7 (±11.1) Ma at a depth of 530–535 m and 71.2 (±12.9) Ma at a depth of 2114–2362 m (Fig. 4.5, Tab. 4.7). The AFT ages decrease almost continuously with increasing depth (Fig. 4.5). In the upper part of the well, sample EA-01 shows a younger age of 111.0 (±12.1) Ma than sample EA-02. The AFT ages of the Triassic and Jurassic samples are younger than the corresponding sedimentation age of the sampled rock, while the Lower Cretaceous samples reveal similar or older AFT ages. All single grain age distributions fulfilled the requirement of the χ^2-test with values between 14 and 97 %.

4.1.2.3 Etch pit size and track length distribution

Etch pit size (D_{par}) and confined spontaneous fission-track lengths were measured in every sample. A total of 254 D_{par} values were determined for all apatite grains (Tab. 4.8). The mean D_{par} values for each sample reveal a range between 1.4 (±0.2) and 1.9 (±0.2) µm. Two samples show a negative skewness of -0.020 and -0.133, while the other samples exhibit a positive skewness between 0.177 and 0.320. The largest spread in etch pit size varying between 1.3 (±0.1) and 2.7 (±0.1) µm was measured in sample EA-02. No positive correlation between single grain ages and D_{par} values has been detected.

A total of 142 confined fission-track lengths were measured in four samples (Tab. 4.8). The obtained mean track lengths differ from 9.9 (±0.4) to 12.0 (±1.3) µm. The track length distributions of the samples show a positive skewness ranging between 0.039 and 1.630. The largest track length of 14.8 (±0.1) µm as well as the smallest of 9.2 (±0.1) µm was measured in sample EA-02. After the correction of the confined track lengths for their crystallographic orientation, the mean confined fission-track lengths changed to a distribution between 11.9 (±0.4) and 13.3 (±1.2) µm. The skewness of the c-axis corrected track length distributions indicates a variation from -1.134 to 0.681. The largest track length after c-axis correction of 15.5 (±0.1) µm and the smallest of 9.8 (±0.1) µm was determined in sample EA-02.

Table 4.6: Apatite (U-Th-Sm)/He data from well El Amra-1 of the Tarfaya Basin

Sample	Recent T [°C]	Mass [µg]	Radius [µm]	U [µg/g]	Th [µg/g]	Sm [µg/g]	eU [µg/g]	Th/U	^{4}He [nmol/g]	F_t	Raw age [Ma]	Error ± 1σ [Ma]	Corr. age [Ma]	Error ± 1σ [Ma]
EA-02.1	33	4.5	57.0	7	1	14	8	0.1	5.84	0.755	139.9	8.4	185.4	11.1
EA-02.2	**33**	**5.5**	**59.0**	**20**	**33**	**50**	**27**	**1.7**	**16.01**	**0.753**	**105.7**	**6.3**	**140.3**	**8.4**
EA-02.3	33	13.1	74.8	13	13	51	16	1.0	13.22	0.811	145.8	8.7	179.6	10.8
EA-05.1	51	24.0	55.5	2	7	17	3	3.9	0.33	0.735	18.2	1.1	24.7	1.5
EA-05.2	**51**	**29.1**	**57.0**	**1**	**3**	**16**	**2**	**3.1**	**0.09**	**0.749**	**8.5**	**0.5**	**11.4**	**0.7**

eU = [U] + 0.235 [Th] + 0.0053 [Sm] (concentrations in weight %); F_t: α-ejection correction factor; raw ages are corrected after Farley et al. (1996); radius calculated according to Shuster et al. (2006) and Ketcham (2009). Data in bold: youngest apatite (U-Th-Sm)/He grain of each sample discussed in the text.

Table 4.7: Apatite fission-track data from well El Amra-1 of the Tarfaya Basin

Sample	Recent T [°C]	n	U (std) [µg/g]	Sp. Tracks ρ_s	Sp. Tracks N_s	Ind. Tracks ρ_i	Ind. Tracks N_i	$P(\chi^2)$ [%]	Central age [Ma]	Error ± 1σ [Ma]
EA-01	25	11	17.4 (12.0)	7.686	171	17.799	396	51.1	111.0	12.1
EA-02	33	20	19.4 (13.4)	8.878	499	15.533	873	96.7	146.7	11.5
EA-05	51	5	19.5 (13.5)	12.277	91	26.983	200	60.0	117.2	16.1
EA-06	61	6	22.95 (11.0)	8.220	68	30.702	254	14.3	75.7	13.7
EA-07	76	6	15.3 (10.9)	3.736	47	13.594	171	38.7	71.2	12.9

U (std): Uranium concentration and standard deviation; n: number of counted apatite grains; ρ_s: density of spontaneous tracks (10^5 tr/cm^2); N_s: number of spontaneous tracks; ρ_i: density of induced tracks (10^5 tr/cm^2); N_i: number of induced tracks; $P(\chi^2)$: probability that single grains are consistent and belong to the same population. Test is passed if $P(\chi^2) > 5$ % (Galbraith, 1981). Nd = 13338 tracks counted on CN5 dosimeter glass. Central ages are calculated using a ζ-value of 333.36 ± 17.89. Samples were irradiated at the FRM II reactor facility in Garching, Germany with a fluence of 1×10^{16} neutrons/cm^2.

Table 4.8: Confined fission-track length data from well El Amra-1 of the Tarfaya Basin

Sample	n CT	CT mean [µm]	CT std [µm]	CT skew	CT min [µm]	CT max [µm]	L_c mean [µm]	L_c std [µm]	L_c skew	L_c min [µm]	L_c max [µm]	n D_{par}	D_{par} mean [µm]	D_{par} std [µm]	D_{par} skew	D_{par} min [µm]	D_{par} max [µm]
EA-01	16	11.9	1.3	0.406	9.4	13.0	13.3	0.8	0.681	12.2	14.1	52	1.6	0.2	0.206	1.2	2.2
EA-02	122	12.0	1.3	0.039	9.2	14.8	13.3	1.2	-0.607	9.8	15.5	119	1.9	0.2	0.177	1.3	2.7
EA-05	3	9.9	0.4	1.630	9.6	10.4	11.9	0.4	-1.134	11.5	12.2	25	1.7	0.3	-0.020	1.1	2.3
EA-06	1	14.5	-	-	14.5	14.5	15.5	-	-	15.5	15.5	28	1.5	0.4	0.320	1.0	2.1
EA-07	n.da.	-	-	-	-	-	-	-	-	-	-	30	1.4	0.2	-0.133	1.0	1.8

n: number of measured individual confined tracks (CT) and etch pit diameter (D_{par}); CT mean: mean confined track length; L_c mean: mean track length after c-axis correction; D_{par} mean: mean etch pit diameter; std: standard deviation; skew: skewness of distribution relative to the mean value; min: minimum single values; max: maximum single values; n.da.: no data.

4.1.3 Puerto Cansado-1

4.1.3.1 Apatite (U-Th-Sm)/He ages

Six samples from well Puerto Cansado-1 with three to six single grain aliquots have been analysed by apatite (U-Th-Sm)/He dating. One sample contained no apatite grains for AHe processing. Raw AHe ages cover a range from 1.9 (±0.1) to 53.8 (±3.2) Ma (Tab. 4.9). α-ejection correction after Farley et al. (1996) was applied to all grains resulting in ages between 3.5 (±0.2) and 62.6 (±3.8) Ma (Tab. 4.9). The youngest α-ejection corrected single grain age of each sample range from 34.0 (±2.0) Ma at a depth of 433.50–499.50 m to 3.5 (±0.1) Ma at a depth of 2296.50–2297.50 m (Fig. 4.8, Tab. 4.9). Based on the calculated current temperature in 3668–3669.80 m depth, the AHe age of sample PC-07 has been set as 0.0 Ma. The ages decrease almost continuously with increasing depth (Fig. 4.8). All single grain aliquot ages are significantly younger than the corresponding sedimentation age of the sampled rock and younger than the apatite fission-track age. The samples from the Puerto Cansado-1 well show no clear positive correlation between single grain age and effective Uranium concentration (Fig. 4.7).

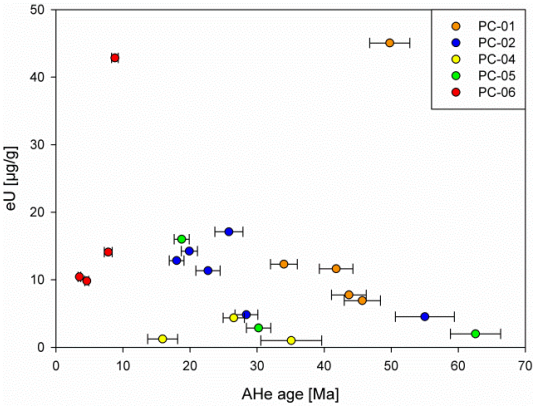

Fig. 4.7: AHe single grain ages (1σ error) from well Puerto Cansado-1 plotted against eU.

According to Reiners and Farley (2001), a clear positive correlation between equivalent grain radius and AHe age distribution was determined in sample PC-05 (Fig. 4.9). A positive correlation is indicative for a long residence time in the PRZ.

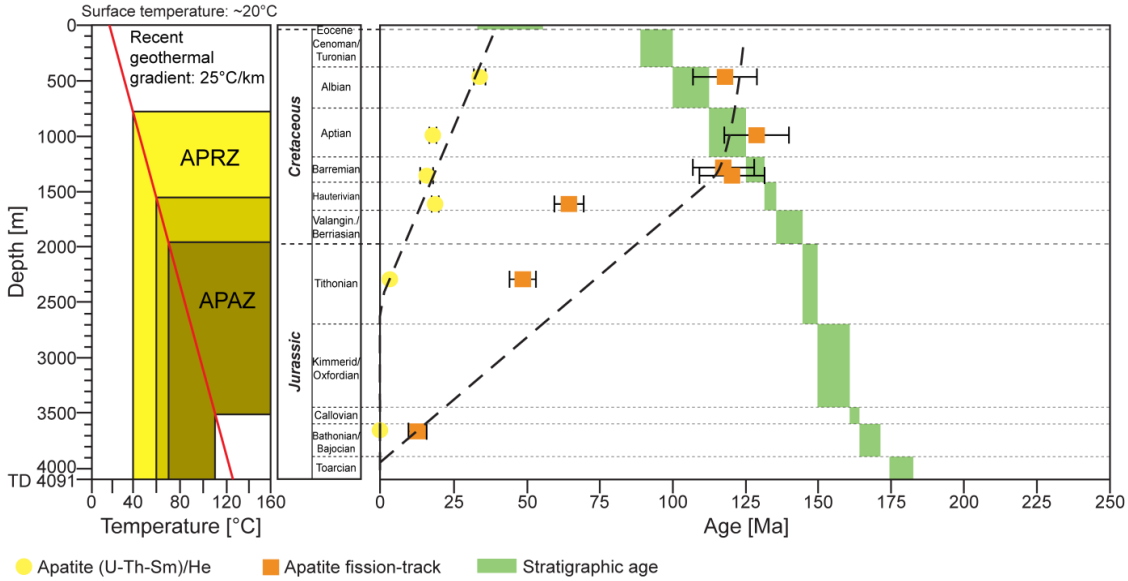

Fig. 4.8: Thermochronometric age (1σ error) – depth distribution of the Puerto Cansado-1 well. On the left side the recent temperature distribution as well as a schematic stratigraphic profile according to Wenke et al. (2011) is displayed.

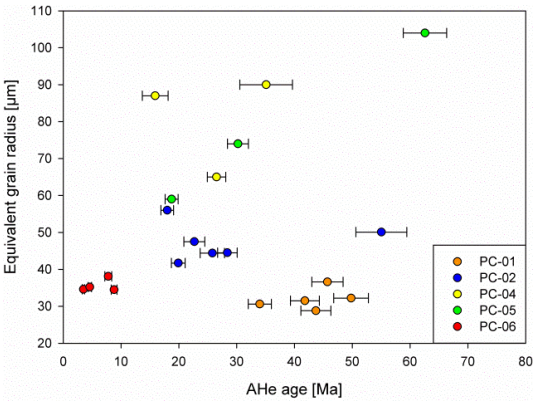

Fig. 4.9: AHe single grain ages (1σ error) from well Puerto Cansado-1 plotted against equivalent grain radius.

4.1.3.2 Apatite fission-track ages

In the Puerto Cansado-1 well every sample has been analysed by apatite fission-track dating. The AFT central ages range from 128.6 (±11.0) Ma at a depth of 890–1095.80 m to 12.8 (±3.1) Ma at a depth of 3668–3669.80 m (Fig. 4.8, Tab. 4.10). The apatite fission-track ages decrease almost continuously with increasing depth, whereby sample PC-01 is slightly younger than sample PC-02 (Fig. 4.8). While the Jurassic to Barremian samples reveal ages younger than the corresponding sedimentation age, the Albian and Aptian samples (PC-01, PC-02) show similar AFT and stratigraphic ages. Except for sample PC-07, all single grain age distributions fulfilled the requirement of the χ^2-test with values between 93 and 100 %.

4.1.3.3 Etch pit size and track length distribution

Etch pit size (D_{par}) and confined spontaneous fission-track lengths were measured in every sample. A total of 803 D_{par} values were determined for all apatite grains (Tab. 4.11). The mean D_{par} values for each sample reveal a range between 1.5 (±0.3) and 1.7 (±0.4) µm. All samples show a positive skewness ranging from 0.027 to 1.359. The largest etch pit size of 2.8 (±0.1) µm was measured in sample PC-02. Sample PC-06 shows the largest spread in etch pit size ranging between 0.6 (±0.1) and 2.6 (±0.1) µm. In sample PC-02, a positive correlation between single grain ages and D_{par} values has been detected (Fig. 4.10). The positive correlation indicates an inhomogeneous chemical composition concerning the fluorine and chlorine content of the apatite grains.

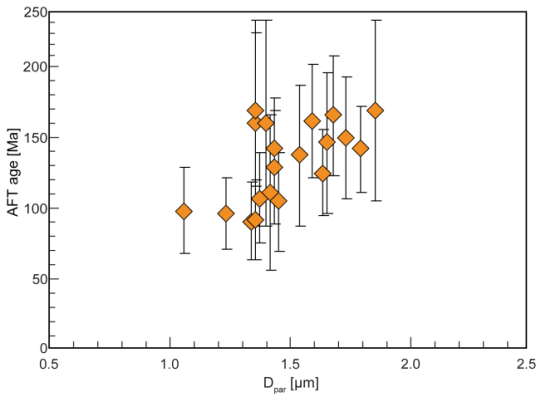

Fig. 4.10: AFT ages (1σ error) from sample PC-02 plotted against D_{par} values.

Confined spontaneous fission-track lengths were detected in every sample. A total of 112 track lengths were measured (Tab. 4.11). The obtained mean track lengths range from 11.0 (±1.7) to 12.3 (±1.3) µm. The track length distributions of the samples show a skewness ranging between -1.056 and 1.427. The largest track length of 15.3 (±0.1) µm was measured in sample PC-02, while the smallest of 7.6 (±0.1) µm was measured in sample PC-01. After correcting of the confined track lengths for their crystallographic orientation, the mean confined fission-track lengths changed to a distribution between 12.8 (±0.8) and 13.8 (±0.7) µm. The c-axis corrected track length distributions of the samples show a skewness ranging between -1.672 and 1.302. The largest track length after c-axis correction of 15.9 (±0.1) µm and the smallest of 10.3 (±0.1) µm was determined in sample PC-02.

Table 4.9: Apatite (U-Th-Sm)/He data from well Puerto Cansado-1 of the Tarfaya Basin

Sample	Recent T [°C]	Mass [µg]	Radius [µm]	U [µg/g]	Th [µg/g]	Sm [µg/g]	eU [µg/g]	Th/U	^{4}He [nmol/g]	F_t	Raw age [Ma]	Error ± 1σ [Ma]	Corr. age [Ma]	Error ± 1σ [Ma]
PC-01.1	32	0.9	31.5	7	18	105	12	2.5	1.57	0.560	23.4	1.4	41.8	2.5
PC-01.2	**32**	**0.7**	**30.6**	**3**	**38**	**95**	**12**	**11.5**	**1.26**	**0.520**	**17.7**	**1.0**	**34.0**	**2.0**
PC-01.3	32	1.0	28.8	3	21	121	8	7.7	1.18	0.570	24.9	1.5	43.7	2.6
PC-01.4	32	0.8	32.2	35	41	31	45	1.2	6.79	0.560	27.9	1.7	49.8	3.0
PC-01.5	32	1.4	36.6	3	15	64	7	4.4	1.13	0.610	27.9	1.6	45.7	2.7
PC-02.1	45	4.1	50.1	1	13	66	5	9.6	1.08	0.712	39.2	3.1	55.0	4.4
PC-02.2	45	2.8	47.5	2	41	76	11	22.8	1.00	0.679	15.4	1.2	22.7	1.8
PC-02.3	45	2.6	44.4	7	45	157	17	7.0	1.79	0.670	17.3	1.4	25.8	2.1
PC-02.4	45	1.9	41.7	3	47	126	14	15.1	1.07	0.640	12.7	0.8	19.9	1.2
PC-02.5	45	2.8	44.5	1	15	84	5	12.8	0.58	0.680	19.3	1.2	28.4	1.7
PC-02.6	**45**	**5.2**	**56.0**	**1**	**49**	**72**	**13**	**36.5**	**0.95**	**0.720**	**13.0**	**0.8**	**18.0**	**1.1**
PC-04.1	54	7.9	65.0	3	6	8	4	1.9	0.49	0.775	20.6	1.2	26.5	1.6
PC-04.2	**54**	**22.7**	**87.0**	**1**	**3**	**24**	**1**	**5.2**	**0.10**	**0.837**	**13.3**	**1.9**	**15.9**	**2.2**
PC-04.3	54	24.6	90.0	<1	3	19	1	5.5	0.20	0.840	29.5	3.8	35.1	4.5
PC-05.1	**60**	**6.0**	**59.0**	**12**	**15**	**55**	**16**	**1.2**	**1.27**	**0.761**	**14.3**	**0.9**	**18.8**	**1.1**
PC-05.2	60	12.8	74.0	2	4	21	3	2.1	0.40	0.808	24.4	1.5	30.2	1.8
PC-05.3	60	37.3	104.0	1	6	25	2	8.9	0.64	0.860	53.8	3.2	62.6	3.8
PC-06.1	**78**	**0.9**	**34.6**	**1**	**39**	**33**	**10**	**30.7**	**0.11**	**0.550**	**1.9**	**0.1**	**3.5**	**0.2**
PC-06.2	78	1.4	38.1	7	29	25	14	4.1	0.38	0.610	4.8	0.4	7.8	0.6
PC-06.3	78	1.0	34.5	28	64	61	43	2.3	1.20	0.580	5.1	0.3	8.8	0.5
PC-06.4	78	1.2	35.2	1	36	78	10	26.2	0.15	0.570	2.6	0.2	4.6	0.3

eU = [U] + 0.235 [Th] + 0.0053 [Sm] (concentrations in weight %); F_t: α-ejection correction factor; raw ages are corrected after Farley et al. (1996); radius calculated according to Shuster et al. (2006) and Ketcham (2009). Data in bold: youngest apatite (U-Th-Sm)/He grain of each sample discussed in the text.

Table 4.10: Apatite fission-track data from well Puerto Cansado-1 of the Tarfaya Basin

Sample	Recent T [°C]	n	U (std) [µg/g]	Sp. Tracks ρ_s	Sp. Tracks N_s	Ind. Tracks ρ_i	Ind. Tracks N_i	$P(\chi^2)$ [%]	Central age [Ma]	Error ± 1σ [Ma]
PC-01	32	20	20.0 (16.6)	9.257	262	18.867	534	100.0	117.8	10.9
PC-02	45	20	6.8 (6.5)	3.040	352	5.665	656	94.4	128.6	11.0
PC-03	53	20	6.2 (5.3)	2.979	290	6.091	593	94.9	117.3	10.5
PC-04	54	16	8.0 (5.2)	3.911	259	8.470	561	100.0	120.2	11.1
PC-05	60	20	14.3 (11.3)	4.639	402	18.694	1620	93.3	64.5	5.0
PC-06	78	30	19.8 (18.0)	4.267	211	21.113	1044	98.7	48.7	4.5
PC-07	112	30	26.0 (44.2)	0.959	97	20.205	2043	0.0	12.8	3.1

U (std): Uranium concentration and standard deviation; n: number of counted apatite grains ρ_s: density of spontaneous tracks (10^5 tr/cm^2); N_s: number of spontaneous tracks; ρ_i: density of induced tracks (10^5 tr/cm^2); N_i: number of induced tracks; $P(\chi^2)$: probability that single grains are consistent and belong to the same population. Test is passed if $P(\chi^2) > 5$ % (Galbraith, 1981). Nd = 16835 tracks counted on CN5 dosimeter glass. Central ages are calculated using a ζ-value of 333.36 ± 17.89. Samples were irradiated at the FRM II reactor facility in Garching, Germany with a fluence of 1 x 10^{16} neutrons/cm^2.

Table 4.11: Confined fission-track length data from well Puerto Cansado-1 of the Tarfaya Basin

Sample	n CT	CT mean [µm]	CT std [µm]	CT skew	CT min [µm]	CT max [µm]	L_c mean [µm]	L_c std [µm]	L_c skew	L_c min [µm]	L_c max [µm]	n D_{par}	D_{par} mean [µm]	D_{par} std [µm]	D_{par} skew	D_{par} min [µm]	D_{par} max [µm]
PC-01	13	11.0	1.8	-0.147	7.6	13.6	12.8	1.0	-0.230	11.3	14.1	114	1.6	0.2	1.243	1.2	2.5
PC-02	74	11.0	1.7	0.132	8.3	15.3	13.0	1.1	-0.010	10.3	15.9	205	1.7	0.4	0.527	0.9	2.8
PC-03	5	11.6	2.6	-0.861	7.7	14.3	13.7	1.2	-0.270	12.3	15.0	107	1.6	0.2	1.251	1.1	2.6
PC-04	3	12.3	1.3	-1.056	10.8	13.4	13.8	0.7	-1.672	13.0	14.3	75	1.7	0.3	0.027	0.6	2.4
PC-05	6	11.2	1.7	1.427	9.6	14.3	13.3	1.0	1.378	12.5	15.1	92	1.7	0.3	1.359	1.3	2.6
PC-06	4	11.4	1.1	0.091	10.2	12.6	13.3	0.6	0.771	12.7	14.0	120	1.6	0.3	0.444	0.6	2.6
PC-07	7	10.8	1.5	0.171	9.1	12.8	12.8	0.8	1.302	12.1	14.3	90	1.5	0.3	0.323	0.8	2.2

n: number of measured individual confined tracks (CT) and etch pit diameter (D_{par}); CT mean: mean confined track length; L_c mean: mean track length after c-axis correction; D_{par} mean: mean etch pit diameter; std: standard deviation; skew: skewness of distribution relative to the mean value; min: minimum single values; max: maximum single values; n.da.: no data.

4.1.4 Cap Juby-1

4.1.4.1 Apatite (U-Th-Sm)/He ages

Four samples from the offshore well Cap Juby-1 with two or three single grain aliquots have been analysed by apatite (U-Th-Sm)/He dating. Raw AHe ages cover a range from 0.6 (±0.0) to 9.3 (±2.1) Ma (Tab. 4.12). α-ejection correction after Farley et al. (1996) was applied to all grains resulting in ages between 0.8 (±0.0) and 12.1 (±2.7) Ma, whereas the youngest α-ejection corrected single grain age of each sample range from 9.1 (±0.5) Ma at a depth of 780–1100 m to 0.8 (±0.0) Ma at a depth of 1560–1850 m (Fig. 4.13, Tab. 4.12). The AHe ages decrease continuously with increasing depth (Fig. 4.13). All single grain aliquot ages are significantly younger than the corresponding sedimentation age of the sampled rock as well as younger than the apatite fission-track age.

The samples from the Cap Juby-1 well show no clear positive correlation between single grain age and effective Uranium concentration (Fig. 4.11).

Except for sample CJ-04, no clear positive correlation between equivalent grain radius and AHe age distribution was determined (Fig. 4.12).

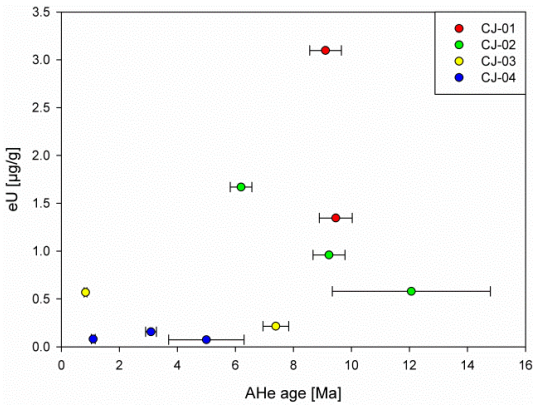

Fig. 4.11: AHe single grain ages (1σ error) from well Cap Juby-1 plotted against eU.

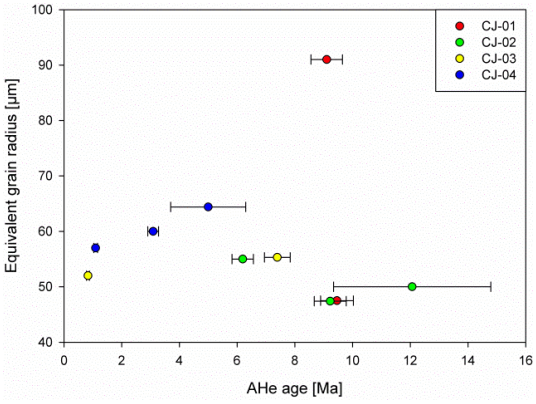

Fig. 4.12: AHe single grain ages (1σ error) from well Cap Juby-1 plotted against equivalent grain radius.

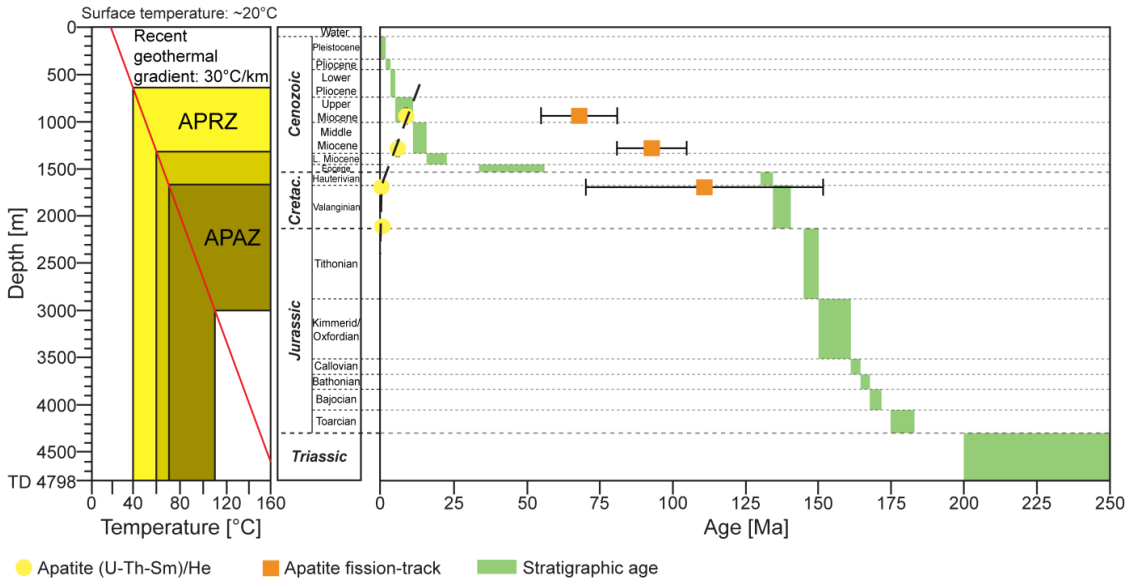

Fig. 4.13: Thermochronometric age (1σ error) – depth distribution of the Cap Juby-1 well. On the left side the recent temperature distribution as well as a schematic stratigraphic profile according to Wenke et al. (2011) is displayed.

4.1.4.2 Apatite fission-track ages

Three of four samples from offshore well Cap Juby-1 have been determined by apatite fission-track dating. One sample contained no apatite grains. The AFT ages range between 67.3 (±12.8) Ma at a depth of 780–1100 m and 110.8 (±40.5) Ma at a depth of 1560–1850 m (Fig. 4.13, Tab. 4.13). In contrast to the onshore wells, the apatite fission-track ages increase with increasing depth (Fig. 4.13). The Neogene samples show significantly older AFT ages than the corresponding sedimentation age. While two single grain age distributions fulfilled the requirement of the χ^2-test with high values of 81 and 98 %, sample CJ-02 reveals a large spread in the single grain age distribution and reaches a low value of 23 % for the χ^2-test indicating several age populations.

4.1.4.3 Etch pit size and track length distribution

Etch pit size (D_{par}) and confined spontaneous fission-track lengths were measured in every sample. A total of 73 D_{par} values were determined for all apatite grains (Tab. 4.14). The mean D_{par} values for each sample reveal a range between 1.4 (±0.4) and 2.0 (±0.2) µm. The samples show skewness between -0.293 and 1.458. The largest spread in etch pit size varying between 0.6 (±0.1) and 3.6 (±0.1) µm was measured in sample CJ-02. This sample shows also the largest spread in etch pit size ranging between 0.6 (±0.1) and 3.6 (±0.1) µm. No positive correlation between single grain ages and D_{par} values has been detected.

In two samples, only 5 confined fission-track lengths were detected (Tab. 4.14). Sample CJ-02 show a mean track length of 10.8 (±2.5) µm and a skewness of 0.605. After correcting of the confined track lengths for their crystallographic orientation, the mean confined fission-track lengths of sample CJ-02 changed to a distribution of 12.9 (±1.8) µm with a skewness of 0.473 and a maximum track length of 15.2 (±0.1) µm.

Table 4.12: Apatite (U-Th-Sm)/He data from well Cap Juby-1 of the Tarfaya Basin

Sample	Recent T [°C]	Mass [µg]	Radius [µm]	U [µg/g]	Th [µg/g]	Sm [µg/g]	eU [µg/g]	Th/U	^{4}He [nmol/g]	F_t	Raw age [Ma]	Error ± 1σ [Ma]	Corrected age [Ma]	Error ± 1σ [Ma]
CJ-01.2	**48**	**21.7**	**91.0**	**1**	**8**	**13**	**3**	**6.9**	**0.13**	**0.832**	**7.6**	**0.5**	**9.1**	**0.5**
CJ-01.3	48	8.4	47.5	<1	4	83	1	10.2	0.08	0.765	7.2	0.4	9.5	0.6
CJ-02.1	**58**	**9.8**	**55.0**	**<1**	**5**	**82**	**1**	**10.3**	**0.06**	**0.782**	**4.8**	**0.3**	**6.2**	**0.4**
CJ-02.2	58	6.0	47.4	<1	2	38	1	5.2	0.05	0.754	7.0	0.4	9.2	0.6
CJ-02.3	58	8.6	50.0	<1	2	40	1	9.6	0.05	0.773	9.3	2.1	12.1	2.7
CJ-03.1	**71**	**2.9**	**52.0**	**<1**	**2**	**1**	**1**	**7.5**	**0.00**	**0.689**	**0.6**	**0.0**	**0.8**	**0.0**
CJ-03.2	71	3.8	55.3	<1	1	1	<1	6.2	0.01	0.711	5.3	0.3	7.4	0.4
CJ-04.1	**83**	**5.1**	**57.0**	**<1**	**<1**	**1**	**<1**	**23.8**	**0.00**	**0.736**	**0.8**	**0.0**	**1.1**	**0.1**
CJ-04.2	83	5.3	60.0	<1	1	1	<1	43.7	0.00	0.736	2.3	0.1	3.1	0.2
CJ-04.3	83	6.7	64.4	<1	<1	<1	<1	29.8	0.00	0.757	3.8	1.0	5.0	1.3

eU = [U] + 0.235 [Th] + 0.0053 [Sm] (concentrations in weight %); F_t: α-ejection correction factor; raw ages are corrected after Farley et al. (1996); radius calculated according to Shuster et al. (2006) and Ketcham (2009). Data in bold: youngest apatite (U-Th-Sm)/He grain of each sample discussed in the text.

Table 4.13: Apatite fission-track data from well Cap Juby-1 of the Tarfaya Basin

Sample	Recent T [°C]	n	U (std) [µg/g]	Sp. Tracks ρ_s	Sp. Tracks N_s	Ind. Tracks ρ_i	Ind. Tracks N_i	$P(\chi^2)$ [%]	Central age [Ma]	Error ± 1σ [Ma]
CJ-01	48	4	26.1 (16.4)	9.791	38	36.845	143	80.5	67.3	12.8
CJ-02	58	10	15.4 (15.7)	4.720	116	12.940	318	22.8	92.8	11.9
CJ-03	71	2	7.2 (6.7)	2.930	11	6.660	25	98.3	110.8	40.5

U (std): Uranium concentration and standard deviation; n: number of counted apatite grains; ρ_s: density of spontaneous tracks (10^5 tr/cm^2); N_s: number of spontaneous tracks; ρ_i: density of induced tracks (10^5 tr/cm^2); N_i: number of induced tracks; $P(\chi^2)$: probability that single grains are consistent and belong to the same population. Test is passed if $P(\chi^2) > 5$ % (Galbraith, 1981). Nd = 15419 tracks counted on CN5 dosimeter glass. Central ages are calculated using a ζ-value of 333.36 ± 17.89. Samples were irradiated at the FRM II reactor facility in Garching, Germany with a fluence of 1 x 10^{16} neutrons/cm^2.

Table 4.14: Confined fission-track length data from well Cap Juby-1 of the Tarfaya Basin

Sample	n CT	CT mean [µm]	CT std [µm]	CT skew	CT min [µm]	CT max [µm]	L_c mean [µm]	L_c std [µm]	L_c skew	L_c min [µm]	L_c max [µm]	n D_{par}	D_{par} mean [µm]	D_{par} std [µm]	D_{par} skew	D_{par} min [µm]	D_{par} max [µm]
CJ-01	1	10.9	-	-	10.9	10.9	13.2	-	-	13.2	13.2	18	2.0	0.2	-0.293	1.4	2.4
CJ-02	4	10.8	2.5	0.605	8.1	14.1	12.9	1.8	0.473	10.9	15.2	45	1.6	0.7	1.111	0.6	3.6
CJ-03	n.da.	-	-	-	-	-	-	-	-	-	-	10	1.4	0.4	1.458	0.9	2.4

n: number of measured individual confined tracks (CT) and etch pit diameter (D_{par}); CT mean: mean confined track length; L_c mean: mean track length after c-axis correction; D_{par} mean: mean etch pit diameter; std: standard deviation; skew: skewness of distribution relative to the mean value; min: minimum single values; max: maximum single values; n.da.: no data.

4.1.5 Outcrop samples

4.1.5.1 Apatite (U-Th-Sm)/He ages

Two Lower Cretaceous outcrop samples from the Tarfaya Basin have been analysed by apatite (U-Th-Sm)/He dating, whereas 18 samples contained no apatite or no suitable apatite grains for AHe processing and 10 samples could not be determined. Raw AHe ages cover a wide range from 38.1 (±2.3) to 185.6 (±11.1) Ma (Tab. 4.15). α-ejection correction after Farley et al. (1996) was applied to all grains resulting in ages between 63.5 (±3.8) and 302.3 (±18.1) Ma (Tab. 4.15). The large spread in the single grain ages is probably caused by uranium and thorium rich inclusions that might not have been completely dissolved during sample digestion. The youngest α-ejection corrected single grain age of sample MA-19 is 63.5 (±3.8) Ma and 72.6 (±4.4) Ma of sample MA-24 (Fig. 4.14, Tab. 4.15). Both samples contain one AHe

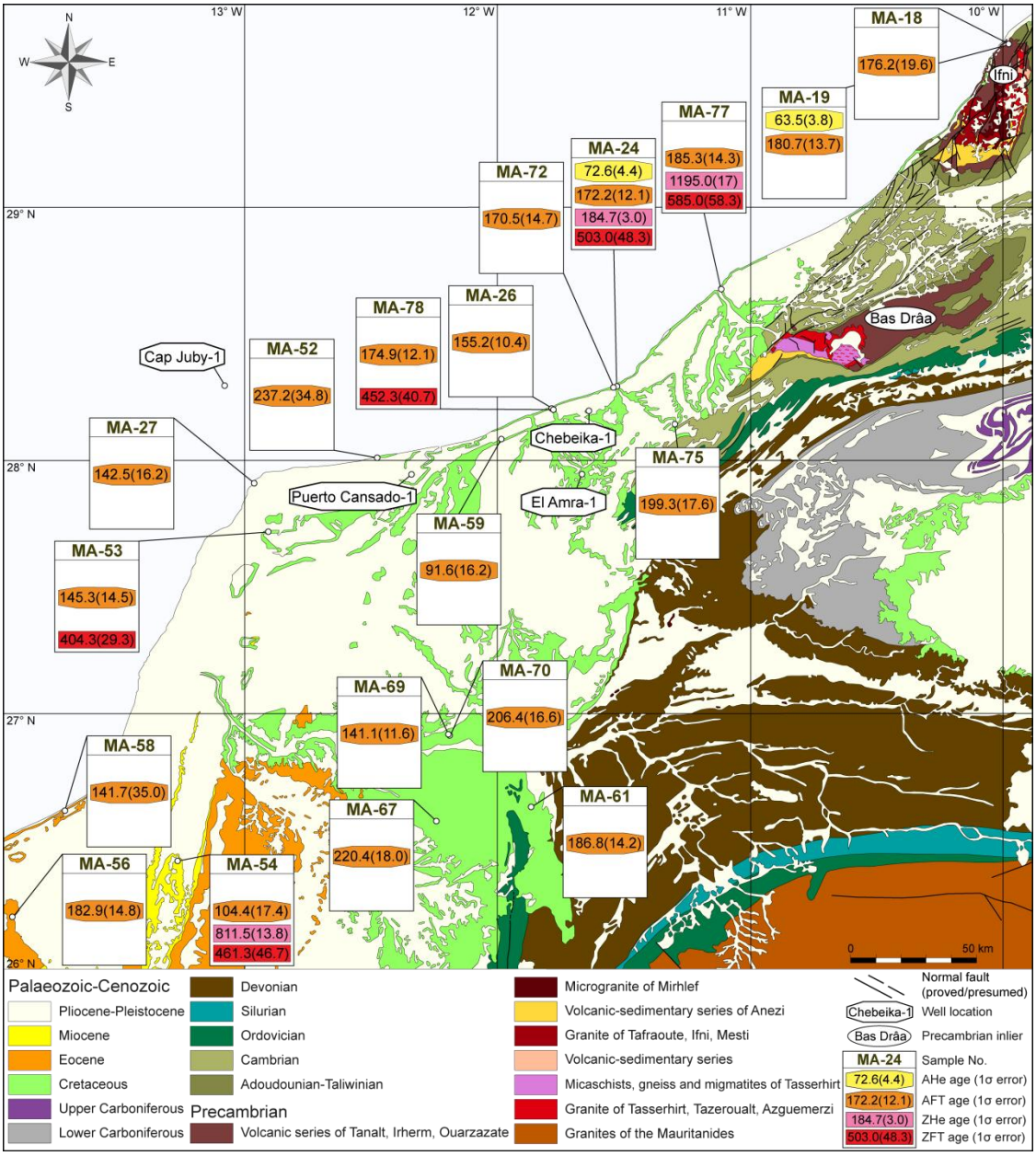

Fig. 4.14: Geological map of the Tarfaya Basin with sample locations, AFT and ZFT central ages, ZHe ages as well as the youngest AHe age (1σ error).

single grain age younger than the respective sedimentation age of the sampled rock and younger than the AFT.

The samples show no clear correlation between single grain age and effective Uranium concentration (Fig. 4.15).

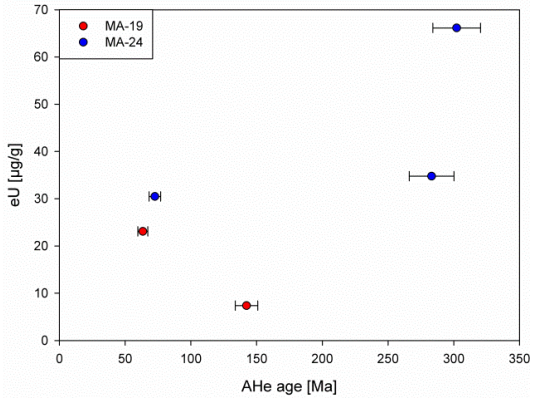

Fig. 4.15: AHe single grain ages (1σ error) from outcrop samples of the Tarfaya Basin plotted against eU.

In the outcrop samples from the Tarfaya Basin, no correlation between equivalent grain radius and AHe age distribution has been determined (Fig. 4.16).

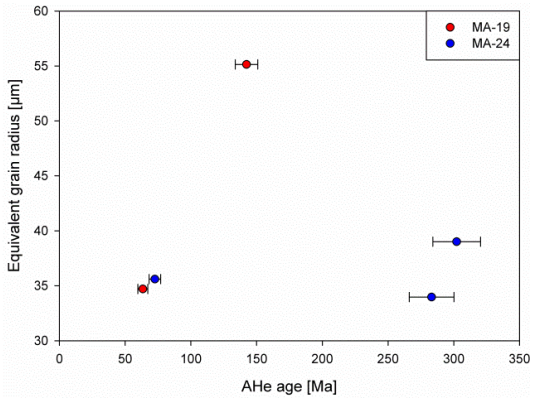

Fig. 4.16: AHe single grain ages (1σ error) from outcrop samples of the Tarfaya Basin plotted against equivalent grain radius.

4.1.5.2 Apatite fission-track ages

19 of 30 outcrop samples from the Tarfaya Basin have been analysed by apatite fission-track dating covering the entire study area. Eleven samples contained no apatite grains. The AFT central ages cover a wide range from 91.6 (±16.2) to 237.2 (±34.8) Ma (Fig. 4.14, Tab. 4.16). All ages are older than the respective sedimentation age of the sampled rock. The single grain age distributions of ten samples fulfilled the requirement of the χ^2-test with values between 13 and 100 %, while nine samples failed the χ^2-test indicating several age populations. Based on the large spread in the AFT age distribution, a differentiated consideration is necessary.

The ages of seven Lower Cretaceous samples (MA-18, MA-19, MA-24, MA-61, MA-72, MA-75 and MA-77) are equal within the standard deviation ranging between 170.5 (±14.7) and 199.3 (±17.6) Ma (Fig. 4.17, Tab. 4.16). The AFT ages are slightly older than the corresponding sedimentation age and the single grain age distributions fulfilled the requirement of the χ^2-test with values between 66 and 100 % (Fig. 4.17).

The Upper Cretaceous samples (MA-26, MA-67, MA-69, MA-70 and MA-78) show ages that range from 141.1 (±11.6) to 220.4 (±18.0) Ma. The AFT ages are significantly older than the corresponding sedimentation age and mostly older than the Lower Cretaceous AFT ages (Fig. 4.17). While the single grain age distribution of the Cenomanian–Turonian samples passed the χ^2-test with values of 89 and 98 %, the Coniacian and Campanian samples reveal low values between 0 and 13 %.

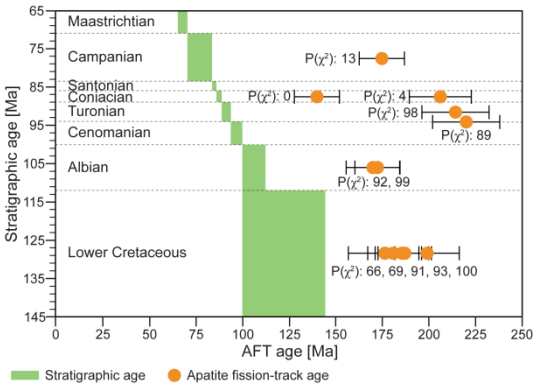

Fig. 4.17: AFT ages (1σ error) from Cretaceous samples of the Tarfaya Basin plotted against stratigraphic age.

The AFT ages of the seven Neogene samples (MA-27, MA-52, MA-53, MA-54, MA-56,

MA-58 and MA-59) cover a wide range between 91.6 (±16.2) and 237.2 (±34.8) Ma. The youngest as well as the oldest age was obtained from Pliocene sandstone samples (MA-52, MA-59) at similar elevations of 25 and 80 m. All ages are significantly older than the corresponding sedimentation age of the sampled rock. All single grain age distributions failed the requirement of the χ^2-test with a value of 0 %.

The age-elevation plot for the entire Tarfaya Basin shows the large spread in the age distribution (Fig. 4.18). The majority of the samples reveal AFT ages significantly older than the sedimentation age. Consequently, no age-elevation relationship exists, since the ages represent solely or partially the thermal history of the source area.

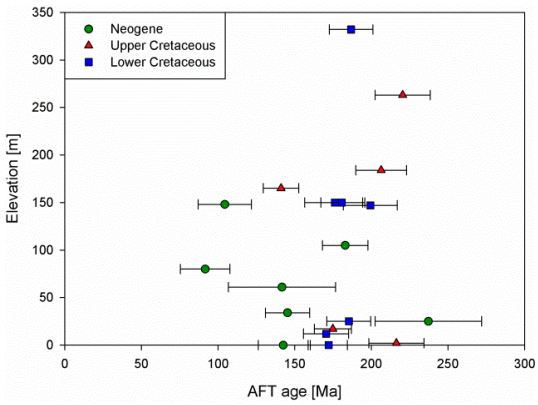

Fig. 4.18: AFT age (1σ error) – elevation plot from outcrop samples of the Tarfaya Basin.

4.1.5.3 Etch pit size and track length distribution

Etch pit size (D_{par}) and confined spontaneous fission-track lengths were measured in 19 outcrop samples from the Tarfaya Basin. A total of 1998 D_{par} values were determined for all apatite grains (Tab. 4.17). The mean D_{par} values for each sample reveal a narrow range between 1.3 (±0.1) and 1.9 (±0.3) µm. The narrow range indicates a very homogenous chemical composition concerning the fluorine and chlorine content of the apatites. Except for samples MA-26 (-0.653), MA-61 (-0.784), MA-70 (-0.136) and MA-75 (-0.047), all samples exhibit a positive skewness between 0.009 and 1.583. The largest etch pit size of 2.9 (±0.1) was measured in samples MA-67 and MA-69. Sample MA-53 shows the largest spread in etch pit size ranging between 0.9 (±0.1) and 2.7 (±0.1) µm. A slightly positive correlation between single grain ages and D_{par} values has been detected in sample MA-56 (Fig. 4.19).

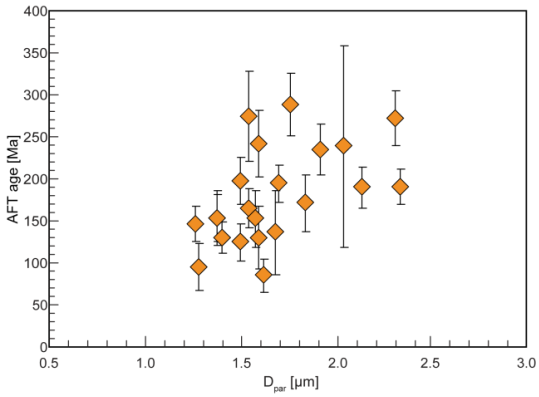

Fig. 4.19: AFT ages (1σ error) from sample MA-56 plotted against D_{par} values.

A total of 504 track lengths of confined spontaneous fission-tracks were measured (Tab. 4.17). The obtained mean track lengths range from 10.4 (±0.6) to 13.8 (±0.6) µm. The track length distributions of the samples show no significant skewness ranging between -1.567 and 0.935. The largest track length of 16.3 (±0.1) µm was measured in sample MA-56, while the smallest of 6.7 (±0.1) µm was measured in sample MA-19. After correcting of the confined track lengths for their crystallographic orientation, the mean confined fission-track lengths changed to a distribution between 12.2 (±0.3) and 14.6 (±1.0) µm. The c-axis corrected track length distributions of the samples show no significant skewness ranging between -0.602 and 1.028. The largest track length after c-axis correction of 16.6 (±0.1) µm was measured in sample MA-56, whereas the smallest of 10.7 (±0.1) µm was determined in sample MA-19.

4.1.5.4 Zircon (U-Th-Sm)/He ages

Three outcrop samples from the Tarfaya Basin with three single grain aliquots have been determined by zircon (U-Th-Sm)/He analysis. Raw ZHe ages cover a wide range from 33.9 (±0.8) to 904.6 (±12.5) Ma (Tab. 4.18). α-ejection correction after Farley et al. (1996) was applied to all grains resulting in ages between 47.7 (±0.8) and 1195.0 (±17.1) Ma (Tab. 4.18). The ZHe ages with the lowest eU content of the aliquots are presented in Figure 4.14. However, for further interpretation and discussion all single grain ages were used. Two samples (MA-54, MA-77) show similar ages between 506.7 (±8.7) and 1195.0 (±17.1) Ma. These ages are significantly older than the corresponding sedimentation and AFT age of the sampled rock. Sample MA-24 yielded two single grain ages of 184.7 (±3.0) and 384.6 (±6.6) Ma that are older than the sedimentation, AFT and AHe age. In contrast, grain MA-24.2 with an age of 47.7 (±8.7) Ma is younger than the sedimentation, AFT and AHe age (Tab. 4.18). This could be due to an analytical error or the relatively high U content, since ZHe ages decrease rapidly to anomalously young and unreproducible ages at U concentrations of ~1000 ppm (Reiners, 2005). Eight single grains yielded detrital ages and therefore represent the thermal history of the source area. Except for grain MA-24.1 with an age of 184.7 (±3.0) Ma, the ZHe ages of the Tarfaya Basin are significantly older than the ZHe and ZFT ages of the western Anti-Atlas mountain belt (Fig. 4.23).

4.1.5.5 Zircon fission-track ages

Five outcrop samples from the Tarfaya Basin have been analysed by zircon fission-track dating. The zircon fission-track central ages range between 404.3 (±29.3) and 585.0 (±58.3) Ma (Fig. 4.14, Tab. 4.19). All ages are significantly older than the corresponding sedimentation and AFT age of the sampled rock. Single grain ages of the samples are similar to the ZHe ages. The single grain age distribution of four samples fulfilled the requirement of the χ^2-test with values between 54 and 100 %, while sample MA-54 failed the χ^2-test with a value of 1 % indicating several age populations. However, all samples show a vast spread in the single grain age distribution ranging from 226.5 to 1207.8 Ma (Fig. 5.9, Fig. 5.10 and Fig. 5.12).

The ZFT central ages represent the thermal history of the source area. 49 of the 142 determined single grain ages are in the range of the ZFT ages from outcrop samples of the western Anti-Atlas (Fig. 5.9, Fig. 5.10 and Fig. 5.12). Additionally 52 single grain ages correspond to the ZFT age range of the wells Adrar Zougar-1 and Oum Doul-1, whereas 41 ages are older than any ZFT ages determined in the western Anti-Atlas mountain belt (Fig. 5.9, Fig. 5.10 and Fig. 5.12).

Table 4.15: Apatite (U-Th-Sm)/He data from outcrop samples of the Tarfaya Basin

Sample	Mass [µg]	Radius [µm]	U [µg/g]	Th [µg/g]	Sm [µg/g]	eU [µg/g]	Th/U	^{4}He [nmol/g]	F_t	Raw age [Ma]	Error ± 1σ [Ma]	Corrected age [Ma]	Error ± 1σ [Ma]
MA-19.1	**1.1**	**34.7**	**21**	**10**	**46**	**23**	**0.5**	**4.83**	**0.600**	**38.1**	**2.3**	**63.5**	**3.8**
MA-19.2	4.0	55.1	3	17	62	8	5.1	4.35	0.711	101.3	6.1	142.3	8.5
MA-24.1	1.5	39.0	44	96	21	66	2.2	67.40	0.614	185.6	11.1	302.3	18.1
MA-24.2	0.9	34.0	29	23	50	35	0.8	31.46	0.577	163.5	9.8	283.2	17.0
MA-24.3	**1.1**	**35.6**	**28**	**12**	**8**	**31**	**0.4**	**7.27**	**0.606**	**44.0**	**2.6**	**72.6**	**4.4**

eU = [U] + 0.235 [Th] + 0.0053 [Sm] (concentrations in weight %); F_t: α-ejection correction factor; raw ages are corrected after Farley et al. (1996); radius calculated according to Shuster et al. (2006) and Ketcham (2009). Data in bold: youngest apatite (U-Th-Sm)/He grain of each sample discussed in the text.

Table 4.16: Apatite fission-track data from outcrop samples of the Tarfaya Basin

Sample	Elevation [m a.s.l.]	n	U (std) [µg/g]	Sp. Tracks ρ_s	Sp. Tracks N_s	Ind. Tracks ρ_i	Ind. Tracks N_i	$P(\chi^2)$ [%]	Central age [Ma]	Error ± 1σ [Ma]
MA-18	150	6	17.1 (12.5)	14.816	214	14.677	212	93.4	176.2	19.6
MA-19	150	20	12.4 (8.8)	9.039	727	8.741	703	100.0	180.7	13.7
MA-24	0	20	14.2 (8.4)	12.129	1003	12.347	1021	98.8	172.2	12.1
MA-26	2	9	12.0 (4.6)	14.179	564	11.464	456	97.5	216.3	18.0
MA-27	0	20	18.2 (12.7)	13.324	1224	15.338	1409	0.0	142.5	16.2
MA-52	25	19	10.0 (7.4)	9.838	606	59.206	3647	0.0	237.2	34.8
MA-53	34	23	13.7 (6.3)	8.751	723	75.505	6238	0.0	145.3	14.5
MA-54	148	15	8.3 (5.3)	4.025	245	48.164	2932	0.0	104.4	17.4
MA-56	105	22	10.3 (4.8)	9.340	1203	61.194	7882	0.0	182.9	14.8
MA-58	61	9	17.0 (8.5)	8.998	162	104.198	1876	0.0	141.7	35.0
MA-59	80	24	10.2 (3.9)	4.071	580	60.927	8681	0.0	91.6	16.2
MA-61	332	7	10.4 (4.1)	10.846	327	70.846	2136	65.8	186.8	14.2
MA-67	263	20	11.2 (8.5)	12.736	437	13.989	480	88.5	220.4	18.0
MA-69	165	22	22.2 (20.6)	10.695	1085	18.709	1898	0.0	141.1	11.6
MA-70	184	16	12.9 (6.8)	12.391	523	72.191	3047	3.9	206.4	16.6
MA-72	12	20	10.5 (6.5)	9.836	335	13.888	473	91.7	170.5	14.7
MA-75	147	8	11.3 (6.3)	10.581	212	64.836	1299	68.9	199.3	17.6
MA-77	25	20	4.3 (3.1)	3.849	317	25.414	2093	90.5	185.3	14.3
MA-78	17	20	10.4 (3.8)	8.915	668	63.030	4723	12.5	174.9	12.1

U (std): Uranium concentration and standard deviation; n: number of counted apatite grains; ρ_s: density of spontaneous tracks (10^5 tr/cm^2); N_s: number of spontaneous tracks; ρ_i: density of induced tracks (10^5 tr/cm^2); N_i: number of induced tracks; $P(\chi^2)$: probability that single grains are consistent and belong to the same population. Test is passed if $P(\chi^2) > 5$ % (Galbraith, 1981). Nd = 17386 tracks counted on CN5 dosimeter glass. Central ages are calculated using a ζ-value of 333.36 ± 17.89 for samples MA-18 to MA-27 and 334.55 ± 15.80 for samples MA-52 to MA-78. Samples MA-18 to MA-27 were irradiated at the FRM II reactor facility in Garching, Germany with a fluence of 1 x 10^{16} neutrons/cm^2. Samples MA-52 to MA-78 were irradiated at the Triga reactor facility in Mainz, Germany.

Table 4.17: Confined fission-track length data from outcrop samples of the Tarfaya Basin

Sample	n CT	CT mean [µm]	CT std [µm]	CT skew	CT min [µm]	CT max [µm]	L_c mean [µm]	L_c std [µm]	L_c skew	L_c min [µm]	L_c max [µm]	n D_{par}	D_{par} mean [µm]	D_{par} std [µm]	D_{par} skew	D_{par} min [µm]	D_{par} max [µm]
MA-18	n.da.	-	-	-	-	-	-	-	-	-	-	30	1.3	0.1	1.073	1.2	1.6
MA-19	112	11.5	1.6	-0.356	6.7	15.4	13.3	1.0	-0.160	10.7	16.1	250	1.5	0.1	0.319	1.1	2.0
MA-24	117	11.9	1.7	-0.009	7.7	15.9	13.6	1.1	-0.011	11.0	16.4	240	1.5	0.2	0.838	1.0	2.4
MA-26	6	11.9	1.3	0.085	10.1	13.6	13.6	0.9	0.646	12.8	14.9	45	1.3	0.1	-0.653	1.0	1.6
MA-27	17	11.6	1.9	0.262	8.8	15.6	13.6	1.0	0.549	12.4	15.8	95	1.6	0.3	0.505	1.3	2.3
MA-52	5	11.3	2.0	-0.207	8.7	13.7	13.5	1.0	0.062	12.4	14.6	90	1.7	0.3	1.583	1.2	2.7
MA-53	14	12.0	2.5	-1.044	7.1	14.4	13.7	1.1	-0.576	12.0	15.2	111	1.6	0.4	1.326	0.9	2.7
MA-54	n.da.	-	-	-	-	-	-	-	-	-	-	69	1.5	0.4	1.149	0.9	2.6
MA-56	98	12.6	1.5	-0.015	8.9	16.3	14.0	1.0	0.072	11.8	16.6	151	1.6	0.3	1.117	1.2	2.6
MA-58	3	13.8	0.6	0.935	13.3	14.5	14.6	0.7	1.028	14.0	15.4	37	1.5	0.2	0.009	1.1	1.9
MA-59	37	12.0	1.7	-0.123	8.7	15.8	13.7	1.1	-0.129	11.5	15.9	147	1.5	0.3	0.028	0.9	2.0
MA-61	10	12.6	2.1	-0.968	7.9	15.7	14.2	1.1	0.068	12.1	16.2	35	1.6	0.2	-0.784	1.0	1.9
MA-67	8	11.6	1.9	-0.417	8.4	14.1	13.3	1.4	-0.207	11.1	15.2	100	1.8	0.4	1.188	1.2	2.9
MA-69	27	11.9	1.7	-0.478	7.7	14.9	13.6	1.0	-0.059	11.7	15.7	107	1.9	0.3	0.989	1.3	2.9
MA-70	5	12.4	0.5	-1.567	11.6	12.9	14.0	0.5	-0.602	13.4	14.4	80	1.6	0.2	-0.136	1.1	1.9
MA-72	2	10.4	0.6	0.000	9.9	10.8	12.2	0.3	0.000	12.0	12.4	95	1.9	0.3	0.569	1.3	2.8
MA-75	2	12.1	1.3	0.000	11.1	13.0	13.2	0.2	0.000	13.0	13.3	39	1.5	0.1	-0.047	1.2	1.7
MA-77	18	11.7	1.8	-0.704	7.4	14.6	13.5	0.9	-0.231	12.2	15.1	137	1.4	0.2	0.306	0.8	2.2
MA-78	23	11.8	1.4	0.878	10.1	15.4	13.5	1.0	0.530	11.6	16.0	140	1.5	0.3	0.699	1.0	2.4

n: number of measured individual confined tracks (CT) and etch pit diameter (D_{par}); CT mean: mean confined track length; L_c mean: mean track length after c-axis correction; D_{par} mean: mean etch pit diameter; std: standard deviation; skew: skewness of distribution relative to the mean value; min: minimum single values; max: maximum single values; n.da.: no data.

Table 4.18: Zircon (U-Th-Sm)/He data from outcrop samples of the Tarfaya Basin

Sample	Mass [µg]	Radius [µm]	U [µg/g]	Th [µg/g]	Sm [µg/g]	eU [µg/g]	Th/U	^{4}He [nmol/g]	Ft	Raw age [Ma]	Error ± 1σ [Ma]	Corrected age [Ma]	Error ± 1σ [Ma]
MA-24.1	**1.9**	**42.3**	**658**	**262**	**n.d.**	**720**	**0.41**	**518.5**	**0.718**	**132.5**	**2.2**	**184.7**	**3.0**
MA-24.2	2.3	41.1	916	88	n.d.	936	0.10	170.8	0.710	33.9	0.6	47.7	0.8
MA-24.3	1.7	38.2	696	108	n.d.	721	0.16	1062.7	0.696	267.7	4.5	384.6	6.6
MA-54.1	5.0	53.1	150	71	n.d.	167	0.49	767.0	0.784	796.4	13.4	1015.9	17.6
MA-54.2	**6.1**	**57.4**	**118**	**48**	**n.d.**	**130**	**0.42**	**477.1**	**0.797**	**646.5**	**10.8**	**811.5**	**13.8**
MA-54.3	7.9	62.3	153	44	n.d.	164	0.29	373.8	0.808	409.5	7.0	506.7	8.7
MA-77.1	**3.3**	**46.4**	**115**	**68**	**n.d.**	**131**	**0.60**	**689.0**	**0.757**	**904.6**	**12.5**	**1195.0**	**17.1**
MA-77.2	4.2	51.0	135	27	n.d.	142	0.20	621.6	0.777	761.0	11.6	979.0	15.3
MA-77.3	2.4	42.8	261	96	n.d.	284	0.38	679.2	0.728	428.4	8.9	588.5	12.4

eU = [U] + 0.235 [Th] + 0.0053 [Sm] (concentrations in weight %); F_t: α-ejection correction factor; raw ages are corrected after Farley et al. (1996); radius calculated according to Reiners et al. (2004) and Ketcham (2009). Data in bold and red marked data are discussed in the text.

Table 4.19: Zircon fission-track data from outcrop samples of the Tarfaya Basin

Sample	Etch time at 200 °C [h]	n	U (std) [µg/g]	Sp. Tracks ρ_s	Sp. Tracks N_s	Ind. Tracks ρ_i	Ind. Tracks N_i	$P(\chi^2)$ [%]	Central age [Ma]	Error ± 1σ [Ma]
MA-24	5.0	27	112.5 (38.3)	261.295	1808	21.534	149	99.5	503.0	48.3
MA-53	5.0	41	145.7 (48.1)	278.315	3234	28.744	334	85.9	404.3	29.3
MA-54	4.0	24	141.7 (69.4)	290.966	2745	25.864	244	0.7	461.3	46.7
MA-77	4.0	26	123.5 (48.2)	341.141	1915	23.871	134	92.9	585.0	58.3
MA-78	5.0	24	160.6 (64.3)	319.510	1994	29.163	182	53.8	452.3	40.7

Etch time in KOH:NaOH (7:5) eutectic melt at 200 ± 2 °C; U (std): Uranium concentration and standard deviation; n: number of counted apatite grains; ρ_s: density of spontaneous tracks (10^5 tr/cm^2); N_s: number of spontaneous tracks; ρ_i: density of induced tracks (10^5 tr/cm^2); N_i: number of induced tracks; $P(\chi^2)$: probability that single grains are consistent and belong to the same population. Test is passed if $P(\chi^2)$ > 5% (Galbraith, 1981). Nd = 6044 tracks counted on CN1 dosimeter glass. Central ages are calculated using a ζ-value of 140.83 ± 5.93. Samples were irradiated at the FRM II reactor facility in Garching, Germany with a fluence of 1 x 10^{15} neutrons/cm^2.

4.1.6 Time-temperature modelling

Four Lower Cretaceous samples from the Tarfaya Basin (EA-02, PC-02, MA-19 and MA-24) with more than 50 measured confined fission-track lengths were used to test geological constraints against the thermo-chronological data set (Fig. 4.20). Whenever possible the AFT data set were combined with apatite (U-Th-Sm)/He data. An AFT+AHe based time-temperature (t-T) modelling with 'HeFTy' was performed in three of the four samples. In sample EA-02, the AFT+AHe based t-T modelling yielded no good and acceptable fit results, due to the AHe age. Therefore, only AFT data were used to model the individual thermal history of sample EA-02. In all numerical models, we used the youngest AHe age of the three single grain aliquots of each sample (see Tab. 4.9, 4.15). To improve the thermal modelling, depositional ages were implemented as external t-T constraint. The uncertainty is presented in the diagrams in green and brown colour depending on the reliability level (see Fig. 4.20).

All samples have been tested by 50000 inverse models against the data set. The obtained t-T models of all samples indicate a goodness of fit (G.O.F.) greater than 90 % for the AFT and AHe age. Two samples (EA-02, PC-02) reveal a G.O.F. greater than 90 % for the confined FT length distribution, whereas in samples MA-19 and MA-24 the length distribution could not be reproduced better than 55 %. All obtained t-T models of the Lower Cretaceous samples from the Tarfaya Basin have at least 48 good and 1067 acceptable t-T paths, while sample PC-02 shows the largest number with 472 good and 2650 acceptable t-T paths.

The numerical modelling of the four samples yielded a well-defined thermal history with numerous possible t-T paths (Fig. 4.20). The thermal models reveal that all four samples underwent a cooling, followed by a reheating after the deposition and an ongoing cooling to present time. They show an overall similar pattern with a three-phase thermal history. Based on the partially reset AFT ages, the cooling history in the source area is poorly constrained. The exhumation to the surface occurred approximately between Carboniferous–Permian (300 Ma) and Aptian–Albian (110 Ma). After the deposition during the Lower Cretaceous, the samples underwent a heating from 20 °C to 60–75 °C in the Tarfaya Basin. The subsidence occurred from Aptian–Albian until Palaeocene–Eocene (65–50 Ma) in samples EA-02, PC-02 and MA-24 and until Lower Miocene (20 Ma) in sample MA-19. Since then, a slow continuous cooling event can be observed throughout the final part of the thermal history.

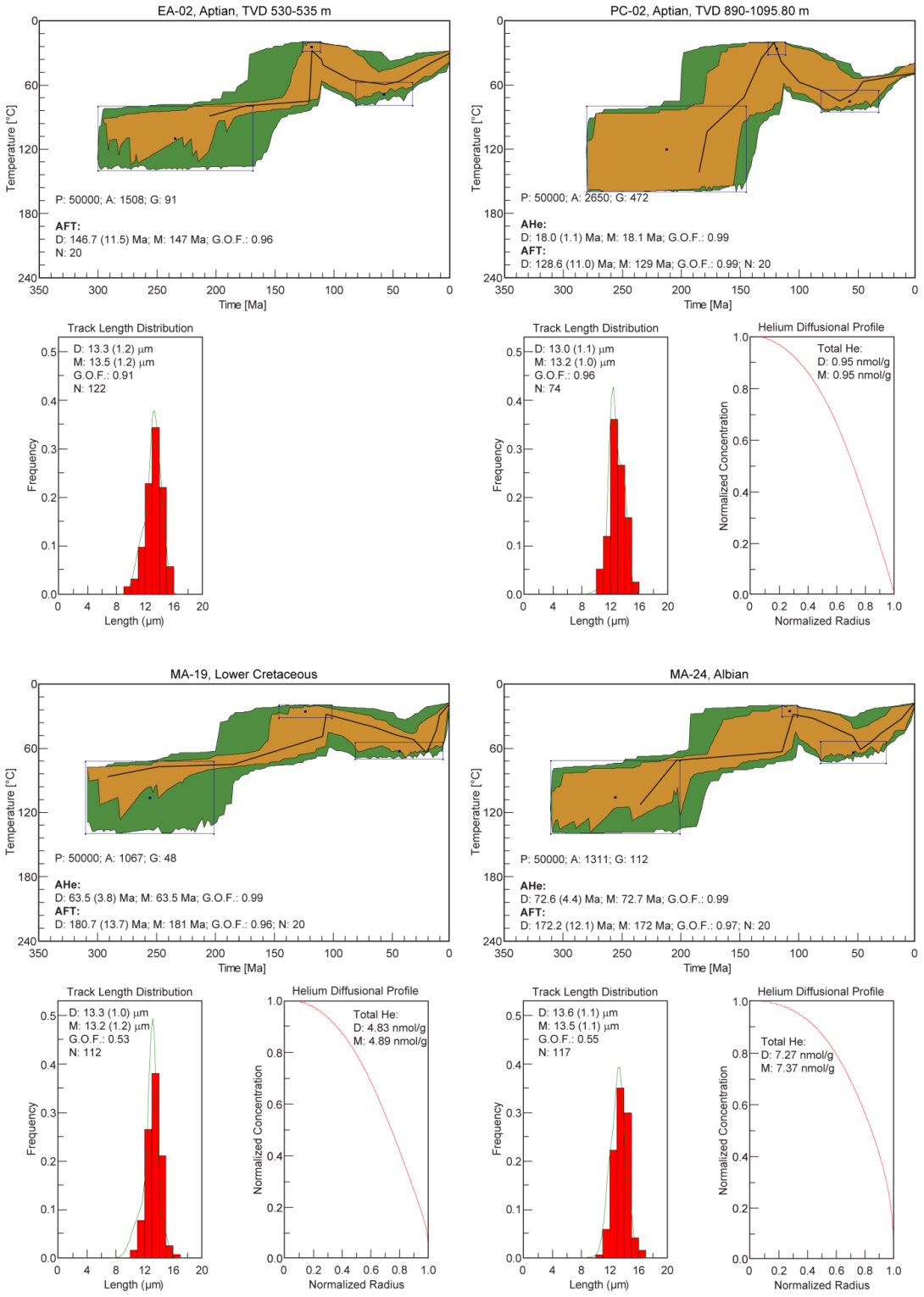

Fig. 4.20: Results from numerical modelling of Lower Cretaceous samples from the Tarfaya Basin. Displayed are the t-T paths (left), the c-axis corrected confined fission-track length (L_c) frequency distribution overlain by a calculated probability density function (best fit) and the modelled helium diffusional profiles. The modelling tests possible t-T curves that fit independent geological constraints (squares) against the thermochronological data set. The results in the t-T curve show three different reliability levels (green: acceptable fit = all t-T paths with a goodness of fit (G.O.F.) of > 0.05 (5 %); brown: good fit = all t-T paths with a G.O.F. of > 0.5 (50 %); black line: best fit). P: number of total tested inverse models; A: acceptable fit models; G: good fit models; D: determined AHe and AFT age (1σ error), mean L_c and He content; M: modelled AHe and AFT age, mean L_c and He content; G.O.F.: goodness of fit of best fit model; N: number of single grains and measured confined fission-track lengths.

4.1.7 Age population calculation

Upper Cretaceous to Neogene samples from the Tarfaya Basin show a large spread in the single grain age distribution of the apatite fission-track analysis. Therefore age population calculation of eight Neogene and three Upper Cretaceous samples have been performed by 'Popshare' software (Dunkl and Székely, 2002). In ten samples applying computer code 'Popshare' yielded two or three age populations, whereas sample MA-52 reveals no good fitting results (Fig. 4.21, Fig. 4.22). Seven samples show two age components and samples MA-58 and MA-69 three components, while population calculation of sample MA-27 yielded good fitting result with two as well as three components.

The different calculated age populations of the Upper Cretaceous samples range from 114.7 (±20.6) to 260.3 (±6.8) Ma (Fig. 4.21). While a young population as in the Cenozoic samples is missing, sample MA-69 shows an age component of 114.7 (±20.6). In every sample a middle age component ranging between 144.1 (±21.8) and 171.6 (±3.9) Ma and an old age population ranging from 200.0 (±8.9) to 260.3 (±6.8) Ma has been determined. Samples MA-69 and MA-70 from the same outcrop reveal identical middle and old age populations, whereas the younger population is missing in sample MA-70.

The different calculated age populations of the seven Miocene to Pliocene samples range overall from 22.9 (±14.2) to 262.9 (±0.9) Ma (Fig. 4.22). Five samples (MA-27, MA-54, MA-58, MA-59 and CJ-02) reveal a young age component ranging between 22.9 (±14.2) and 87.5 (±14.8) Ma. Every Neogene sample shows a middle age component ranging from 130.7 (±58.6) to 179.9 (±28.5) Ma. Furthermore, in samples MA-27, MA-53, MA-56 and MA-58, an old age population has been determined that range between 215.9 (±9.1) and 262.9 (±0.9) Ma.

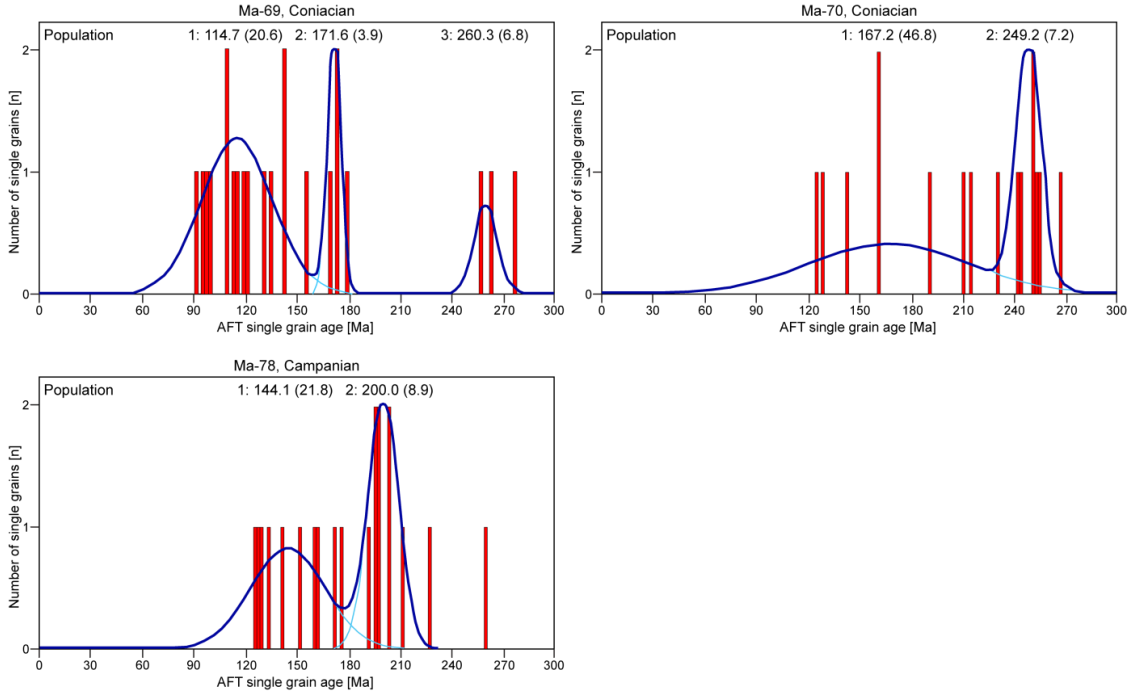

Fig. 4.21: AFT single grain age distribution of Upper Cretaceous samples from the Tarfaya Basin overlain by the age population curve calculated with the computer code 'Popshare' (Dunkl and Székely, 2002).

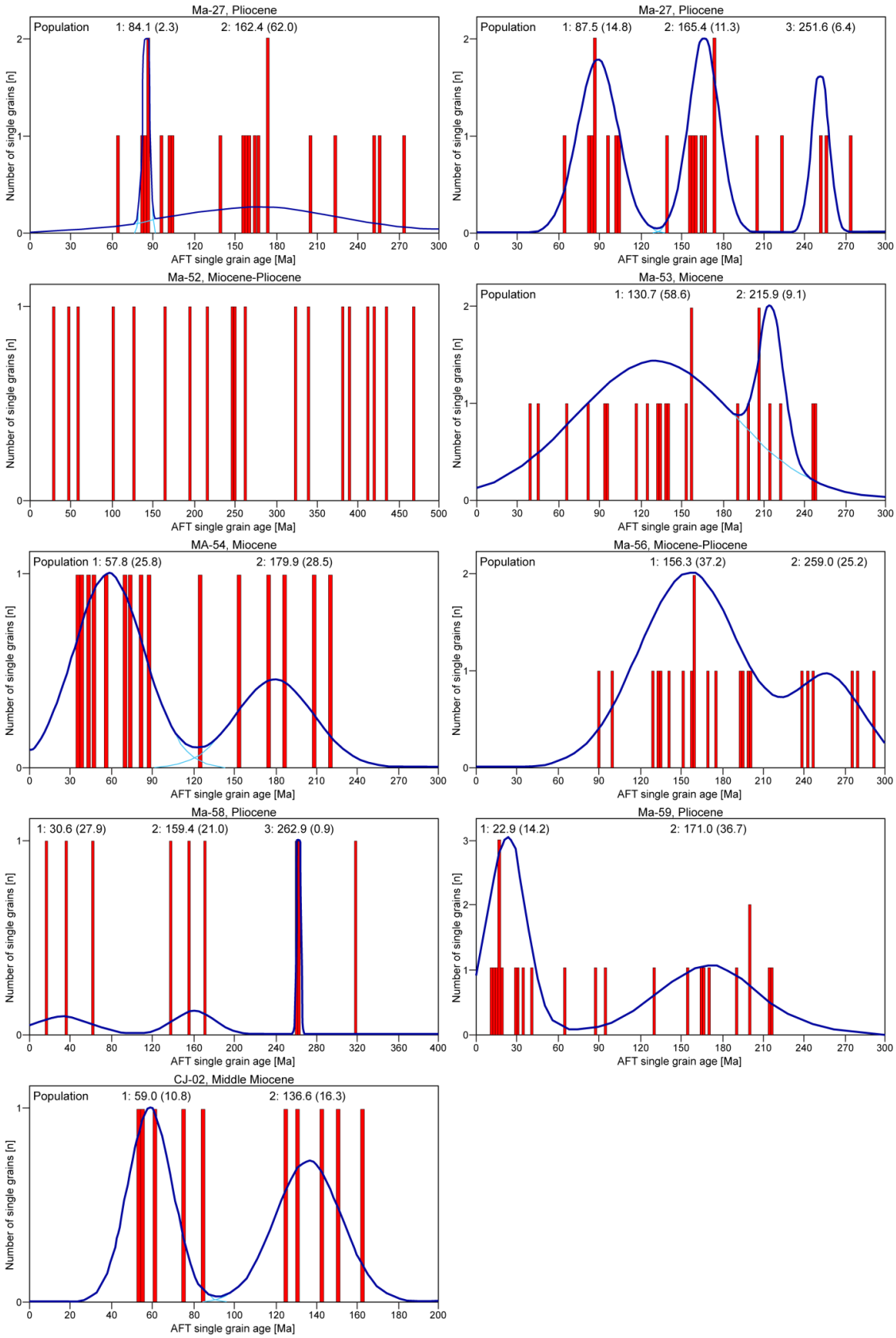

Fig. 4.22: AFT single grain age distribution of Cenozoic samples from the Tarfaya Basin overlain by the age population curve calculated with the computer code 'Popshare' (Dunkl and Székely, 2002).

4.2 Western Anti-Atlas

23 Precambrian outcrop samples, five Palaeozoic samples from the Oum Doul-1 well and six samples from Adrar Zougar-1 well have been collected and prepared for low-temperature thermochronology. Every sample containing apatite grains were processed for apatite fission-track analysis. Whenever suitable grains were available, apatite (U-Th-Sm)/He dating were carried out. Zircon (U-Th-Sm)/He and zircon fission-track analysis were performed on designated samples distributed over the entire study area. The complete thermochronological data set as well as location and description of samples from the western Anti-Atlas (WAA) are presented in Figure 4.23 and Tables 4.20, 4.21.

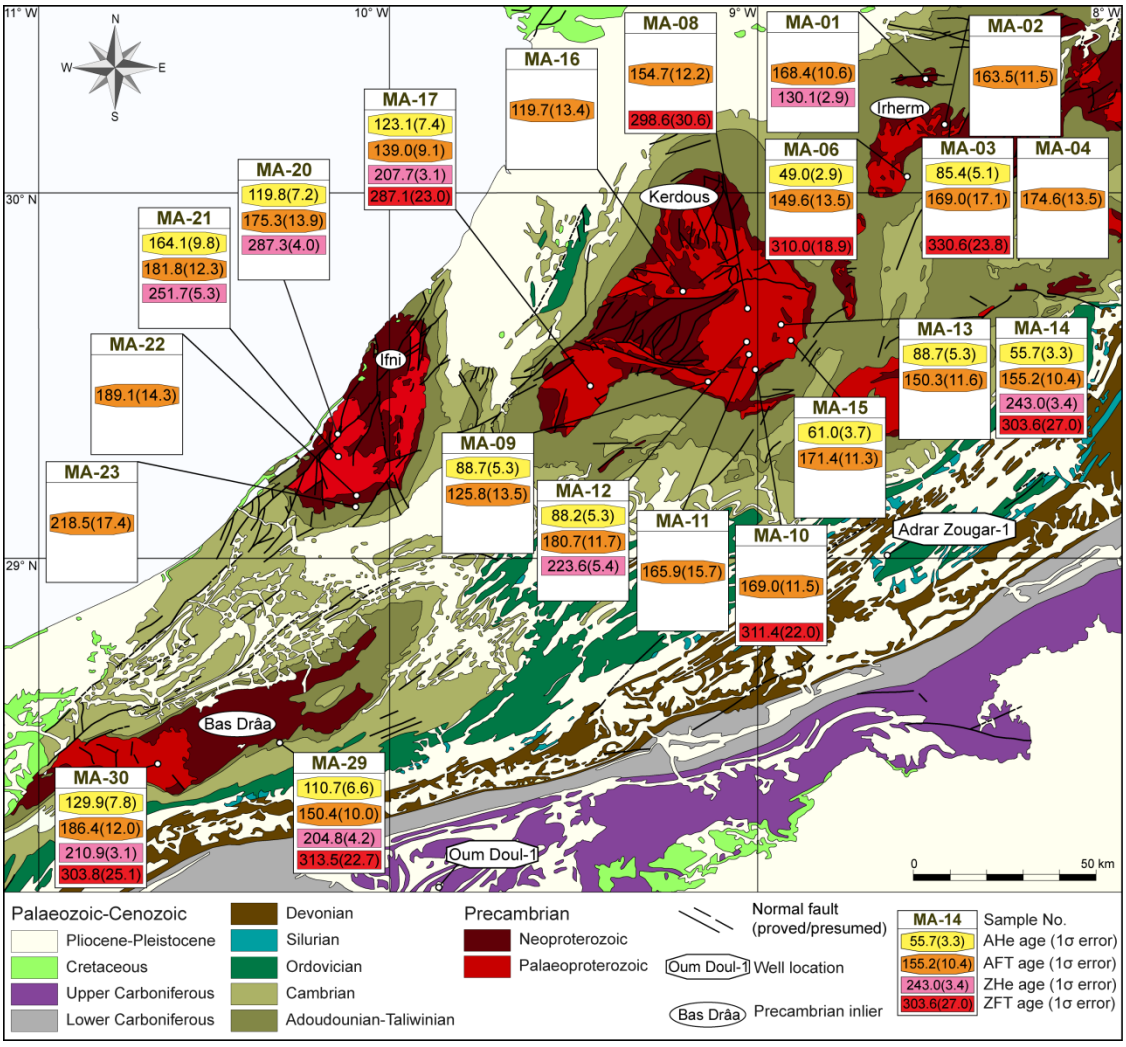

Fig. 4.23: Geological map of the western Anti-Atlas with sample locations, AFT and ZFT central ages, ZHe ages as well as the youngest AHe age (1σ error).

Table 4.20: All thermochronological data from outcrop samples of the western Anti-Atlas and sample location with description

Sample	Coordinates (WGS84) N Latitude DD°MM'SS.S"	W Longitude DD°MM'SS.S"	Elevation [m a.s.l.]	Lith.	Stratigraphic age	Apatite (U-Th-Sm)/He [Ma]	Error ± 1σ [Ma]	Apatite FT [Ma]	Error ± 1σ [Ma]	Zircon (U-Th-Sm)/He [Ma]	Error ± 1σ [Ma]	Zircon FT [Ma]	Error ± 1σ [Ma]
MA-01	30°18'22"	8°32'14"	1018	rhyo	Precambrian III	no ap.	-	168.4	10.6	130.1	2.9	n.d.	-
MA-02	30°10'57"	8°28'55"	1410	quart	Precambrian II[3]	no ap.	-	163.5	11.5	n.d.	-	n.d.	-
MA-03	30°10'57"	8°28'55"	1410	congl	Precambrian II[3]	85.4	5.1	169.0	17.1	n.d.	-	330.6	23.8
MA-04	30°10'57"	8°28'55"	1410	congl	Precambrian II[3]	no ap.	-	174.6	13.5	n.d.	-	n.d.	-
MA-05	30°07'55"	8°23'31"	1786	rhyo	Precambrian III	no ap.	-	no ap.	-	n.d.	-	n.d.	-
MA-06	30°02'19"	8°35'32"	1885	quart	Precambrian	49.0	2.9	149.6	13.5	n.d.	-	310.0	18.9
MA-07	29°44'35"	8°57'44"	1003	gr	Precambrian II[3]	no ap.	-	no ap.	-	n.d.	-	n.d.	-
MA-08	29°41'06"	9°01'14"	1053	gr	Precambrian II[1]	no ap.	-	154.7	12.2	n.d.	-	298.6	30.6
MA-09	29°28'47"	9°07'06"	1285	dia	Precambrian II[2]	88.7	5.3	125.8	13.5	n.d.	-	n.d.	-
MA-10	29°31'03"	9°00'21"	1437	quart	Precambrian II[2]	no ap.	-	169.0	11.5	n.d.	-	311.4	22.0
MA-11	29°33'15"	9°00'57"	1418	gr	Precambrian I	no ap.	-	165.9	15.7	n.d.	-	n.d.	-
MA-12	29°35'19"	9°01'23"	1082	gr	Precambrian II[3]	88.2	5.3	180.7	11.7	223.6	5.4	n.d.	-
MA-13	29°38'02"	8°56'07"	1603	gr	Precambrian I	88.7	5.3	150.3	11.6	n.d.	-	n.d.	-
MA-14	29°38'02"	8°56'07"	1603	peg	Precambrian I	55.7	3.3	155.2	10.4	243.0	3.4	303.6	27.0
MA-15	29°35'01"	8°54'15"	1522	gab	Precambrian II[2]	61.0	3.7	171.4	11.3	n.d.	-	n.d.	-
MA-16	29°43'20"	9°12'05"	715	rhyo	Precambrian III	no ap.	-	119.7	13.4	n.d.	-	n.d.	-
MA-17	29°28'20"	9°27'18"	530	gr	Precambrian I	123.1	7.4	139.0	9.1	207.7	3.1	287.1	23.0
MA-20	29°20'23"	10°08'33"	60	grd	Precambrian D'Ifni	119.8	7.2	175.3	13.9	287.3	4.0	n.d.	-
MA-21	29°16'49"	10°08'35"	260	gr	Precambrian D'Ifni	164.1	9.8	181.8	12.3	251.7	5.3	n.d.	-
MA-22	29°10'00"	10°05'29"	570	ignim	Precambrian D'Ifni	no ap.	-	189.1	14.3	n.d.	-	n.d.	-
MA-23	29°08'26"	10°05'48"	414	brec	Precambrian D'Ifni	no ap.	-	218.5	17.4	n.d.	-	n.d.	-
MA-29	28°29'35"	10°17'50"	344	congl	Precambrian	110.7	6.6	150.4	10.0	204.8	4.2	313.5	22.7
MA-30	28°26'03"	10°38'00"	134	gr	Precambrian I	129.9	7.8	186.4	12.0	210.9	3.1	303.8	25.1

Elevation in meter above sea level; Lith.: Lithology; rhyo: rhyolite; quart: quartzite; congl: conglomerate; gr: granite; dia: diabase; peg: pegmatite; gab: gabbro; grd: granodiorite; ignim: ignimbrite; brec: breccia; no ap.: no apatite; n.d.: not determined.

Table 4.21: All thermochronological data from wells Oum Doul-1 and Adrar Zougar-1 of the Anti-Atlas and sample location with description

Sample	Depth [m b.s.]	Rec. T [°C]	Lithology	Stratigraphic age	Apatite (U-Th-Sm)/He [Ma]	Error ± 1σ [Ma]	Apatite FT [Ma]	Error ± 1σ [Ma]	Zircon (U-Th-Sm)/He [Ma]	Error ± 1σ [Ma]	Zircon FT [Ma]	Error ± 1σ [Ma]
Oum Doul-1												
OD-01	531 - 567	34	sdst, clyst	Lower Carboniferous	no ap.	-	no ap.	-	n.d.	-	483.3	59.4
OD-02	1066 - 1179	48	sdst, slst	Lower Carboniferous	n.d.	-	177.1	14.5	276.5	22.1	369.4	28.8
OD-03	1751 - 1847	65	slst	Upper Devonian	n.d.	-	69.9	18.5	289.7	23.2	no zr.	-
OD-04	3098 - 3147	98	sdst, slst	Lower-Middle Devonian	no ap.	-	25.2	2.6	90.7	7.3	337.5	43.3
OD-05	3388 - 3463	106	sdst, slst	Lower-Middle Devonian	no ap.	-	no ap.	-	n.d.	-	327.7	33.5
Adrar Zougar-1												
AZ-01	455 - 463	31	sdst	Middle Ordovician	16.4	1.0	114.9	12.2	202.1	16.2	366.1	28.6
AZ-02	1090 - 1113	48	sdst	Lower Ordovician	8.7	0.5	163.0	32.3	n.d.	-	345.8	33.6
AZ-03	1988 - 2095	71	sdst, slst	Lower Cambrian	0.0	0.0	53.7	4.9	n.d.	-	312.9	22.7
AZ-04	2541 - 2587	84	sdst	Taliwinian	0.0	0.0	29.5	2.9	131.6	10.5	295.5	23.4
AZ-05	3021 - 3059	96	sdst	Adoudounian	0.0	0.0	8.9	1.2	n.d.	-	260.2	19.9
AZ-06	3315 - 3387	104	sdst	Precambrian	0.0	0.0	9.5	1.4	81.4	6.5	257.8	17.6

Depth in meter below surface; Rec. T: Recent calculated temperature; sdst: sandstone; clyst: claystone; slst: siltstone; no ap.: no apatite; no zr.: no zircon; n.d.: not determined.

4.2.1 Irherm inlier

4.2.1.1 Apatite (U-Th-Sm)/He ages

Two samples from the Irherm inlier of the western Anti-Atlas with three single grain aliquots have been determined by apatite (U-Th-Sm)/He analysis (AHe). Four samples contained no apatite grains for AHe processing. Raw AHe ages cover a wide range from 28.4 (±1.7) to 96.2 (±5.8) Ma (Tab. 4.22). α-ejection correction after Farley et al. (1996) was applied to all grains resulting in ages between 49.0 (±2.9) and 167.8 (±10.1) Ma (Tab. 4.22). Since the youngest AHe age of the aliquots is generally considered to reveal the most accurate date of cooling, the youngest single grain age of every sample was used for further interpretation and discussion. These α-ejection corrected individual grain ages revealed an age spectra from 49.0 (±2.9) to 85.4 (±5.1) Ma (Fig. 4.24, Tab. 4.22). Since the three single grain aliquot ages of sample MA-03 are very similar, the AHe age is more accurate and reliable than sample MA-06. The ages are significantly younger than the corresponding sedimentation, metamorphic or intrusive age of the sampled rock. From every sample at least two AHe single grain ages are younger than the apatite fission-track age.

A positive correlation between single grain age and effective Uranium concentration (eU = [U] + 0.235 [Th] + 0.0053 [Sm]; e.g. Shuster et al., 2006; Spiegel et al., 2009) could not be observed in samples from the Irherm inlier (Fig. 4.25).

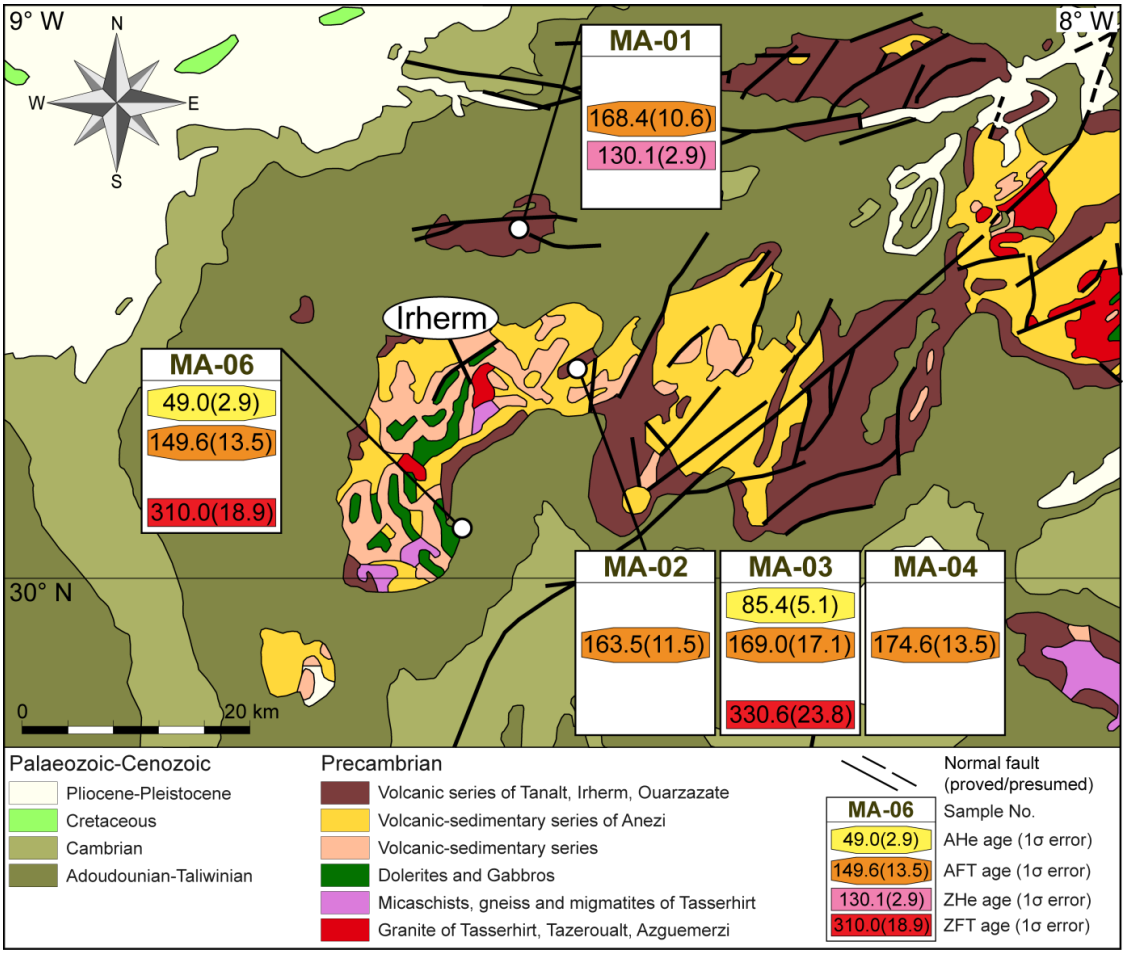

Fig. 4.24: Geological map of the Irherm inlier with sample locations, AFT and ZFT central ages, ZHe ages as well as the youngest AHe age (1σ error).

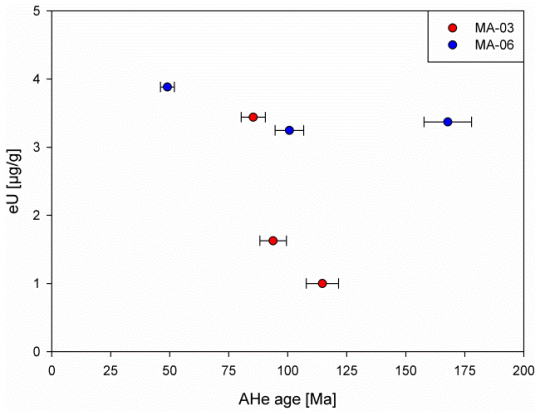

Fig. 4.25: AHe single grain ages (1σ error) from the Irherm inlier plotted against eU.

No clear positive correlation between equivalent grain radius and AHe age distribution was determined (Reiners and Farley, 2001) (Fig. 4.26).

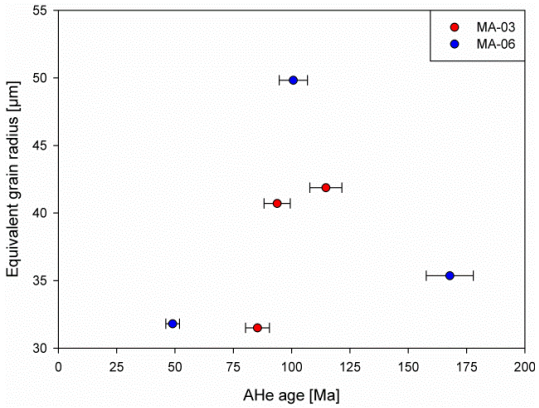

Fig. 4.26: AHe single grain ages (1σ error) from the Irherm inlier plotted against equivalent grain radius.

4.2.1.2 Apatite fission-track ages

Five samples from the Irherm inlier have been analysed by apatite fission-track dating (AFT). One sample contained no apatite grains. The apatite fission-track central ages cover a range from 149.6 (±13.5) to 174.6 (±13.5) Ma yielding an average age of 165.0 (±13.2) Ma (Fig. 4.24, Tab. 4.23). The samples of the Irherm inlier were collected from elevations between 1018 m and 1885 m. The youngest age of 149.6 (±13.5) Ma was obtained from a quartzite sample (MA-06) with the highest elevation of 1885 m. Precambrian quartzite and conglomerate samples (MA-02, MA-03, MA-04) from the same outcrop show identical AFT ages. The apatite fission-track ages of the five samples analysed are virtually equal within the standard deviation indicating a rapid exhumation of the Irherm inlier between 170–150 Ma. All ages are significantly younger than the corresponding sedimentation, metamorphic or intrusive age of the sampled rock. All single grain age distributions fulfilled the requirement of the χ^2-test indicating a homogenous distribution with respect to 1σ error of the single grain ages (Galbraith, 1981). Whereas the test is passed when $\chi^2 > 5$ %, the samples reached values from 83 to 100 %.

4.2.1.3 Etch pit size and track length distribution

A total of 550 D_{par} values were determined for all apatite grains (Tab. 4.24). The mean D_{par} values for each sample reveal a very narrow range between 1.4 (±0.1) and 1.6 (±0.1) µm. The narrow range indicates a very homogeneous chemical composition concerning the fluorine and chlorine content of the apatites. The samples exhibit a minor skewness between -0.361 and 0.521. The skewness is a factor of symmetry of the D_{par} value distribution. A large skewness value indicates a larger variation in the etch pit size. The largest etch pit size of 2.0 (±0.1) µm was measured in samples MA-01 and MA-04. Sample MA-04 shows also the largest spread in etch pit size ranging between 1.1 (±0.1) and 2.0 (±0.1) µm. No positive correlation between single grain ages and D_{par} values has been detected.

A total of 199 track lengths of confined spontaneous fission-tracks were measured (Tab. 4.24). The obtained mean track lengths range from 10.9 (±1.5) to 12.0 (±1.0) µm. All samples show a unimodal, narrow track length distribution. The track length distributions of the samples show no significant skewness ranging between -0.738 and 0.244. This indicates a simple cooling history with no obvious reheating events. The largest track

length of 15.8 (±0.1) µm as well as the smallest of 6.6 (±0.1) µm was measured in sample MA-02. No relation between track length distribution and elevation or variation of AFT ages has been determined. After correcting of the confined track lengths for their crystallographic orientation by the computer code 'HeFTy', the mean confined fission-track lengths changed to a distribution between 12.9 (±1.0) and 13.6 (±0.6) µm. The c-axis corrected track length distributions of the samples show no significant skewness ranging between 0.095 and 1.096. The largest track length after c-axis correction of 16.3 (±0.1) µm as well as the smallest of 10.3 (±0.1) µm was measured in sample MA-02. Even with this correction, no relation exists between track length distribution and elevation or variation of AFT ages.

4.2.1.4 Zircon (U-Th-Sm)/He ages

One sample from the Irherm inlier with three single grain aliquots has been determined by zircon (U-Th-Sm)/He analysis (ZHe). Raw ZHe ages cover a range from 60.5 (±1.4) to 114.3 (±2.4) Ma (Tab. 4.25). α-ejection correction after Farley et al. (1996) was applied to all grains resulting in ages between 87.8 (±2.0) and 162.2 (±3.4) Ma (Tab. 4.25). Since the ZHe age with the lowest eU content of the aliquots is generally considered to reveal the most accurate date of cooling, these single grain ages were used for further interpretation and discussion. This α-ejection corrected individual grain age is 130.1 (±2.9) Ma for sample MA-01 (Fig. 4.24, Tab. 4.25). The age is significantly younger than the corresponding intrusive age of the sampled rock and anomalously younger than every AFT age of samples from the Irherm inlier.

In sample MA-01, a negative correlation between single grain age and effective Uranium concentration has been observed (Fig. 4.27). A negative correlation is given by an increasing He diffusivity as numerous traps are connected depending on the radiation damage and cooling history of the hosting rock (Guenthner and Reiners, 2010). The influence of radiation damage on ZHe ages is minor as long as U concentrations are less than ~1000 ppm (Reiners, 2005). At higher U concentrations the ZHe ages decrease rapidly to anomalously young and unreproducible ages (Reiners, 2005). Consequently, based on the determined eU concentrations between 1107 and 2515 ppm in sample MA-01, the ZHe single grain aliquot ages could be anomalously young and unreproducible (Tab. 4.25).

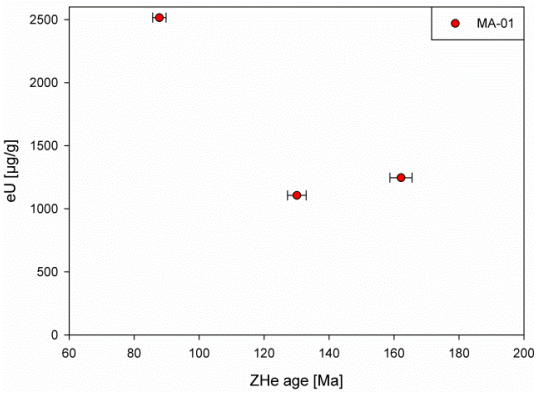

Fig. 4.27: ZHe single grain ages (1σ error) from the Irherm inlier plotted against eU.

No clear positive correlation between equivalent grain radius and ZHe age distribution was determined (Reiners and Farley, 2001) (Fig. 4.28).

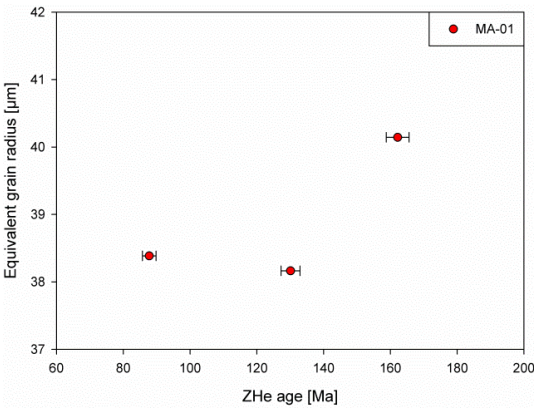

Fig. 4.28: ZHe single grain ages (1σ error) from the Irherm inlier plotted against equivalent grain radius.

4.2.1.5 Zircon fission-track ages

Two samples from the Irherm inlier have been analysed by zircon fission-track dating (ZFT). The zircon fission-track central ages are equal within the standard deviation ranging between 310.0 (±18.9) and 330.6 (±23.8) Ma (Fig. 4.24, Tab. 4.26). All ages are significantly younger than the corresponding sedimentation, metamorphic or intrusive age of the sampled rock. ZFT ages are older than ZHe, AFT and AHe ages, which is consistent with the difference in closure temperature between the thermochronological systems. All single grain age distributions fulfilled the requirement of the χ^2-test with values of 100 %.

4.2.1.6 Summary

The age-elevation plot shows similar ages of the different thermochronometric methods (Fig. 4.29). However, all ages of sample MA-06 with the highest elevation of 1885 m are slightly younger yielding a minor negative slope (Fig. 4.29). This negative slope is indicative for a general decay in relief (Braun, 2002).

Except for the ZHe age of sample MA-01 with a very high eU concentration of 1107 µg/g, the comparison of all data reveals an age distribution appropriate to the closure temperatures of the respective thermo-chronological methods (Fig. 4.29).

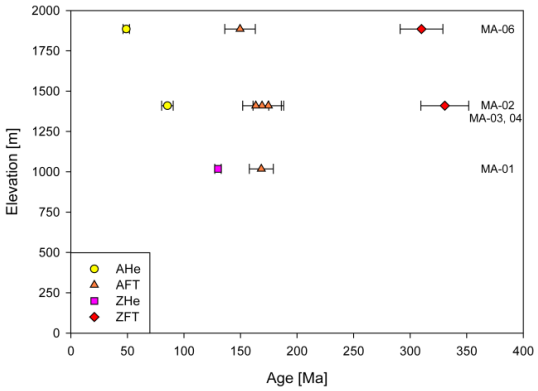

Fig. 4.29: AHe, AFT, ZHe and ZFT age (1σ error) – elevation plot from the Irherm inlier.

Table 4.22: Apatite (U-Th-Sm)/He data from the Irherm inlier

Sample	Mass [µg]	Radius [µm]	U [µg/g]	Th [µg/g]	Sm [µg/g]	eU [µg/g]	Th/U	^{4}He [nmol/g]	F_t	Raw age [Ma]	Error ± 1σ [Ma]	Corrected age [Ma]	Error ± 1σ [Ma]
MA-03.1	1.8	41.9	<1	2	7	1	8.9	0.33	0.628	72.0	4.3	114.7	6.9
MA-03.2	**1.2**	**31.5**	**2**	**6**	**87**	**3**	**3.1**	**1.14**	**0.592**	**50.5**	**3.0**	**85.4**	**5.1**
MA-03.3	1.9	40.7	1	2	35	2	2.0	0.61	0.629	59.0	3.5	93.8	5.6
MA-06.1	3.2	49.8	3	1	28	3	0.3	1.34	0.706	71.1	4.3	100.7	6.0
MA-06.2	**1.1**	**31.8**	**2**	**9**	**85**	**4**	**4.6**	**0.71**	**0.580**	**28.4**	**1.7**	**49.0**	**2.9**
MA-06.3	1.0	35.4	2	7	64	3	4.4	2.04	0.573	96.2	5.8	167.8	10.1

eU = [U] + 0.235 [Th] + 0.0053 [Sm] (concentrations in weight %); F_t: α-ejection correction factor; raw ages are corrected after Farley et al. (1996); radius calculated according to Shuster et al. (2006) and Ketcham (2009). Data in bold: youngest apatite (U-Th-Sm)/He grain of each sample discussed in the text.

Table 4.23: Apatite fission-track from the Irherm inlier

Sample	Elevation [m a.s.l.]	n	U (std) [µg/g]	Sp. Tracks ρ_s	Sp. Tracks N_s	Ind. Tracks ρ_i	Ind. Tracks N_i	$P(\chi^2)$ [%]	Central age [Ma]	Error ± 1σ [Ma]
MA-01	1018	20	27.4 (7.4)	23.929	2105	24.381	2066	98.9	168.4	10.6
MA-02	1410	20	21.6 (10.6)	17.895	1011	18.161	1026	98.0	163.5	11.5
MA-03	1410	20	2.9 (2.3)	2.703	277	2.664	273	99.9	169.0	17.1
MA-04	1410	20	7.7 (12.2)	6.393	684	6.122	655	100.0	174.6	13.5
MA-06	1885	10	26.5 (38.2)	12.557	366	14.169	413	82.8	149.6	13.5

U (std): Uranium concentration and standard deviation; n: number of counted apatite grains; ρ_s: density of spontaneous tracks (10^5 tr/cm^2); N_s: number of spontaneous tracks; ρ_i: density of induced tracks (10^5 tr/cm^2); N_i: number of induced tracks; $P(\chi^2)$: probability that single grains are consistent and belong to the same population. Test is passed if $P(\chi^2) > 5$ % (Galbraith, 1981). Nd = 15419 tracks counted on CN5 dosimeter glass. Central ages are calculated using a ζ-value of 333.36 ± 17.89. Samples were irradiated at the FRM II reactor facility in Garching, Germany with a fluence of 1×10^{16} neutrons/cm^2.

Table 4.24: Confined fission-track length data from the Irherm inlier

Sample	n CT	CT mean [µm]	CT std [µm]	CT skew	CT min [µm]	CT max [µm]	L_c mean [µm]	L_c std [µm]	L_c skew	L_c min [µm]	L_c max [µm]	n D_{par}	D_{par} mean [µm]	D_{par} std [µm]	D_{par} skew	D_{par} min [µm]	D_{par} max [µm]
MA-01	106	11.7	1.4	0.076	8.3	15.3	13.4	0.9	0.095	10.4	16.0	180	1.6	0.1	0.253	1.3	2.0
MA-02	46	10.9	1.5	0.244	6.6	15.8	12.9	1.0	0.422	10.3	16.3	136	1.4	0.2	0.521	1.1	1.9
MA-03	7	12.0	1.0	-0.738	10.2	13.3	13.6	0.6	0.279	12.7	14.6	88	1.4	0.1	-0.354	1.0	1.6
MA-04	34	11.5	1.4	-0.056	7.6	15.1	13.2	0.9	1.096	11.6	15.9	98	1.5	0.2	0.437	1.1	2.0
MA-06	6	11.2	1.7	0.154	9.3	13.3	12.9	1.0	0.279	11.6	14.3	48	1.4	0.1	-0.361	1.0	1.6

n: number of measured individual confined tracks (CT) and etch pit diameter (D_{par}); CT mean: mean confined track length; L_c mean: mean track length after c-axis correction; D_{par} mean: mean etch pit diameter; std: standard deviation; skew: skewness of distribution relative to the mean value; min: minimum single values; max: maximum single values.

Table 4.25: Zircon (U-Th-Sm)/He data from the Irherm inlier

Sample	Mass [µg]	Radius [µm]	U [µg/g]	Th [µg/g]	Sm [µg/g]	eU [µg/g]	Th/U	^{4}He [nmol/g]	Ft	Raw age [Ma]	Error ± 1σ [Ma]	Corrected age [Ma]	Error ± 1σ [Ma]
MA-01.1	1.9	38.4	2301	911	n.d.	2515	0.41	822.7	0.690	60.5	1.4	87.8	2.0
MA-01.2	**1.7**	**38.2**	**1075**	**135**	**n.d.**	**1107**	**0.13**	**539.0**	**0.692**	**90.0**	**2.0**	**130.1**	**2.9**
MA-01.3	2.1	40.1	1179	286	n.d.	1246	0.25	773.2	0.705	114.3	2.4	162.2	3.4

eU = [U] + 0.235 [Th] + 0.0053 [Sm] (concentrations in weight %); F_t: α-ejection correction factor; raw ages are corrected after Farley et al. (1996); radius calculated according to Reiners et al. (2004) and Ketcham (2009). Data in bold are discussed in the text.

Table 4.26: Zircon fission-track data from the Irherm inlier

Sample	Etch time at 200 °C [h]	n	U (std) [µg/g]	Sp. Tracks ρ_s	Sp. Tracks N_s	Ind. Tracks ρ_i	Ind. Tracks N_i	$P(X^2)$ [%]	Central age [Ma]	Error ± 1σ [Ma]
MA-03	3.5	21	169.6 (39.0)	260.080	3035	28.622	334	100.0	330.6	23.8
MA-06	5.0	20	165.5 (36.4)	225.100	5131	26.454	603	100.0	310.0	18.9

Etch time in KOH:NaOH (7:5) eutectic melt at 200 ± 2 °C; U (std): Uranium concentration and standard deviation; n: number of counted apatite grains; ρ_s: density of spontaneous tracks (10^5 tr/cm^2); N_s: number of spontaneous tracks; ρ_i: density of induced tracks (10^5 tr/cm^2); N_i: number of induced tracks; $P(\chi^2)$: probability that single grains are consistent and belong to the same population. Test is passed if $P(\chi^2) > 5\%$ (Galbraith, 1981). Nd = 11255 tracks counted on CN1 dosimeter glass. Central ages are calculated using a ζ-value of 140.83 ± 5.93. Samples were irradiated at the FRM II reactor facility in Garching, Germany with a fluence of 1×10^{15} neutrons/cm^2.

4.2.2 Kerdous inlier

4.2.2.1 Apatite (U-Th-Sm)/He ages

Six samples from the Kerdous inlier of the western Anti-Atlas with two or three single grain aliquots have been determined by apatite (U-Th-Sm)/He analysis. Four samples contained no apatite grains for AHe processing. Raw AHe ages cover a wide range from 40.1 (±2.4) to 173.6 (±10.4) Ma (Tab. 4.27). α-ejection correction after Farley et al. (1996) was applied to all grains resulting in ages between 55.7 (±3.3) and 236.7 (±14.2) Ma (Tab. 4.27). The youngest α-ejection corrected single grain ages revealed an age spectra from 55.7 (±3.3) to 123.1 (±7.4) Ma (Fig. 4.30, Tab. 4.27). All single grain ages of three samples (MA-09, MA-12, MA-13) are equal within the standard deviation ranging between 88.2 (±5.3) and 97.3 (±5.8) Ma (Tab. 4.27). In

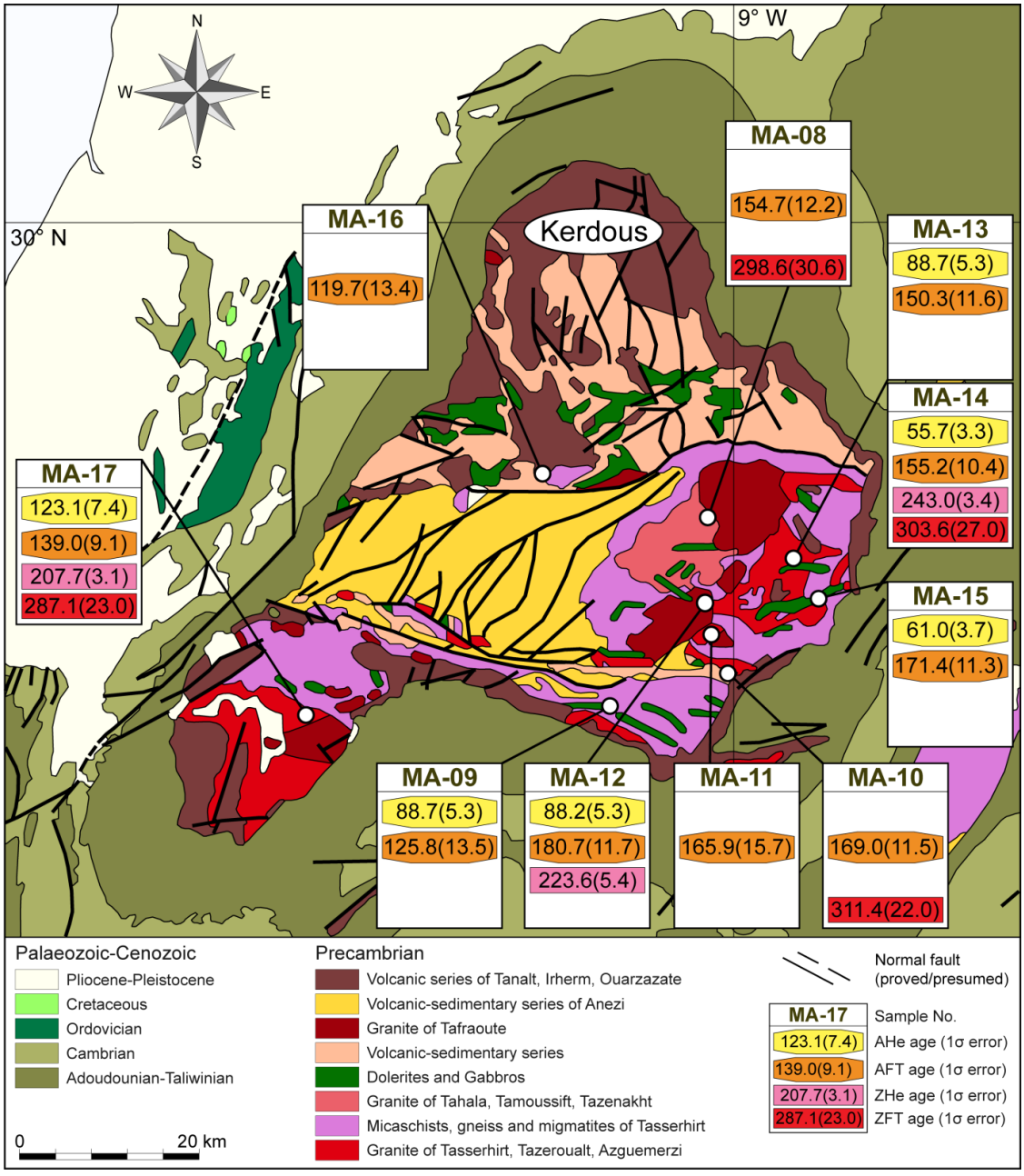

Fig. 4.30: Geological map of the Kerdous inlier with sample locations, AFT and ZFT central ages, ZHe ages as well as the youngest AHe age (1σ error).

contrast, samples MA-14 and MA-15 show a large spread in the single grain ages including a younger age and ages between 80 and 90 Ma. Consequently, the youngest AHe age of samples MA-09, MA-12 and MA-13 is more accurate and reliable. A substantial difference in the AHe age can be observed between a Precambrian granite sample (MA-13) and an intruded pegmatite sample (MA-14) from the same outcrop. Whereas the Pegmatite sample yielded an age of 55.7 (±3.3) Ma, the granite sample reveal a significant older age of 88.7 (±5.3) Ma. Fitzgerald et al. (2006) recommended the calculation of weighted mean ages and the determination of 'most representative ages'. The weighted mean ages are equal within the standard deviation yielding ages of 91.1 (±8.2) Ma (MA-13) and 88.2 (±5.3) Ma (MA-14). However, the most representative ages slightly differ from each other with an age of 89.9 (±6.8) Ma for sample MA-13 and 72.0 (±4.3) Ma for sample MA-14. Sample MA-17, from a lower elevation of 530 m compared to the eastern Kerdous inlier, shows a significant older single grain age of 123.1 (±7.4). All ages are significantly younger than the corresponding sedimentation, metamorphic or intrusive age of the sampled rock. From every sample, at least one AHe single grain age is younger than the apatite fission-track age.

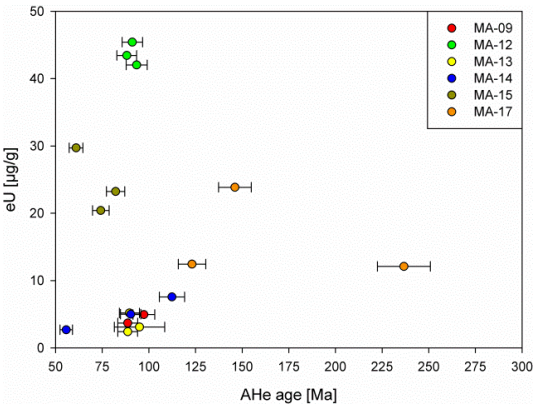

Fig. 4.31: AHe single grain ages (1σ error) from the Kerdous inlier plotted against eU.

A positive correlation between single grain age and effective Uranium concentration has been observed in sample MA-14 of the Kerdous inlier (Fig. 4.31). A positive correlation is indicative for a long residence time in the PRZ. No clear positive correlation between equivalent grain radius and AHe age distribution was determined (Fig. 4.32).

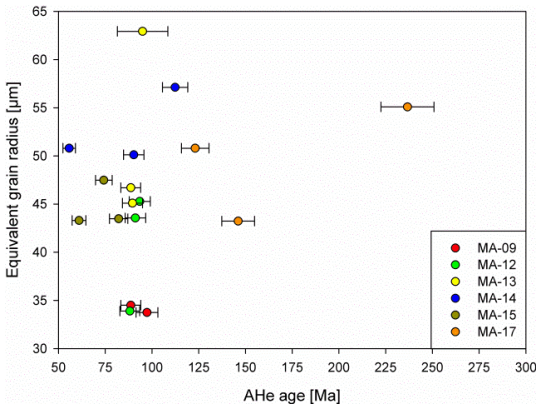

Fig. 4.32: AHe single grain ages (1σ error) from the Kerdous inlier plotted against equivalent grain radius.

4.2.2.2 Apatite fission-track ages

All samples from the Kerdous inlier have been analysed by apatite fission-track dating. The samples reveal different apatite fission-track central ages between 119.7 (±13.4) and 180.7 (±11.7) Ma from elevations between 530 m and 1603 m (Fig. 4.30, Tab. 4.28). Based on the large spread in the AFT age distribution, the data were grouped into two areas. In the eastern Kerdous inlier, seven samples (MA-08, MA-10, MA-11, MA-12, MA-13, MA-14 and MA-15) show a narrow age spectra ranging from 150.3 (±11.6) to 180.7 (±11.7) Ma and yielding an average age of 163.9 (±12.1) Ma (Fig. 4.30). In contrast to the AHe ages, the granite sample (MA-13) and an intruded pegmatite sample (MA-14) from the same outcrop yielded identical AFT ages of 150.3 (±11.6) and 155.2 (±10.4) Ma. In the western Kerdous inlier, the AFT ages are substantial younger compared to the eastern part. A rhyolite sample (MA-16) taken at 715 m revealed the youngest obtained age of 119.7

(±13.4) Ma from the entire WAA. Furthermore, two samples (MA-09, MA-17) yielded ages of 125.8 (±13.5) and 139.0 (±9.1) Ma. The three samples that were collected from elevations between 530 m and 1285 m yielded an average age of 128.2 (±12.0) Ma. The Kerdous inlier consist of three different domains intersected by two E–W trending shear zones, the Ameln Valley faulted zone to the north and the Tasrirt–Tahala faulted zone to the south (Soulaimani and Piqué, 2004). The younger age population is separated by these faults from samples of the eastern Kerdous inlier. All ages are significantly younger than the corresponding sedimentation, metamorphic or intrusive age of the sampled rock. The single grain age distributions fulfilled the requirement of the χ^2-test with values between 89 and 100 % indicating a homogenous distribution with respect to 1σ error of the single grain ages.

4.2.2.3 Etch pit size and track length distribution

A total of 1450 D_{par} values were determined for all apatite grains (Tab. 4.29). The mean D_{par} values for each sample reveal a very narrow range between 1.3 (±0.1) and 1.7 (±0.1) µm. Except for sample MA-17 (-0.239), all samples exhibit a positive skewness between 0.057 and 2.179. Sample MA-08 shows the largest track length and spread in etch pit size ranging between 1.2 (±0.1) and 2.7 (±0.1) µm. No positive correlation between single grain ages and D_{par} values has been detected.

A total of 490 track lengths of confined spontaneous fission-tracks were measured (Tab. 4.29). The obtained mean track lengths range from 10.0 (±0.7) to 12.0 (±1.7) µm. All samples show a unimodal, narrow track length distribution. The track length distributions of the samples show a skewness ranging between -1.258 and 1.686. The largest track length of 15.4 (±0.1) µm was measured in sample MA-14. After correcting of the confined track lengths for their crystallographic orientation, the mean confined fission-track lengths changed to a distribution of 11.5 (±1.0) and 13.6 (±1.5) µm. The c-axis corrected track length distributions of the samples show a skewness ranging between -1.740 and 1.732. The largest track length after c-axis correction of 15.9 (±0.1) µm was measured in sample MA-14.

4.2.2.4 Zircon (U-Th-Sm)/He age

Three samples from the Kerdous inlier with three single grain aliquots have been determined by zircon (U-Th-Sm)/He analysis. Raw ZHe ages cover a range from 106.2 (±21.9) to 177.3 (±2.5) Ma (Tab. 4.30). α-ejection correction after Farley et al. (1996) was applied to all grains resulting in ages between 133.2 (±27.5) and 243.0 (±3.4) Ma (Tab. 4.30). The single grains with the lowest eU concentration revealed similar ages from 207.7 (±3.1) to 243.0 (±3.4) Ma (Fig. 4.30, Tab. 4.30). All ages are significantly younger than the corresponding sedimentation, metamorphic or intrusive age of the sampled rock as well as older than the AHe and AFT ages.

In sample MA-12, a negative correlation between single grain age and effective Uranium concentration has been observed (Fig. 4.33). A negative correlation is given by an increasing He diffusivity as numerous traps are connected depending on the radiation damage and cooling history of the hosting rock (Guenthner and Reiners, 2010). The influence of radiation damage on ZHe ages is minor as long as U concentrations are less than ~1000 ppm (Reiners, 2005). At higher U concentrations the ZHe ages decrease rapidly to anomalously young and unreproducible ages (Reiners, 2005). In sample MA-12 eU concentrations of more than 1000 ppm were determined (Tab. 4.30). Especially the single grains MA-12.1 and MA-12.2 show anoma-

lously young and unreproducible ages (Tab. 4.30).

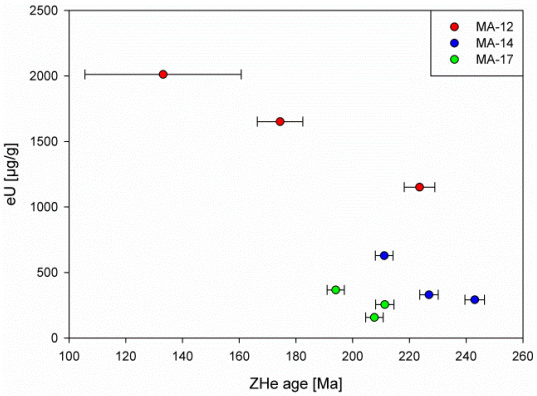

Fig. 4.33: ZHe single grain ages (1σ error) from the Kerdous inlier plotted against eU.

No clear positive correlation between equivalent grain radius and ZHe age distribution was determined (Fig. 4.34).

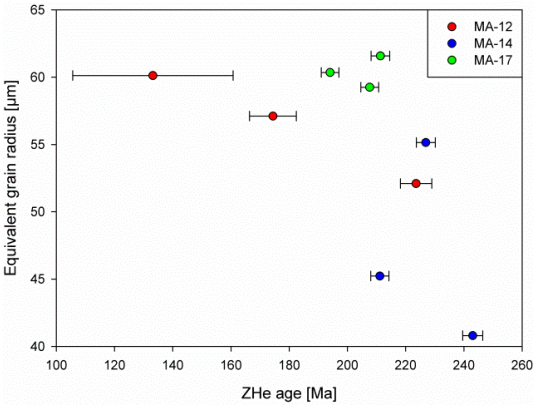

Fig. 4.34: ZHe single grain ages (1σ error) from the Kerdous inlier plotted against equivalent grain radius.

4.2.2.5 Zircon fission-track ages

Four samples from the Kerdous inlier have been analysed by zircon fission-track dating. The zircon fission-track central ages are equal within the standard deviation ranging between 287.1 (±23.0) and 311.4 (±22.0) Ma (Fig. 4.30, Tab. 4.31). All ages are significantly younger than the corresponding sedimentation, metamorphic or intrusive age of the sampled rock. ZFT ages are older than ZHe, AFT and AHe ages, which is consistent with the difference in closure temperature between the thermochronological systems. All single grain age distributions fulfilled the requirement of the χ^2-test with values of 100 %.

4.2.2.6 Summary

The age-elevation plot shows similar or identical ages of the ZHe and ZFT method (Fig. 4.35). AHe ages increase with decreasing elevation and AFT data reveal two slightly different age populations (Fig. 4.35).

The comparison of all data reveals an age distribution appropriate to the closure temperatures of the respective thermochronological methods (Fig. 4.35).

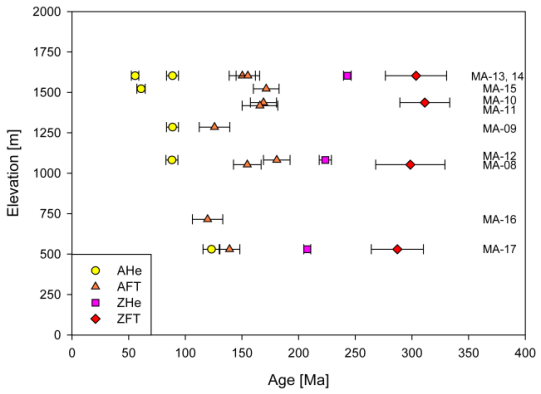

Fig. 4.35: AHe, AFT, ZHe and ZFT age (1σ error) – elevation plot from the Kerdous inlier.

Table 4.27: Apatite (U-Th-Sm)/He data from the Kerdous inlier

Sample	Mass [µg]	Radius [µm]	U [µg/g]	Th [µg/g]	Sm [µg/g]	eU [µg/g]	Th/U	^{4}He [nmol/g]	F_t	Raw age [Ma]	Error ± 1σ [Ma]	Corrected age [Ma]	Error ± 1σ [Ma]
MA-09.1	**1.2**	**34.5**	**3**	**5**	**29**	**4**	**1.7**	**1.13**	**0.596**	**52.9**	**3.2**	**88.7**	**5.3**
MA-09.2	0.9	33.7	3	9	69	5	3.4	1.63	0.558	54.3	3.3	97.3	5.8
MA-12.1	2.8	45.3	38	19	38	42	0.5	14.51	0.676	63.2	3.8	93.5	5.6
MA-12.2	2.1	43.6	41	18	47	45	0.4	15.06	0.666	60.7	3.6	91.1	5.5
MA-12.3	**1.1**	**33.9**	**39**	**20**	**41**	**43**	**0.5**	**12.30**	**0.588**	**51.9**	**3.1**	**88.2**	**5.3**
MA-13.1	**3.0**	**46.7**	**2**	**1**	**6**	**2**	**0.4**	**0.83**	**0.700**	**62.1**	**3.7**	**88.7**	**5.3**
MA-13.2	2.7	62.9	3	2	6	3	1.0	2.93	0.755	71.7	10.2	95.0	13.5
MA-13.3	2.4	45.1	5	1	6	5	0.2	1.74	0.683	61.2	3.7	89.6	5.4
MA-14.1	4.3	57.1	7	1	6	8	0.2	3.46	0.745	83.7	5.0	112.4	6.7
MA-14.2	2.9	50.1	5	<1	5	5	0.1	1.75	0.714	64.4	3.9	90.3	5.4
MA-14.3	**3.4**	**50.8**	**2**	**2**	**6**	**3**	**0.7**	**0.59**	**0.720**	**40.1**	**2.4**	**55.7**	**3.3**
MA-15.1	**2.6**	**43.3**	**26**	**14**	**45**	**30**	**0.5**	**6.71**	**0.676**	**41.2**	**2.5**	**61.0**	**3.7**
MA-15.2	3.0	47.5	19	7	37	20	0.4	5.76	0.692	51.4	3.1	74.2	4.5
MA-15.3	2.2	43.5	22	6	34	23	0.3	7.01	0.670	55.0	3.3	82.2	4.9
MA-17.1	3.6	55.1	11	3	23	12	0.2	11.69	0.734	173.6	10.4	236.7	14.2
MA-17.2	1.8	43.2	23	4	23	24	0.2	12.80	0.670	97.9	5.9	146.1	8.8
MA-17.3	**3.4**	**50.8**	**12**	**1**	**20**	**12**	**0.1**	**6.12**	**0.726**	**89.4**	**5.4**	**123.1**	**7.4**

eU = [U] + 0.235 [Th] + 0.0053 [Sm] (concentrations in weight %); F_t: α-ejection correction factor; raw ages are corrected after Farley et al. (1996); radius calculated according to Shuster et al. (2006) and Ketcham (2009). Data in bold: youngest apatite (U-Th-Sm)/He grain of each sample discussed in the text.

Table 4.28: Apatite fission-track from the Kerdous inlier

Sample	Elevation [m a.s.l.]	n	U (std) [µg/g]	Sp. Tracks ρ_s	Sp. Tracks N_s	Ind. Tracks ρ_i	Ind. Tracks N_i	$P(\chi^2)$ [%]	Central age [Ma]	Error ± 1σ [Ma]
MA-08	1053	20	13.4 (9.2)	8.680	495	14.204	810	98.9	154.7	12.2
MA-09	1285	20	5.2 (4.5)	3.802	203	5.131	274	100.0	125.8	13.5
MA-10	1437	20	25.4 (13.7)	22.724	1216	22.836	1222	99.9	169.0	11.5
MA-11	1418	20	7.2 (6.3)	5.263	329	5.423	339	99.0	165.9	15.7
MA-12	1082	20	24.5 (7.4)	21.973	1374	30.800	1926	89.3	180.7	11.7
MA-13	1603	20	7.3 (3.1)	5.427	622	6.238	715	99.6	150.3	11.6
MA-14	1603	20	15.1 (6.8)	11.132	1056	18.174	1724	88.5	155.2	10.4
MA-15	1522	20	22.3 (7.1)	19.965	1470	20.168	1485	99.8	171.4	11.3
MA-16	715	19	6.0 (7.3)	2.728	177	3.977	258	100.0	119.7	13.4
MA-17	530	20	22.1 (9.5)	16.279	1179	30.791	2230	98.2	139.0	9.1

U (std): Uranium concentration and standard deviation; n: number of counted apatite grains; ρ_s: density of spontaneous tracks (10^5 tr/cm^2); N_s: number of spontaneous tracks; ρ_i: density of induced tracks (10^5 tr/cm^2); N_i: number of induced tracks; $P(\chi^2)$: probability that single grains are consistent and belong to the same population. Test is passed if $P(\chi^2) > 5$ % (Galbraith, 1981). Nd = 15419 tracks counted on CN5 dosimeter glass. Central ages are calculated using a ζ-value of 333.36 ± 17.89. Samples were irradiated at the FRM II reactor facility in Garching, Germany with a fluence of 1 x 10^{16} neutrons/cm^2.

Table 4.29: Confined fission-track length data from the Kerdous inlier

Sample	n CT	CT mean [µm]	CT std [µm]	CT skew	CT min [µm]	CT max [µm]	L_c mean [µm]	L_c std [µm]	L_c skew	L_c min [µm]	L_c max [µm]	n D_{par}	D_{par} mean [µm]	D_{par} std [µm]	D_{par} skew	D_{par} min [µm]	D_{par} max [µm]
MA-08	13	11.1	0.7	1.686	10.0	13.0	12.8	0.8	-0.628	11.1	14.3	115	1.5	0.2	2.179	1.2	2.7
MA-09	5	12.0	1.6	-1.258	9.5	13.4	13.6	1.5	-1.740	11.1	14.8	81	1.3	0.1	0.301	1.1	1.6
MA-10	12	11.9	1.4	0.168	9.6	14.6	13.5	1.0	0.383	12.0	15.3	100	1.4	0.2	0.237	1.0	1.8
MA-11	2	10.0	0.7	0.000	9.5	10.5	11.5	1.0	0.000	10.8	12.1	93	1.3	0.1	1.489	1.0	2.1
MA-12	109	11.8	1.4	0.180	9.2	15.3	13.5	0.9	0.541	12.0	15.5	180	1.7	0.1	0.057	1.2	2.2
MA-13	27	11.6	1.5	0.426	8.5	14.8	13.5	1.1	-0.565	10.5	15.8	177	1.4	0.2	0.604	1.1	2.0
MA-14	95	12.0	1.7	0.140	9.1	15.4	13.6	1.2	-0.039	10.7	15.9	245	1.6	0.2	1.091	1.1	2.6
MA-15	112	12.0	1.3	-0.133	8.7	14.6	13.6	0.9	-0.154	11.0	15.8	145	1.5	0.1	0.339	1.1	1.8
MA-16	4	11.2	2.2	0.954	9.4	14.2	13.0	1.5	1.732	11.9	15.3	84	1.3	0.2	0.961	0.9	1.9
MA-17	111	10.7	1.4	0.223	7.8	14.2	12.8	0.8	0.374	11.3	15.0	230	1.7	0.1	-0.239	1.2	2.0

n: number of measured individual confined tracks (CT) and etch pit diameter (D_{par}); CT mean: mean confined track length; L_c mean: mean track length after c-axis correction; D_{par} mean: mean etch pit diameter; std: standard deviation; skew: skewness of distribution relative to the mean value; min: minimum single values; max: maximum single values.

Table 4.30: Zircon (U-Th-Sm)/He data from the Kerdous inlier

Sample	Mass [µg]	Radius [µm]	U [µg/g]	Th [µg/g]	Sm [µg/g]	eU [µg/g]	Th/U	^{4}He [nmol/g]	Ft	Raw age [Ma]	Error ± 1σ [Ma]	Corrected age [Ma]	Error ± 1σ [Ma]
MA-12.1	8.1	60.1	1979	141	n.d.	2012	0.07	1158.8	0.798	106.2	21.9	133.2	27.5
MA-12.2	7.6	57.1	1617	147	n.d.	1651	0.09	1234.1	0.788	137.4	6.3	174.4	8.0
MA-12.3	**5.9**	**52.1**	**1125**	**112**	**n.d.**	**1151**	**0.10**	**1090.5**	**0.777**	**173.6**	**4.2**	**223.6**	**5.4**
MA-14.1	**2.9**	**40.8**	**281**	**47**	**n.d.**	**292**	**0.17**	**276.8**	**0.715**	**173.8**	**2.4**	**243.0**	**3.4**
MA-14.2	4.2	45.2	611	74	n.d.	628	0.12	532.6	0.737	155.6	2.3	211.1	3.1
MA-14.3	8.0	55.1	320	43	n.d.	330	0.14	319.1	0.781	177.3	2.5	226.9	3.2
MA-17.1	9.4	61.6	240	65	n.d.	255	0.28	235.5	0.802	169.5	2.6	211.3	3.2
MA-17.2	**7.5**	**59.3**	**151**	**25**	**n.d.**	**157**	**0.17**	**141.1**	**0.795**	**165.1**	**2.4**	**207.7**	**3.1**
MA-17.3	8.8	60.3	353	59	n.d.	367	0.17	309.4	0.799	154.9	2.4	194.0	3.0

eU = [U] + 0.235 [Th] + 0.0053 [Sm] (concentrations in weight %); F_t: α-ejection correction factor; raw ages are corrected after Farley et al. (1996); radius calculated according to Reiners et al. (2004) and Ketcham (2009). Data in bold and red marked data are discussed in the text.

Table 4.31: Zircon fission-track data from the Kerdous inlier

Sample	Etch time at 200 °C [h]	n	U (std) [µg/g]	Sp. Tracks ρ_s	Sp. Tracks N_s	Ind. Tracks ρ_i	Ind. Tracks N_i	$P(X^2)$ [%]	Central age [Ma]	Error ± 1σ [Ma]
MA-08	7.0	13	193.4 (58.0)	243.632	1065	29.739	130	100.0	298.6	30.6
MA-10	5.0	22	161.3 (40.3)	212.746	3054	24.869	357	100.0	311.4	22.0
MA-14	5.0	15	174.5 (38.4)	243.837	1551	29.242	186	100.0	303.6	27.0
MA-17	7.0	20	159.6 (36.7)	202.373	1954	25.685	248	99.8	287.1	23.0

Etch time in KOH:NaOH (7:5) eutectic melt at 200 ± 2 °C; U (std): Uranium concentration and standard deviation; n: number of counted apatite grains; ρ_s: density of spontaneous tracks (10^5 tr/cm^2); N_s: number of spontaneous tracks; ρ_i: density of induced tracks (10^5 tr/cm^2); N_i: number of induced tracks; $P(\chi^2)$: probability that single grains are consistent and belong to the same population. Test is passed if $P(\chi^2)$ > 5% (Galbraith, 1981). Nd = 11255 tracks counted on CN1 dosimeter glass. Central ages are calculated using a ζ-value of 140.83 ± 5.93. Samples were irradiated at the FRM II reactor facility in Garching, Germany with a fluence of 1 x 10^{15} neutrons/cm^2.

4.2.3 Ifni inlier

4.2.3.1 Apatite (U-Th-Sm)/He ages

Two samples from the Ifni inlier of the western Anti-Atlas with three single grain aliquots have been determined by apatite (U-Th-Sm)/He analysis. Raw AHe ages cover a wide range from 67.0 (±4.0) to 145.0 (±8.7) Ma (Tab. 4.32). α-ejection correction after Farley et al. (1996) was applied to all grains resulting in ages between 119.8 (±7.2) and 223.7 (±13.4) Ma (Tab. 4.32). Both samples show a large spread in the single grain ages. The youngest α-ejection corrected single grain age of the two samples range from 119.8 (±7.2) to 164.1 (±9.8) Ma (Fig. 4.37, Tab. 4.32). The ages are significantly younger than the corresponding sedimentation, metamorphic or intrusive age of the sampled rock. From every sample, at least one AHe single grain age is younger than the apatite fission-track age.

A positive correlation between single grain age and effective Uranium concentration has been observed in sample MA-21 of the Ifni inlier (Fig. 4.36). A positive correlation is indicative for a long residence time in the PRZ.

No clear positive correlation between equivalent grain radius and AHe age distribution was determined (Fig. 4.38).

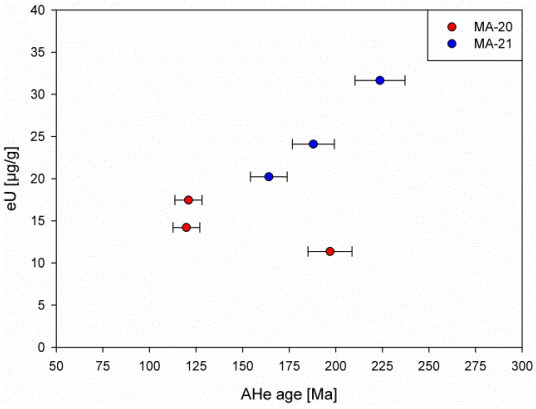

Fig. 4.36: AHe single grain ages (1σ error) from the Ifni inlier plotted against eU.

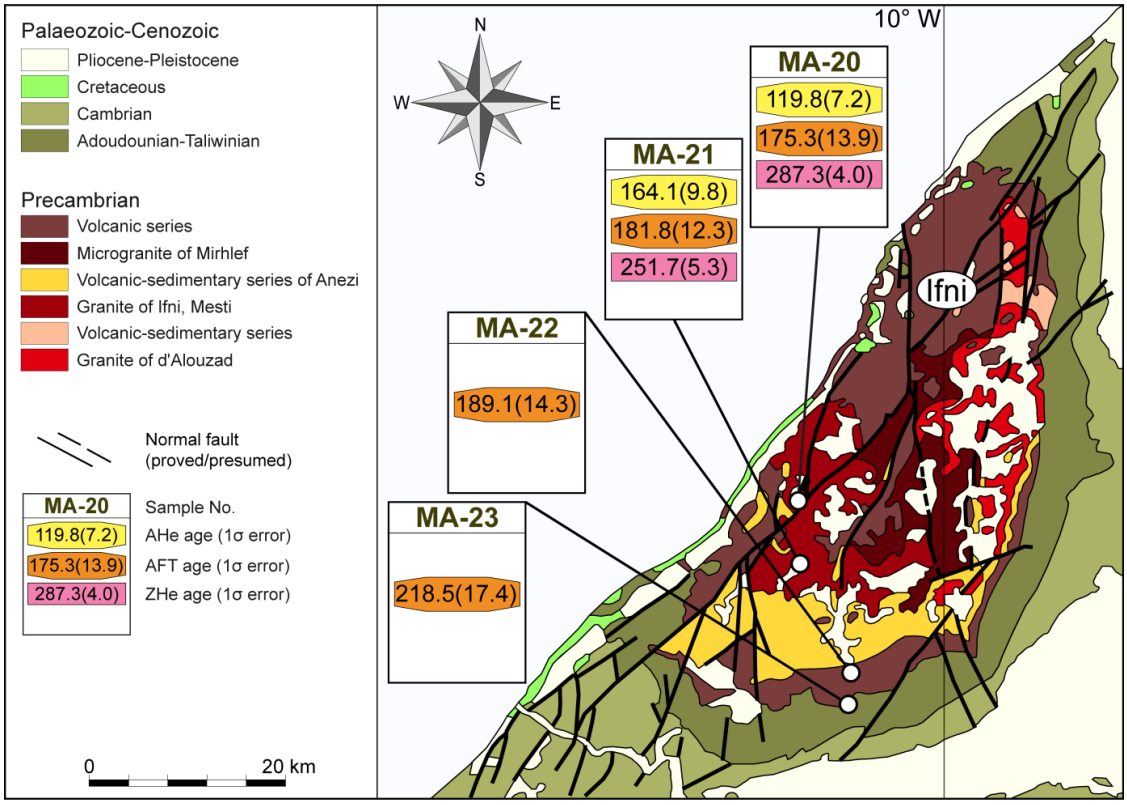

Fig. 4.37: Geological map of the Ifni inlier with sample locations, AFT central ages, ZHe ages as well as the youngest AHe age (1σ error).

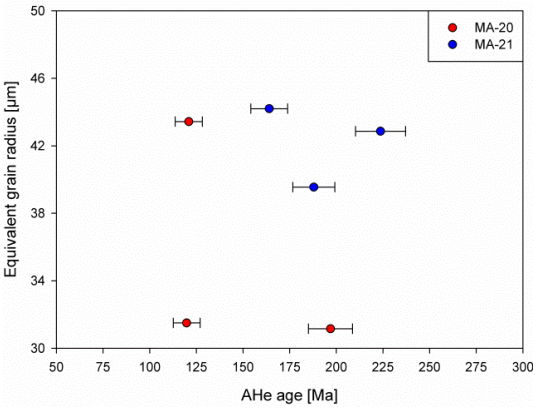

Fig. 4.38: AHe single grain ages (1σ error) from the Ifni inlier plotted against equivalent grain radius.

4.2.3.2 Apatite fission-track ages

All samples from the Ifni inlier have been analysed by apatite fission-track dating. The samples reveal slightly different apatite fission-track central ages between 175.3 (±13.9) and 218.5 (±17.4) Ma from lower elevations between 60 m and 570 m (Fig. 4.37, Tab. 4.33). Three samples show identical ages (MA-20, MA-21 and MA-22) yielding an average age of 182.1 (±13.5) Ma. The oldest age of 218 (±17.4) Ma was obtained from a breccia sample (MA-23) close to the ignimbrite sample MA-22. All ages are significantly younger than the corresponding sedimentation, metamorphic or intrusive age of the sampled rock. The single grain age distributions fulfilled the requirement of the χ^2-test with values between 95 and 99 % indicating a homogeneous distribution with respect to 1σ error of the single grain ages.

4.2.3.3 Etch pit size and track length distribution

A total of 704 D_{par} values were determined for all apatite grains (Tab. 4.34). The mean D_{par} values for each sample reveal a very narrow range between 1.4 (±0.2) and 1.7 (±0.3) µm. The samples exhibit a positive skewness of 0.127 and 2.913. Sample MA-21 shows the largest spread in etch pit size ranging between 1.2 (±0.1) and 3.4 (±0.1) µm. No positive correlation between single grain ages and D_{par} values has been detected.

A total of 232 track lengths of confined spontaneous fission-tracks were measured (Tab. 4.34). The obtained mean track lengths range from 11.8 (±1.3) to 12.6 (±1.1) µm. All samples show a unimodal, narrow track length distribution. The track length distributions of the samples show no significant skewness ranging between -0.316 and 0.914. The largest track length of 15.1 (±0.1) µm was measured in sample MA-21. After correcting of the confined track lengths for their crystallographic orientation, the mean confined fission-track lengths changed to a distribution of 13.5 (±0.9) and 14.0 (±0.7) µm. The c-axis corrected track length distributions of the samples show no significant skewness ranging between -0.504 and 0.520. Sample MA-29 shows the largest spread in track length after c-axis correction ranging between 10.1 (±0.1) and 15.4 (±0.1) µm.

4.2.3.4 Zircon (U-Th-Sm)/He ages

Two samples from the Ifni inlier with three single grain aliquots have been determined for zircon (U-Th-Sm)/He analysis. Raw ZHe ages cover a wide range from 130.7 (±3.5) to 270.3 (±4.0) Ma (Tab. 4.35). α-ejection correction after Farley et al. (1996) was applied to all grains resulting in ages between 173.2 (±4.7) and 362.0 (±5.4) Ma (Tab. 4.35). The single grains with the lowest eU concentration revealed similar ages of 251.7 (±5.3) and 287.3 (±4.0) Ma (Fig. 4.37, Tab. 4.35). All ages are significantly younger than the corresponding sedimentation, metamorphic or intrusive age of the sampled rock as well as older than the AHe and AFT ages.

In sample MA-21, a negative correlation between single grain age and effective Uranium concentration has been observed (Fig. 4.39). A negative correlation is given by an increasing He diffusivity as numerous traps are

connected depending on the radiation damage and cooling history of the hosting rock (Guenthner and Reiners, 2010). The influence of radiation damage on ZHe ages is minor as long as U concentrations are less than ~1000 ppm (Reiners, 2005). At higher U concentrations the ZHe ages decrease rapidly to anomalously young and unreproducible ages (Reiners, 2005). Consequently, based on the determined eU concentrations of 1099 and 1156 ppm in sample MA-21, two ZHe single grain aliquot ages could be anomalously young and unreproducible (Tab. 4.35).

No clear positive correlation between equivalent grain radius and ZHe age distribution was determined (Fig. 4.40).

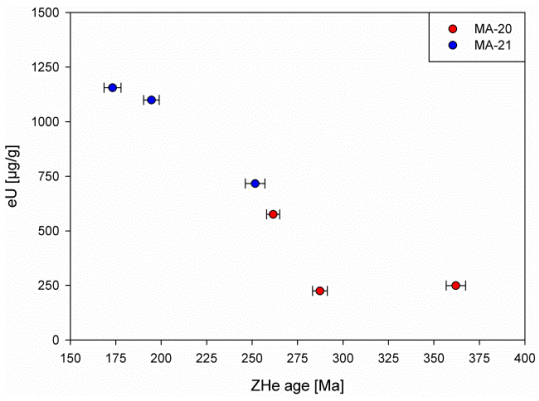

Fig. 4.39: ZHe single grain ages (1σ error) from the Ifni inlier plotted against eU.

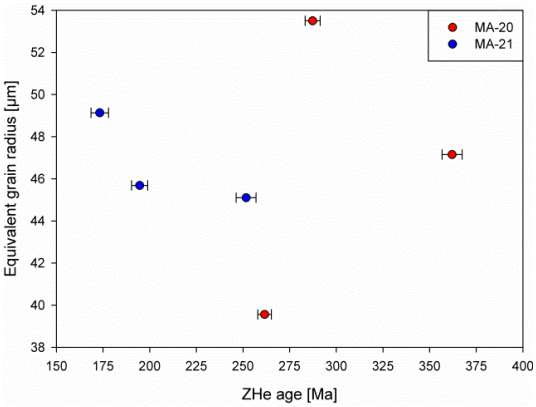

Fig. 4.40: ZHe single grain ages (1σ error) from the Ifni inlier plotted against equivalent grain radius.

4.2.3.5 Summary

The age-elevation plot shows similar ages of the AFT method, while AHe and ZHe ages are slightly different (Fig. 4.41).

The comparison of all data shows an age distribution appropriate to the closure temperatures of the respective thermochronological methods (Fig. 4.41).

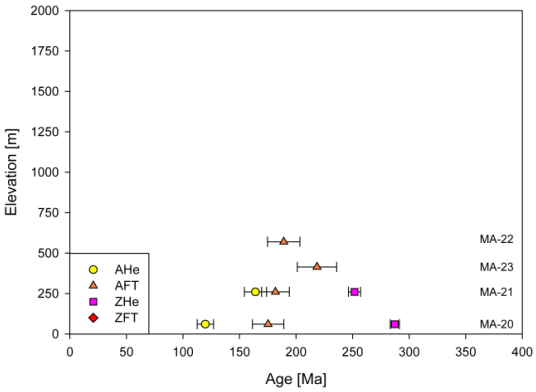

Fig. 4.41: AHe, AFT and ZHe age (1σ error) – elevation plot from the Ifni inlier.

Table 4.32: Apatite (U-Th-Sm)/He data from the Ifni inlier

Sample	Mass [µg]	Radius [µm]	U [µg/g]	Th [µg/g]	Sm [µg/g]	eU [µg/g]	Th/U	^{4}He [nmol/g]	F_t	Raw age [Ma]	Error ± 1σ [Ma]	Corrected age [Ma]	Error ± 1σ [Ma]
MA-20.1	2.2	43.4	13	20	90	17	1.5	7.79	0.652	78.9	4.7	120.9	7.3
MA-20.2	**0.9**	**31.5**	**10**	**19**	**102**	**14**	**2.0**	**5.90**	**0.559**	**67.0**	**4.0**	**119.8**	**7.2**
MA-20.3	0.7	31.2	7	17	86	11	2.2	6.88	0.532	104.7	6.3	196.9	11.8
MA-21.1	1.4	39.6	18	25	23	24	1.3	15.51	0.624	117.2	7.0	188.0	11.3
MA-21.2	1.8	42.9	23	35	18	32	1.5	25.18	0.648	145.0	8.7	223.7	13.4
MA-21.3	**2.4**	**44.2**	**15**	**21**	**18**	**20**	**1.4**	**12.25**	**0.673**	**110.4**	**6.6**	**164.1**	**9.8**

eU = [U] + 0.235 [Th] + 0.0053 [Sm] (concentrations in weight %); F_t: α-ejection correction factor; raw ages are corrected after Farley et al. (1996); radius calculated according to Shuster et al. (2006) and Ketcham (2009). Data in bold: youngest apatite (U-Th-Sm)/He grain of each sample discussed in the text.

Table 4.33: Apatite fission-track from the Ifni inlier

Sample	Elevation [m a.s.l.]	n	U (std) [µg/g]	Sp. Tracks ρ_s	Sp. Tracks N_s	Ind. Tracks ρ_i	Ind. Tracks N_i	$P(\chi^2)$ [%]	Central age [Ma]	Error ± 1σ [Ma]
MA-20	60	20	8.9 (2.6)	7.821	501	11.318	725	95.3	175.3	13.9
MA-21	260	20	18.7 (4.7)	17.416	1044	25.239	1513	99.1	181.8	12.3
MA-22	570	18	14.7 (6.5)	14.326	767	13.242	709	99.0	189.1	14.3
MA-23	414	18	12.1 (8.2)	11.642	675	9.296	539	99.0	218.5	17.4

U (std): Uranium concentration and standard deviation; n: number of counted apatite grains; ρ_s: density of spontaneous tracks (10^5 tr/cm^2); N_s: number of spontaneous tracks; ρ_i: density of induced tracks (10^5 tr/cm^2); N_i: number of induced tracks; $P(\chi^2)$: probability that single grains are consistent and belong to the same population. Test is passed if $P(\chi^2) > 5$ % (Galbraith, 1981). Nd = 15419 tracks counted on CN5 dosimeter glass. Central ages are calculated using a ζ-value of 333.36 ± 17.89. Samples were irradiated at the FRM II reactor facility in Garching, Germany with a fluence of 1×10^{16} neutrons/cm^2.

Table 4.34: Confined fission-track length data from the Ifni inlier

Sample	n CT	CT mean [µm]	CT std [µm]	CT skew	CT min [µm]	CT max [µm]	L_c mean [µm]	L_c std [µm]	L_c skew	L_c min [µm]	L_c max [µm]	n D_{par}	D_{par} mean [µm]	D_{par} std [µm]	D_{par} skew	D_{par} min [µm]	D_{par} max [µm]
MA-20	105	11.8	1.3	0.126	8.8	14.6	13.5	0.9	-0.504	10.1	15.4	230	1.6	0.2	0.880	1.2	2.2
MA-21	111	12.1	1.4	-0.316	8.9	15.1	13.7	1.0	-0.438	11.1	15.6	297	1.7	0.3	2.913	1.2	3.4
MA-22	10	12.6	1.1	0.914	11.3	14.5	14.0	0.7	0.520	12.9	15.4	87	1.4	0.2	0.703	0.9	2.0
MA-23	6	12.2	1.1	-0.087	10.7	13.7	13.8	0.8	0.147	12.7	15.0	90	1.5	0.2	0.127	1.0	2.1

n: number of measured individual confined tracks (CT) and etch pit diameter (D_{par}); CT mean: mean confined track length; L_c mean: mean track length after c-axis correction; D_{par} mean: mean etch pit diameter; std: standard deviation; skew: skewness of distribution relative to the mean value; min: minimum single values; max: maximum single values.

Table 4.35: Zircon (U-Th-Sm)/He data from the Ifni inlier

Sample	Mass [µg]	Radius [µm]	U [µg/g]	Th [µg/g]	Sm [µg/g]	eU [µg/g]	Th/U	^{4}He [nmol/g]	Ft	Raw age [Ma]	Error ± 1σ [Ma]	Corrected age [Ma]	Error ± 1σ [Ma]
MA-20.1	2.1	39.6	528	204	n.d.	576	0.40	576.7	0.701	183.4	2.5	261.6	3.6
MA-20.2	**4.8**	**53.5**	**207**	**76**	**n.d.**	**224**	**0.38**	**275.7**	**0.780**	**224.1**	**3.1**	**287.3**	**4.0**
MA-20.3	3.4	47.2	223	111	n.d.	249	0.51	370.4	0.747	270.3	4.0	362.0	5.4
MA-21.1	4.0	49.1	1085	303	n.d.	1156	0.29	821.2	0.755	130.7	3.5	173.2	4.7
MA-21.2	3.1	45.7	1051	207	n.d.	1099	0.20	859.9	0.739	143.7	3.2	194.6	4.3
MA-21.3	**3.3**	**45.1**	**666**	**217**	**n.d.**	**717**	**0.33**	**729.3**	**0.740**	**186.3**	**3.9**	**251.7**	**5.3**

eU = [U] + 0.235 [Th] + 0.0053 [Sm] (concentrations in weight %); F_t: α-ejection correction factor; raw ages are corrected after Farley et al. (1996); radius calculated according to Reiners et al. (2004) and Ketcham (2009). Data in bold are discussed in the text.

4.2.4 Bas Drâa inlier

4.2.4.1 Apatite (U-Th-Sm)/He ages

Two samples from the lower elevated Bas Drâa inlier of the western Anti-Atlas with three single grain aliquots have been determined by apatite (U-Th-Sm)/He analysis. Raw AHe ages cover a wide range from 74.9 (±4.5) to 164.9 (±9.9) Ma (Tab. 4.36). α-ejection correction after Farley et al. (1996) was applied to all grains resulting in ages between 110.7 (±6.6) and 227.4 (±13.6) Ma (Tab. 4.36). Both samples show a large spread in the single grain ages. The youngest α-ejection corrected single grain age of the two samples range from 110.7 (±6.6) to 129.9 (±7.8) Ma (Fig. 4.43, Tab. 4.36). The ages are significantly younger than the corresponding sedimentation, metamorphic or intrusive age of the sampled rock. From every sample, at least one AHe single grain age is younger than the apatite fission-track age.

A positive correlation between single grain age and effective Uranium concentration has been observed in sample MA-29 of the Bas Drâa inlier (Fig. 4.42). A positive correlation is indicative for a long residence time in the PRZ.

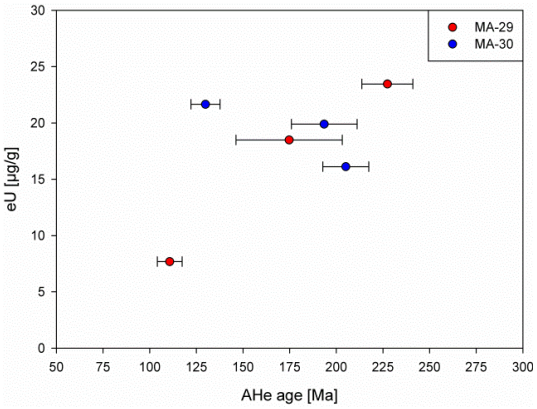

Fig. 4.42: AHe single grain ages (1σ error) from the Bas Drâa inlier plotted against eU.

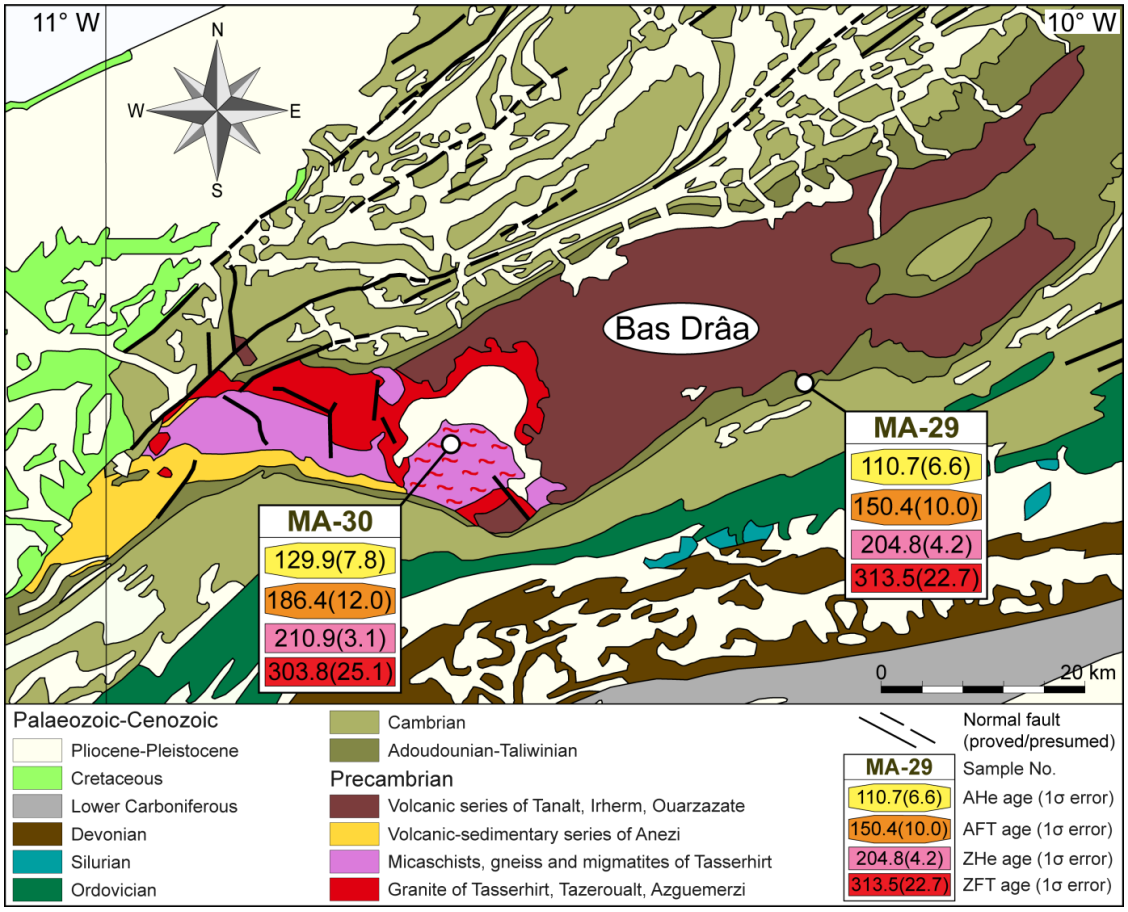

Fig. 4.43: Geological map of the Bas Drâa inlier with sample locations, AFT and ZFT central ages, ZHe ages as well as the youngest AHe age (1σ error).

In both samples a positive correlation between equivalent grain radius and AHe age distribution was determined indicating a long residence time in the PRZ (Reiners and Farley, 2001) (Fig. 4.44).

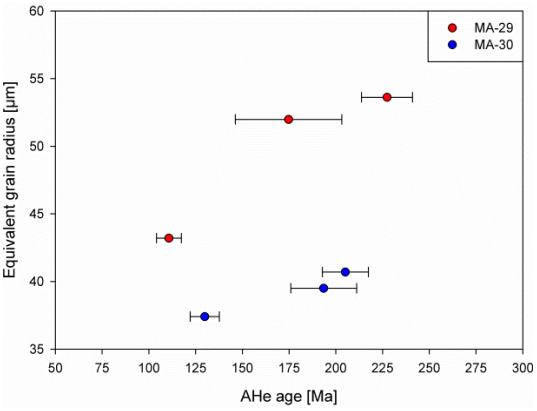

Fig. 4.44: AHe single grain ages (1σ error) from the Bas Drâa inlier plotted against equivalent grain radius.

4.2.4.2 Apatite fission-track ages

Both samples from the Bas Drâa inlier have been analysed by apatite fission-track dating. The samples reveal slightly different apatite fission-track central ages of 150.4 (±10.0) and 186.4 (±12.0) Ma from lower elevations of 134 m and 344 m (Fig. 4.43, Tab. 4.37). All ages are significantly younger than the corresponding sedimentation, metamorphic or intrusive age of the sampled rock. The single grain age distributions fulfilled the requirement of the χ^2-test with values of 93 and 99 % indicating a homogenous distribution with respect to 1σ error of the single grain ages.

4.2.4.3 Etch pit size and track length distribution

A total of 335 D_{par} values were determined for all apatite grains (Tab. 4.38). The mean D_{par} values for each sample reveal a very narrow range between 1.4 (±0.1) and 1.7 (±0.1) µm. The samples exhibit a minor positive skewness of 0.107 and 0.229. Sample MA-29 shows the largest spread in etch pit size ranging between 1.3 (±0.1) and 2.1 (±0.1) µm.

A total of 223 track lengths of confined spontaneous fission-tracks were measured (Tab. 4.38). The obtained mean track lengths range from 11.7 (±1.5) to 12.2 (±1.5) µm. Both samples show a unimodal, narrow track length distribution. The track length distributions of the samples show a negative skewness ranging between -0.886 and -0.410. The largest track length of 16.2 (±0.1) µm as well as the smallest of 5.3 (±0.1) µm was measured in sample MA-29. After correcting of the confined track lengths for their crystallographic orientation, the mean confined fission-track lengths changed to a distribution of 13.5 (±0.9) and 13.8 (±1.0) µm. The c-axis corrected track length distributions of the samples show no significant, negative skewness. Sample MA-29 shows the largest spread in track length after c-axis correction ranging between 11.4 (±0.1) and 16.4 (±0.1) µm.

4.2.4.4 Zircon (U-Th-Sm)/He ages

Both samples from the Bas Drâa inlier with three single grain aliquots have been determined by zircon (U-Th-Sm)/He analysis. Raw ZHe ages cover a range from 151.4 (±3.1) to 187.1 (±2.9) Ma (Tab. 4.39). α-ejection correction after Farley et al. (1996) was applied to all grains resulting in ages between 204.1 (±3.5) and 246.2 (±3.8) Ma (Tab. 4.39). The single grains with the lowest eU concentration revealed identical ages of 204.8 (±4.2) and 210.9 (±3.1) Ma (Fig. 4.43, Tab. 4.39). All ages are significantly younger than the corresponding sedimentation, metamorphic or intrusive age of the sampled rock as well as older than the AHe and AFT ages.

The age–eU concentration plot shows no clear positive or negative correlation in samples from the Bas Drâa inlier (Fig. 4.45). Whereas the three single grain ages of sample MA-30 are equal within the standard deviation, sample MA-29 reveals no obvious correlation between eU content and ZHe age.

No clear positive correlation between equiva-

lent grain radius and ZHe age distribution was determined (Fig. 4.46).

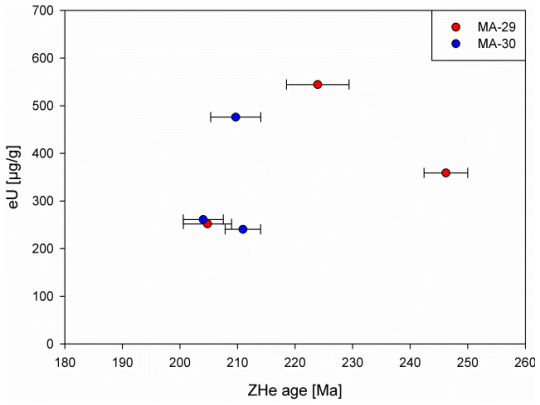

Fig. 4.45: ZHe single grain ages (1σ error) from the Bas Drâa inlier plotted against eU.

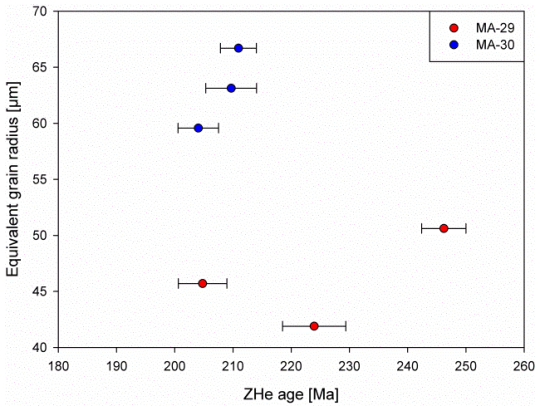

Fig. 4.46: ZHe single grain ages (1σ error) from the Bas Drâa inlier plotted against equivalent grain radius.

4.2.4.5 Zircon fission-track ages

All samples from the Bas Drâa inlier have been analysed by zircon fission-track dating. The zircon fission-track central ages are equal within the standard deviation ranging between 303.8 (±25.1) and 313.5 (±22.7) Ma (Fig. 4.43, Tab. 4.40). All ages are significantly younger than the corresponding sedimentation, metamorphic or intrusive age of the sampled rock. ZFT ages are older than ZHe, AFT and AHe ages, which is consistent with the difference in closure temperature between the thermochronological systems. All single grain age distributions fulfilled the requirement of the χ^2-test with values of 100 %.

4.2.4.6 Summary

The age-elevation plot shows similar or identical ages of the different thermochronometric methods (Fig. 4.47). However, AHe and AFT ages of sample MA-29 are slightly younger yielding a minor negative slope (Fig. 4.47). This negative slope is indicative for a general decay in relief (Braun, 2002). The comparison of all data shows an age distribution appropriate to the closure temperatures of the respective thermochronological methods (Fig. 4.47).

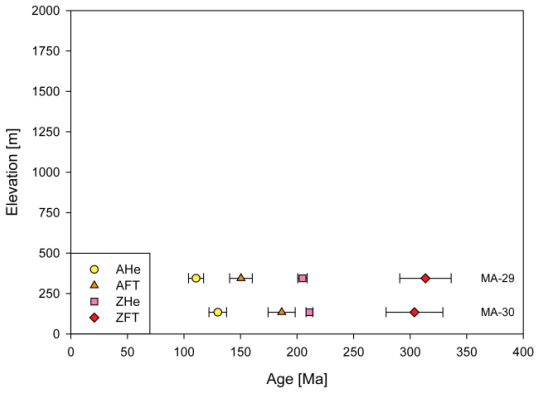

Fig. 4.47: AHe, AFT, ZHe and ZFT age (1σ error) – elevation plot from the Bas Drâa inlier.

Table 4.36: Apatite (U-Th-Sm)/He data from the Bas Drâa inlier

Sample	Mass [µg]	Radius [µm]	U [µg/g]	Th [µg/g]	Sm [µg/g]	eU [µg/g]	Th/U	^{4}He [nmol/g]	F_t	Raw age [Ma]	Error ± 1σ [Ma]	Corrected age [Ma]	Error ± 1σ [Ma]
MA-29.1	**2.7**	**43.2**	**6**	**6**	**41**	**8**	**0.9**	**3.26**	**0.676**	**74.9**	**4.5**	**110.7**	**6.6**
MA-29.2	1.5	52.0	17	6	61	18	0.3	35.98	0.717	125.3	20.4	174.7	28.5
MA-29.3	3.9	53.6	22	7	86	23	0.3	21.79	0.725	164.9	9.9	227.4	13.6
MA-30.1	0.9	39.5	19	4	48	20	0.2	20.97	0.642	124.3	11.3	193.5	17.6
MA-30.2	1.5	40.7	15	3	48	16	0.2	12.04	0.652	133.7	8.0	205.1	12.3
MA-30.3	**1.2**	**37.4**	**21**	**4**	**70**	**22**	**0.2**	**9.91**	**0.633**	**82.2**	**4.9**	**129.9**	**7.8**

eU = [U] + 0.235 [Th] + 0.0053 [Sm] (concentrations in weight %); F_t: α-ejection correction factor; raw ages are corrected after Farley et al. (1996); radius calculated according to Shuster et al. (2006) and Ketcham (2009). Data in bold: youngest apatite (U-Th-Sm)/He grain of each sample discussed in the text.

Table 4.37: Apatite fission-track from the Bas Drâa inlier

Sample	Elevation [m a.s.l.]	n	U (std) [µg/g]	Sp. Tracks ρ_s	Sp. Tracks N_s	Ind. Tracks ρ_i	Ind. Tracks N_i	$P(\chi^2)$ [%]	Central age [Ma]	Error ± 1σ [Ma]
MA-29	344	20	18.4 (11.4)	13.145	1320	15.406	1547	98.5	150.4	10.0
MA-30	134	20	16.3 (4.7)	15.842	1411	22.140	1972	92.9	186.4	12.0

U (std): Uranium concentration and standard deviation; n: number of counted apatite grains; ρ_s: density of spontaneous tracks (10^5 tr/cm^2); N_s: number of spontaneous tracks; ρ_i: density of induced tracks (10^5 tr/cm^2); N_i: number of induced tracks; $P(\chi^2)$: probability that single grains are consistent and belong to the same population. Test is passed if $P(\chi^2) > 5$ % (Galbraith, 1981). Nd = 15419 tracks counted on CN5 dosimeter glass. Central ages are calculated using a ζ-value of 333.36 ± 17.89. Samples were irradiated at the FRM II reactor facility in Garching, Germany with a fluence of 1 x 10^{16} neutrons/cm^2.

Table 4.38: Confined fission-track length data from the Bas Drâa inlier

Sample	n CT	CT mean [µm]	CT std [µm]	CT skew	CT min [µm]	CT max [µm]	L_c mean [µm]	L_c std [µm]	L_c skew	L_c min [µm]	L_c max [µm]	n D_{par}	D_{par} mean [µm]	D_{par} std [µm]	D_{par} skew	D_{par} min [µm]	D_{par} max [µm]
MA-29	117	12.2	1.5	-0.886	5.3	16.2	13.8	1.0	-0.021	11.4	16.4	110	1.4	0.1	0.107	1.0	1.7
MA-30	106	11.7	1.5	-0.410	7.9	14.3	13.5	0.9	-0.304	11.3	15.3	225	1.7	0.1	0.229	1.3	2.1

n: number of measured individual confined tracks (CT) and etch pit diameter (D_{par}); CT mean: mean confined track length; L_c mean: mean track length after c-axis correction; D_{par} mean: mean etch pit diameter; std: standard deviation; skew: skewness of distribution relative to the mean value; min: minimum single values; max: maximum single values.

Table 4.39: Zircon (U-Th-Sm)/He data from the Bas Drâa inlier

Sample	Mass [µg]	Radius [µm]	U [µg/g]	Th [µg/g]	Sm [µg/g]	eU [µg/g]	Th/U	^{4}He [nmol/g]	Ft	Raw age [Ma]	Error ± 1σ [Ma]	Corrected age [Ma]	Error ± 1σ [Ma]
MA-29.1	4.3	50.6	310	208	n.d.	359	0.69	366.8	0.760	187.1	2.9	246.2	3.8
MA-29.2	2.3	41.9	490	231	n.d.	545	0.48	475.4	0.715	160.2	3.8	223.9	5.4
MA-29.3	**3.5**	**45.7**	**209**	**183**	**n.d.**	**252**	**0.90**	**207.8**	**0.739**	**151.4**	**3.1**	**204.8**	**4.2**
MA-30.1	7.0	59.6	250	47	n.d.	261	0.19	231.3	0.796	162.4	2.8	204.1	3.5
MA-30.2	**11.8**	**66.7**	**230**	**44**	**n.d.**	**241**	**0.19**	**228.3**	**0.824**	**173.9**	**2.5**	**210.9**	**3.1**
MA-30.3	10.8	63.1	463	56	n.d.	476	0.12	439.6	0.807	169.3	3.5	209.7	4.4

eU = [U] + 0.235 [Th] + 0.0053 [Sm] (concentrations in weight %); F_t: α-ejection correction factor; raw ages are corrected after Farley et al. (1996); radius calculated according to Reiners et al. (2004) and Ketcham (2009). Data in bold are discussed in the text.

Table 4.40: Zircon fission-track data from the Bas Drâa inlier

Sample	Etch time at 200 °C [h]	n	U (std) [µg/g]	Sp. Tracks ρ_s	Sp. Tracks N_s	Ind. Tracks ρ_i	Ind. Tracks N_i	$P(X^2)$ [%]	Central age [Ma]	Error ± 1σ [Ma]
MA-29	5.0	20	149.9 (30.0)	206.306	2837	23.925	329	99.9	313.5	22.7
MA-30	3.5	20	180.2 (36.0)	250.332	1880	29.960	225	100.0	303.8	25.1

Etch time in KOH:NaOH (7:5) eutectic melt at 200 ± 2 °C; U (std): Uranium concentration and standard deviation; n: number of counted apatite grains; ρ_s: density of spontaneous tracks (10^5 tr/cm^2); N_s: number of spontaneous tracks; ρ_i: density of induced tracks (10^5 tr/cm^2); N_i: number of induced tracks; $P(\chi^2)$: probability that single grains are consistent and belong to the same population. Test is passed if $P(\chi^2) > 5\%$ (Galbraith, 1981). Nd = 11255 tracks counted on CN1 dosimeter glass. Central ages are calculated using a ζ-value of 140.83 ± 5.93. Samples were irradiated at the FRM II reactor facility in Garching, Germany with a fluence of 1 x 10^{15} neutrons/cm^2.

4.2.5 Precambrian inliers – Summary

The Precambrian inliers show identical age populations in the various thermochronological methods. Therefore, the data were presented and discussed by comparison.

4.2.5.1 Apatite (U-Th-Sm)/He ages

The AHe ages revealed an age spectra from 49.0 (±2.9) to 164.1 (±9.8) Ma (Fig. 4.23, Fig. 4.48). Based on the large spread in the age distribution and the very different nature of the topography from northeast to southwest in the sampling area, the data were grouped into two areas:

(1) Elevated northeastern part with the Irherm and Kerdous inliers
(2) Lower southwest area including the Ifni and Bas Drâa inliers and the southwestern part of the Kerdous inlier

(1) In the Irherm and Kerdous inliers, seven Precambrian samples yielded significant younger AHe ages than in the Ifni and Bas Drâa inliers ranging from 49.0 (±2.9) to 88.7 (±5.3) Ma (Fig. 4.48). The area reveals two different AHe age populations that are not separable regionally, topographically or by major structural features. Ages of the younger population range between 49.0 (±2.9) and 61.0 (±3.7) Ma yielding an average age of 55.2 (±3.3) Ma (Fig. 4.48). The youngest age of 49.0 (±2.9) Ma was obtained from a quartzite sample (MA-06) taken at 1885 m, the highest elevation of all samples. The AHe ages of the older population from the Irherm and Kerdous inliers are equal within the standard deviation ranging from 85.4 (±5.1) to 88.7 (±5.3) Ma and yielding an average age of 87.8 (±5.3) Ma.
(2) The AHe ages of samples from the lower southwestern inliers Bas Drâa and Ifni including a sample from the Kerdous inlier cover a range from 110.7 (±6.6) to 164.1 (±9.8) Ma (Fig. 4.48). Except for a granite sample from the Ifni inlier with an age of 164.1 (±9.8) Ma, the samples reveal a very narrow age spectra ranging from 110.7 (±6.6) to 129.9 (±7.8) Ma. The five samples were taken from lower elevations between 134 and 530 m and yielded an average age of 129.7 (±7.8) Ma.

The age-elevation plot for the entire sampling area shows a rather large scatter in the age distribution and no obvious relationship (Fig. 4.48). However, the separate areas described above indicate an apparent relationship between elevation and AHe ages and an increasing impact of the Atlasian orogeny from southwest to northeast in the western Anti-Atlas.

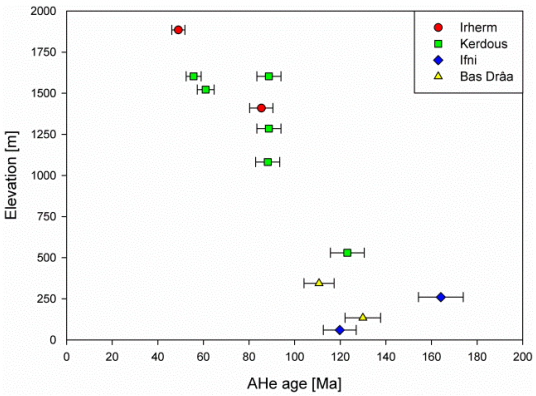

Fig. 4.48: AHe age (1σ error) – elevation plot from outcrop samples of the western Anti-Atlas.

4.2.5.2 Apatite fission-track ages

The apatite fission-track central ages cover a wide range from 119.7 (±13.4) to 218.5 (±17.4) Ma (Fig. 4.23, Fig. 4.49), while 17 ages range between 150 and 190 Ma. Based on the large spread in the AFT age distribution, the data were grouped into three areas.

(1) Northeastern block (Irherm and Eastern Kerdous inliers)
(2) Southwestern block (Ifni and Bas Drâa inliers)
(3) Middle block (Western Kerdous inlier)

(1) In the northeastern block, 12 samples revealed a narrow age spectra ranging from 149.6 (±13.5) to 180.7 (±11.7) Ma (Fig. 4.49). The samples from the Irherm and eastern Kerdous inliers were collected from elevations between 1018 m and 1885 m yielding an average age of 164.4 (±12.6) Ma.

(2) In the lower southwestern block including samples from the Ifni and Bas Drâa inliers, the AFT ages are somewhat older than in the northeastern block. The six central ages determined range between 150.4 (±10.0) and 218.5 (±17.4) Ma yielding an average age of 183.6 (±13.3) Ma (Fig. 4.49). In this block a large degree of scatter in the age distribution can be observed. Four samples revealed a narrow age spectra from 175.3 (±13.9) to 189.1 (±14.3) Ma yielding an average age of 183.2 (±13.1). A sample from the Bas Drâa inlier show a significantly younger age of 150.4 (±10.0) Ma similar to the youngest ages of the northeastern block.

(3) In the western Kerdous inlier the AFT ages are substantial younger compared to the other blocks. The central ages range between 119.7 (±13.4) and 139.0 (±9.1) Ma yielding an average age of 128.2 (±12.0) Ma (Fig. 4.49).

The age-elevation plot for the entire sampling area shows a large spread in the age distribution and no obvious relationship is visible (Fig. 4.49).

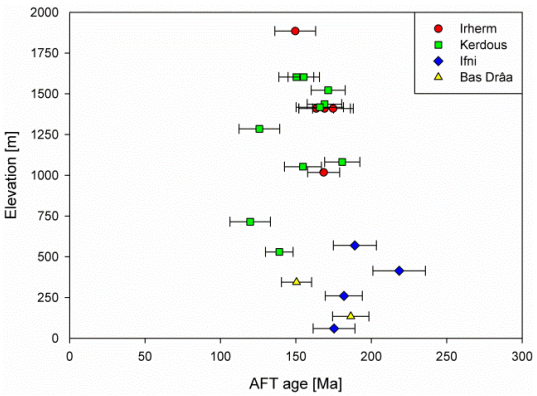

Fig. 4.49: AFT age (1σ error) – elevation plot from outcrop samples of the western Anti-Atlas.

However, the separate blocks indicate a minor relationship between elevation and AFT central ages. Considering all ages from the northeastern block, the narrow age spectrum indicates a rapid exhumation between 180 and 150 Ma in this part of the study area.

4.2.5.3 Zircon (U-Th-Sm)/He age

The ZHe ages of the entire study area revealed an age spectra from 130.1 (±2.9) to 287.3 (±4.0) Ma (Fig. 4.23, Fig. 4.50). A regional separation of the sampling area based on the ZHe ages could not be determined. Five samples from the Kerdous and Bas Drâa inliers show a narrow age range between 204.8 (±4.2) and 243.0 (±3.4) Ma, whereas the two ZHe ages of the Ifni inlier are slightly older ranging from 251.7 (±5.3) to 287.3 (±4.0) Ma. The ZHe age of 130.1 (±2.9) Ma from the Irherm inlier is an anomalously young and unreproducible age due to the very high eU concentration.

The age-elevation plot for the entire sampling area shows a scatter in the age distribution and no obvious relationship (Fig. 4.50). Excluding samples from the Ifni inlier, the ZHe data show a relatively narrow age distribution. Considering ages from the Kerdous and Bas Drâa inliers, the age spectra indicates a rapid exhumation in the study area between 250 and 200 Ma.

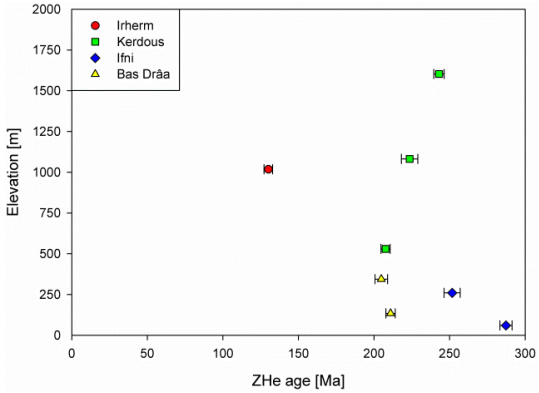

Fig. 4.50: ZHe age (1σ error) – elevation plot from outcrop samples of the western Anti-Atlas.

4.2.5.4 Zircon fission-track ages

The zircon fission-track central ages cover a narrow range between 287.1 (±23.0) and 330.6 (±23.8) Ma (Fig. 4.23, Fig. 4.51). A separation of the study area in several blocks based on the ZFT ages could not be determined. The ZFT ages show no elevation- or regional-dependent distribution. The analysed samples were collected from elevations between 134 m and 1885 m and yielded an average age of 307.3 (±24.1) Ma. The age-elevation plot shows the narrow range in the age distribution for the entire sampling area (Fig. 4.51). The zircon fission-track central ages of the eight samples are equal within the standard deviation to the calculated average age of 307.3 (±24.1) Ma indicating a rapid exhumation in the study area between 330 and 290 Ma.

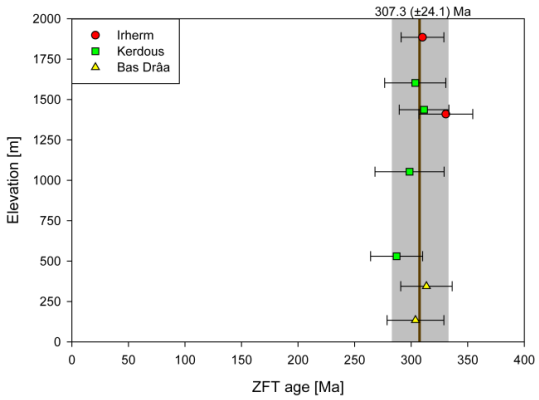

Fig. 4.51: ZFT age (1σ error) – elevation plot from outcrop samples of the western Anti-Atlas.

4.2.5.5 Summary

A comparison of all thermochronological data shows an age distribution appropriate to the closure temperatures of the respective thermochronometric methods (Fig. 4.52). All apatite (U-Th-Sm)/He ages are younger than the corresponding apatite fission-track age of the sample. Except for sample MA-01 with a very high eU concentration of 1107 µg/g, the zircon (U-Th-Sm)/He ages are older than the AFT and AHe ages. According to the higher closure temperature, the zircon fission-track data show significant older ages than the corresponding AHe, AFT and ZHe age of the sampled rock.

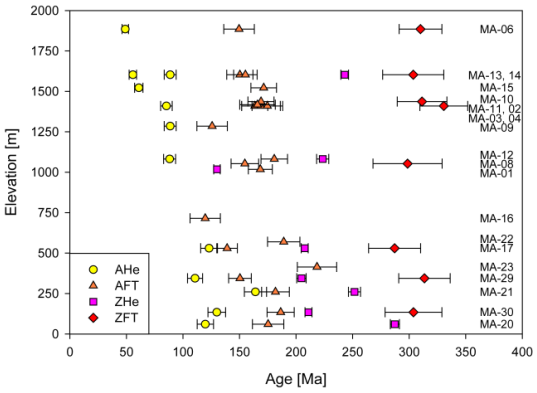

Fig. 4.52: AHe, AFT, ZHe and ZFT age (1σ error) – elevation plot from outcrop samples of the western Anti-Atlas.

4.2.6 Adrar Zougar-1

4.2.6.1 Apatite (U-Th-Sm)/He ages

Three samples from well Adrar Zougar-1 with three and four, respectively single grain aliquots have been analysed by apatite (U-Th-Sm)/He dating. Raw AHe ages cover a range from 0.0 (±0.0) to 27.2 (±1.6) Ma (Tab. 4.41). α-ejection correction after Farley et al. (1996) was applied to all grains resulting in ages between 0.0 (±0.0) and 40.0 (±2.4) Ma (Tab. 4.41). The youngest α-ejection corrected single grain age of each sample range from 16.4 (±1.0) Ma at a depth of 455–463 m to 0.0 (±0.0) Ma at a depth of 1988–2095 m (Fig. 4.54, Tab. 4.41). Based on the AHe age of 0.0 Ma from sample AZ-03 and the increment of the current temperature with increasing depth, AHe ages of samples AZ-04 to AZ-06 are also 0.0 Ma. The ages decrease continuously with increasing depth (Fig. 4.54). All single grain aliquot ages are significantly younger than the corresponding sedimentation age of the sampled rock and younger than the apatite fission-track age.

A positive correlation between single grain age and effective Uranium concentration has been observed in sample AZ-01, while the other samples show no obvious correlation (Fig. 4.53). A positive correlation is indicative for a long residence time in the PRZ.

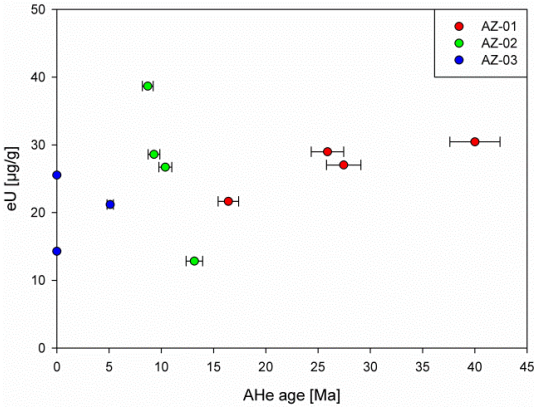

Fig. 4.53: AHe single grain ages (1σ error) from Adrar Zougar-1 well plotted against eU.

In samples from the Adrar Zougar-1 well, no clear correlation between equivalent grain radius and AHe age distribution was determined (Fig. 4.55).

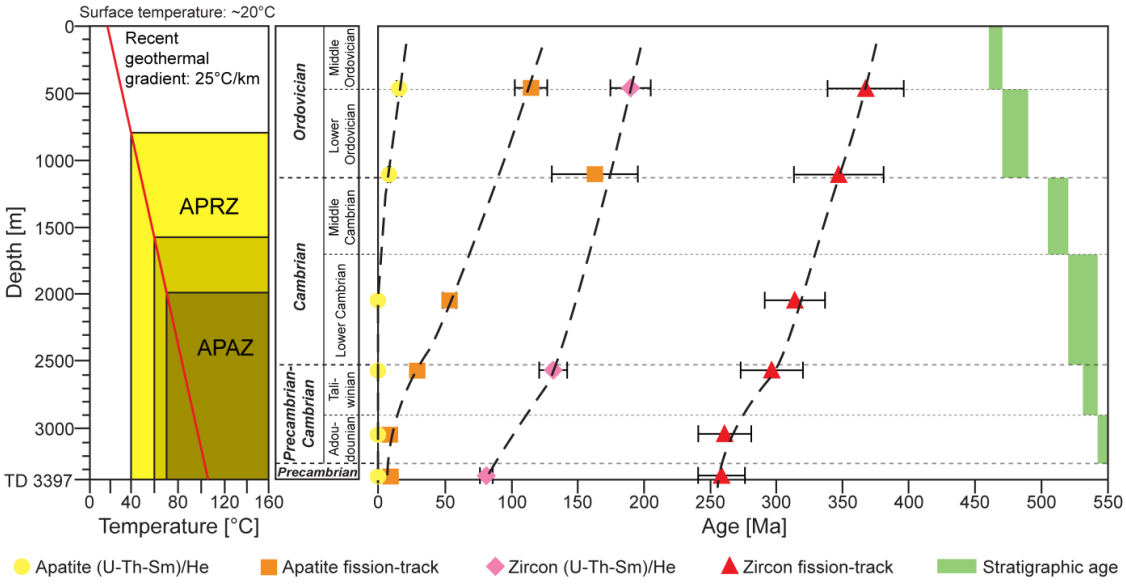

Fig. 4.54: Thermochronometric age (1σ error) – depth distribution of the Adrar Zougar-1 well. On the left side the recent temperature distribution as well as a schematic stratigraphic profile is displayed.

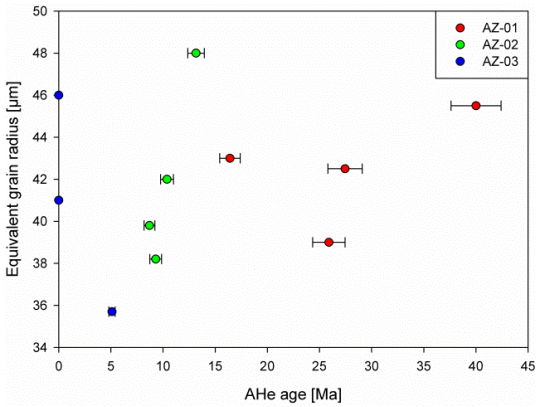

Fig. 4.55: AHe single grain ages (1σ error) from Adrar Zougar-1 well plotted against equivalent grain radius.

4.2.6.2 Apatite fission-track ages

Every sample has been analysed by apatite fission-track dating. The AFT central ages range between 163.0 (±32.3) Ma at a depth of 1090–1113 m and 8.9 (±1.2) Ma at a depth of 3021–3059 m (Fig. 4.54, Tab. 4.42). Except for sample AZ-02 the ages decrease continuously from the top to the bottom of the well (Fig. 4.54). The scatter in the upper part of the well is due to the very low amount of apatite single grains. Whereas in sample AZ-01 an age of 114.9 (±12.2) Ma was determined by four grains, in sample AZ-02 only one grain was analysed resulting in an AFT age of 163.0 (±32.3) Ma. All ages are significantly younger than the corresponding sedimentation age of the sampled rock. All single grain age distributions fulfilled the requirement of the χ^2-test with values between 8 and 100 %.

4.2.6.3 Etch pit size and track length distribution

Etch pit size (D_{par}) and confined spontaneous fission-track lengths were measured in every sample from well Adrar Zougar-1. A total of 292 D_{par} values were determined for all apatite grains (Tab. 4.43). The mean D_{par} values for each sample reveal a very narrow range between 1.3 (±0.2) and 1.6 (±0.2) µm. All samples exhibit a positive skewness between 0.097 and 1.749. The largest etch pit size of 2.2 (±0.1) µm as well as the largest spread in etch pit size was measured in sample AZ-06. Between single grain ages and D_{par} values no positive correlation has been detected.

Confined spontaneous fission-track lengths were detected in only one sample. A total of 4 track lengths were measured (Tab. 4.43). The obtained mean track lengths of sample AZ-04 is 11.5 (±1.7) µm. After correcting of the confined track lengths for their crystallographic orientation, the mean confined fission-track lengths changed to 13.0 (±1.4) µm. The largest track length after c-axis correction is 14.3 (±0.1) µm.

4.2.6.4 Zircon (U-Th-Sm)/He ages

Three samples with three single grain aliquots each have been analysed by zircon (U-Th-Sm)/He dating, while three samples were not determined. Raw ZHe ages cover a range from 49.7 (±4.0) to 150.1 (±12.0) Ma (Tab. 4.44). α-ejection correction after Farley et al. (1996) was applied to all single grains resulting in ages between 59.2 (±4.7) and 207.8 (±16.6) Ma (Tab. 4.44). The single grains with the lowest eU concentration revealed ages of 202.1 (±16.2) Ma (AZ-01) and 131.6 (±10.5) Ma (AZ-04) (Fig. 4.54, Tab. 4.44). Sample AZ-06 yielded a ZHe age of 174.2 (±13.9) for the single grain (AZ-06.2) with the lowest effective Uranium concentration (Tab. 4.44). Since this single grain age is substantially older than sample AZ-04, single grain AZ-06.1 with a significantly younger age of 81.4 (±6.5) and similar eU content was used for further interpretation and discussion (Tab. 4.44). The ZHe ages decrease continuously with increasing depth (Fig. 4.54). All single grain ages are significantly younger than the corresponding sedimentation age of the sampled rock and older than the apatite fission-track age.

The age–eU concentration plot shows no clear positive or negative correlation in the samples

of the Adrar Zougar-1 well (Fig. 4.56). Whereas the three single grain ages of samples AZ-01 and AZ-04 are equal within the standard deviation, sample AZ-06 show no obvious correlation between eU content and ZHe age.

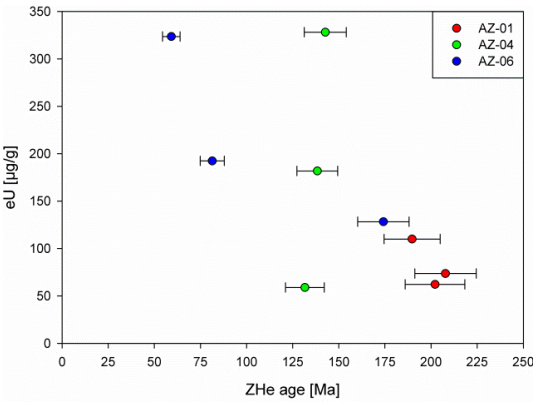

Fig. 4.56: ZHe single grain ages (1σ error) from Adrar Zougar-1 well plotted against eU.

In samples from the Adrar Zougar-1 well, no clear positive correlation between equivalent grain radius and ZHe age distribution was determined (Fig. 4.57).

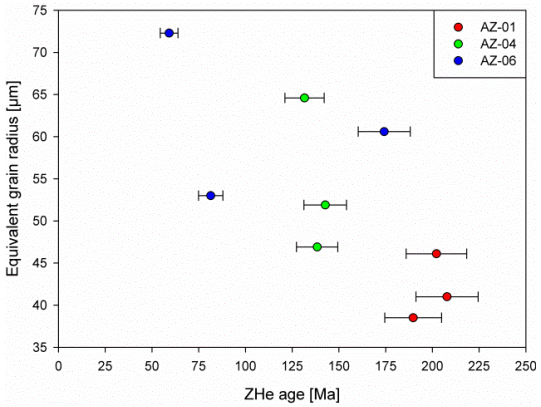

Fig. 4.57: ZHe single grain ages (1σ error) from Adrar Zougar-1 well plotted against equivalent grain radius.

4.2.6.5 Zircon fission-track ages

All samples were analysed by zircon fission-track dating. The ZFT central ages range between 366.1 (±28.6) Ma at a depth of 455–463 m and 257.8 (±17.6) Ma at a depth of 3315–3387 m (Fig. 4.54, Tab. 4.45). The ZFT ages decrease continuously with increasing depth (Fig. 4.54). All ages are significantly younger than the corresponding sedimentation age of the sampled rock. All single grain age distributions fulfilled the requirement of the χ^2-test with values between 94 and 100 %.

Table 4.41: Apatite (U-Th-Sm)/He data from well Adrar Zougar-1

Sample	Recent T [°C]	Mass [µg]	Radius [µm]	U [µg/g]	Th [µg/g]	Sm [µg/g]	eU [µg/g]	Th/U	^{4}He [nmol/g]	F_t	Raw age [Ma]	Error ± 1σ [Ma]	Corrected age [Ma]	Error ± 1σ [Ma]
AZ-01.1	**31**	**4.6**	**43.0**	**11**	**46**	**92**	**22**	**4.2**	**1.31**	**0.656**	**10.8**	**0.6**	**16.4**	**1.0**
AZ-01.2	31	3.4	39.0	18	47	76	29	2.6	2.60	0.628	16.3	1.0	25.9	1.6
AZ-01.3	31	5.5	45.5	19	48	87	30	2.5	4.58	0.679	27.2	1.6	40.0	2.4
AZ-01.4	31	4.5	42.5	16	47	85	27	3.1	2.83	0.654	18.0	1.1	27.4	1.6
AZ-02.1	48	3.2	48.0	10	10	30	13	1.0	0.66	0.705	9.3	0.6	13.2	0.8
AZ-02.2	48	3.0	38.2	23	25	42	29	1.1	0.91	0.627	5.8	0.3	9.3	0.6
AZ-02.3	**48**	**3.8**	**39.8**	**23**	**68**	**66**	**39**	**3.0**	**1.16**	**0.630**	**5.5**	**0.3**	**8.7**	**0.5**
AZ-02.4	48	3.3	42.0	19	34	46	27	1.7	0.91	0.654	6.8	0.4	10.4	0.6
AZ-03.1	71	3.5	46.0	11	16	68	14	1.5	0.00	0.688	-0.1	0.0	-0.1	0.0
AZ-03.2	**71**	**4.0**	**41.0**	**22**	**13**	**76**	**26**	**0.6**	**0.00**	**0.659**	**0.0**	**0.0**	**0.0**	**0.0**
AZ-03.3	71	2.7	35.7	17	16	106	21	0.9	0.37	0.612	3.1	0.2	5.1	0.3

eU = [U] + 0.235 [Th] + 0.0053 [Sm] (concentrations in weight %); F_t: α-ejection correction factor; raw ages are corrected after Farley et al. (1996); radius calculated according to Shuster et al. (2006) and Ketcham (2009). Data in bold: youngest apatite (U-Th-Sm)/He grain of each sample discussed in the text.

Table 4.42: Apatite fission-track data from well Adrar Zougar-1

Sample	Recent T [°C]	n	U (std) [µg/g]	Sp. Tracks ρ_s	Sp. Tracks N_s	Ind. Tracks ρ_i	Ind. Tracks N_i	$P(\chi^2)$ [%]	Central age [Ma]	Error ± 1σ [Ma]
AZ-01	31	4	14.1 (10.0)	8.774	176	18.645	374	96.9	114.9	12.2
AZ-02	48	1	23.7 (-)	20.422	46	30.632	69	-	163.0	32.3
AZ-03	71	20	17.7 (15.9)	4.403	223	20.296	1028	99.7	53.7	4.9
AZ-04	84	16	31.3 (14.7)	4.359	260	37.475	2235	10.5	29.5	2.9
AZ-05	96	24	30.9 (22.9)	1.281	118	35.497	3270	7.8	8.9	1.2
AZ-06	104	26	19.8 (22.0)	0.848	73	22.740	1958	31.7	9.5	1.4

U (std): Uranium concentration and standard deviation; n: number of counted apatite grains; ρ_s: density of spontaneous tracks (10^5 tr/cm^2); N_s: number of spontaneous tracks; ρ_i: density of induced tracks (10^5 tr/cm^2); N_i: number of induced tracks; $P(\chi^2)$: probability that single grains are consistent and belong to the same population. Test is passed if $P(\chi^2) > 5$ % (Galbraith, 1981). Nd = 16296 tracks counted on CN5 dosimeter glass. Central ages are calculated using a ζ-value of 333.36 ± 17.89. Samples were irradiated at the FRM II reactor facility in Garching, Germany with a fluence of 1 x 10^{16} neutrons/cm^2.

Table 4.43: Confined fission-track length data from well Adrar Zougar-1

Sample	n CT	CT mean [µm]	CT std [µm]	CT skew	CT min [µm]	CT max [µm]	L_c mean [µm]	L_c std [µm]	L_c skew	L_c min [µm]	L_c max [µm]	n D_{par}	D_{par} mean [µm]	D_{par} std [µm]	D_{par} skew	D_{par} min [µm]	D_{par} max [µm]
AZ-01	n.da.	-	-	-	-	-	-	-	-	-	-	18	1.6	0.2	0.097	1.2	2.0
AZ-02	n.da.	-	-	-	-	-	-	-	-	-	-	5	1.3	0.2	1.749	1.2	1.6
AZ-03	n.da.	-	-	-	-	-	-	-	-	-	-	76	1.5	0.2	0.369	1.2	1.5
AZ-04	4	11.5	1.7	0.000	9.6	13.3	13.0	1.4	-0.474	11.3	14.3	70	1.5	0.2	0.454	1.1	2.1
AZ-05	n.da.	-	-	-	-	-	-	-	-	-	-	60	1.3	0.2	1.307	1.0	2.0
AZ-06	n.da.	-	-	-	-	-	-	-	-	-	-	63	1.6	0.2	0.615	1.2	2.2

n: number of measured individual confined tracks (CT) and etch pit diameter (D_{par}); CT mean: mean confined track length; L_c mean: mean track length after c-axis correction; D_{par} mean: mean etch pit diameter; std: standard deviation; skew: skewness of distribution relative to the mean value; min: minimum single values; max: maximum single values; n.da.: no data.

Table 4.44: Zircon (U-Th-Sm)/He data from well Adrar Zougar-1

Sample	Mass [µg]	Radius [µm]	U [µg/g]	Th [µg/g]	Sm [µg/g]	eU [µg/g]	Th/U	^{4}He [nmol/g]	Ft	Raw age [Ma]	Error ± 1σ [Ma]	Corrected age [Ma]	Error ± 1σ [Ma]
AZ-01.1	**4.6**	**46.1**	**54**	**37**	**1**	**62**	**0.68**	**51.0**	**0.743**	**150.1**	**12.0**	**202.1**	**16.2**
AZ-01.2	2.9	41.0	56	77	<1	74	1.39	59.3	0.710	147.5	11.8	207.8	16.6
AZ-01.3	2.4	38.5	94	68	<1	110	0.72	79.2	0.696	132.1	10.6	189.7	15.2
AZ-04.1	4.4	46.9	161	87	1	182	0.54	102.7	0.750	103.8	8.3	138.3	11.1
AZ-04.2	**11.7**	**64.6**	**55**	**17**	**1**	**59**	**0.31**	**34.5**	**0.818**	**107.7**	**8.6**	**131.6**	**10.5**
AZ-04.3	6.0	51.9	321	31	1	328	0.10	198.3	0.778	111.0	8.9	142.7	11.4
AZ-06.1	**6.2**	**53.2**	**160**	**140**	**2**	**192**	**0.88**	**65.9**	**0.776**	**63.2**	**5.1**	**81.4**	**6.5**
AZ-06.2	11.3	60.6	119	39	1	128	0.33	98.3	0.806	140.4	11.2	174.2	13.9
AZ-06.3	19.4	72.3	313	45	1	324	0.14	87.0	0.839	49.7	4.0	59.2	4.7

eU = [U] + 0.235 [Th] + 0.0053 [Sm] (concentrations in weight %); F_t: α-ejection correction factor; raw ages are corrected after Farley et al. (1996); radius calculated according to Reiners et al. (2004) and Ketcham (2009). Data in bold are discussed in the text.

Table 4.45: Zircon fission-track data from well Adrar Zougar-1

Sample	Etch time at 200 °C [h]	n	U (std) [µg/g]	Sp. Tracks ρ_s	Sp. Tracks N_s	Ind. Tracks ρ_i	Ind. Tracks N_i	P(X^2) [%]	Central age [Ma]	Error ± 1σ [Ma]
AZ-01	8.0	20	151.3 (27.2)	252.779	2611	24.978	258	99.8	366.1	28.6
AZ-02	6.5	18	199.9 (52.0)	296.955	1394	31.101	146	100.0	345.8	33.6
AZ-03	7.0	20	128.5 (36.0)	182.171	2846	21.123	330	99.9	312.9	22.7
AZ-04	5.0	20	177.7 (40.9)	234.150	2083	28.777	256	98.7	295.5	23.4
AZ-05	6.0	20	223.3 (69.2)	248.969	2030	34.831	284	98.2	260.2	19.9
AZ-06	3.5	20	223.2 (51.3)	256.558	2890	36.220	408	93.8	257.8	17.6

Etch time in KOH:NaOH (7:5) eutectic melt at 200 ± 2 °C; U (std): Uranium concentration and standard deviation; n: number of counted apatite grains; ρ_s: density of spontaneous tracks (10^5 tr/cm^2); N_s: number of spontaneous tracks; ρ_i: density of induced tracks (10^5 tr/cm^2); N_i: number of induced tracks; P(χ^2): probability that single grains are consistent and belong to the same population. Test is passed if P(χ^2) > 5% (Galbraith, 1981). Nd = 11255 tracks counted on CN1 dosimeter glass. Central ages are calculated using a ζ-value of 140.83 ± 5.93. Samples were irradiated at the FRM II reactor facility in Garching, Germany with a fluence of 1 x 10^{15} neutrons/cm^2.

4.2.7 Oum Doul-1

4.2.7.1 Apatite fission-track ages

In the Oum Doul-1 well, three of five samples contained apatite grains for fission-track dating. The apatite fission-track central ages range from 177.1 (±14.5) Ma at a depth of 1066–1179 m to 25.2 (±2.6) Ma at a depth of 3098–3147 m (Fig. 4.58, Tab. 4.46). The AFT ages decrease continuously with increasing depth (Fig. 4.58). All ages are younger than the corresponding sedimentation age of the sampled rock. All single grain age distributions fulfilled the requirement of the χ^2-test indicating a homogeneous distribution with values between 39 and 100 %.

4.2.7.2 Etch pit size and track length distribution

Etch pit size (D_{par}) and confined spontaneous fission-track lengths were measured in three samples. A total of 293 D_{par} values were determined for all apatite grains (Tab. 4.47). The mean D_{par} values for each sample reveal a very narrow range between 1.3 (±0.1) and 1.7 (±0.3) µm. The largest etch pit size of 2.4 (±0.1) µm as well as the largest spread in etch pit size was measured in sample OD-02. No positive correlation between single grain ages and D_{par} values has been detected.

Confined spontaneous fission-track lengths were detected in only two samples (Tab. 4.47). A total of 77 track lengths were measured. Sample OD-02 show a mean track lengths of 11.3 (±1.8) and a minor skewness of 0.195 indicating a simple cooling history with no obvious reheating events. After correcting of the confined track lengths for their crystallographic orientation, the mean confined fission-track lengths of sample OD-02 changed to 13.2 (±1.1) µm with a skewness of 0.544. The largest track length after c-axis correction is 16.0 (±0.1) µm.

4.2.7.3 Zircon (U-Th-Sm)/He ages

Three samples with two or three single grain aliquots each have been analysed by zircon (U-Th-Sm)/He dating, while two samples were not determined. Raw ZHe ages cover a wide range from 63.0 (±5.0) to 278.3 (±22.3) Ma (Tab. 4.48). α-ejection correction after Farley et al. (1996) was applied to all single grains resulting in ages between 87.4 (±7.0) and 391.4 (±31.3) Ma (Tab. 4.48). The α-ejection

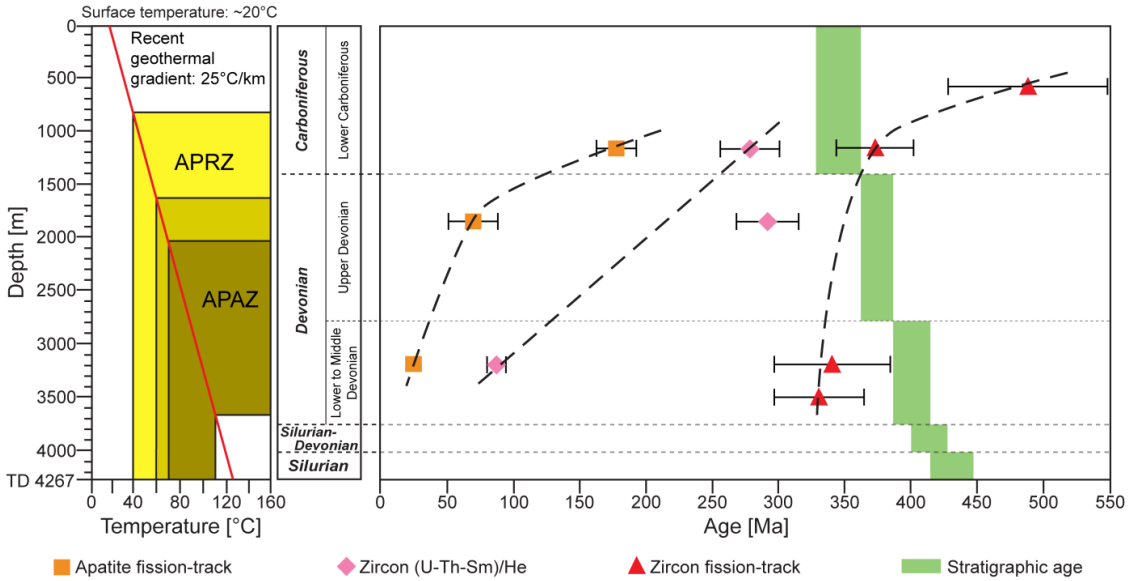

Fig. 4.58: Thermochronometric age (1σ error) – depth distribution of the Oum Doul-1 well. On the left side the recent temperature distribution as well as a schematic stratigraphic profile is displayed.

corrected ZHe ages with the lowest eU content revealed an age spectra from 276.5 (±22.1) Ma at a depth of 1066–1179 m to 90.7 (±7.3) Ma at a depth of 3098–3147 m (Fig. 4.58, Tab. 4.48). Sample OD-03 yielded a ZHe age of 391.4 (±31.3) for the single grain (OD-3.1) with the lowest effective Uranium concentration (Tab. 4.48). As this single grain age is substantially older than sample OD-02 and does not fit in the age distribution, single grain OD-3.3 with a significantly younger age of 289.7 (±23.2) and a similar eU content was used for further interpretation and discussion (Tab. 4.48). All single grain ages are significantly younger than the corresponding sedimentation age of the sampled rock as well as older than the apatite fission-track age.

The age–eU concentration plot shows no clear positive or negative correlation in samples of the Oum Doul-1 well (Fig. 4.59). Whereas the three single grain ages of sample OD-04 are equal within the standard deviation, samples OD-02 and OD-03 reveal no obvious correlation between eU content and ZHe age.

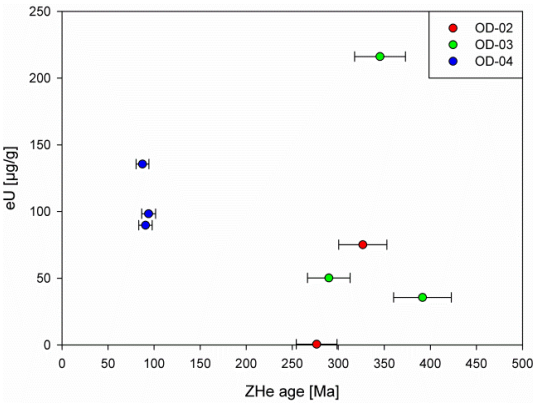

Fig. 4.59: ZHe single grain ages (1σ error) from Oum Doul-1 well plotted against eU.

In samples from the Oum Doul-1 well, no clear positive correlation between equivalent grain radius and ZHe age distribution was determined (Fig. 4.60).

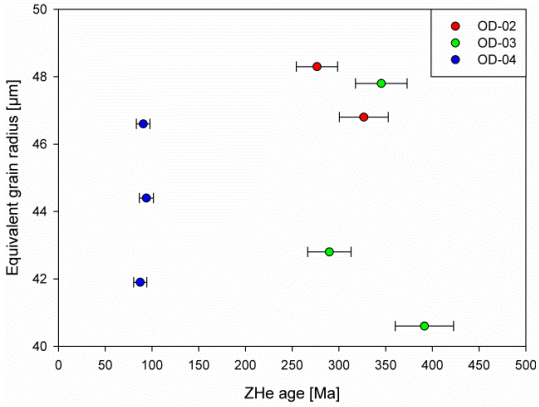

Fig. 4.60: ZHe single grain ages (1σ error) from Oum Doul-1 well plotted against equivalent grain radius.

4.2.7.4 Zircon fission-track ages

In the Oum Doul-1 well, four of five samples contained zircon grains for fission-track analysis. The zircon fission-track central ages range from 483.3 (±59.4) Ma at a depth of 531–567 m to 327.7 (±33.5) Ma at a depth of 3388–3463 m (Fig. 4.58, Tab. 4.49). The ZFT ages decrease continuously with increasing depth (Fig. 4.58). Whereas the Devonian samples reveal a younger ZFT age than their corresponding sedimentation age, the Lower Carboniferous samples show similar or older ages than their depositional age. All single grain age distributions fulfilled the requirement of the χ^2-test with values of 100 %.

Table 4.46: Apatite fission-track data from well Oum Doul-1

Sample	Recent T [°C]	n	U (std) [µg/g]	Sp. Tracks ρ_s	Sp. Tracks N_s	Ind. Tracks ρ_i	Ind. Tracks N_i	$P(\chi^2)$ [%]	Central age [Ma]	Error ± 1σ [Ma]
OD-02	48	20	16.4 (8.2)	12.780	451	18.390	649	99.5	177.1	14.5
OD-03	65	5	9.3 (4.9)	3.360	19	12.203	69	99.5	69.9	18.5
OD-04	98	11	45.1 (24.4)	6.139	146	62.732	1492	38.8	25.2	2.6

U (std): Uranium concentration and standard deviation; n: number of counted apatite grains; ρ_s: density of spontaneous tracks (10^5 tr/cm^2); N_s: number of spontaneous tracks; ρ_i: density of induced tracks (10^5 tr/cm^2); N_i: number of induced tracks; $P(\chi^2)$: probability that single grains are consistent and belong to the same population. Test is passed if $P(\chi^2) > 5$ % (Galbraith, 1981). Nd = 15419 tracks counted on CN5 dosimeter glass. Central ages are calculated using a ζ-value of 333.36 ± 17.89. Samples were irradiated at the FRM II reactor facility in Garching, Germany with a fluence of 1 x 10^{16} neutrons/cm^2.

Table 4.47: Confined fission-track length data from well Oum Doul-1

Sample	n CT	CT mean [µm]	CT std [µm]	CT skew	CT min [µm]	CT max [µm]	L_c mean [µm]	L_c std [µm]	L_c skew	L_c min [µm]	L_c max [µm]	n D_{par}	D_{par} mean [µm]	D_{par} std [µm]	D_{par} skew	D_{par} min [µm]	D_{par} max [µm]
OD-02	76	11.3	1.8	0.195	7.6	15.4	13.2	1.1	0.544	11.2	16.0	224	1.7	0.3	0.415	1.1	2.4
OD-03	1	11.0	-	-	11.0	11.0	13.3	-	-	13.3	13.3	21	1.3	0.1	-0.953	1.0	1.4
OD-04	n.da.		-	-	-	-		-	-	-	-	48	1.5	0.3	0.551	0.9	2.2

n: number of measured individual confined tracks (CT) and etch pit diameter (D_{par}); CT mean: mean confined track length; L_c mean: mean track length after c-axis correction; D_{par} mean: mean etch pit diameter; std: standard deviation; skew: skewness of distribution relative to the mean value; min: minimum single values; max: maximum single values; n.da.: no data.

Table 4.48: Zircon (U-Th-Sm)/He data from well Oum Doul-1

Sample	Mass [µg]	Radius [µm]	U [µg/g]	Th [µg/g]	Sm [µg/g]	eU [µg/g]	Th/U	^{4}He [nmol/g]	Ft	Raw age [Ma]	Error ± 1σ [Ma]	Corrected age [Ma]	Error ± 1σ [Ma]
OD-02.1	4.3	46.8	70	23	<1	75	0.33	102.1	0.755	246.5	19.7	326.6	26.1
OD-02.3	**5.0**	**48.3**	**<1**	**<1**	**0**	**1**	**0.70**	**0.6**	**0.754**	**208.5**	**16.7**	**276.5**	**22.1**
OD-03.1	2.6	40.6	33	13	0	36	0.39	54.8	0.711	278.3	22.3	391.4	31.3
OD-03.2	5.3	47.8	198	79	1	216	0.40	313.0	0.759	262.2	21.0	345.3	27.6
OD-03.3	**3.4**	**42.8**	**42**	**35**	**<1**	**50**	**0.83**	**57.7**	**0.722**	**209.3**	**16.7**	**289.7**	**23.2**
OD-04.1	**4.5**	**46.6**	**70**	**84**	**2**	**90**	**1.20**	**32.8**	**0.742**	**67.3**	**5.4**	**90.7**	**7.3**
OD-04.2	2.8	41.9	122	59	1	136	0.49	46.3	0.721	63.0	5.0	87.4	7.0
OD-04.3	3.7	44.4	92	25	<1	98	0.27	37.0	0.738	69.5	5.6	94.1	7.5

eU = [U] + 0.235 [Th] + 0.0053 [Sm] (concentrations in weight %); F_t: α-ejection correction factor; raw ages are corrected after Farley et al. (1996); radius calculated according to Reiners et al. (2004) and Ketcham (2009). Data in bold are discussed in the text.

Table 4.49: Zircon fission-track data from well Oum Doul-1

Sample	Etch time at 200 °C [h]	n	U (std) [µg/g]	Sp. Tracks ρ_s	Sp. Tracks N_s	Ind. Tracks ρ_i	Ind. Tracks N_i	$P(\chi^2)$ [%]	Central age [Ma]	Error ± 1σ [Ma]
OD-01	7.0	14	130.7 (35.3)	263.580	1095	19.498	81	100.0	483.3	59.4
OD-02	7.0	20	164.8 (46.1)	268.574	2674	26.215	261	100.0	369.4	28.8
OD-04	7.0	14	201.5 (74.6)	273.692	710	29.297	76	100.0	337.5	43.3
OD-05	7.0	16	215.0 (75.3)	287.749	1170	31.726	129	100.0	327.7	33.5

Etch time in KOH:NaOH (7:5) eutectic melt at 200 ± 2 °C; U (std): Uranium concentration and standard deviation; n: number of counted apatite grains; ρ_s: density of spontaneous tracks (10^5 tr/cm^2); N_s: number of spontaneous tracks; ρ_i: density of induced tracks (10^5 tr/cm^2); N_i: number of induced tracks; $P(\chi^2)$: probability that single grains are consistent and belong to the same population. Test is passed if $P(\chi^2) > 5$% (Galbraith, 1981). Nd = 11255 tracks counted on CN1 dosimeter glass. Central ages are calculated using a ζ-value of 140.83 ± 5.93. Samples were irradiated at the FRM II reactor facility in Garching, Germany with a fluence of 1 x 10^{15} neutrons/cm^2.

4.2.8 Time-temperature modelling

4.2.8.1 Outcrop samples

10 Precambrian outcrop samples from the western Anti-Atlas (MA-01, MA-02, MA-12, MA-14, MA-15, MA-17, MA-20, MA-21, MA-29 and MA-30) with more than 46 measured confined fission-track lengths were used to test geological constraints against the thermo-chronological data set (Fig. 4.61, Fig. 4.62 and Fig. 4.63). Whenever possible the AFT data set were combined with apatite and zircon (U-Th-Sm)/He data. An AFT+AHe+ZHe based time-temperature (t-T) modelling with 'HeFTy' was performed in the five samples MA-12, MA-14, MA-20, MA-29 and MA-30, whereas the modelling of sample MA-15 is based on the AFT+AHe data set. In two samples (MA-17, MA-21) an AFT+AHe+ZHe based t-T modelling yielded no good and acceptable fit results, due to the AHe age. Therefore only AFT+ZHe data were used to model the individual thermal history of samples MA-17 and MA-21. In all numerical models, we used the youngest AHe age and the ZHe age with the lowest effective U concentration (eU) of the three single grain aliquots of each sample (see Table 4.20). To improve the thermal modelling, ZFT ages were implemented as external t-T constraint. Frizon de Lamotte et al. (2009), Ruiz et al. (2011) and Zouhri et al. (2008) suggested that the Anti-Atlas was covered by Cretaceous deposits. Based on this assumption, the models were forced to move towards the surface in the Lower Cretaceous and subsequently to bury during the Cretaceous–Eocene (Fig. 4.61, Fig. 4.62 and Fig. 4.63). Therefore, two external geological constraints were implemented. The uncertainty is presented in the diagrams in green and brown colour depending on the reliability level (see Fig. 4.61).

All samples have been tested by 50000 inverse models against the data set. The obtained t-T models of six samples (MA-01, MA-02, MA-14, MA-17, MA-21 and MA-29) indicate a goodness of fit (G.O.F.) greater than 79 % for the AFT age and the confined FT length distribution. In four samples (MA-12, MA-15, MA-20 and MA-30) the length distribution and/or the AFT age could not be reproduced better than 28 %. Whereas in seven samples the models reveal a G.O.F. greater than 95 % for the AHe and ZHe age, in sample MA-20 the modelled AHe age matches the measured one with 72 % confidence. All t-T models have at least 14 good and 2039 acceptable t-T paths. The majority (eight samples) reveals more than 440 good and 3500 acceptable t-T paths, while sample MA-02 shows the largest number with 3677 good and 11924 acceptable t-T paths.

The numerical modelling of 10 samples yielded a well-defined thermal history with numerous possible t-T paths (Fig. 4.61, Fig. 4.62 and Fig. 4.63). They have been grouped according to locality in the study area. The thermal models show that all 10 samples underwent continuous cooling until the Lower Cretaceous, followed by reheating during Upper Cretaceous and a cooling phase in Cenozoic times. They show an overall similar pattern with a three- or four-phase thermal history. Four of seven ZHe based samples (MA-12, MA-17, MA-29 and MA-30) reveal a slow initial cooling between 310 and 230–210 Ma, followed by rapid cooling event during Triassic, Jurassic and Lower Cretaceous until ~120 Ma. In contrast samples MA-01, MA-02, MA-14, MA-15, MA-20 and MA-21 show an incipient continuous fast cooling from 310 to ~125 Ma. During this time span every sample cooled down from 240 °C to ~20–40 °C. The samples entered into the apatite partial annealing zone (PAZ) between 240 and 190 Ma. After the exhumation towards the surface, the samples underwent a reheating up to 55–75 °C. In the majority of the models, the subsidence occurred during the Upper Cretaceous until

95–70 Ma. Since then, a cooling event can be observed throughout the final part of the thermal history.

Four Precambrian outcrop samples from the western Anti-Atlas (MA-03, MA-06, MA-09 and MA-13) with solely AHe data were used to test geological constraints against the thermo-chronological data set (Fig. 4.64). In all numerical models, we used the youngest AHe age of the two or three single grain aliquots of each sample (see Tab. 4.20). To improve the thermal modelling, ZFT and AFT ages and two geological constraints as described above were implemented as external t-T constraint. All samples have been tested by 30000 inverse models against the data set. The obtained t-T models of every sample indicate a G.O.F. of 100 % for the AHe age. All t-T models have at least 2776 good and 5108 acceptable t-T paths, while sample MA-13 shows the largest number with 3847 good and 7157 acceptable t-T paths.

The numerical modelling of the four samples yielded similar to the AFT+AHe+ZHe based models a well-defined thermal history with numerous possible t-T paths. They have been grouped according to locality in the study area

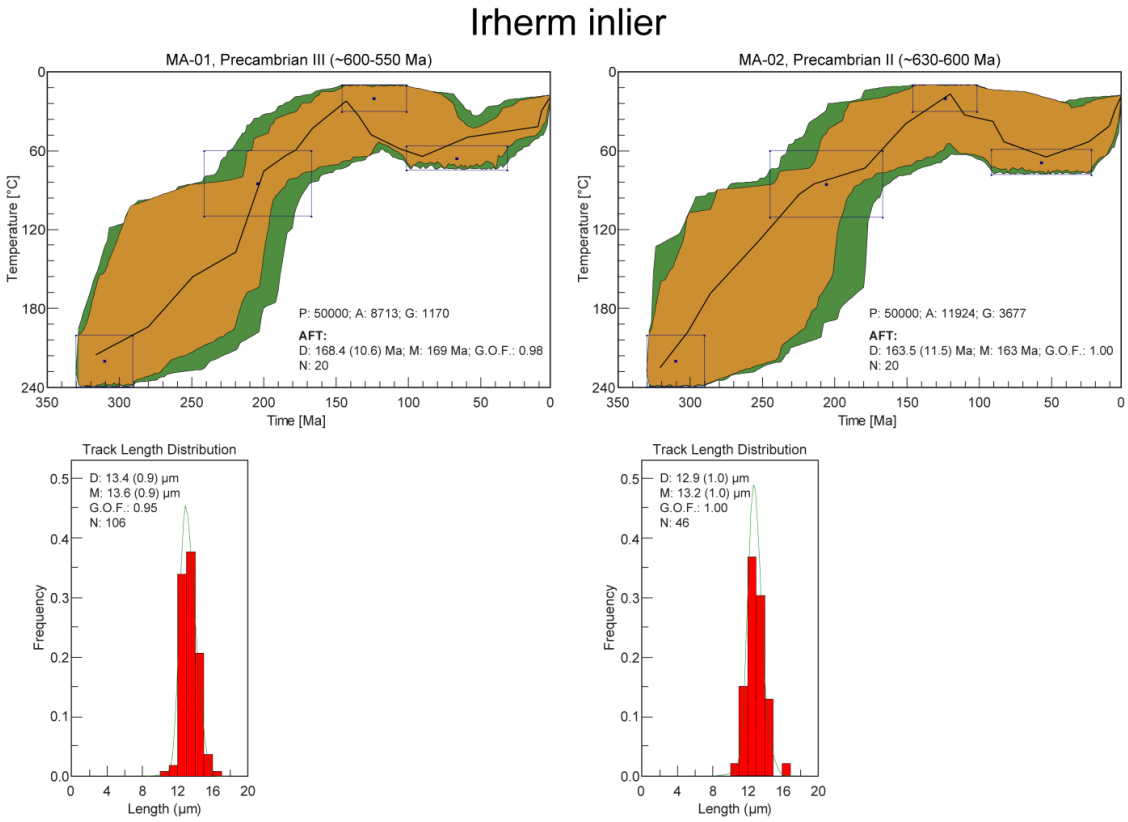

Fig. 4.61: Results from numerical modelling of outcrop samples from the western Anti-Atlas ('HeFTy', Ketcham, 2005; Ketcham, 2011; Ketcham et al., 2007a, b; Ketcham et al., 2009). Displayed are the t-T paths (left), the c-axis corrected confined fission-track length (L_c) frequency distribution overlain by a calculated probability density function (best fit) and the modelled helium diffusional profiles. The modelling tests possible t-T curves that fit independent geological constraints (squares) against the thermochronological data set. The results in the t-T curve show three different reliability levels (green: acceptable fit = all t-T paths with a goodness of fit (G.O.F.) of 0.05 (5 %); brown: good fit = all t-T paths with a G.O.F. of > 0.5 (50 %); black line: best fit). P: number of total tested inverse models; A: acceptable fit models; G: good fit models; D: determined AHe, AFT and ZHe age (1σ error), mean L_c and He content; M: modelled AHe, AFT and ZHe age, mean L_c and He content; G.O.F.: goodness of fit of best fit model; N: number of single grains and measured confined fission-track lengths.

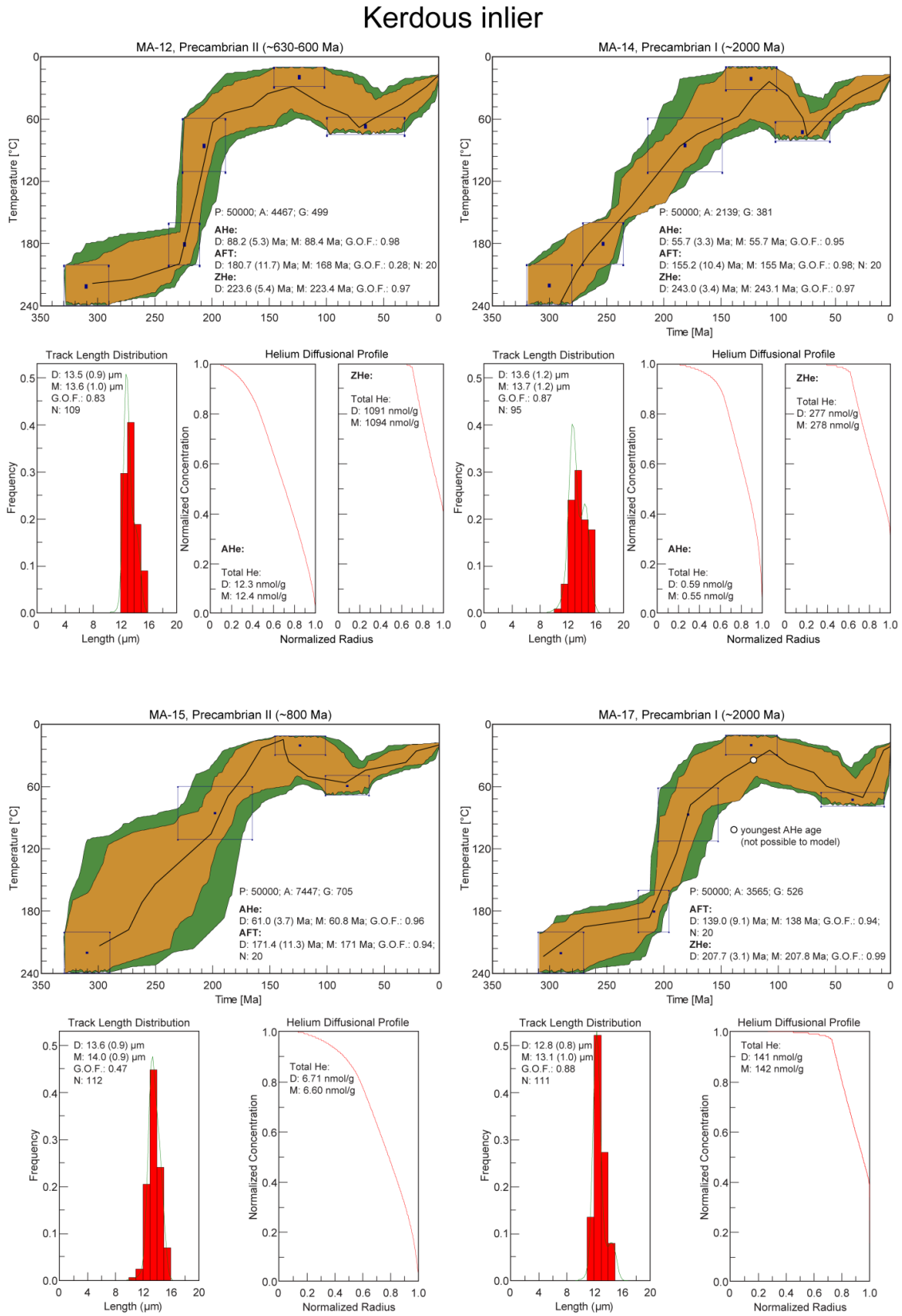

Fig. 4.62: Results from numerical modelling of outcrop samples from the western Anti-Atlas (for further explanation see Fig. 4.61).

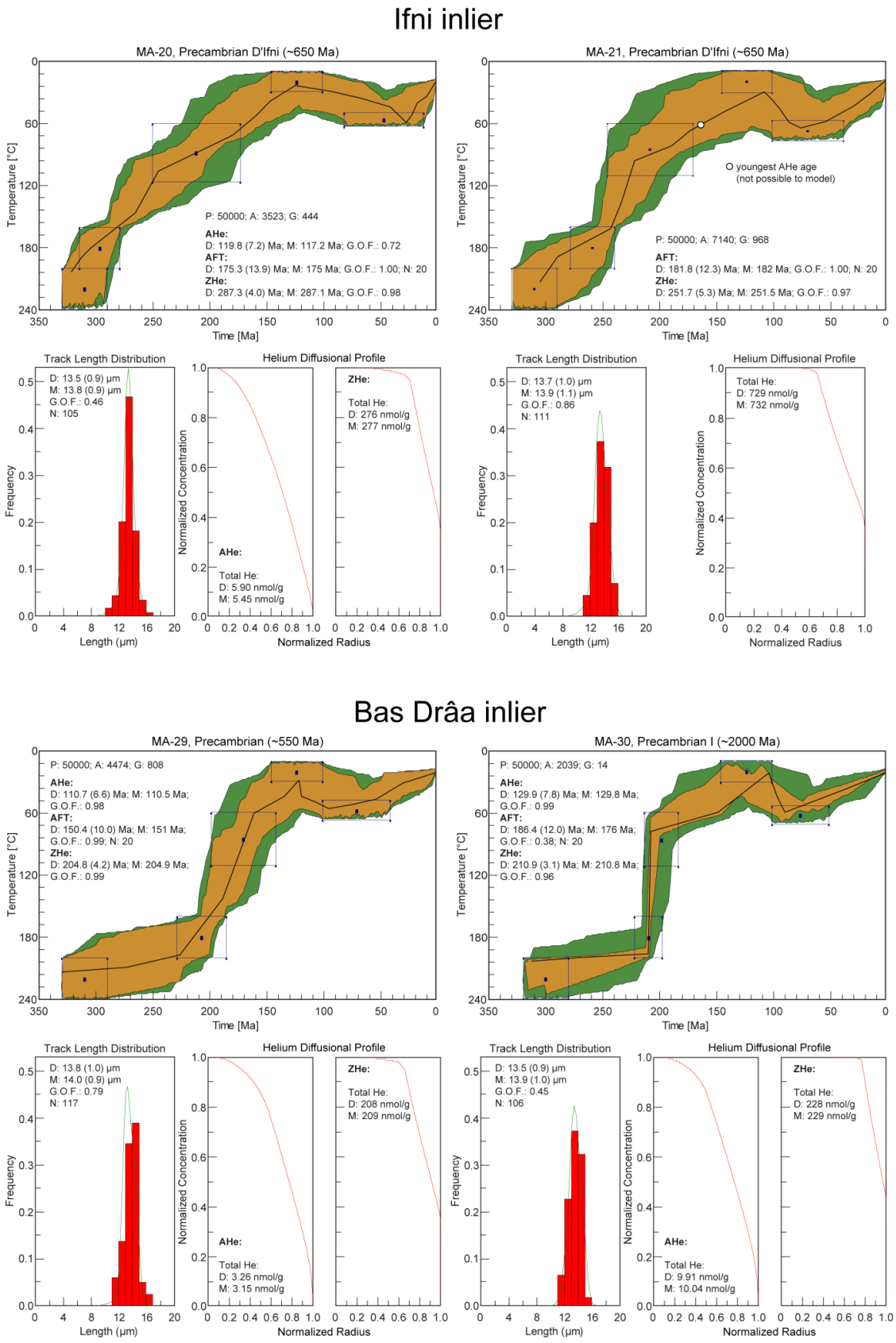

Fig. 4.63: Results from numerical modelling of outcrop samples from the western Anti-Atlas (for further explanation see Fig. 4.61).

(Fig. 4.64). The thermal models show that all samples underwent continuous cooling until the Lower Cretaceous, followed by reheating during Upper Cretaceous and a cooling phase in Cenozoic times. They show an overall similar pattern with a three-phase thermal history. Based on the lack of ZHe ages and confined fission-track length distributions, the t-T models are less constrained in large temperature ranges and so they are only significant to a limited extent. Every sample reveals an initial continuous cooling until the Lower Cretaceous. During this time span, every sample cooled down from 240 °C to ~20–40 °C. After the exhumation towards the surface, the samples underwent a reheating up to 50–70 °C. In

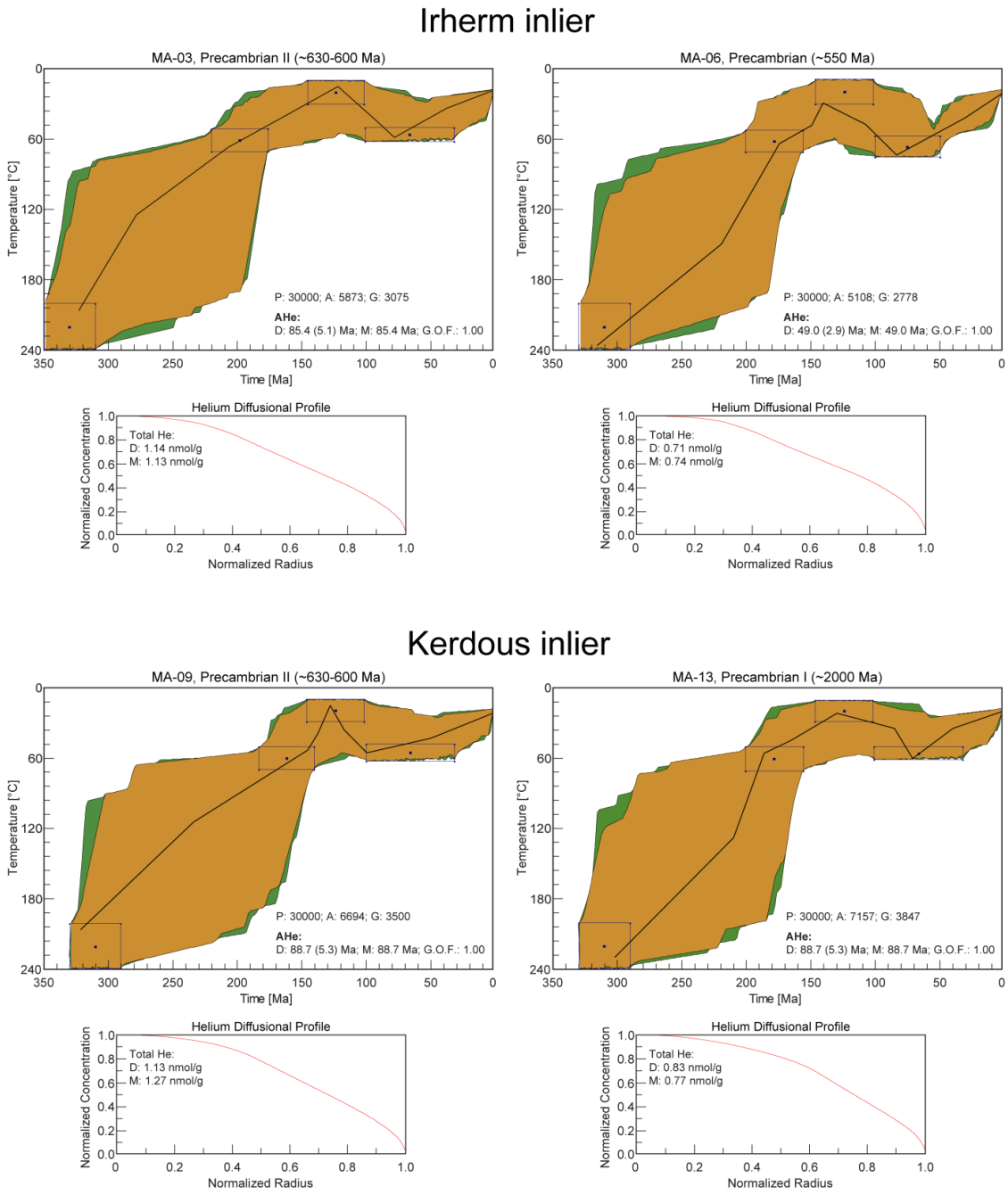

Fig. 4.64: Results from numerical modelling of outcrop samples from the western Anti-Atlas (for further explanation see Fig. 4.61).

the majority of the models, the subsidence occurred during the Upper Cretaceous until 80–70 Ma. Since then a cooling event through the final part of the thermal history was observed.

4.2.8.2 Adrar Zougar-1/Oum Doul-1

Three samples from the Oum Doul-1 well (OD-02, OD-03 and OD-04) with more than 76 measured confined fission-track lengths or ZHe data were used to test geological constraints against the thermochronological data set (Fig. 4.65). To improve the thermal modelling, depositional ages and ZFT ages were implemented as external t-T constraints.

All samples have been tested by 30000 inverse models against the data set. The obtained t-T models of two samples (OD-03, OD-04) indicate a G.O.F. of 100 % for the ZHe age. Sample OD-02 reveals a G.O.F. greater than 98 % for the AFT and ZHe age, whereas the confined FT length distribution could not be reproduced better than 74 %. The AFT+ZHe based model of sample OD-02 has 942 good and 4790 acceptable t-T paths, while samples OD-03 and OD-04 show a significant larger number of good and acceptable results.

The thermal models indicate that all samples underwent a continuous heating after the deposition and subsequently, after the maximum subsidence, a cooling to recent temperature (Fig. 4.65). They show an overall similar pattern with a three-phase thermal history. The samples (OD-02, OD-03 and OD-04) reveal a rapid initial heating after the deposition in the Devonian and Carboniferous. In samples OD-02 and OD-03, the maximum heating in the Upper Carboniferous–Lower Permian is followed by a fast cooling during Permian and Triassic until ~210 Ma. During this time span sample OD-02 cooled down from 180 °C to ~65 °C and entered into the APAZ at 240 Ma. Subsequently, a slow cooling phase to recent temperature occurred and lasted until present time.

Three samples from the Adrar Zougar-1 well (AZ-01, AZ-04 and AZ-06) with AHe and ZHe data were used to test geological constraints against the thermochronometric data set (Fig. 4.65). To improve the thermal modelling, depositional ages and ZFT ages were implemented as external t- T constraints.

All samples have been tested by 30000 inverse models against the data set. The obtained t-T models of every sample indicate a G.O.F. greater than 99 % for the AHe and ZHe age. The AHe+ZHe based model of sample AZ-01 has 792 good and 2803 acceptable t-T paths, while sample AZ-04 shows the largest number with 3975 good and 7353 acceptable t-T paths.

The thermal models indicate that all samples underwent a continuous heating after the deposition and subsequently, after the maximum subsidence, a cooling to recent temperature (Fig. 4.65). They show an overall similar pattern with a two- or three-phase thermal history. The samples (AZ-01, AZ-04 and AZ-06) reveal a fast initial heating after the deposition in the Precambrian–Ordovician. In samples AZ-01 and AZ-04 the maximum heating in the Carboniferous–Permian is followed by a relatively continuous cooling to recent temperature between Lower Permian and present.

Due to the lack of apatite confined fission-track length distributions, t-T path modelling is imprecise in comparison to thermal models of the Precambrian outcrop samples and therefore, has been performed without a subsidence event in the Upper Cretaceous.

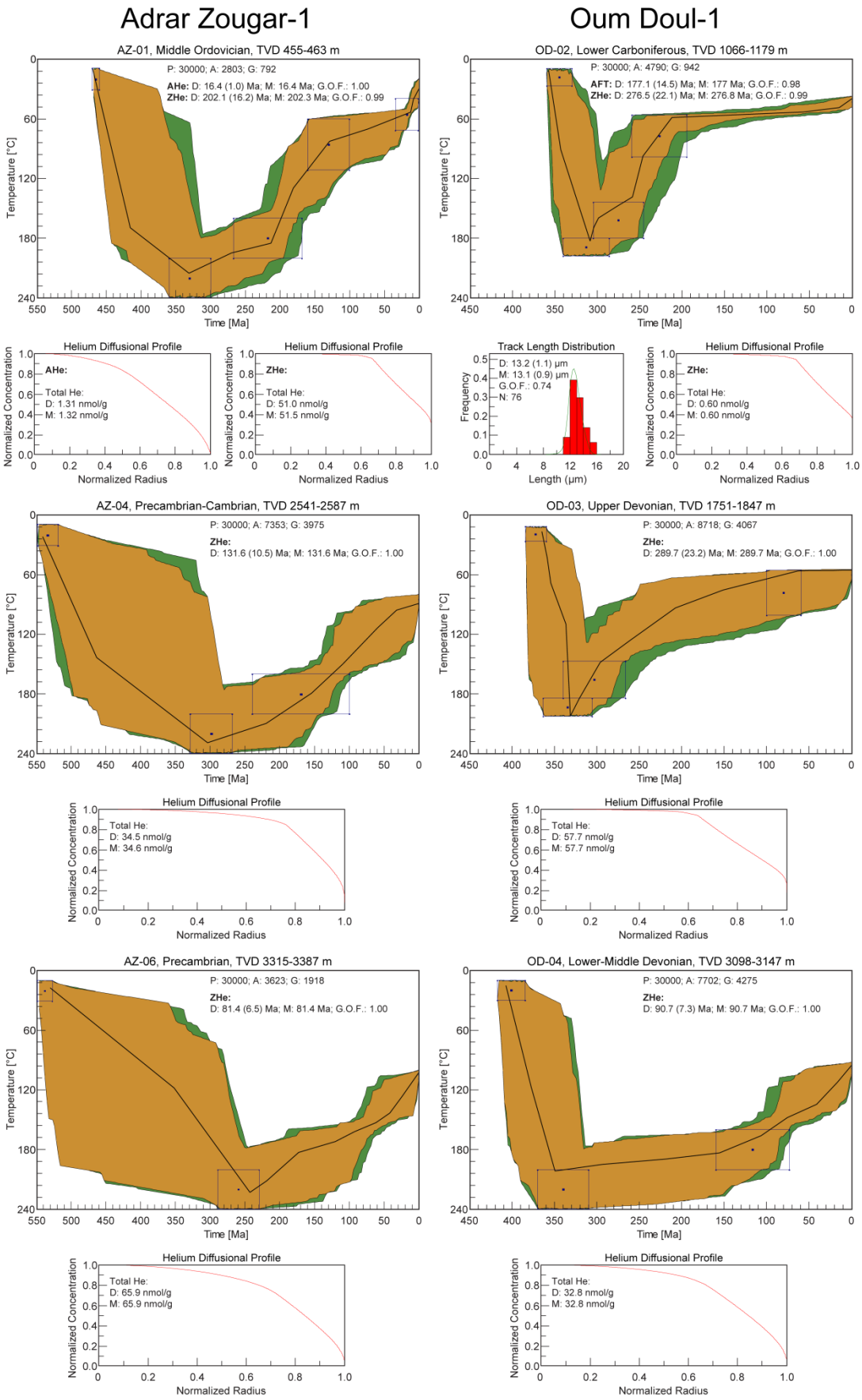

Fig. 4.65: Results from numerical modelling of wells Adrar Zougar-1 and Oum Doul-1 from the Anti-Atlas (for further explanation see Fig. 4.61).

5

DISCUSSION

Contents

5.1 Thermal, subsidence and exhumation history of the Tarfaya Basin

The main objective of the present study was the determination of the time-temperature (t-T) development of the Tarfaya Basin, especially of the pre-Palaeogene sediments for a better understanding of the hydrocarbon generation in time and space.

5.1.1 Geothermal gradient

In sedimentary basins three temperature ranges can be distinguished for thermochronological methods (Fig. 5.1). The range covering the lowest temperatures, i.e. the uppermost section in the borehole, does not record any depositional history but shows the thermal history of the source areas of the sediments, if no burial with a later exhumation occurred (Armstrong, 2005; Naeser, 1979) (Fig. 5.1). The second area, i.e. the middle section in the borehole, is the range which can reveal the thermal evolution of the sedimentary basin, whereas the lowest section in the borehole has lost all its previous information (Fig. 5.1). The exact depths of these zones in a well depend primarily on the geothermal gradient.

A geothermal gradient has been determined by thermochronological and literature data due to the lack of measured bottom hole temperatures in the different wells of the Tarfaya Basin.

The southern Atlantic margin is, beside the Rif mountains and the Middle Atlas, the region with the highest crustal temperatures in Morocco (Rimi, 1999). The geothermal gradient along the entire Atlantic margin vary between 23–34 °C/km, whereas the gradient is slightly lower ranging between 20–30 °C/km in the Tarfaya-Laâyoune-Dakhla Basin (Rimi, 1990; Zarhloule et al., 2005). The appreciable increase of the gradient offshore towards the

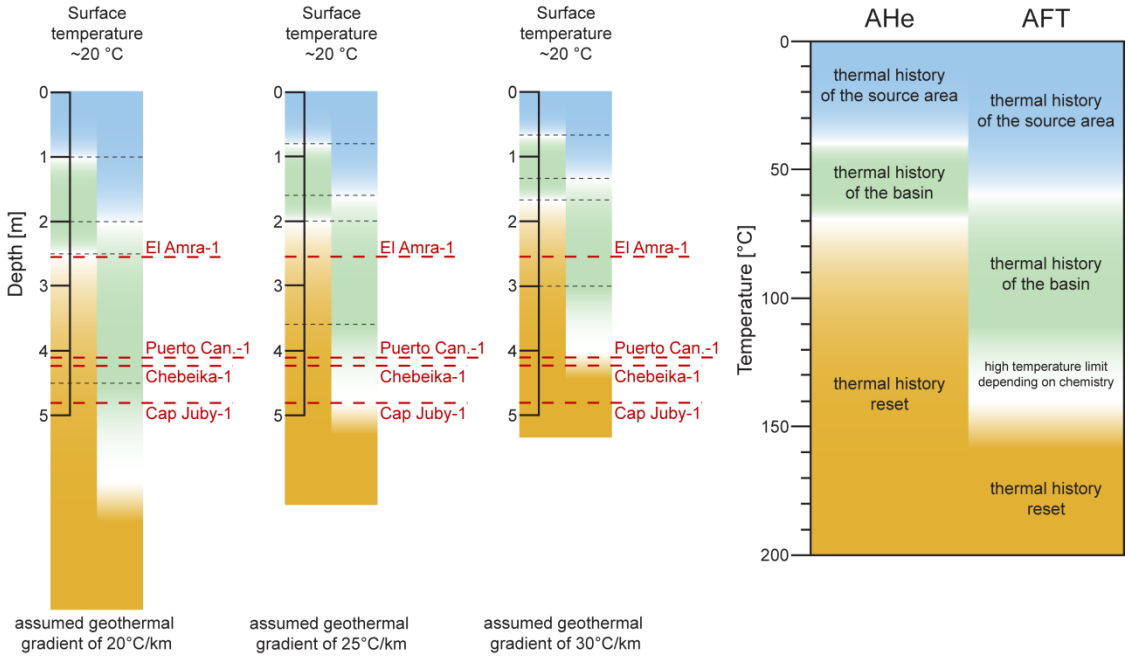

Fig. 5.1: Schematic overview of the relevant temperature ranges for the applied thermochronological methods AHe and AFT on wells of the Tarfaya Basin. The left side represents the TVD with corresponding temperatures expected in wells assuming different geothermal gradients. On the right side the meaning of the temperature ranges relevant for each dating technique is displayed. Red dashed lines refer to TVD of wells El Amra-1, Puerto Cansado-1, Chebeika-1 and Cap Juby-1. Black dashed lines refer to closure temperatures of the thermochronological methods AHe and AFT as well as the upper boundary of the APAZ and APRZ.

Canary Islands can be explained by the intensive hot spot volcanism (Rimi, 2001; Zarhloule et al., 2005). Since AFT ages are completely reset in a depth of 4.2 km in well Chebeika-1 and AHe data are nearly completely reset in a depth of 2.2 km in wells Chebeika-1 and Puerto Cansado-1, thermochronological data indicate a current geothermal gradient of approximately 25 °C/km in the onshore basin. The completely reset AHe ages in a depth of 1.6–1.8 km in well Cap Juby-1 suggest a higher geothermal gradient of 30 °C/km in the offshore Tarfaya Basin. Consequently, a geothermal gradient of 25 °C/km in the onshore and 30 °C/km in the offshore basin and a surface temperature of 20 °C have been used for calculation of exhumation and subsidence rates as well as overburden thickness in the Tarfaya Basin.

5.1.2 Thermochronological data

5.1.2.1 Chebeika-1/El Amra-1/Puerto Cansado-1

In total, 25 Triassic to Aptian and two Precambrian samples from the three onshore wells Chebeika-1, El Amra-1 and Puerto Cansado-1 of the Tarfaya Basin have been analysed by low-temperature thermochronology.

Thermochronological data and t-T modelling indicate a similar subsidence and exhumation history of the three wells. The wells El Amra-1 and Chebeika-1 are situated close together, whereas well Puerto Cansado-1 is located approximately 70 km west of El Amra-1 and Chebeika-1 (Fig. 4.14). A comparative display of the thermochronological data shows the similar ages and trend in the age distribution (Fig. 5.2). AHe ages are substantially younger than the corresponding sedimentation age varying between 34 (±2) and 0 (±0) Ma. AFT data of Precambrian to Jurassic samples are also younger than the respective deposition age ranging from 120 (±11) to 0 (±0) Ma. In contrast, Lower Cretaceous samples reveal similar or slightly older AFT ages varying between 147 (±11) and 111 (±12) Ma. The three wells show a typical age distribution of a sedimentary basin without obvious rock uplift after maximum subsidence. In a well with currently maximum temperatures at any depth, the shallowest/coolest samples should have relatively old AFT ages, due to detrital ages that are at least as old as the depositional age (Armstrong, 2005; Naeser, 1979) (Fig. 3.9a). The considerable scatter in the AFT ages in the shallow section (Lower Cretaceous) is based on the variation in source areas with diverse exhumation histories (Fig. 5.2). AFT ages can either decrease or increase down the section in the upper part of the well (Fig. 3.9a). Furthermore, in an uplifted well the accumulation of fission-tracks generates a fossil PAZ and fossil total annealing zone, which is non-existent in the three onshore wells (Armstrong, 2005; Fitzgerald and Gleadow, 1990; Naeser, 1979) (Fig. 3.9b).

However, the obvious difference in AFT ages of well (111–147 Ma) and outcrop (171–199 Ma) samples points to a low thermal imprint of the Tarfaya Basin on the Lower Cretaceous well samples. A heating to more than 60 °C yields a nowadays eroded overburden of at least 1 km of Cretaceous–Cenozoic sedimentary rocks on top of the Lower Cretaceous succession and a minor exhumation during Cenozoic times. Sachse et al. (2011) suggested a maximum burial of about 2 km for the Cretaceous sediments according to vitrinite reflectance data and the geological setting. The peak Atlasian deformation and surface uplift strongly affected the northeastern Tarfaya Basin in the Maastrichtian to Lower Oligocene resulting in the erosion of the Meso- to Cenozoic succession down to the Lower Cretaceous (Choubert et al., 1966; Ranke et al., 1982; Wenke et al., 2011, 2013).

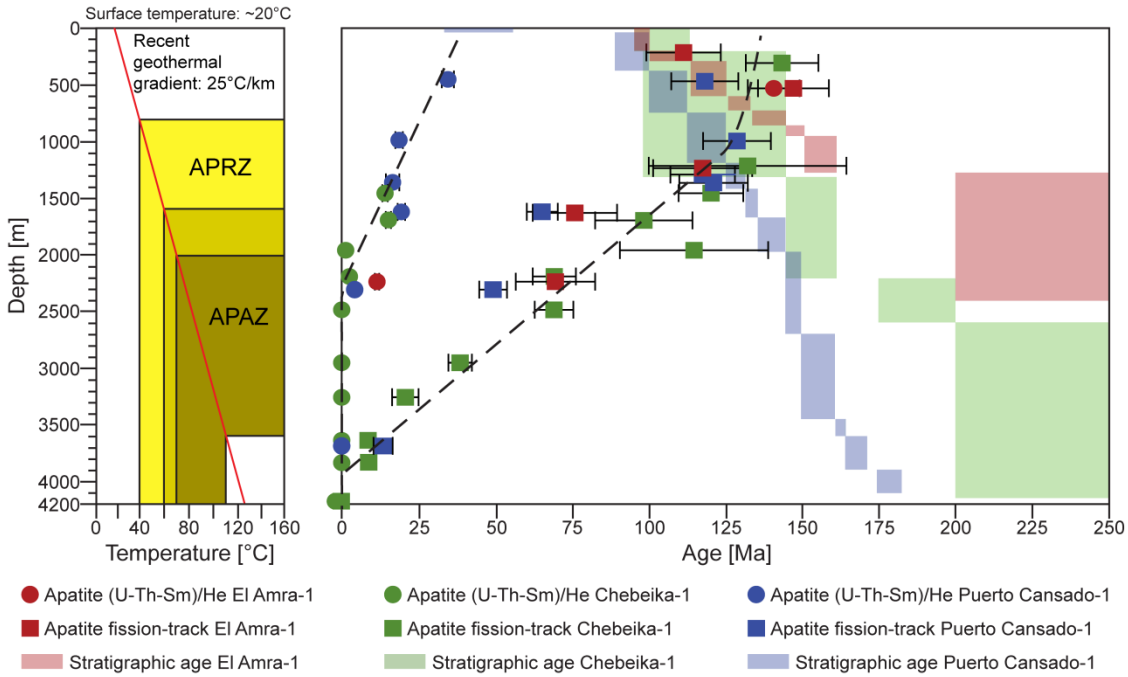

Fig. 5.2: Thermochronometric age (1σ error) – depth distribution of the Chebeika-1, El Amra-1 and Puerto Cansado-1 well. On the left side the recent temperature distribution is displayed.

5.1.2.2 Cap Juby-1

In total, four Valanginian to Upper Miocene samples from the offshore well Cap Juby-1 of the Tarfaya Basin have been analysed by low-temperature thermochronology.

The offshore well Cap Juby-1 differs from the onshore wells including a 1.5 km thick Paleogene to Neogene sedimentary cover. AHe ages are substantially younger than the corresponding sedimentation age ranging between 9 (±1) and 1 (±0) Ma. AFT data of the Miocene samples are older than the respective deposition age varying from 93 (±12) to 67 (±13) Ma. The Lower Cretaceous sample reveals an older AFT age of 111 (±41) Ma. The nearly continuous sedimentary succession from Triassic to Pleistocene and the negative trend in the apatite fission-track data point to a basin without rock uplift and an ongoing subsidence phase (Fig. 4.13). As described above, in a well with currently maximum temperatures at any depth, the shallowest/coolest samples should have relatively old AFT ages, due to detrital ages that are at least as old as the depositional age (Armstrong, 2005; Naeser, 1979) (Fig. 4.13). Besides, a Miocene sample shows a considerable scatter in the detrital AFT single grain age distribution which is based on the variation in source areas with different exhumation histories (Fig. 4.22). Contrary to the northeastern onshore Tarfaya Basin, an ongoing subsidence episode of the offshore basin is attested to by an increasing periodic sediment flux of detrital material from Upper Cretaceous onward (Hafid et al., 2008; Wenke et al., 2011, 2013).

5.1.2.3 Outcrop samples

In total, 28 Cretaceous to Cenozoic and two Lower Ordovician samples of the Tarfaya Basin have been analysed by low-temperature thermochronology.

Thermochronological data are indicative of a similar subsidence and exhumation history of the Lower Cretaceous from the northeastern onshore Tarfaya Basin. Apatite (U-Th-Sm)/He ages of 64 (±4) and 73 (±4) Ma are younger than the corresponding sedimentation age indicating a subsidence and heating to approximately 70 °C until the Cretaceous/

Palaeogene boundary. Apatite fission-track central ages varying between 171 (±15) and 199 (±18) Ma are slightly older than the deposition age. The increasing AFT ages from Lower to Upper Cretaceous suggest a partially reset of the Lower Cretaceous AFT data confirming a heating to about 70 °C in the Tarfaya Basin (Fig. 5.3).

The AHe and AFT data set point to a basin inversion and rock uplift phase due to the Atlasian deformation after maximum subsidence. On the basis of the postulated geothermal gradient, a less than 2 km thick sedimentary pile on top of the Lower Cretaceous succession seems realistic. As aforementioned, Sachse et al. (2011) supposed a maximum burial of about 2 km for the Cretaceous sediments according to vitrinite reflectance data and the geological setting.

Except for an anomalously young and unreproducible age of 48 (±1) Ma due to an U concentration of ~1000 ppm, zircon (U-Th-Sm)/He ages ranging from 185 (±3) to 1195 (±17) Ma and zircon fission-track central ages varying between 503 (±48) and 585 (±58) Ma are significantly older than the respective deposition age. Both thermochronometers reveal no thermal imprint of the Tarfaya Basin representing solely the thermal history of the source area. The observed vast spread in the detrital ZHe and ZFT single grain age distribution is related to variations in source regions with diverse exhumation histories (Fig. 5.8, Fig. 5.9).

Thermochronological data from Upper Cretaceous samples are essentially older than the corresponding sedimentation age, whereby AFT ages range between 141 (±12) and 220 (±18) Ma and a single ZFT age reaches a value of 452 (±41) Ma indicating no heating above 60 °C in the Tarfaya Basin (Fig. 5.3). Since the Upper Cretaceous never experienced temperatures higher than 60 °C, the samples reveal no thermal imprint of the Tarfaya Basin

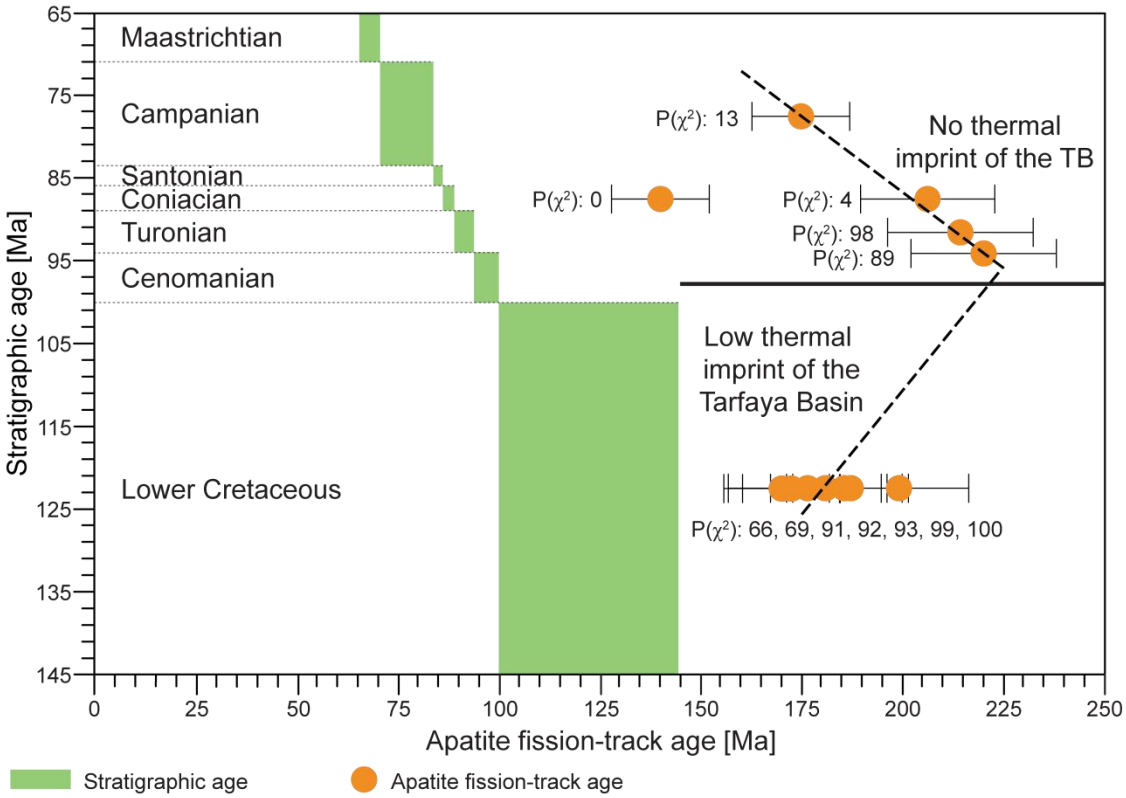

Fig. 5.3: AFT ages (1σ error) from Cretaceous samples of the Tarfaya Basin plotted against stratigraphic ages.

and represent solely the thermal history of the source areas. Except for the Cenomanian–Turonian, a vast spread in the detrital AFT and ZFT single grain age distribution has been observed indicating variations in source regions with different exhumation histories (Fig. 4.21, Fig. 5.10).

The Cretaceous outcrop samples show a typical AFT age distribution, including detrital ages in the Coniacian to Campanian, of a sedimentary basin without obvious rock uplift after maximum subsidence (Armstrong, 2005; Naeser, 1979) (Fig. 3.8a, Fig. 5.3).

Thermochronometric data from Neogene samples are also substantially older than the respective deposition age, whereby AFT ages range between 92 (±16) and 237 (±35) Ma, ZHe single grain aliquot ages from 507 (±9) to 1016 (±18) Ma and ZFT ages between 404 (±29) and 461 (±47) Ma. Similar to the Upper Cretaceous, the Neogene samples never experienced temperatures higher than 60 °C revealing no thermal imprint of the Tarfaya Basin and representing solely the thermal history of the source areas. The observed vast spread in the detrital AFT and ZFT single grain age distribution is due to variations in source regions with different exhumation histories (Fig. 4.22, 5.12). Consequently, provenance analysis of the Cretaceous–Cenozoic sedimentary succession has been carried out and is described in chapter 5.3.

The thermochronological ages confirm that Cretaceous and Cenozoic sedimentary rocks of the Tarfaya Basin never experienced high diagenetic temperatures (Michard et al., 2008a). Furthermore, the data set preclude a Neogene heating event in the onshore Tarfaya Basin caused by the flow of Canary mantle plume material (Duggen et al., 2009).

5.1.3 Hydrocarbon potential

In the Tarfaya Basin exists a large variety of Jurassic, Cretaceous and Cenozoic source rocks. The vast majority of Mesozoic-Cenozoic source rocks in the Tarfaya Basin derive from two stratigraphic intervals, the Upper Cretaceous (particularly Cenomanian–Turonian) and Eocene. High quality petroleum source rocks with high C_{org} content and hydrogen index values were found in the Cenomanian, Turonian, Coniacian and Eocene of the onshore Tarfaya Basin (Sachse, 2011; Sachse et al., 2011; Sachse et al., 2012). However, Cenomanian to Campanian and Eocene samples point to immature to early mature organic matter according to vitrinite reflectance data (Macgregor, 1996; Sachse et al., 2014; Sachse et al., 2011; Sachse et al., 2012). Since the Upper Cretaceous and Eocene never underwent temperatures higher than 60 °C, thermochronological data confirm immature to early mature Cenomanian to Campanian and Eocene source rocks in the onshore Tarfaya Basin.

5.1.4 Interpretation of t-T path modelling

Numerical modelling based on AHe and AFT data sets, yielded a similar, well-defined thermal history of the Lower Cretaceous from the entire northeastern onshore Tarfaya Basin with numerous possible t-T paths (Fig. 4.20). The best fit paths of the thermal models show that all samples underwent continuous cooling in the source area until Lower Cretaceous, followed by heating during Upper Cretaceous to Palaeocene and a cooling phase to recent time (Fig. 5.4).

On the basis of the partially reset AFT ages, the cooling history in the source area is poorly constrained. The rock uplift and exhumation to the surface occurred approximately between Carboniferous–Permian (300 Ma) and Aptian–Albian (110 Ma). Since rock uplift and exhumation in the western Anti-Atlas lasted from Upper Carboniferous to Lower Cretaceous, the WAA is a potential source area for the Lower Cretaceous samples. The elevation of the

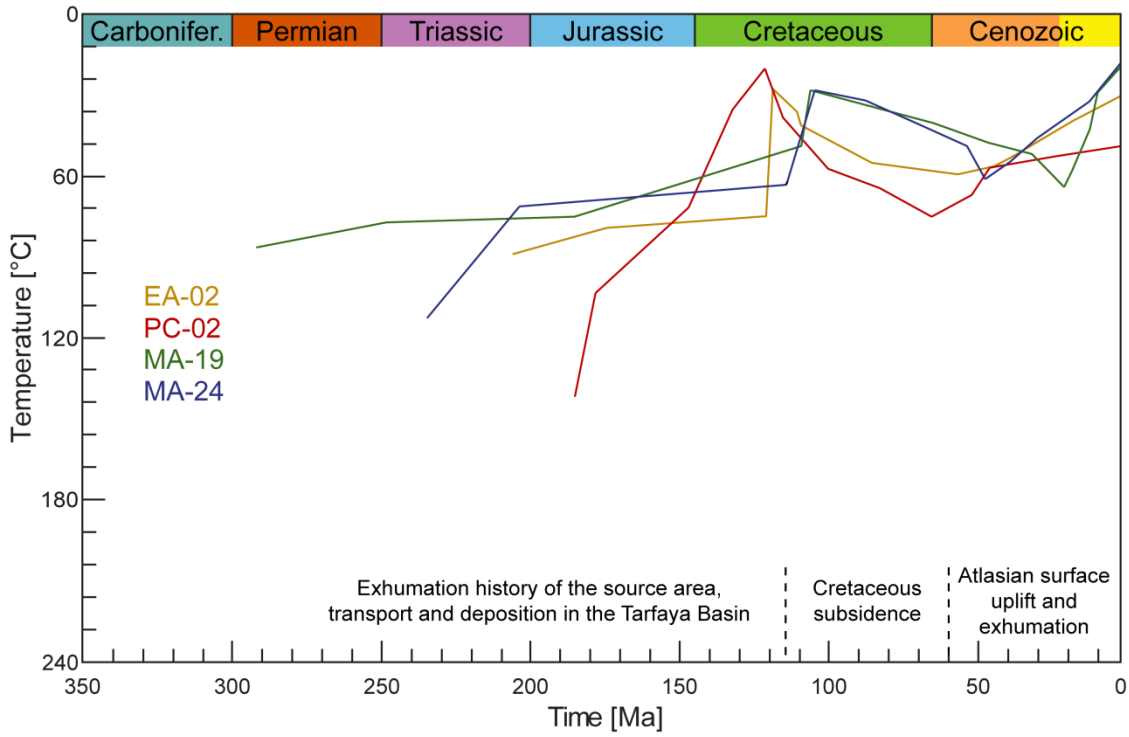

Fig. 5.4: Comparative presentation of best fit paths from Lower Cretaceous samples of the Tarfaya Basin.

hinterland during Lower Cretaceous, which can be recognized along the whole West African passive continental margin, induced a huge amount of clastic sediment material transported to the Tarfaya Basin (Green et al., 2002; Miller and Duddy, 1989).

After the deposition, the Lower Cretaceous underwent a minor subsidence in the Upper Cretaceous–Palaeogene (Fig. 5.4). The modelled t-T paths indicate a heating to temperatures of 60–75 °C until 65–20 Ma. Subsidence rates between 0.019 and 0.040 mm/a, calculated from thermal models, are in accordance with values of < 0.025 mm/a obtained by seismic interpretation (von Rad and Einsele, 1980; Wenke et al., 2013) (Fig. 2.11, Tab. 5.1). Therefore, t-T path modelling points to sedimentation in the entire onshore Tarfaya Basin due to the Cenomanian–Turonian transgression and similar to the western Anti-Atlas during Upper Cretaceous–Palaeogene, resulting in a 1.2–1.6 km thick nowadays eroded sedimentary pile on top of the Lower Cretaceous samples. In the Upper Cretaceous, no significant amounts of sediment have been deposited in this basin (Fig. 5.6). The absent clastic sediment flux from the hinterland led to stable conditions in the Tarfaya Basin proposing a thin overburden on the Lower Cretaceous rocks (Wenke et al., 2013). Preserved Upper Cretaceous to Palaeogene deposits reach a maximum thickness of 2 km in the Tarfaya-Laâyoune-Dakhla Basin (Hafid et al., 2008; Ranke et al., 1982). According to vitrinite reflectance data, Sachse et al. (2011) suggested a maximum burial of approximately 2 km for the Cretaceous sedimentary rocks.

The inversion of the northeastern onshore Tarfaya Basin after maximum subsidence started in the Palaeogene and lasted until recent times (Fig. 5.4). The final rock uplift and exhumation is documented in the modelled t-T paths by a cooling from 60–75 °C to current temperature. The amount of exhumation that occurred during this episode was 1.2–1.6 km, with varying rates between 0.018 and 0.090 mm/a depending on the onset of cooling (Tab. 5.1). The calculated exhumation rates are

consistent with maximum values of 80 mm/a determined by Wenke et al. (2013) (Fig. 2.11). An increasing exhumation from west to east in the northern Tarfaya Basin has been observed. A compressive deformation and related surface uplift took place in the Atlas system as early as the Senonian, while the main inversion of the Mesozoic extensional rift systems began in the Middle to Upper Eocene and is still active at present time (Barbero et al., 2007; Ellouz et al., 2003; Frizon de Lamotte et al., 2009; Laville et al., 1995). The northeastern Tarfaya Basin was strongly affected by peak Atlasian deformation and surface uplift in the Maastrichtian to Lower Oligocene resulting in the erosion of the Meso- to Cenozoic succession down to the Lower Cretaceous (Choubert et al., 1966; Ranke et al., 1982; Wenke et al., 2011, 2013). Besides, von Rad and Einsele (1980) recommended a rock uplift in the Neogene, contemporaneously to the Canary volcanism.

Therefore, final exhumation in the t-T path modelling corresponds to a proposed rock uplift phase in the northeastern Tarfaya Basin starting at the Upper Cretaceous/Palaeogene boundary, whereas a single model confirm a later onset in Neogene times.

The rock uplift and exhumation stage of the northeastern onshore Tarfaya Basin suggests a sediment transport to the surrounding regions in the Cenozoic. An increasing periodic influx of detrital material into the offshore and southern onshore TB since Palaeocene correlates to massive erosion in the northeastern onshore Tarfaya Basin due to major Atlasian surface uplift (Hafid et al., 2008; Wenke et al., 2011, 2013) (Fig. 5.6). Consequently, the northeastern onshore Tarfaya Basin is a potential source area for the Cenozoic sedimentary pile of the offshore and southern onshore Tarfaya Basin.

Table 5.1: Main t-T segments and calculated subsidence and exhumation rates from samples of the Tarfaya Basin

Sample	Depth [m b.s.]	Cooling	Heating	t-t segment [Ma]	T-T segment [°C]	Cooling/heating gradient [°C/Ma]	Geothermal gradient [°C/km]	Subsidence rate [mm/a]	Exhumation rate [mm/a]
EA-02	530–535		Fast	120–55	25–60	0.54	25	0.022	
		Fast		55–recent	60–30	0.55	25		0.022
PC-02	890–1095.80		Fast	120–65	20–75	1.00	25	0.040	
		Slow		65–recent	75–45	0.46	25		0.018
	Elevation [m a.s.l.]								
MA-19	150		Slow	105–20	25–65	0.47	25	0.019	
		Very fast		20–recent	65–20	2.25	25		0.090
MA-24	0		Fast	105–50	25–60	0.64	25	0.026	
		Fast		50–recent	60–20	0.80	25		0.032

Exhumation rates were calculated considering cooling rate, surface temperature and geothermal gradient. Based on literature data geothermal gradients of 25 °C/km were applied (see text for further explanations).

5.2 Thermal, subsidence and exhumation history of the western Anti-Atlas

The present study was focused on the determination of the thermal, subsidence and exhumation history of potential source areas, i.e. the western Anti-Atlas mountain belt.

5.2.1 Precambrian inliers

5.2.1.1 Geothermal gradient

The calculation of exhumation and subsidence rates as well as overburden thickness requires the determination of (palaeo-) geothermal gradients and surface temperatures.

The western Anti-Atlas marks the northwestern fringe of the WAC. Geothermal gradients as well as heat flow densities at Precambrian shields are in general substantial lower compared to other continental areas. In the southern WAC the gradient vary between 10 and 15 °C/km (Brigaud et al., 1985). Comparable with the WAC and further Precambrian shields, the Anti-Atlas mountain belt shows a very low gradient ranging between 12–16 °C/km (Rimi, 1990, 2000). In contrast, Ruiz et al. (2011) and Zarhloule et al. (2005) proposed a geothermal gradient of 20–25 °C/km for the western Anti-Atlas based on the lithosphere thickness.

Since the Anti-Atlas show the lowest crustal temperatures in Morocco and therefore underwent no significant thermal or tectonic reactivation since the Precambrian, a substantial higher palaeogeothermal gradient is implausible (Rimi, 1999). Contrary to large parts of Morocco, the CAMP magmatism is lacking in the WAA. Ruiz et al. (2008) considered a significant higher palaeogeothermal gradient of 35–50 °C/km in the Anti-Atlas Basin during the Palaeozoic. As typical gradients for sedimentary basins with thick infill are ~25 °C/km or less, the value is probably too high for the more than 10 km thick Anti-Atlas Basin (Allen and Allen, 1990). Consequently, a palaeogeothermal gradient of 25 °C/km from Carboniferous to Lower Cretaceous and a gradient of 20 °C/km to recent times have been used for calculation of exhumation and subsidence rates as well as overburden thickness in the WAA. The current annual mean surface temperature in the WAA is ~20 °C.

5.2.1.2 Thermochronological data

In total, 23 Precambrian samples from the four inliers (Irherm, Kerdous, Ifni and Bas Drâa) of the western Anti-Atlas have been analysed by low-temperature thermochronology.

Thermochronological data and t-T modelling reveal a similar thermal and exhumation history of the entire study area. The zircon fission-track central ages determined are equal within the standard deviation ranging between 287 (±23) and 331 (±24) Ma and indicating a simultaneous rapid exhumation in the study area between Upper Carboniferous and Lower Permian. The ZFT data confirm published ages from granites and schists of the Kerdous and Ifni inliers ranging from 319 (±32) to 358 (±31) Ma (Sebti et al., 2009). Furthermore, the data are consistent with K-Ar ages (white micas, biotite) varying between 291 (±7) and 357 (±9) Ma of the Kerdous inlier and the Lakhssas Plateau (Bonhomme and Hassenforder, 1985; Margoum, 2001; Soulaimani and Piqué, 2004). Several authors suggested that the rock uplift and exhumation of the Precambrian basement and the deformation and erosion of the Palaeozoic cover is mainly related to the Variscan orogeny in the Upper Carboniferous–Lower Permian (Burkhard et al., 2006; Gasquet et al., 2008; Helg et al., 2004). ZFT and K-Ar data of the western Anti-Atlas confirm a simultaneous rock uplift and exhumation of the entire Precambrian basement in the Carboniferous associated with the Variscan folding and post-folding erosion.

Except for an anomalously young and unre-

producible age of 130 (±3) Ma due to an U concentration of more than 1000 ppm, the zircon (U-Th-Sm)/He ages range from 205 (±4) to 243 (±3) Ma in the Kerdous and Bas Drâa inliers and from 252 (±5) to 287 (±4) Ma in the Ifni inlier. The data are in consistence with four published ZHe ages varying between 193 (±15) and 248 (±20) Ma of the Irherm inlier (Ruiz et al., 2011). The majority of apatite fission-track central ages of the entire study area cover a range from 150 (±14) to 189 (±14) Ma. Two ages south of the Tasrirt–Tahala fault and an age north of the Ameln Valley fault ranging between 120 (±13) and 139 (±9) Ma indicate a slightly later exhumation in the southern and northern domain of the Kerdous inlier during the drifting process(Soulaimani and Piqué, 2004). The AFT data confirm published ages from the Kerdous and Ifni inliers varying between 121 (±8) and 173 (±23) Ma (Ruiz et al., 2011). ZHe and AFT ages are related to the last significant exhumation phase of the Precambrian inliers occurring during Triassic rifting and Lower to Middle Jurassic transtensional tectonic processes, as the AA formed the denudation shoulder of the Central Atlantic rift (El Arabi et al., 2006; El Harfi et al., 2006; Gasquet et al., 2008; Hafid et al., 2008; Laville et al., 2004; Malusà et al., 2007).

The apatite (U-Th-Sm)/He data from the western Anti-Atlas reveal a large spread in the age distribution. In the elevated northeastern part including the Irherm and Kerdous inliers, the ages range from 49 (±3) to 89 (±5) Ma. Excluding a single age of 148 (±2), published AHe ages varying from 58 (±1) to 104 (±4) Ma of the Irherm inlier are consistent with the determined data (Ruiz et al., 2011). Samples from the lower southwestern inliers Bas Drâa and Ifni yielded substantial older ages ranging between 111 (±7) and 164 (±10) Ma. The final minor exhumation of the Precambrian inliers took place in the Upper Eocene to present, contemporaneously with the surface uplift of the Atlas belt due to the convergence of the African and Eurasian plates (Frizon de Lamotte et al., 2004; Frizon de Lamotte et al., 2000; Gasquet et al., 2008; Helg et al., 2004; Missenard et al., 2006; Teixell et al., 2005). While the Atlasian surface uplift is negligible in the lower inliers Ifni and Bas Drâa, AHe ages of the elevated inliers Irherm and Kerdous are a crucial indication for an increasing impact of the Atlasian orogeny from southwest to northeast in the western Anti-Atlas. Burkhard et al. (2006) proposed that the present-day topography of the western AA is the result of a recent slight exhumation.

5.2.1.3 Interpretation of t-T path modelling

Numerical modelling based on AHe, AFT and ZHe data sets, yielded a similar, well-defined thermal history of the entire western Anti-Atlas with numerous possible t-T paths (Fig. 4.61, Fig. 4.62 and Fig. 4.63). The best fit paths of the thermal models show that all samples underwent continuous cooling from Upper Carboniferous to Lower Cretaceous, followed by reheating during Upper Cretaceous and finally a cooling phase in Cenozoic times (Fig. 5.5).

The Anti-Atlas area was affected by post-Pan-African rifting and extensional tectonics in the Palaeozoic until the Lower Carboniferous resulting in the vast subsidence of the Anti-Atlas Basin (Burkhard et al., 2006; Michard et al., 2008b; Pique et al., 1999) (Fig. 2.28). The uppermost Proterozoic to Upper Carboniferous sedimentary succession reaches a thickness of up to 12 km in the westernmost Anti-Atlas near Tiznit (Burkhard et al., 2006; Faik et al., 2001; Helg et al., 2004; Michard, 1976; Michard et al., 2008b; Pique and Michard, 1989). In the Upper Carboniferous, the Precambrian samples were buried in the depth at approximately 240 °C (Fig. 5.5). Based on the postulated palaeogeothermal gradient

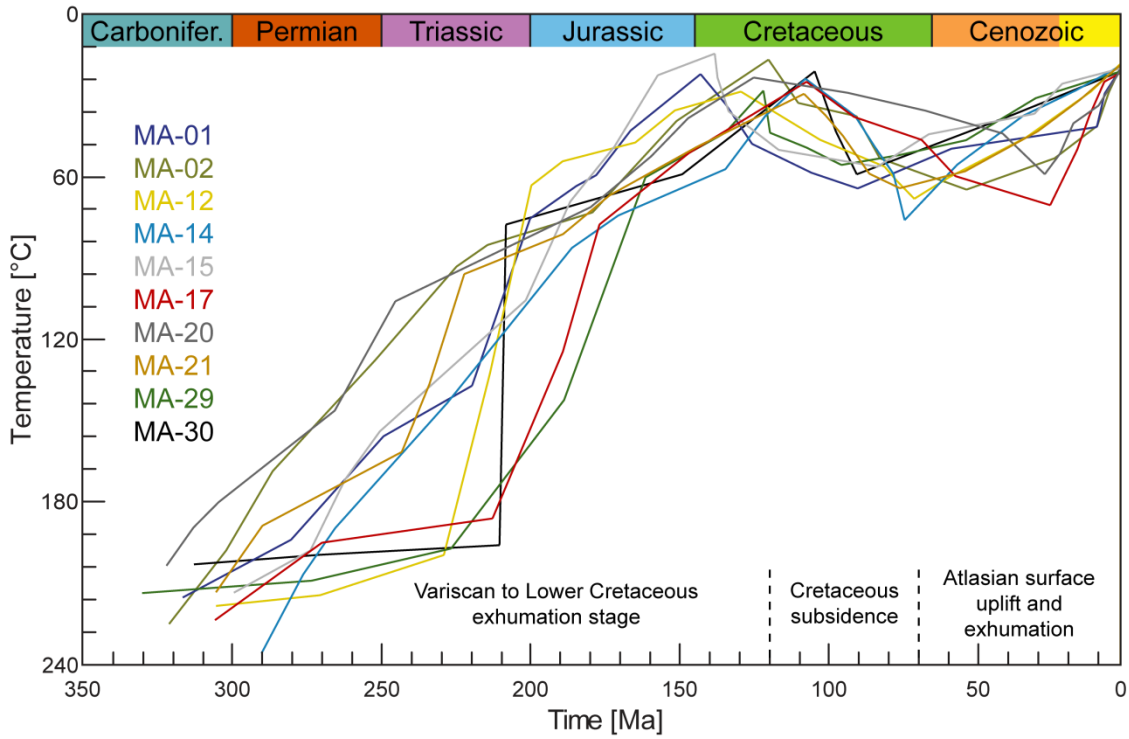

Fig. 5.5: Comparative presentation of best fit paths from thermal models of the western Anti-Atlas.

and surface temperature, the recent surface of the Precambrian inliers was overlain by 9 km of Precambrian to Palaeozoic rocks. Ruiz et al. (2011) and Sebti et al. (2009) assumed a common geological evolution of the Precambrian inliers in the western Anti-Atlas with a burial of 7–9 km in the Carboniferous.

On the basis of ZFT data, the onset of cooling took place in the Upper Carboniferous during the Variscan orogeny, yielding an intense inversion and folding of the Anti-Atlas Basin. The cooling event is assigned to the Variscan folding, followed by rapid exhumation and post-folding erosion of the Palaeozoic sedimentary cover (Burkhard et al., 2006; Gasquet et al., 2008; Helg et al., 2004; Sebti et al., 2009) (Fig. 5.5). The initial deformation of the western Anti-Atlas is generally considered as Upper Carboniferous due to the youngest age of deformed and tilted sediments (Helg et al., 2004; Michard, 1976; Pique and Michard, 1989). The post-folding erosion of the western Anti-Atlas correlates with northwestern source areas of the detrital input in the Jebel Reounia sandstones (Upper Namurian) of the Tindouf Basin, suggesting that the western Anti-Atlas has been uplifted and eroded as early as ~320 Ma (Cavaroc et al., 1976; Michard et al., 2008b; Sebti et al., 2009). According to different ZHe ages, some samples reveal a slow initial cooling from Upper Carboniferous to Upper Triassic with exhumation rates between 0.020 and 0.029 mm/a (Fig. 5.5, Tab. 5.2). Subsequently, a rapid cooling event occurred between Upper Triassic and Lower Cretaceous until ~120 Ma with exhumation rates from 0.061 to 0.068 mm/a (Fig. 5.5, Tab. 5.2). In contrast, several samples show an incipient continuous fast cooling from 310 to ~125 Ma with exhumation rates between 0.042 and 0.053 mm/a (Fig. 5.5, Tab. 5.2). Considering the entire study area, the cooling phase lasted from the Upper Carboniferous to the Lower Cretaceous, whereby the majority of the 9 km of Precambrian to Palaeozoic overburden has been eroded. Ruiz et al. (2011) postulated that the western Anti-Atlas experienced a slow and continuous phase of denudation from Central

Table 5.2: Main t-T segments and calculated subsidence and exhumation rates from outcrop samples of the western Anti-Atlas

Sample	Elevation [m a.s.l.]	Cooling	Heating	t-t segment [Ma]	T-T segment [°C]	Cooling/heating gradient [°C/Ma]	Geothermal gradient [°C/km]	Subsidence rate [mm/a]	Exhumation rate [mm/a]
Irherm inlier									
MA-01	1018	Fast		310–145	240–20	1.33	25		0.053
			Fast	145–90	20–65	0.82	20	0.041	
		Slow		90–10	65–40	0.31	20		0.016
		Very fast		10–recent	40–20	2.00	20		0.100
MA-02	1410	Fast		310–120	240–20	1.16	25		0.046
			Fast	120–55	20–65	0.69	20	0.035	
		Slow		55–10	65–40	0.56	20		0.028
		Very fast		10–recent	40–20	2.00	20		0.100
Kerdous inlier									
MA-12	1082	Slow		310–230	240–200	0.50	25		0.020
		Very fast		230–130	200–30	1.70	25		0.068
			Fast	130–70	30–70	0.67	20	0.033	
		Fast		70–recent	70–20	0.71	20		0.036
MA-14	1603	Fast		300–110	240–25	1.13	25		0.045
			Very fast	110–75	25–75	1.43	20	0.071	
		Fast		75–recent	75–20	0.73	20		0.037
MA-15	1522	Fast		310–140	240–20	1.29	25		0.052
			Fast	140–85	20–55	0.64	20	0.032	
		Slow		85–recent	55–20	0.41	20		0.021
MA-17	530	Slow		290–215	240–185	0.73	25		0.029
		Very fast		215–110	185–25	1.52	25		0.061
			Slow	110–25	25–70	0.53	20	0.026	
		Very fast		25–recent	70–20	2.00	20		0.100
Ifni inlier									
MA-20	60	Fast		310–125	240–25	1.16	25		0.046
			Slow	125–30	25–60	0.37	20	0.018	
		Very fast		30–recent	60–20	1.33	20		0.067
MA-21	260	Fast		310–110	240–30	1.05	25		0.042
			Fast	110–75	30–65	1.00	20	0.050	
		Slow		75–recent	65–20	0.60	20		0.030
Bas Drâa inlier									
MA-29	344	Slow		310–225	240–195	0.53	25		0.021
		Very fast		225–120	195–30	1.57	25		0.063
			Fast	120–95	30–55	1.00	20	0.050	
		Slow		95–recent	55–20	0.37	20		0.018
MA-30	134	Slow		300–210	240–195	0.50	25		0.020
		Very fast		210–105	195–20	1.67	25		0.067
			Very fast	105–90	20–60	2.67	20	0.133	
		Slow		90–recent	60–20	0.44	20		0.022

Subsidence and exhumation rates were calculated considering cooling rate, surface temperature and geothermal gradient. Based on literature data geothermal gradients of 20 °C/km and 25 °C/km were applied (see text for further explanations).

Atlantic continental rifting in the Permian–Triassic until the Lower Cretaceous. Caused by the Central Atlantic and Tethys rifting, the Anti-Atlas was affected by vertical movements in the Upper Permian–Lower Triassic (El Arabi et al., 2006; Knight et al., 2004). Various authors supposed the last significant exhumation phase of the Precambrian inliers during Triassic rifting and Lower to Middle Jurassic transtensional tectonic processes, as the AA formed the denudation shoulder of the Central Atlantic rift (El Arabi et al., 2006; El Harfi et al., 2006; Gasquet et al., 2008; Hafid et al., 2008; Laville et al., 2004; Malusà et al., 2007). A Lower Cretaceous rock uplift of the passive continental margin is reported for the whole Central Atlantic region (Green et al., 2002; Miller and Duddy, 1989).

The rock uplift and exhumation episode of the Precambrian inliers led to a huge amount of sediment material transported to the surrounding basins since the Variscan orogeny. Therefore, the Anti-Atlas mountain belt has to be considered as a potential source area for the Triassic to Lower Cretaceous sedimentary pile of the Tarfaya Basin. In the Triassic to Lower Jurassic up to 5 km of clastic material has been deposited in the Basin (El Khatib et al., 1995; Le Roy and Piqué, 2001). Whereas the Middle–Upper Jurassic is dominated by a carbonate platform, the sediment flux of clastic material increased enormously due to the elevation of the hinterland during Lower Cretaceous yielding the deposition of a 1–4 km thick continental sequence (El Khatib et al., 1995; Hafid et al., 2008; Ranke et al., 1982). The sediment flux diagram reveals a continuous relatively high input in the Tarfaya Basin between Triassic and Lower Cretaceous (Wenke et al., 2013) (Fig. 5.6). Peak clastic sediment flux rates can be recognized for the Central Atlantic rift stage in the Upper Triassic and delta formation in the Lower Cretaceous, interrupted by peak during carbonate platform build-up in the Middle–Upper Jurassic (Fig. 5.6). The general continuous sediment flux to the Tarfaya Basin corresponds to the modelled consistent rock uplift and erosion in the western Anti-Atlas between Triassic and Lower Cretaceous times.

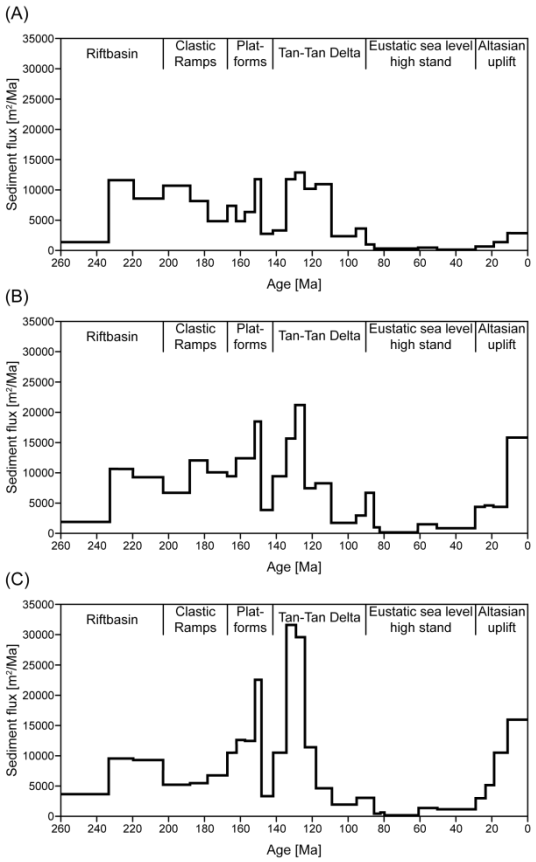

Fig. 5.6: Permian to present day sediment flux at the outer shelf of the (A) Tan-Tan area, (B) Cap Juby area and (C) Laâyoune area (Wenke et al., 2013).

After the exhumation phase, the Precambrian inliers underwent a minor subsidence in the Upper Cretaceous (Fig. 5.5). A burial phase during Upper Cretaceous–Eocene is attested to by thermochronological studies in the western Anti-Atlas (Ruiz et al., 2011) and in the Meseta region (Ghorbal et al., 2008; Saddiqi et al., 2009). The modelled t-T paths show a reheating to temperatures of 55–75 °C. In the majority of the models, the subsidence occurred until 95–70 Ma. Except for one sample, subsidence rates range between 0.018 and 0.071 mm/a (Tab. 5.2). Therefore,

t-T path modelling suggests sedimentation in the Anti-Atlas mountain belt during late Lower Cretaceous–Upper Cretaceous resulting in a 1.5–2.5 km thick sedimentary pile on top of the Precambrian–Palaeozoic rocks. Corresponding to a widespread transgression across the North African continent in the Cenomanian–Turonian, a flooding of the entire northern Morocco, including the Anti-Atlas is presumable (Frizon de Lamotte et al., 2008; Guiraud et al., 2005; Michard et al., 2008b). Zouhri et al. (2008) postulated that the Anti-Atlas was covered by shallow marine Cenomanian–Turonian carbonates eroded during Senonian–Cenozoic times. Since preserved Cretaceous deposits reach a thickness of 1–2 km in the Atlantic Basins and the Meseta, which is probably a minimum value because of post-deposition Atlasian denudation (Hafid et al., 2008; Mustaphi et al., 1997; Saddiqi et al., 2009; Zühlke et al., 2004), a calculated Cretaceous sedimentary pile of 1.5–2.5 km seems realistic for the western Anti-Atlas. Ruiz et al. (2011) proposed a nowadays eroded Cretaceous–Eocene sedimentary succession of 1.5 km in the WAA.

On the basis of transgression and sedimentation in the Anti-Atlas, an enormously decreasing clastic sediment flux from the mountain belt can be assumed during Upper Cretaceous. The widespread transgression led to the deposition of a thin shallow marine sedimentary succession in the Tarfaya Basin (El Khatib et al., 1995). In the Upper Cretaceous no substantial amounts of sediment have been deposited in the TB and the clastic sediment flux from the hinterland starved (Wenke et al., 2013) (Fig. 5.6). Therefore, an absent clastic sediment flux to the Tarfaya Basin corresponds to the modelled subsidence and sedimentation in the western Anti-Atlas during Upper Cretaceous.

The final cooling and exhumation of the Precambrian inliers started in the late Upper Cretaceous and continued until recent times (Fig. 5.5). In some samples, the final exhumation started in the Eocene–Oligocene (Fig. 5.5, Tab. 5.2). The modelled t-T paths indicate a cooling from 55–75 °C to surface temperature. The amount of exhumation that took place during this episode was approximately 2 km, with varying rates between 0.016 and 0.100 mm/a depending on the onset of cooling (Tab. 5.2). An initial convergence of the African and Eurasian continents occurred in the Upper Cretaceous (90 Ma) due to the opening of the South Atlantic Ocean (Rosenbaum et al., 2002). The onset of compressive deformation and related surface uplift in the Atlas system took place as early as the Senonian (90–65 Ma), while the main inversion of the Mesozoic extensional rift systems began in the Middle to Upper Eocene and is still active at present time (Barbero et al., 2007; Beauchamp et al., 1999; Ellouz et al., 2003; Frizon de Lamotte et al., 2009; Laville et al., 1995; Teixell et al., 2005). In the Anti-Atlas mountain belt, a minor exhumation of the Precambrian inliers occurred in the Upper Eocene–Oligocene to recent times, contemporaneously with the surface uplift of the Atlas belt due to the convergence of the African and Eurasian plates (Burkhard et al., 2006; Frizon de Lamotte et al., 2004; Frizon de Lamotte et al., 2000; Gasquet et al., 2008; Helg et al., 2004; Missenard et al., 2006). The majority of the thermal models are in accordance with an initial surface of the Atlas system in the Senonian, whereas two models confirm a later final exhumation associated with the main Atlasian surface uplift in the Oligocene.

The rock uplift and exhumation phase of the Precambrian inliers led to an increasing sediment transport to the surrounding basins in the Cenozoic. Therefore, the western Anti-Atlas is a potential source area for the Cenozoic sedimentary pile of the Tarfaya Basin. In the Palaeogene and Neogene the sedimentation in the basin is dominated by continental sandstones reaching a maximum thickness of

2 km, whereby a Cenozoic sedimentary succession is lacking in the northeastern basin due to flexural rock uplift since the Maastrichtian (Davison, 2005; El Khatib et al., 1995; Hafid et al., 2008; Ranke et al., 1982; Wenke et al., 2011). The sediment flux diagram reveals an increasing input in the Tarfaya Basin from Palaeocene onward, with a peak clastic sediment flux in the Middle Miocene to Pleistocene (Wenke et al., 2013) (Fig. 5.6). Consequently, the modelled continuous exhumation in the western Anti-Atlas between late Upper Cretaceous and recent times corresponds to an increasing clastic sediment flux to the Tarfaya Basin since Palaeocene.

Summarising, based on t-T path modelling and thermochronological data of samples from the Precambrian inliers Irherm, Kerdous, Ifni und Bas Drâa, exhumation took place at least since the Upper Carboniferous related to the Variscan folding and post-folding erosion in the western Anti-Atlas. The exhumation phase lasted beyond the Central Atlantic rift and drift stage until the Lower Cretaceous, whereby 9 km of Precambrian–Palaeozoic overburden has been eroded, with exhumation rates between 0.020 and 0.068 mm/a. In the Upper Cretaceous the Precambrian inliers underwent a minor subsidence with varying rates between 0.018 and 0.133 mm/a. The modelled t-T paths indicate sedimentation in the Anti-Atlas mountain belt during late Lower Cretaceous–Upper Cretaceous resulting in a 1.5–2.5 km thick sedimentary pile on top of the Precambrian–Palaeozoic rocks. The final exhumation phase started in the late Upper Cretaceous and continued until present time. During this exhumation episode, rates vary between 0.016–0.100 mm/a. The Anti-Atlas mountain belt could have been a potential source area for the Tarfaya Basin since the Triassic. Except for a hiatus in the Upper Cretaceous, a continuous clastic sediment flux to the TB could have been occurred to recent times.

5.2.2 Oum Doul-1/Adrar Zougar-1

5.2.2.1 Geothermal gradient

A geothermal gradient has been determined by thermochronological and literature data, due to the lack of measured bottom hole temperatures.

The wells Oum Doul-1 and Adrar Zougar-1 are situated in the southwestern Anti-Atlas close to the Tindouf Basin. The Anti-Atlas mountain belt shows a very low gradient ranging between 12–16 °C/km (Rimi, 1990, 2000), whereas Ruiz et al. (2011) and Zarhloule et al. (2005) proposed a geothermal gradient of 20–25 °C/km. In the Tindouf Basin, the gradient varies between 20 and 34 °C/km (Rimi, 1990). Therefore, a geothermal gradient higher than 20 °C/km at the Anti-Atlas/Tindouf Basin boundary seems realistic. Since AHe ages are completely reset in a depth of 2 km in well Adrar Zougar-1, thermochronological data indicate a current geothermal gradient of approximately 25 °C/km. The following calculated exhumation and subsidence rates are based on the assumption of this geothermal gradient and a surface temperature of 20 °C.

5.2.2.2 Interpretation of thermochronological data and t-T path modelling

In total, 11 Precambrian to Palaeozoic samples from wells Oum Doul-1 and Adrar Zougar-1 have been analysed by low-temperature thermochronology. The wells contain the virtually complete stratigraphic succession from Precambrian to Lower Carboniferous sedimentary rocks (Fig. 5.7).

Thermochronological data illustrate a common thermal history of the entire succession. Except for two zircon fission-track ages of Lower Carboniferous samples, thermochronometric ages are younger than the

corresponding sedimentation age (Fig. 5.7). AHe ages determined ranging between 16 (±1) and 0 (±0) Ma and AFT central ages varying from 177 (±15) to 10 (±1) Ma are significantly younger than the stratigraphic age of the sampled rock. Excluding a Lower to Middle Devonian sample, zircon (U-Th-Sm)/He data alternating between 290 (±23) and 81 (±7) Ma and zircon fission-track central ages ranging between 483 (±59) and 258 (±18) Ma reveal a continuous age decrease with increasing depth across the entire succession (Fig. 5.7). Thermochronological data from both wells suggest an uplifted succession after maximum burial due to the absence of detrital ages, except for ZFT ages of the Upper Carboniferous (Armstrong, 2005; Naeser, 1979) (Fig. 5.7). Appropriate to the postulated geothermal gradient and surface temperature, the recent surface of the Adrar Zougar-1 well was overlain by approximately 8 km of Upper Ordovician to Carboniferous sedimentary rocks, since the entire succession was buried in a depth at approximately 240 °C in the Upper Carboniferous. The late Proterozoic to Palaeozoic sedimentary succession reaches a thickness of up to 12 km in the westernmost Anti-Atlas near Tiznit (Burkhard et al., 2006; Faik et al., 2001; Helg et al., 2004; Michard, 1976; Michard et al., 2008b; Pique and Michard, 1989). An overburden of ~8km is consistent with a suggested Upper Ordovician to Upper Carboniferous sedimentary pile of about 7 km in the western Anti-Atlas (Helg et al., 2004).

The t-T path modelling shows a continuous heating after the deposition during the Palaeozoic, as the Anti-Atlas was affected by post-Pan-African rifting and extensional tectonics that caused a vast subsidence of the Anti-Atlas Basin and the deposition of a thick sedimentary pile (Burkhard et al., 2006; Michard et al., 2008b; Pique et al., 1999). Excluding sample AZ-06, the subsidence phase lasted until 330–305 Ma with a maximum rate of 0.065 mm/a (Tab. 5.3). Subsequently, the inversion of the Anti-Atlas Basin started in the

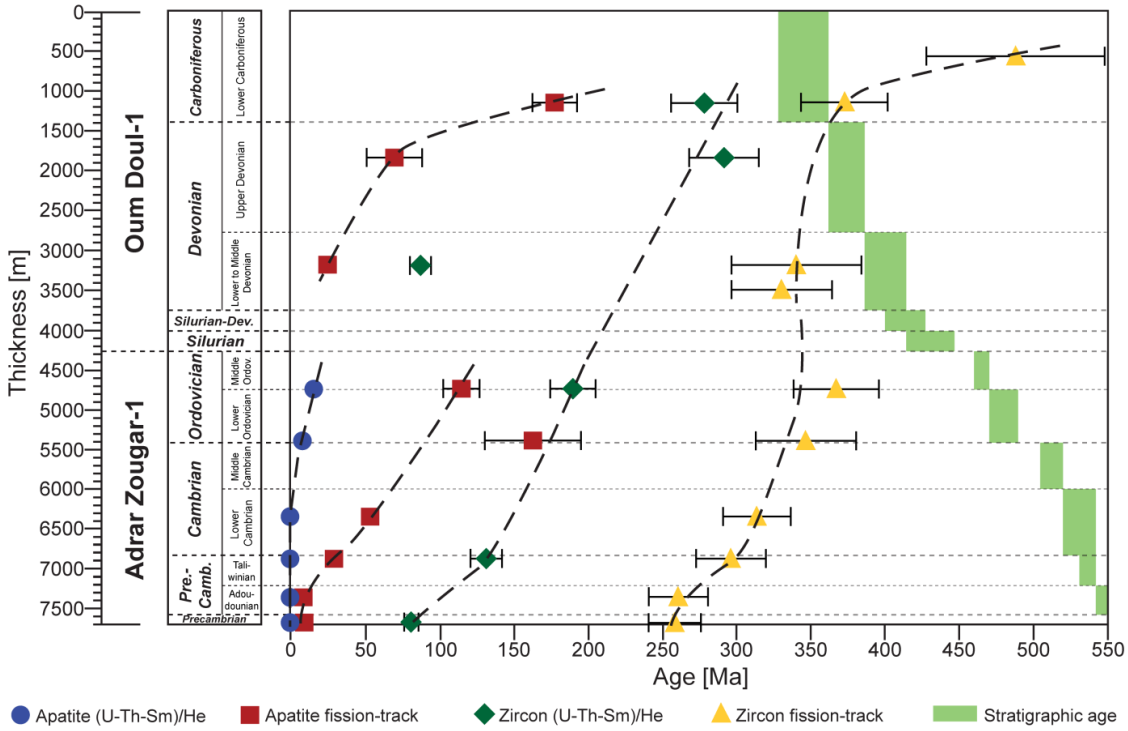

Fig. 5.7: Thermochronometric age (1σ error) – depth distribution from wells Adrar Zougar-1 and Oum Doul-1. On the left side a schematic stratigraphic profile is displayed.

Upper Carboniferous and continued until recent time. During this nearly continuous cooling episode the 8 km overburden has been eroded with varying exhumation rates between 0.019 and 0.029 mm/a (Tab. 5.3). The initial exhumation phase is assigned to the Variscan folding, followed by rapid exhumation and post-folding erosion of the Palaeozoic sedimentary cover (Burkhard et al., 2006; Gasquet et al., 2008; Helg et al., 2004; Sebti et al., 2009). Similar to the Precambrian inliers, exhumation in the southwestern Anti-Atlas took place during Triassic rifting, Jurassic transtensional tectonic processes, Lower Cretaceous delta formation and finally during Atlasian deformation (Burkhard et al., 2006; Gasquet et al., 2008; Laville et al., 2004).

The recent surface of the Oum Doul-1 well was overlain by approximately 5 km of Palaeozoic sedimentary rocks based on the postulated geothermal gradient and surface temperature, since the entire succession was buried in depth at approximately 170–180 °C in the Upper Carboniferous. In the western Anti-Atlas, the Carboniferous reach a maximum thickness of ~2 km (Helg et al., 2004). Therefore, a nowadays eroded overburden of 5 km on top of the Oum Doul-1 succession is implausible. The maximum heating temperatures and calculated overburden is due to reset ZHe ages of Devonian to Lower Carboniferous samples. The ZHe single grain aliquot ages of these samples reveal a large spread, including old non-reset ages which are assumed to be the more accurate data (Tab. 4.48). The non-reset ZHe ages, ranging from 327 (±26) to 391 (±31) Ma, yield a heating to temperatures below 130–140 °C of the entire

Table 5.3: Main t-T segments and calculated subsidence and exhumation rates from wells Oum Doul-1 and Adrar Zougar-1 of the southwestern Anti-Atlas

Sample	Depth [m b.s.]	Cooling	Heating	t-t segment [Ma]	T-T segment [°C]	Cooling/heating gradient [°C/Ma]	Geothermal gradient [°C/km]	Subsidence rate [mm/a]	Exhumation rate [mm/a]
Oum Doul-1									
OD-02	1066–1179		Very fast	340–310	20–180	5.33	25	0.213	
		Fast		310–210	180–65	1.15	25		0.046
		Very slow		210–recent	65–50	0.07	25		0.003
OD-03	1751–1847		Very fast	370–330	20–195	4.38	25	0.175	
		Fast		330–210	195–100	0.79	25		0.032
		Very slow		210–recent	100–65	0.17	25		0.007
OD-04	3098–3147		Very fast	400–350	20–240	4.40	25	0.176	
		Slow		350–155	240–185	0.28	25		0.011
		Slow		155–recent	185–100	0.55	25		0.022
Adrar Zougar-1									
AZ-01	455–463		Very fast	465–330	20–240	1.63	25	0.065	
		Slow		330–215	240–185	0.48	25		0.019
		Fast		215–recent	185–30	0.72	25		0.029
AZ-04	2541–2587		Fast	545–305	20–240	0.92	25	0.037	
		Slow		305–recent	240–85	0.51	25		0.020
AZ-06	3315–3387		Fast	545–245	20–240	0.73	25	0.029	
		Slow		245–recent	240–105	0.55	25		0.022

Subsidence and exhumation rates were calculated considering cooling rate, surface temperature and geothermal gradient. Based on literature data a geothermal gradient of 25 °C/km was applied (see text for further explanations).

Oum Doul-1 succession resulting in an overburden of ~3 km. Besides, a higher palaeogeothermal gradient of 30 °C/km would yield in a less overburden of ~2.5 km. Ruiz et al. (2008) considered a substantial higher palaeogeothermal gradient of 35–50 °C/km in the Anti-Atlas Basin during the Palaeozoic.

The t-T path modelling shows a continuous heating after the deposition similar to the Adrar Zougar-1 well during the Palaeozoic, as the Anti-Atlas was affected by post-Pan-African rifting and extensional tectonics resulting in the vast subsidence of the Anti-Atlas Basin and the deposition of a thick sedimentary pile (Burkhard et al., 2006; Michard et al., 2008b; Pique et al., 1999). Excluding sample OD-04, the subsidence phase lasted until 330–310 Ma with a maximum rate of 0.213 mm/a (Tab. 5.3). Subsequently, the inversion of the Anti-Atlas Basin started in the Upper Carboniferous and continued until present time. During this cooling episode the less than 5 km overburden has been eroded. The initial fast exhumation phase with rates between 0.032 and 0.046 mm/a is assigned to the Variscan folding, post-folding erosion and Triassic rifting (Burkhard et al., 2006; Gasquet et al., 2008; Helg et al., 2004; Sebti et al., 2009) (Tab. 5.3). Afterwards, a slow cooling phase to recent temperature occurred during Jurassic to Cenozoic with exhumation rates between 0.003 and 0.007 mm/a (Tab. 5.3).

5.3 Provenance analysis – Detrital thermochronology

The third key objective of the present study was the provenance analysis of the Cretaceous to Neogene sedimentary rocks from the Tarfaya Basin. Due to their low thermal imprint below the partial annealing zone and partial retention zone, the Cretaceous/Cenozoic sedimentary succession indicates the t-T evolution of the source area, so-called provenance.

5.3.1 Triassic to Jurassic succession

The oldest Mesozoic sedimentary rocks of the Tarfaya Basin are Triassic continental to restricted marine red conglomerates and sandstones with a maximum thickness of 5 km in the offshore basin (El Khatib et al., 1995; Le Roy and Piqué, 2001; Ranke et al., 1982). The Jurassic is dominated by an extensive carbonate platform (Hafid et al., 2008). During this time span, exhumation occurred in the Anti-Atlas mountain belt, as the AA formed the denudation shoulder of the Atlantic rift (El Harfi et al., 2006; Gasquet et al., 2008; Malusà et al., 2007). On the basis of thermochronological data of the current study and further geological data, the AA was a potential source area for the continental sedimentary rocks of the surrounding basins (El Arabi et al., 2006; El Harfi et al., 2006; Gasquet et al., 2008; Laville et al., 2004). The Triassic and Jurassic well samples show apatite fission-track and (U-Th-Sm)/He ages significantly younger than the corresponding stratigraphic age, indicating a partial or complete reset in the Tarfaya Basin. Since the t-T evolution of the source area is overprinted by a thermal imprint of the TB, a provenance analysis based on AHe and AFT dating techniques is not feasible.

5.3.2 Lower Cretaceous

The Cretaceous and Cenozoic sedimentary succession of the Tarfaya Basin is suitable for provenance analysis, as the rocks never experienced high diagenetic temperatures (Michard et al., 2008a).

In the Lower Cretaceous, an important regression resulted in the deposition of a 1 – 4 km thick continental to transitional sequence and the establishment of widespread delta systems in the Tan-Tan and Boujdour area (Hafid et al., 2008; Ranke et al., 1982; von Rad and Wissmann, 1982). The offshore Boujdour Delta developed due to rock uplift and erosion in the Reguibat Shield and Anti-Atlas (Davison, 2005). The regionally extensive deltas were linked by incised valleys with the eastern source areas (AA, Reguibat Shield) (Wenke et al., 2013). Jarvis et al. (1999) suggested that the Lower Cretaceous sedimentary rocks were sourced from the Tindouf Basin and the West African Craton. Ali (2012) and Ali et al. (2014) proposed the Reguibat Shield and the Mauritanides as dominant source areas due to geochemical and petrographic data. Thermal modelling and published geological data reveal that the Anti-Atlas mountain belt as well as the entire Central Atlantic passive continental margin was affected by denudation processes in the Lower Cretaceous (Green et al., 2002; Miller and Duddy, 1989; Ruiz et al., 2011).

The large variety in thermochronological data of the Cretaceous samples is more complicated to interpret and therefore necessitate differentiated considerations.

The Lower Cretaceous outcrop samples show AHe ages substantially younger than the respective stratigraphic age indicating a complete reset in the Tarfaya Basin. In contrast, the AFT ages are slightly older than the stratigraphic age. On the basis of t-T modelling, the Lower Cretaceous samples underwent a heating to approximately 70 °C after deposition confirming a low thermal imprint in the basin. Since similar AFT data appear in the western Anti-Atlas, the WAA can be considered as potential source area for the apatite

grains. Besides, Malusà et al. (2007) published similar AFT ages from the eastern Anti-Atlas. Due to the maximum heating temperature of the Lower Cretaceous in the TB, zircon (U-Th-Sm)/He and zircon fission-track data represent the thermal history of the source area.

Contrary to the western Anti-Atlas, the ZHe single grain aliquot ages reveal a large spread varying from 185 to 1195 Ma (Fig. 5.8). In the WAA, the ZHe ages cover a range between 88 and 362 Ma. Published ZHe ages of the Irherm inlier (WAA) vary from 193 to 248 Ma (Ruiz et al., 2011). Except for two single grain aliquot ages of the Tarfaya Basin, the ZHe ages of the WAA are significantly younger (Fig. 5.8). Therefore, based on the Precambrian ZHe ages, an additional cratonic source area seems realistic.

The ZFT single grain age distribution, ranging from 331 to 1208 Ma, shows a larger spread than the western Anti-Atlas (Fig. 5.9). In the WAA, the ZFT ages vary between 226 and 616 Ma. Published ZFT central ages of the Kerdous and Irherm inlier (WAA) cover a range from 319 to 358 Ma (Sebti et al., 2009). These data are consistent with K-Ar ages (white micas, biotite) varying between 291 (±7) and 357 (±9) Ma of the Kerdous inlier and the Lakhssas Plateau (Bonhomme and Hassenforder, 1985; Margoum, 2001; Soulaimani and Piqué, 2004). Accordingly, a large number of ZFT single grain ages from the TB are substantially older and cannot connected with data from the WAA suggesting a cratonic source area (Fig. 5.9). Several authors proposed that the cratonic Reguibat Shield constitutes a source area for the clastic sediment material of the Lower Cretaceous (Ali, 2012; Ali et al., 2014; Davison, 2005; Jarvis et al., 1999; Ranke et al., 1982).

Concluding, AFT, ZHe and ZFT ages of the Lower Cretaceous samples from the Tarfaya Basin indicate diverse source areas. While AFT ages are in consistence with data from the western Anti-Atlas, Precambrian ZHe and ZFT data reveal that clastic material were delivered additionally from a cratonic source area.

5.3.3 Upper Cretaceous

In the Upper Cretaceous, a transgression led to the deposition of thinner shallow marine to lagoonal sediments (El Khatib et al., 1995). The Cenomanian–Turonian basin fill has a small thickness and is characterised by decreasing terrigenous influx and increasing plankton input (Ranke et al., 1982). Altogether, the sediment flux reduced significantly in the Tarfaya Basin during Upper Cretaceous (Fig. 5.6). Between Coniacian and Campanian sediment input increased moderately according to the initial Atlasian compression. Ali (2012) has taken the Reguibat Shield, Mauritanides and the western Anti-Atlas as source areas for the Upper Cretaceous due to geochemical and petrographic data of the heavy minerals zircon, tourmaline, rutile, garnet and hornblende into consideration. In contrast, apatite grains are not indicative of a particular provenance

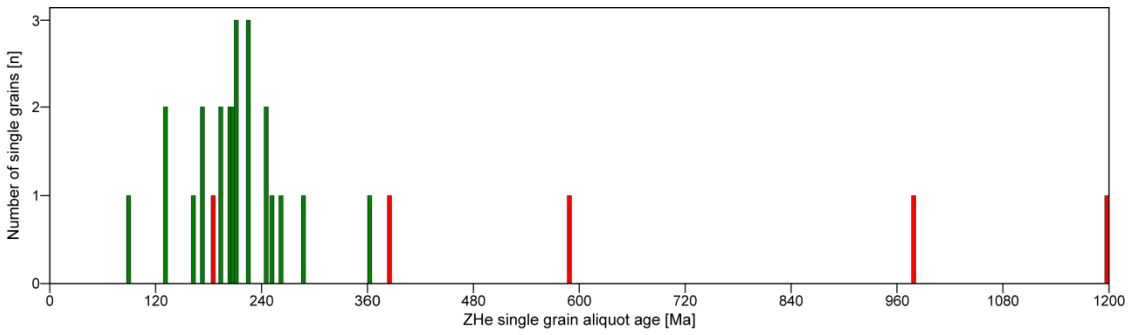

Fig. 5.8: ZHe single grain aliquot ages from outcrop samples of the western Anti-Atlas and the Lower Cretaceous of the Tarfaya Basin. Green: western Anti-Atlas; Red: Tarfaya Basin.

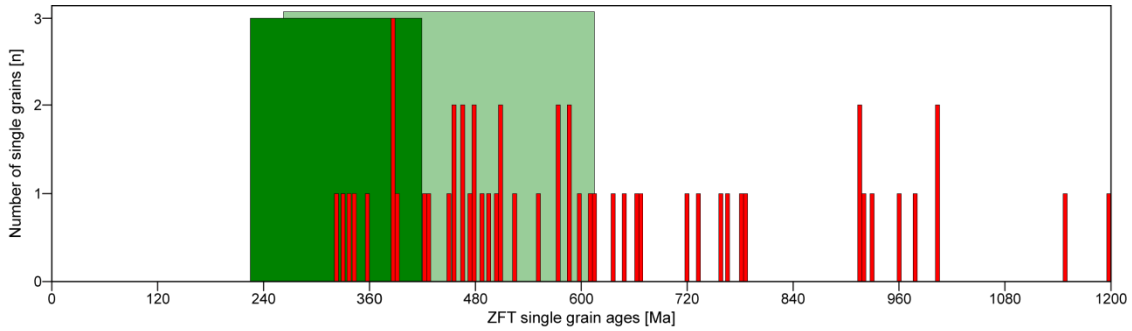

Fig. 5.9: ZFT single grain age distribution of the western Anti-Atlas and the Lower Cretaceous of the Tarfaya Basin. Green: single grain age range from outcrop samples of the WAA; Light Green: single grain age range from well samples of the WAA; Red: Tarfaya Basin.

(Ali, 2012). Various authors as well as t-T path modelling of the present study postulate a sedimentation phase in the AA during Upper Cretaceous (Cenomanian–Turonian) (Frizon de Lamotte et al., 2009; Michard et al., 2008b; Ruiz et al., 2011; Zouhri et al., 2008).

The Upper Cretaceous outcrop samples show AFT data essentially older than the corresponding stratigraphic age indicating no reset in the Tarfaya Basin. Furthermore, the large spread in the single grain age distribution of Coniacian–Campanian samples point to no thermal imprint in the TB for the AFT system (Fig. 4.21). An age population calculation, applying the computer code 'Popshare', yielded at least two different populations (Dunkl and Székely, 2002) (Tab. 5.4). The samples reveal four age populations between 144 and 200 Ma that are in accordance with AFT ages from the western Anti-Atlas of the current study and published data considering the AA as potential source area for the apatite grains of the Upper Cretaceous (Malusà et al., 2007; Ruiz et al., 2011) (Tab. 5.4). The older populations of 249 and 260 Ma are consistent with AFT data of the eastern AA mountain belt or could have been sourced from a cratonic area (Malusà et al., 2007) (Tab. 5.4).

The ZFT single grain age distribution, ranging between 226 and 864 Ma, shows a larger spread compared to ages from 226 to 616 Ma in the western Anti-Atlas (Fig. 5.10). Therefore, some ZFT single grain ages of the Upper Cretaceous samples from the Tarfaya Basin are substantially older and cannot be connected with data from the western Anti-Atlas (Fig. 5.10). On the basis of old Precambrian ZFT ages, an additional cratonic source area is presumable. While apatite grains are not indicative of a particular provenance, geochemical and petrographic data of zircon grains suggest that the Reguibat Shield, Mauritanides and the WAA are potential source areas (Ali, 2012).

Similar to the Lower Cretaceous, the AFT and ZFT ages of the Upper Cretaceous samples from the TB point to mixed source areas, whereby the majority of the detrital material from the Coniacian to Campanian succession could have been delivered from the Anti-Atlas mountain belt.

5.3.4 Cenozoic

The Cenozoic is characterised by marine layers in the Palaeocene–Eocene, continental sandstones and conglomerates in the Oligocene and sandy limestones in the Miocene (Davison, 2005; El Khatib et al., 1995). Ali (2012) and Ali et al. (2014) supposed the Reguibat Shield, Mauritanides and the western Anti-Atlas as source areas for the Cenozoic due to geochemical and petrographic data of the heavy minerals zircon, tourmaline, rutile, garnet and hornblende. Since the Anti-Atlas

Table 5.4: Apatite fission-track age populations from samples of the Tarfaya Basin

Sample	Stratigraphic age	n	Single grain age distribution [Ma]	P(χ^2) [%]	1. Population High Atlas [Ma]	2. Population Tarfaya Basin Anti-Atlas [Ma]	3. Population Reguibat Arch Anti-Atlas [Ma]
CJ-02	Middle Miocene	10	53.3 - 162.5	22.8	59.0 (±10.8)	136.6 (±16.3)	-
MA-27	Lower Pliocene	20	62.8 - 273.9	0.0	87.5 (±14.8)	165.4 (±11.3)	251.6 (±6.4)
MA-27	Lower Pliocene	20	62.8 - 273.9	0.0	84.1 (±2.3)	162.4 (±62.0)	-
MA-53	Miocene	23	38.5 - 249.5	0.0	-	130.7 (±58.6)	215.9 (±9.1)
MA-54	Miocene	15	35.2 - 220.8	0.0	57.8 (±25.8)	179.9 (±28.5)	-
MA-56	Miocene-Pliocene	22	89.5 - 291.7	0.0	-	156.3 (±37.2)	259.0 (±25.2)
MA-58	Pliocene	9	15.1 - 319.1	0.0	30.6 (±27.9)	159.4 (±21.0)	262.9 (±0.9)
MA-59	Pliocene	24	10.4 - 216.3	0.0	22.9 (±14.2)	171.0 (±36.7)	-
MA-69	Coniacian	22	90.4 - 276.2	0.0	114.7 (±20.6)	171.6 (±3.9)	260.3 (±6.8)
MA-70	Coniacian	16	124.8 - 267.2	3.9	-	167.2 (±46.8)	249.2 (±7.2)
MA-78	Campanian	20	125.9 - 258.6	12.5	-	144.1 (±21.8)	200.0 (±8.9)

n: number of counted apatite grains; P(χ^2): probability that single grains are consistent and belong to the same population.

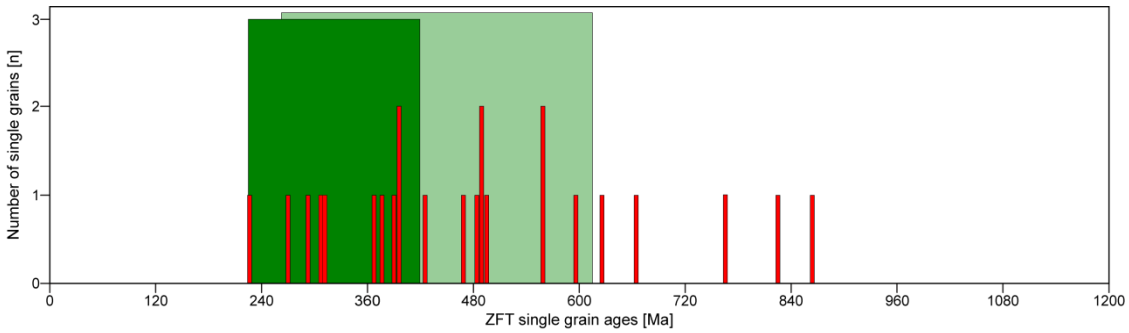

Fig. 5.10: ZFT single grain age distribution of the western Anti-Atlas and the Upper Cretaceous of the Tarfaya Basin. Green: single grain age range from outcrop samples of the WAA; Light Green: single grain age range from well samples of the WAA; Red: Tarfaya Basin.

underwent a recent minor exhumation and erosion starting in the Oligocene (30 Ma), the AA is a potential source area for the Tarfaya Basin during the Cenozoic (Burkhard et al., 2006; Ranke et al., 1982). Furthermore, in the Maastrichtian to Lower Oligocene, the peak Atlasian deformation and surface uplift strongly affected the northeastern onshore TB resulting in flexural rock uplift and erosion of the Meso- to Cenozoic succession down to the Lower Cretaceous (Choubert et al., 1966; Wenke et al., 2011, 2013). Von Rad and Einsele (1980) postulated a rock uplift in the Neogene, contemporaneously to the Canary volcanism. The Atlasian orogeny is reflected in the Tarfaya-Laâyoune-Dakhla Basin by an increasing periodic influx of detrital material into the offshore part of the basin from Upper Cretaceous onward (Hafid et al., 2008; Wenke et al., 2011, 2013).

A provenance analysis of the Palaeogene could not be carried out due to the minor availability of Palaeocene to Oligocene outcrops in the Tarfaya Basin and the lack of apatite and zircon grains in Eocene samples.

Miocene to Pliocene samples have been analysed by the low-temperature thermochronological techniques AFT, ZHe and ZFT. Since the Neogene never experienced temperatures higher than 60 °C, the samples reveal no thermal imprint of the TB and represent solely the thermal history of the source area. The AFT ages are essentially older than the respective stratigraphic age and show a large spread

in the single grain distribution (Fig. 4.22). An age population calculation yielded at least two populations, whereby every sample reveals a population between 131 and 180 Ma (Tab. 5.4). Similar to the Upper Cretaceous samples, the data are in accordance with AFT ages from the Anti-Atlas of the present study and published data considering the AA as source area for the apatite grains of the Neogene (Malusà et al., 2007; Ruiz et al., 2011). Besides, the data correspond to AFT ages from the Cretaceous of the Tarfaya Basin (Tab. 5.4). Since the Meso- to Cenozoic succession has been eroded in large parts of the northeastern onshore TB due to a rock uplift starting in the Palaeogene, the Tarfaya Basin is a further, potential source area for the Neogene sedimentary pile of the western TB (Choubert et al., 1966; Ranke et al., 1982; Wenke et al., 2011, 2013). Thermal modelling of Lower Cretaceous samples confirms exhumation in the northeastern TB since the Palaeocene (Fig. 4.20). An older population ranging from 252 to 263 Ma occurs only in some Miocene to Pliocene samples and correlates with AFT data of the eastern AA mountain belt or could have been sourced from a cratonic area (Malusà et al., 2007) (Tab. 5.4). Contrary to the Upper Cretaceous samples, a younger population varying between 23 and 88 Ma appears in the Neogene samples (Tab. 5.4). The source area of the young population is highly affected by the Atlasian orogeny. Published AFT data of 9–92 Ma from the High Atlas are in consistence with the young population suggesting the HA as source area for the Neogene sedimentary rocks (Balestrieri et al., 2009; Barbero et al., 2007; Missenard et al., 2008). A coastal longitudinal flow, the Canary Current could have delivered the detrital material from the Souss Basin to the Tarfaya Basin.

Three ZHe single grain aliquot ages ranging from 507 to 1016 Ma are significantly older than ZHe ages of the western Anti-Atlas (Fig. 5.11). Consequently, ZHe data are indicative of a cratonic source area for the Miocene to Pliocene rocks.

The ZFT single grain age distribution varying from 245 to 1172 Ma reveals a larger spread than the WAA (Fig. 5.12). As aforementioned, the ZFT ages of the current study and published data range between 226 and 616 Ma in the WAA (Sebti et al., 2009). Hence, some ZFT single grain ages of the Neogene samples from the Tarfaya Basin are substantially older and cannot be associated with data from the western Anti-Atlas pointing to a cratonic source area (Fig. 5.12). A mixed sediment input from the Reguibat Shield, Mauritanides and WAA has been recommended by Ali (2012) and Ali et al. (2014). According to the surface uplift in Morocco due to the Atlasian orogeny in the Cenozoic, the Anti- Atlas, High Atlas and Tarfaya Basin are potential source areas (Burkhard et al., 2006; Frizon de Lamotte et al., 2009; Ranke et al., 1982; von Rad and Einsele, 1980; Wenke et al., 2011).

Concluding, AFT, ZHe and ZFT ages of the Mio- to Pliocene samples from the Tarfaya Basin indicate diverse source areas. The majority of AFT and ZFT ages correspond with data from the western Anti-Atlas and northeastern onshore TB. Similar to the Cretaceous succession, Precambrian ZHe and ZFT ages appear in the thermochronometric data indicating a cratonic source area. In contrast to the Cretaceous, an additional young population points to a further source area highly affected by the Atlasian orogeny.

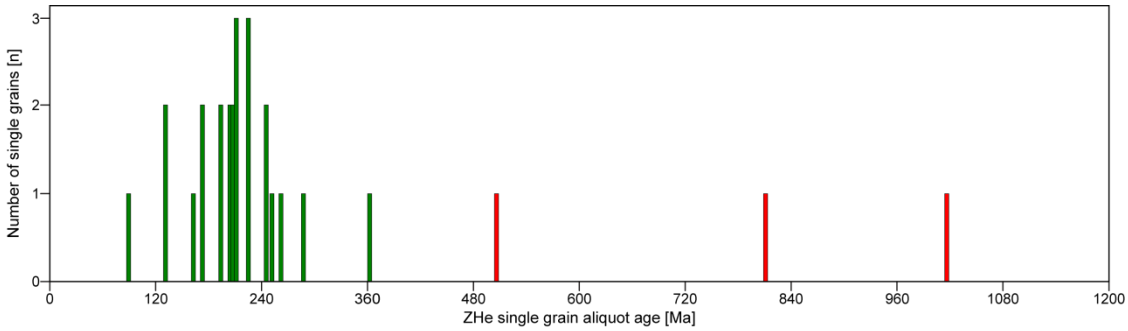

Fig. 5.11: ZHe single grain aliquot ages from outcrop samples of the western Anti-Atlas and the Neogene of the Tarfaya Basin. Green: western Anti-Atlas; Red: Tarfaya Basin.

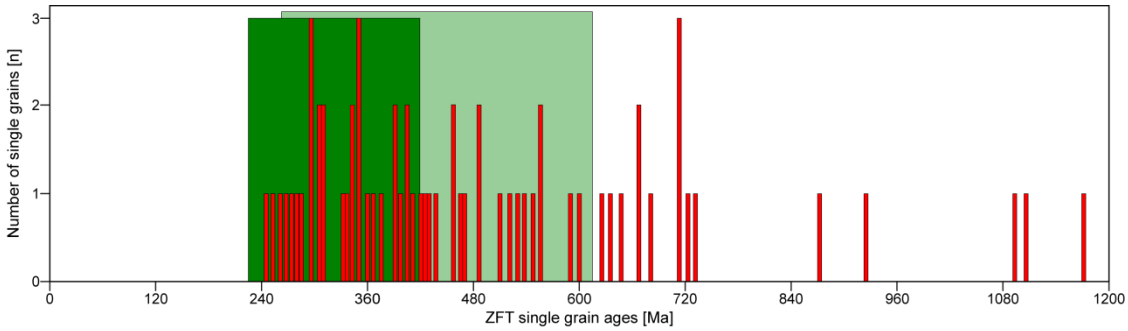

Fig. 5.12: ZFT single grain age distribution of the western Anti-Atlas and the Neogene of the Tarfaya Basin. Green: single grain age range from outcrop samples of the WAA; Light Green: single grain age range from well samples of the WAA; Red: Tarfaya Basin.

Summarising, thermochronological data suggest a continuous sediment transport from the western Anti-Atlas to the Tarfaya Basin from Lower Cretaceous onward to recent times (Fig. 5.13). Furthermore, based on Precambrian ZHe and ZFT ages, a simultaneous sediment input from a cratonic area, i.e. the Reguibat Shield occurred. According to the lack of thermochronological data from the Reguibat Shield, a source-to-sink correlation cannot be established. During the early Upper Cretaceous, a transgression and the deposition of shallow marine sediments in the entire northwestern Morocco led to a decreasing sediment influx from the various source areas into the Tarfaya Basin (Fig. 5.13). Contemporaneously with the surface uplift of the Atlas system, due to the convergence between the African and Eurasian plates in the Neogene, the sediment input from the cratonic area reduced and an influx took place from the High Atlas probably by a coastal longitudinal flow, i.e. the Canary Current. Additionally, the northeastern onshore TB delivered clastic material to the offshore and southern onshore basin.

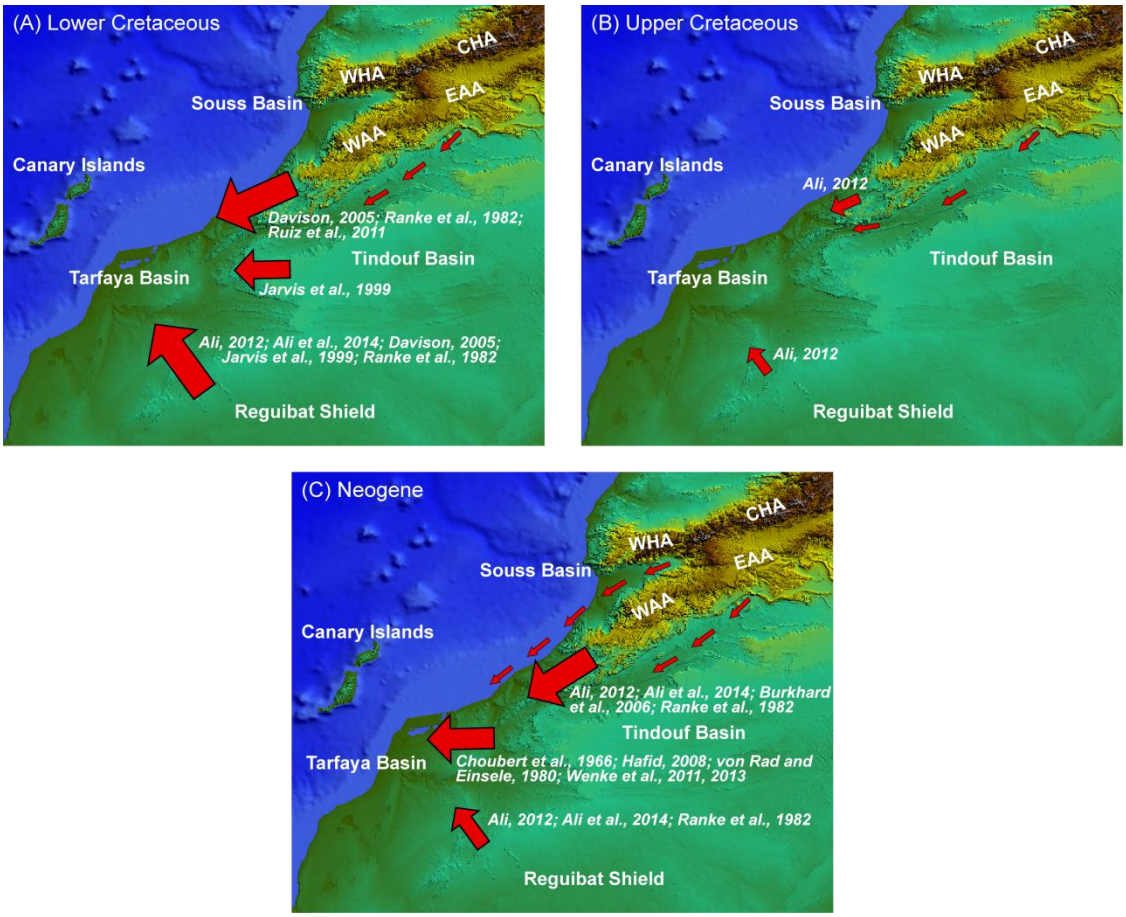

Fig. 5.13: Schematic sediment transport to the Tarfaya Basin based on thermochronological ages and published geological data. WHA: Western High Atlas; CHA: Central High Atlas; WAA: Western Anti-Atlas; EAA: Eastern Anti-Atlas. (A) Lower Cretaceous. (B) Upper Cretaceous. (C) Neogene.

6

CONCLUSIONS

The main research objective was focused on the thermal, subsidence and exhumation history of the Tarfaya Basin in order to better comprehend the hydrocarbon generation in time and space. The Tarfaya Basin is characterised by a vast subsidence history over more than 200 Ma since the onset of the Central Atlantic rifting in Triassic times. In the offshore basin, the subsidence phase continued throughout early to mature drift stages as well as peak Atlasian surface uplift and is still active at present times. In contrast, the northeastern onshore Tarfaya Basin reveals a basin inversion starting in the Palaeogene at 65–50 Ma. The rock uplift and exhumation period resulted in the erosion of a 1.2-1.6 km thick Cretaceous–Palaeogene sedimentary pile at an average rate of 0.025 mm/a. An increasing exhumation from west to east in the onshore basin has been observed. Consequently, the northeastern Tarfaya Basin was strongly affected by peak Atlasian deformation and surface uplift in the Cenozoic. The exhumation stage suggests a sediment transport to the surrounding regions in the Cenozoic and could be an explanation for the increasing periodic influx of detrital material into the offshore and southern onshore Tarfaya Basin since Palaeocene. Besides, thermochronological data substantiate that the Cretaceous to Cenozoic sedimentary rocks never underwent high diagenetic temperatures precluding a Neogene heating event caused by the flow of Canary mantle plume material. The investigation of the Upper Cretaceous–Neogene succession indicates that the major source rock intervals never experienced a heating to 60 °C confirming immature to early mature Cenomanian to Campanian and Eocene source rocks in the onshore Tarfaya Basin. Therefore, future petroleum exploration should concentrate on Jurassic source rocks, which are assumed as sources of the oil shows in the offshore Cap Juby area.

The second objective dealt with the thermal, subsidence and exhumation history of the western Anti-Atlas mountain belt. According to the presence of high surface elevations, the Anti-Atlas constitutes a potential source area for the surrounding basins, i.e. the Tarfaya Basin. Thermochronological data suggest a common geological evolution of the westernmost Precambrian inliers Irherm, Kerdous, Ifni and Bas Drâa. The 300 Ma thermal history of the western Anti-Atlas is dominated by enormous exhumation initiating in the Upper Carboniferous–Lower Permian related to the Variscan folding and post-folding erosion. The rock uplift and exhumation phase lasted beyond the rift and drift stage, as the Anti-Atlas formed the denudation shoulder of the Central Atlantic rift, up to the Lower Cretaceous. Meanwhile, 9 km of Precambrian–Palaeozoic overburden has been eroded at an average rate of 0.046 mm/a. In compliance with the widespread transgression across the

North African continent in the Cenomanian–Turonian, the western Anti-Atlas underwent a minor subsidence phase at an average rate of 0.049 mm/a. Sedimentation in the Anti-Atlas mountain belt during late Lower Cretaceous to Upper Cretaceous yielded a 1.5–2.5 km thick sedimentary pile on top of the Precambrian–Palaeozoic rocks. Subsequently, the final exhumation period started in the Upper Cretaceous, contemporaneously with the earliest record of compressive deformation and surface uplift of the Atlas system in the Senonian (90–65 Ma). The exhumation process and erosion of the 1.5–2.5 km thick Cretaceous overburden continued until present time at an average rate of 0.045 mm/a. Corresponding to the extensive denudation events, the Anti-Atlas mountain belt could have been a potential source area for the Tarfaya Basin since the Triassic. Except for a hiatus in the Upper Cretaceous, a continuous clastic sediment flux to the basin could have been occurred to recent times.

The third objective considered the establishment of a connection between subsidence history of the Tarfaya Basin and exhumation history of the western Anti-Atlas. Consequently, a provenance analysis of the Cretaceous to Neogene sedimentary succession has been performed. Thermochronological data suggest a continuous sediment transport from the western Anti-Atlas to the Tarfaya Basin from Lower Cretaceous onward to recent times. Furthermore, based on Precambrian ages, a simultaneous sediment input from a cratonic area, i.e. the Reguibat Shield, occurred. According to the lack of thermochronometric data from the Reguibat Shield, a source-to-sink correlation cannot be established. During the early Upper Cretaceous, a transgression and the deposition of shallow marine sediments in the entire northwestern Morocco led to a decreasing sediment influx from the various source areas into the Tarfaya Basin. In the Neogene, contemporaneously with the surface uplift of the Atlas mountain belt, the sediment input from the cratonic area reduced and an influx took place from the High Atlas probably by a coastal longitudinal flow, i.e. the Canary Current. Finally, the northeastern onshore Tarfaya Basin delivered clastic material to the offshore and southern onshore basin in the Neogene.

7

REFERENCES

Abou Ali, N., Hafid, M., Chellaï, E.H., Nahim, M., and Zizi, M., 2005, Structure de socle, sismostratigraphie et héritage structural au cours du rifting au niveau de la marge d'Ifni/Tan-Tan (Maroc sud-occidental): Comptes Rendus Geosciences, v. 337, p. 1267-1276.

Ait Brahim, L., Chotin, P., Hinaj, S., Abdelouafi, A., El Adraoui, A., Nakcha, C., Dhont, D., Charroud, M., Sossey Alaoui, F., Amrhar, M., Bouaza, A., Tabyaoui, H., and Chaouni, A., 2002, Paleostress evolution in the Moroccan African margin from Triassic to Present: Tectonophysics, v. 357, p. 187-205.

Ait Malek, H., Gasquet, D., Bertrand, J.M., and Leterrier, J., 1998, Eburnian and Panafrican granitoids from the Igherm, Kerdous and Bas-Draa Proterozoic inliers (western Anti-Atlas, Morocco): U-Pb geochronology on zircon: Comptes Rendus de l'Academie des Sciences Series IIA Earth and Planetary Science, v. 327, p. 819-826.

Algouti, A., Algouti, A., Chbani, B., and Zaim, M., 2001, Sedimentation et volcanisme synsédimentaire de la série de base de l'adoudounien infra-cambrien à travers deux exemples de l'Anti-Atlas du Maroc: Journal of African Earth Sciences, v. 32, p. 541-556.

Ali, S., 2012, Cretaceous to Quaternary Siliciclastic Sediments of the Tarfaya Basin, Marginal Atlantic, SW Morocco: Petrography, Geochemistry, Provenance, Climate and Weathering, Dissertation thesis, Christian-Albrechts-University Kiel.

Ali, S., Stattegger, K., Garbe-Schönberg, D., Kuhnt, W., Kluth, O., and Jabour, H., 2014, Petrography and geochemistry of Cretaceous to quaternary siliciclastic rocks in the Tarfaya basin, SW Morocco: implications for tectonic setting, weathering, and provenance: International Journal of Earth Sciences, v. 103, p. 265-280.

Allen, P.A., and Allen, J.R., 1990, Basin Analysis. Blackwell Scientific Publications, Oxford, 451 pp.

Armstrong, P.A., 2005, Thermochronometers in Sedimentary Basins: Reviews in Mineralogy and Geochemistry, v. 58, p. 499-525.

Babault, J., Teixell, A., Arboleya, M.L., and Charroud, M., 2008, A Late Cenozoic age for long-wavelength surface uplift of the Atlas Mountains of Morocco: Terra Nova, v. 20, p. 102-107.

Balestrieri, M.L., Moratti, G., Bigazzi, G., and Algouti, A., 2009, Neogene exhumation of the Marrakech High Atlas (Morocco) recorded by apatite fission-track analysis: Terra Nova, v. 21, p. 75-82.

Barbarand, J., Hurford, T., and Carter, A., 2003, Variation in apatite fission-track length measurement: implications for thermal history modelling: Chemical Geology, v. 198, p. 77-106.

Barbero, L., Jabaloy, A., Gómez-Ortiz, D., Pérez-Peña, J.V., Rodríguez-Peces, M.J., Tejero, R., Estupiñán, J., Azdimousa, A., Vázquez, M., and Asebriy, L., 2011, Evidence for surface uplift of the Atlas Mountains and the surrounding peripheral plateaux: Combining apatite fission-track results and geomorphic indicators in the Western Moroccan Meseta (coastal Variscan Paleozoic basement): Tectonophysics, v. 502, p. 90-104.

Barbero, L., Teixell, A., Arboleya, M.L., Río, P.d., Reiners, P.W., and Bougadir, B., 2007, Jurassic-to-present thermal history of the central High Atlas (Morocco) assessed by low-temperature thermochronology: Terra Nova, v. 19, p. 58-64.

Bauer, F., Glasmacher, U., Malikwisha, M., Mambo, V., and Mutete, B., 2010, The Eastern Congo—a beauty spot, rediscovered from a geological point of view: Geology Today, v. 26, p. 55-64.

Beauchamp, W., Allmendinger, R.W., Barazangi, M., Demnati, A., El Alji, M., and Dahmani, M., 1999, Inversion tectonics and the evolution of the High Atlas Mountains, Morocco, based on a geological-geophysical transect: Tectonics, v. 18, p. 163-184.

Beauchamp, W., Barazangi, M., Demnati, A., and El Alji, M., 1996, Intracontinental rifting and inversion: Missour Basin and Atlas Mountains, Morocco: AAPG Bulletin, v. 80, p. 1459-1482.

Belfoul, M.A., Falk, F., and Hassenforder, B., 2001, Mise en évidence d'une tectonique tangentielle antérieure au plissenent majeur dans la chaîne hercynienne de l'Anti-Atlas occidental, Maroc: Journal of African Earth Sciences, v. 32, p. 723-739.

Benssaou, M., and Hamoumi, N.m., 2003, Le graben de l'Anti-Atlas occidental (Maroc) : contrôle tectonique de la paléogéographie et des séquences au Cambrien inférieur: Comptes Rendus Geoscience, v. 335, p. 297-305.

Berger, J., Liégeois, J.-P., Ennih, N., and Bonin, B., 2010, Flow of Canary mantle plume material through a subcontinental lithospheric corridor beneath Africa to the Mediterranean: COMMENT: Geology, v. 38, p. e202.

Bertrand, J.M., and Jardim de Sá, E.F., 1990, Where are the Eburnian–Transamazonian collisional belts?: Canadian Journal of Earth Sciences, v. 27, p. 1382-1393.

Bishop, P., 2007, Long-term landscape evolution: linking tectonics and surface processes: Earth Surface Processes and Landforms, v. 32, p. 329-365.

Bonhomme, M.G., and Hassenforder, B., 1985, Le métamorphisme hercynien dans les formations tardi et post-panafricaines de l'Anti-Atlas Occidental (Maroc): données isotopiques Rb/Sr et K/Ar des fractions fines: Sciences Geologiques Bulletin, v. 38, p. 175-183.

Boote, D.R.D., Clark-Lowes, D.D., and Traut, M.W., 1998, Palaeozoic petroleum systems of North Africa: Geological Society, London, Special Publications, v. 132, p. 7-68.

Braun, J., 2002, Quantifying the effect of recent relief changes on age-elevation relationships: Earth and Planetary Science Letters, v. 200, p. 331-343.

Brigaud, F., Lucazeau, F., Ly, S., and Sauvage, J.F., 1985, Heat flow from the West African Shield: Geophys. Res. Lett., v. 12, p. 549-552.

Brix, M.R., Stöckhert, B., Seidel, E., Theye, T., Thomson, S.N., and Küster, M., 2002, Thermobarometric data from a fossil zircon partial annealing zone in high pressure–low temperature rocks of eastern and central Crete, Greece: Tectonophysics, v. 349, p. 309-326.

Broughton, P., and Trepanier, A., 1993, Hydrocarbon generation in the Essaouira Basin of western Morocco: AAPG Bulletin, v. 77, p. 999-1015.

Brown, R.H., 1980, Triassic rocks of Argana Valley, southern Morocco, and their regional structural implications: AAPG Bulletin, v. 64, p. 988-1003.

Burkhard, M., Caritg, S., Helg, U., Robert-Charrue, C., and Soulaimani, A., 2006, Tectonics of the Anti-Atlas of Morocco: Comptes Rendus Geosciences, v. 338, p. 11-24.

Cavaroc, V.V., Padgett, G., Stephens, D.G., Kanes, W.H., Boudda, A., and Woolen, I.D., 1976, Late Paleozoic of the Tindouf Basin, North Africa: Journal of Sedimentary Research, v. 46, p. 77-88.

Charrière, A., Haddoumi, H., Mojon, P.-O., Ferrière, J., Cuche, D., and Zili, L., 2009, Mise en évidence par charophytes et ostracodes de l'âge Paléocène des dépôts discordants sur les rides anticlinales de la région d'Imilchil (Haut Atlas, Maroc) : conséquences paléogéographiques et structurales: Comptes Rendus Palevol, v. 8, p. 9-19.

Choubert, G., 1948, Essai sur la paléogéographie du meso-Crétacé marocain: Volume jubilaire de la Société des sciences naturelles du Maroc, p. 307-329.

Choubert, G., Faure Muret, A., and Hottinger, L., 1966, Aperçu géologique du basin côtier de Tarfaya: Notes et Mémoire du Service Géologique du Maroc, v. 175, p. 9-219.

Cool, T., Katz, B., Dignes, T., Reimers, D., and Fleisher, R., 2008, Hydrocarbon source rock

assessment and revised biostratigraphy of DSDP site 369A, offshore northwest African margin: Journal of Petroleum Geology, v. 31, p. 117-133.

Cowan, G.A., and Adler, H.H., 1976, The variability of the natural abundance of ^{235}U: Geochimica et Cosmochimica Acta, v. 40, p. 1487-1490.

Dalziel, I.W.D., 1997, OVERVIEW: Neoproterozoic-Paleozoic geography and tectonics: Review, hypothesis, environmental speculation: Geological Society of America Bulletin, v. 109, p. 16-42.

Davison, I., 2005, Central Atlantic margin basins of North West Africa: Geology and hydrocarbon potential (Morocco to Guinea): Journal of African Earth Sciences, v. 43, p. 254-274.

Dickin, A.P., 2005, Fission-track dating, Radiogenic Isotope Geology, Cambridge University Press, p. 451-471.

Dodson, M.H., 1973, Closure temperature in cooling geochronological and petrological systems: Contributions to Mineralogy and Petrology, v. 40, p. 259-274.

—, 1979, Theory of Cooling Ages, *in* Jäger, E., and Hunziker, J., eds., Lectures in Isotope Geology, Springer Berlin Heidelberg, p. 194-202.

Donelick, R.A., 1991, Crystallographic orientation dependence of mean etchable fission track length in apatite; an empirical model and experimental observations: American Mineralogist, v. 76, p. 83-91.

—, 1993, A method of fission track analysis utilizing bulk chemical etching of apatite: U.S. Patent #5,267,274.

—, 1995, A method of fission track analysis utilizing bulk chemical etching of apatite: Australia Patent #658,800.

Donelick, R.A., Ketcham, R.A., and Carlson, W.D., 1999, Variability of apatite fission-track annealing kinetics: II. Crystallographic orientation effects: American Mineralogist, v. 84, p. 1224-1234.

Donelick, R.A., Roden, M.K., Mooers, J.D., Carpenter, B.S., and Miller, D.S., 1990, Etchable length reduction of induced fission tracks in apatite at room temperature (≈ 23°C): Crystallographic orientation effects and "initial" mean lengths: International Journal of Radiation Applications and Instrumentation. Part D. Nuclear Tracks and Radiation Measurements, v. 17, p. 261-265.

Duggen, S., Hoernle, K.A., Hauff, F., Klügel, A., Bouabdellah, M., and Thirlwall, M.F., 2009, Flow of Canary mantle plume material through a subcontinental lithospheric corridor beneath Africa to the Mediterranean: Geology, v. 37, p. 283-286.

Dunkl, I., 2002, Trackkey: a Windows program for calculation and graphical presentation of fission track data: Computers & Geosciences, v. 28, p. 3-12.

Dunkl, I., and Székely, B., 2002, Component analysis with visualization of fitting - Popshare, a Windows program for data analysis, Goldschmidt Conference Abstracts, Geochimica et Cosmochimica Acta 66 (15A), p. 201.

Ehlers, T.A., and Farley, K.A., 2003, Apatite (U-Th)/He thermochronometry: methods and applications to problems in tectonic and surface processes: Earth and Planetary Science Letters, v. 206, p. 1-14.

Einsele, G., and Wiedmann, J., 1982, Turonian black shales in the Moroccan coastal basins: first upwelling in the Atlantic Ocean?, *in* von Rad, U., Hinz, K., Sarnthein, M., and Seibold, E., eds., Geology of the northwest African continental margin, Springer Verlag, p. 396-414.

El Arabi, E.H., Diez, J.B., Broutin, J., and Essamoud, R., 2006, Première caractérisation palynologique du Trias moyen dans le Haut Atlas ; implications pour l'initiation du rifting téthysien au Maroc: Comptes Rendus Geoscience, v. 338, p. 641-649.

El Harfi, A., Guiraud, M., and Lang, J., 2006, Deep-rooted "thick skinned" model for the High Atlas Mountains (Morocco). Implications for the structural inheritance of the southern Tethys passive margin: Journal of Structural Geology, v. 28, p. 1958-1976.

El Khatib, J., Ruellan, E., El Foughali, A., and El Morabet, A.M., 1995, Evolution of the southern Morocco Atlantic margin: Tarfaya-Laayoune Basin: Comptes Rendus de l'Académie des Sciences - Series II: Earth and Planetary Science, v. 320, p. 117-124.

El Mostaine, M., 1991, Evaluation du Potentiel Pétrolier du Bassin de Tarfaya-Laayoune onshore. ONAREP internal report #31526, 92 pp.

Ellouz, N., Müller, C., and Faure, J.-L., 1998, Datations et Études Geochimique des Forages BTS1 et MO7 du Bassin de Tarfaya. IFP Internal Report, ONAREP #41016.

Ellouz, N., Patriat, M., Gaulier, J.-M., Bouatmani, R., and Sabounji, S., 2003, From rifting to Alpine inversion: Mesozoic and Cenozoic subsidence history of some Moroccan basins: Sedimentary Geology, v. 156, p. 185-212.

Faik, F., Belfoul, M.A., Bouabdelli, M., and Hassenforder, B., 2001, Les structures de la couverture Néoprotérozoïque terminal et Paléozoïque de la région de Tata, Anti-Atlas centre-occidental, Maroc: déformation polyphasée, ou interactions socle/couverture pendant l'orogenèse hercynienne?: Journal of African Earth Sciences, v. 32, p. 765-776.

Farley, K.A., 2000, Helium diffusion from apatite: General behavior as illustrated by Durango fluorapatite: J. Geophys. Res., v. 105, p. 2903-2914.

—, 2002, (U-Th)/He Dating: Techniques, Calibrations, and Applications: Reviews in Mineralogy and Geochemistry, v. 47, p. 819-844.

Farley, K.A., and Stockli, D.F., 2002, (U-Th)/He Dating of Phosphates: Apatite, Monazite, and Xenotime: Reviews in Mineralogy and Geochemistry, v. 48, p. 559-577.

Farley, K.A., Wolf, R.A., and Silver, L.T., 1996, The effects of long alpha-stopping distances on (U-Th)/He ages: Geochimica et Cosmochimica Acta, v. 60, p. 4223-4229.

Fietchner, L., Friedrichsen, H., and Hammerschmidt, K., 1992, Geochemistry and geochronology of early Mesozoic tholeiites from Central Morocco: Geologische Rundschau, v. 81, p. 45-62.

Fitzgerald, P.G., Baldwin, S.L., Webb, L.E., and O'Sullivan, P.B., 2006, Interpretation of (U-Th)/He single grain ages from slowly cooled crustal terranes: A case study from the Transantarctic Mountains of southern Victoria Land: Chemical Geology, v. 225, p. 91-120.

Fitzgerald, P.G., and Gleadow, A.J.W., 1990, New approaches in fission track geochronology as a tectonic tool: Examples from the transantarctic mountains: International Journal of Radiation Applications and Instrumentation. Part D. Nuclear Tracks and Radiation Measurements, v. 17, p. 351-357.

Fleischer, R.L., Price, P.B., and Walker, R.M., 1965, Tracks of Charged Particles in Solids: Science, v. 149, p. 383-393.

—, 1975, Nuclear Tracks in Solids. Principles and Applications, University of California Press, Berkeley, 605 p.

Flowers, R.M., Ketcham, R.A., Shuster, D.L., and Farley, K.A., 2009, Apatite (U-Th)/He thermochronometry using a radiation damage accumulation and annealing model: Geochimica et Cosmochimica Acta, v. 73, p. 2347-2365.

Flowers, R.M., Shuster, D.L., Wernicke, B.P., and Farley, K.A., 2007, Radiation damage control on apatite (U-Th)/He dates from the Grand Canyon region, Colorado Plateau: Geology, v. 35, p. 447-450.

Frizon de Lamotte, D., Crespo-Blanc, A., Saint-Bezar, B., Comas, M., Fernandez, M., Zeyen, H., Ayarza, P., Robert-Charrue, C., Chalouan, A., Zizi, M., Teixell, A., Arboleya, M.-L., Alvarez-Lobato, F., Julivert, M., and Michard, A., 2004, Transect I: Iberian Meseta, Guadalquivir Basin, Betic Cordillera, Alboran Sea, Rif, Moroccan Meseta, High Atlas, Sahara Domain, *in* Cavazza, W., Roure, F., Spakman, W., Stampfli, G.M., and Ziegler, P.A., eds., The Transmed atlas. The Mediterranean region from crust to mantle.

Frizon de Lamotte, D., Leturmy, P., Missenard, Y., Khomsi, S., Ruiz, G., Saddiqi, O., Guillocheau, F., and Michard, A., 2009, Mesozoic and Cenozoic vertical movements in the Atlas system (Algeria, Morocco, Tunisia): An overview: Tectonophysics, v. 475, p. 9-28.

Frizon de Lamotte, D., Saint Bezar, B., Bracène, R., and Mercier, E., 2000, The two main steps of the Atlas building and geodynamics of the western Mediterranean: Tectonics, v. 19, p. 740-761.

Frizon de Lamotte, D., Zizi, M., Missenard, Y., Hafid, M., El Azzouzi, M., Maury, R.C., Charrière, A., Taki, Z., Benammi, M., and Michard, A., 2008, The Atlas System, *in* Michard, A., Saddiqi, O.,

Chalouan, A., and Frizon de Lamotte, D., eds., Continental Evolution: The Geology of Morocco: Berlin, Heidelberg, Springer-Verlag, p. 133-202.

Froitzheim, N., Stets, J., and Wurster, P., 1988, Aspects of Western High Atlas tectonics, *in* Jacobshagen, V., ed., The Atlas System of Morocco, Volume 15: Lecture Notes in Earth Sciences, Springer Berlin / Heidelberg, p. 219-244.

Fullea, J., Fernàndez, M., Afonso, J.C., Vergés, J., and Zeyen, H., 2010, The structure and evolution of the lithosphere–asthenosphere boundary beneath the Atlantic–Mediterranean Transition Region: Lithos, v. 120, p. 74-95.

Galbraith, R., 1981, On statistical models for fission track counts: Mathematical Geology, v. 13, p. 471-478.

Galbraith, R.F., and Laslett, G.M., 1993, Statistical models for mixed fission track ages: Nuclear Tracks and Radiation Measurements, v. 21, p. 459-470.

Garver, J., 2002, Discussion: "Metamictisation of natural zircon: accumulation versus thermal annealing of radioactivity-induced damage" by Nasdala et al. 2001 (<SMALL>Contributions to Mineralogy and Petrology</SMALL> 141:125-144): Contributions to Mineralogy and Petrology, v. 143, p. 756-757.

Garver, J.I., 2003, Etching zircon age standards for fission-track analysis: Radiation Measurements, v. 37, p. 47-53.

Garver, J.I., and Kamp, P.J.J., 2002, Integration of zircon color and zircon fission-track zonation patterns in orogenic belts: application to the Southern Alps, New Zealand: Tectonophysics, v. 349, p. 203-219.

Gasquet, D., Chevremont, P., Baudin, T., Chalot-Prat, F., Guerrot, C., Cocherie, A., Roger, J., Hassenforder, B., and Cheilletz, A., 2004, Polycyclic magmatism in the Tagragra d'Akka and Kerdous–Tafeltast inliers (Western Anti-Atlas, Morocco): Journal of African Earth Sciences, v. 39, p. 267-275.

Gasquet, D., Ennih, N., Liégeois, J.P., Soulaimani, A., and Michard, A., 2008, The Pan-African Belt, *in* Michard, A., Saddiqi, O., Chalouan, A., and Frizon de Lamotte, D., eds., Continental Evolution: The Geology of Morocco: Berlin, Heidelberg, Springer-Verlag, p. 33-64.

Geisler, T., Ulonska, M., Schleicher, H., Pidgeon, R., and van Bronswijk, W., 2001, Leaching and differential recrystallization of metamict zircon under experimental hydrothermal conditions: Contributions to Mineralogy and Petrology, v. 141, p. 53-65.

Ghorbal, B., Bertotti, G., Foeken, J., and Andriessen, P., 2008, Unexpected Jurassic to Neogene vertical movements in 'stable' parts of NW Africa revealed by low temperature geochronology: Terra Nova, v. 20, p. 355-363.

Giese, P., and Jacobshagen, V., 1992, Inversion tectonics of intracontinental ranges: High and Middle Atlas, Morocco: Geologische Rundschau, v. 81, p. 249-259.

Glasmacher, U.A., Zentilli, M., and Grist, A.M., 1998, Apatite fission track thermochronology of Paleozoic sandstones and the Hill-intrusion, Northern Linksrheinisches Schiefergebirge, Germany, *in* van den Haute, P., and de Corte, F., eds., Advances in Fission-Track Geochronology, Volume 10: Solid Earth Sciences Library, Kluwer Academic Publishers, p. 151-172.

Gleadow, A.J.W., and Fitzgerald, P.G., 1987, Uplift history and structure of the Transantarctic Mountains: new evidence from fission track dating of basement apatites in the Dry Valleys area, southern Victoria Land: Earth and Planetary Science Letters, v. 82, p. 1-14.

Gleadow, A.J.W., Hurford, A.J., and Quaife, R.D., 1976, Fission track dating of zircon: Improved etching techniques: Earth and Planetary Science Letters, v. 33, p. 273-276.

Gouiza, M., Bertotti, G., Hafid, M., and Cloetingh, S., 2010, Kinematic and thermal evolution of the Moroccan rifted continental margin: Doukkala-High Atlas transect: Tectonics, v. 29, p. TC5008.

Gradstein, F., Ogg, J., and Smith, A., 2004, A Geologic Time Scale: Cambridge, Cambridge University Press, 589 p.

Green, P.F., 1981, "Track-in-track" length measurements in annealed apatites: Nuclear Tracks, v. 5, p. 121-128.

—, 1988, The relationship between track shortening and fission track age reduction in apatite: combined influences of inherent instability, annealing anisotropy, length bias and system calibration: Earth and Planetary Science Letters, v. 89, p. 335-352.

Green, P.F., Duddy, I.R., and Bray, R.J., 1995, Applications of Thermal History Reconstruction in inverted basins: Geological Society, London, Special Publications, v. 88, p. 149-165.

Green, P.F., Duddy, I.R., and Hegarty, K.A., 2002, Quantifying exhumation from apatite fission-track analysis and vitrinite reflectance data: precision, accuracy and latest results from the Atlantic margin of NW Europe: Geological Society, London, Special Publications, v. 196, p. 331-354.

Green, P.F., and Durrani, S.A., 1977, Annealing studies of tracks in crystals: Nuclear Track Detection, v. 1, p. 33-39.

Grist, A.M., and Ravenhurst, C.E., 1992a, Mineral separation techniques used at Dalhousie University, *in* Zentilli, M., and Reynolds, P.H., eds., Short course on low temperature thermochronology, Mineralogical Association of Canada Short Course Handbook 20, p. 203-209, Appendix 2.

—, 1992b, A step-by-step laboratory guide to fission-track thermochronology at Dalhousie University, *in* Zentilli, M., and Reynolds, P.H., eds., Short course on low temperature thermochronology Mineralogical Association of Canada Short Course Handbook 20, p. 190-201, Appendix 1.

Grobe, R.W., 2011, Long-term landscape evolution, cooling and exhumation history of Variscan rocks in the western Cantabrian Mountains (NW Spain), Dissertation thesis, University Heidelberg.

Guenthner, W.R., and Reiners, P.W., 2010, Effects and implications of radiation damage on He diffusion in zircon: Thermo2010, 12th International conference on Thermochronology, Glasgow 16-20 August.

Guiraud, R., Bosworth, W., Thierry, J., and Delplanque, A., 2005, Phanerozoic geological evolution of Northern and Central Africa: An overview: Journal of African Earth Sciences, v. 43, p. 83-143.

Gunnell, Y., Calvet, M., Brichau, S., Carter, A., Aguilar, J.P., and Zeyen, H., 2009, Low long-term erosion rates in high-energy mountain belts: Insights from thermo- and biochronology in the Eastern Pyrenees: Earth and Planetary Science Letters, v. 278, p. 208-218.

Hafid, M., Tari, G., Bouhadioui, D., El Moussaid, I., Echarfaoui, H., Ait Salem, A., Nahim, M., and Dakki, M., 2008, Atlantic Basins, *in* Michard, A., Saddiqi, O., Chalouan, A., and Frizon de Lamotte, D., eds., Continental Evolution: The Geology of Morocco: Berlin, Heidelberg, Springer-Verlag, p. 303-329.

Hafid, M., Zizi, M., Bally, A.W., and Ait Salem, A., 2006, Structural styles of the western onshore and offshore termination of the High Atlas, Morocco: Comptes Rendus Geosciences, v. 338, p. 50-64.

Hames, W.E., McHone, J.G., Renne, P.R., and Ruppel, C., 2003, The Central Atlantic Magmatic Province: Insights from fragments of Pangea: Washington DC, American Geophysical Union.

Hames, W.E., Renne, P.R., and Ruppel, C., 2000, New evidence for geologically instantaneous emplacement of earliest Jurassic Central Atlantic magmatic province basalts on the North American margin: Geology, v. 28, p. 859-862.

Hanna, G.C., Westcott, C.H., Lemmel, H.D., Leonard, B.R., Story, J.S., and Attree, P.M., 1969, Revision of values for the 2200 m/s neutron constants for four fissile nuclides: G.E.C. Atomic Energy Review, v. 7, p. 3-92.

Hasebe, N., Mori, S., Tagami, T., and Matsui, R., 2003, Geological partial annealing zone of zircon fission-track system: additional constrains from the deep drilling MITI-Nishikubiki and MITI-Mishima: Chemical Geology, v. 199, p. 45-52.

Helg, U., Burkhard, M., Caritg, S., and Robert-Charrue, C., 2004, Folding and inversion tectonics in the Anti-Atlas of Morocco: Tectonics, v. 23, p. TC4006.

Herbin, J.P., Montadert, L., Muller, C., Gomez, R., Thurow, J., and Wiedmann, J., 1986, Organic-rich sedimentation at the Cenomanian-Turonian boundary in oceanic and coastal basins in the North Atlantic and Tethys: Geological Society, London, Special Publications, v. 21, p. 389-422.

Heyman, M.A.W., 1989, Tectonic and depositional history of the Moroccan continental margin, *in* Tankard, A.J., and Balkwill, H.R., eds., Extensional tectonics and strigraphy of the North Atlantic margins, AAPG Memoir 46, p. 323-340.

Hill, K.C., Hill, K.A., Cooper, G.T., O'Sullivan, A.J., O'Sullivan, P.B., and Richardson, M.J., 1995, Inversion around the Bass Basin, SE Australia: Geological Society, London, Special Publications, v. 88, p. 525-547.

Hoepffner, C., Houari, M.R., and Bouabdelli, M., 2006, Tectonics of the North African Variscides (Morocco, western Algeria): an outline: Comptes Rendus Geosciences, v. 338, p. 25-40.

Hoepffner, C., Soulaimani, A., and Piqué, A., 2005, The Moroccan Hercynides: Journal of African Earth Sciences, v. 43, p. 144-165.

House, M.A., Farley, K.A., and Kohn, B.P., 1999, An empirical test of helium diffusion in apatite: borehole data from the Otway basin, Australia: Earth and Planetary Science Letters, v. 170, p. 463-474.

House, M.A., Farley, K.A., and Stockli, D., 2000, Helium chronometry of apatite and titanite using Nd-YAG laser heating: Earth and Planetary Science Letters, v. 183, p. 365-368.

Hurford, A.J., 1990, Standardization of fission track dating calibration: Recommendation by the Fission Track Working Group of the I.U.G.S. Subcommission on Geochronology: Chemical Geology: Isotope Geoscience section, v. 80, p. 171-178.

Hurford, A.J., and Green, P.F., 1982, A users' guide to fission track dating calibration: Earth and Planetary Science Letters, v. 59, p. 343-354.

—, 1983, The zeta age calibration of fission-track dating: Chemical Geology, v. 41, p. 285-317.

Jabour, H., Morabet, A.M., and Bouchta, R., 2000, Hydrocarbon systems of Morocco, *in* Crasquin-Soleau, S., and Barrier, E., eds., Peri-Thetys Memoir 5; New data on Peri-Tethyan sedimentary basins: Paris, Editions du Museum National d'Histoire Naturelle 182, p. 143-157.

Jaffey, A.H., Flynn, K.F., Glendenin, L.E., Bentley, W.C., and Essling, A.M., 1971, Precision Measurement of Half-Lives and Specific Activities of ^{235}U and ^{238}U: Physical Review C, v. 4, p. 1889-1906.

Jansa, L.F., 1981, Mesozoic carbonate platforms and banks of the eastern North American margin: Marine Geology, v. 44, p. 97-117.

Jarvis, J., Fish, P., and Garwood, T., 1999, Morocco's Tarfaya deepwater prospects encouraging: Oil & Gas Journal, v. 97, p. 90-94.

Ketcham, R.A., 2003, Observations on the relationship between crystallographic orientation and biasing in apatite fission-track measurements: American Mineralogist, v. 88, p. 817-829.

—, 2005, Forward and Inverse Modeling of Low-Temperature Thermochronometry Data: Reviews in Mineralogy and Geochemistry, v. 58, p. 275-314.

—, 2011, HeFTy version 1.7.4, Manual.

Ketcham, R.A., Carter, A., Donelick, R.A., Barbarand, J., and Hurford, A.J., 2007a, Improved measurement of fission-track annealing in apatite using c-axis projection: American Mineralogist, v. 92, p. 789-798.

—, 2007b, Improved modeling of fission-track annealing in apatite: American Mineralogist, v. 92, p. 799-810.

Ketcham, R.A., Donelick, R.A., Balestrieri, M.L., and Zattin, M., 2009, Reproducibility of apatite fission-track length data and thermal history reconstruction: Earth and Planetary Science Letters, v. 284, p. 504-515.

Ketcham, R.A., Donelick, R.A., and Carlson, W.D., 1999, Variability of apatite fission-track annealing kinetics: III. Extrapolation to geological time scales: American Mineralogist, v. 84, p. 1235-1255.

Klitgord, K.D., and Schouten, H., 1986, Plate kinematics of the central Atlantic *in* Vogt, P.R., and Tucholke, B.E., eds., The Western North Atlantic Region: Boulder, Gelogical Society of America, p. 351-378.

Knight, K.B., Nomade, S., Renne, P.R., Marzoli, A., Bertrand, H., and Youbi, N., 2004, The Central Atlantic Magmatic Province at the Triassic-Jurassic boundary: paleomagnetic and $^{40}Ar/^{39}Ar$

evidence from Morocco for brief, episodic volcanism: Earth and Planetary Science Letters, v. 228, p. 143-160.

Kolonic, S., Sinninghe Damsté, J.S., Böttcher, M.E., Kuypers, M.M.M., Kuhnt, W., Beckmann, B., Scheeder, G., and Wagner, T., 2002, Geochemical characterization of Cenomanian/Turonian black shales from the Tarfaya Basin (SW Morocco): Journal of Petroleum Geology, v. 25, p. 325-350.

Kolonic, S., Wagner, T., Forster, A., Sinninghe Damsté, J.S., Walsworth-Bell, B., Erba, E., Turgeon, S., Brumsack, H.-J., Chellai, E.H., Tsikos, H., Kuhnt, W., and Kuypers, M.M.M., 2005, Black shale deposition on the northwest African Shelf during the Cenomanian/Turonian oceanic anoxic event: Climate coupling and global organic carbon burial: Paleoceanography, v. 20, p. PA1006.

Kuhnt, W., Chellai, E.H., Holbourn, A., Luderer, F., Thurow, J., Wagner, T., El Albani, A., Beckmann, B., Herbin, J.-P., Kawamura, H., Kolonic, S., Nederbragt, S., Street, C., and Ravilious, K., 2001, Morocco Basin's sedimentary record may provide correlations for Cretaceous paleoceanographic events worldwide: Eos Trans. AGU, v. 82, p. 361-364.

Kuhnt, W., Herbin, J.P., Thurow, J., and Wiedmann, J., 1990, Distribution of Cenomanian-Turonian organic facies in the western Mediterranean and along the adjacent Atlantic margin, *in* Huc, A.Y., ed., Deposition of organic facies, AAPG Studies in Geology 30, p. 133-160.

Kuhnt, W., Holbourn, A., Gale, A., Chellai, E.H., and Kennedy, W.J., 2009, Cenomanian sequence stratigraphy and sea-level fluctuations in the Tarfaya Basin (SW Morocco): Geological Society of America Bulletin, v. 121, p. 1695-1710.

Kuhnt, W., Luderer, F., Nederbragt, S., Thurow, J., and Wagner, T., 2005, Orbital-scale record of the late Cenomanian–Turonian oceanic anoxic event (OAE-2) in the Tarfaya Basin (Morocco): International Journal of Earth Sciences, v. 94, p. 147-159.

Lancelot, Y., and Winterer, E.L., 1981, Evolution of the Moroccan oceanic basin and adjacent continental margin - a synthesis, Initial Report Deep Sea Drilling Project 50, 801-821.

Laslett, G.M., Gleadow, A.J.W., and Duddy, I.R., 1984, The relationship between fission track length and track density in apatite: Nuclear Tracks and Radiation Measurements (1982), v. 9, p. 29-38.

Laville, E., Charroud, A., Fedan, B., Charroud, M., and Piqué, A., 1995, Inversion négative et rifting atlasique: lèxemple du bassin triasique de Kerrouchène, Maroc: Bulletin de la Société Géologique de France, v. 166, p. 364-374.

Laville, E., Pique, A., Amrhar, M., and Charroud, M., 2004, A restatement of the Mesozoic Atlasic Rifting (Morocco): Journal of African Earth Sciences, v. 38, p. 145-153.

Le Roy, P., Guillocheau, F., Piqué, A., and Morabet, A.M., 1998, Subsidence of the Atlantic Moroccan margin during the Mesozoic: Canadian Journal of Earth Sciences, v. 35, p. 476-493.

Le Roy, P., and Piqué, A., 2001, Triassic-Liassic Western Moroccan synrift basins in relation to the Central Atlantic opening: Marine Geology, v. 172, p. 359-381.

Lecorche, J.P., Bronner, G., Dallmeyer, R.D., Rocci, G., and Roussel, J., 1991, The Mauritanide Orogen and its northern extension (Western Sahara and Zemmour), West Africa, *in* Dallmeyer, R.D., and Lecorche, J.P., eds., The West African orogens and circum-Atlantic correlatives: Berlin, Springer-Verlag, p. 187-227.

Leine, L., 1986, Geology of the Tarfaya oil shale deposit, Morocco: Geologie en Mijnbouw - Netherlands Journal of Geosciences, v. 65, p. 57-74.

Lisker, F., Ventura, B., and Glasmacher, U.A., 2009, Apatite thermochronology in modern geology: Geological Society, London, Special Publications, v. 324, p. 1-23.

Lucazeau, F., Lesquer, A., and Vasseur, G., 1988, Trends of heat flow density from West Africa, Unpublished report, C. G. G.: Montpellier.

Lüning, S., Kolonic, S., Belhadj, E.M., Belhadj, Z., Cota, L., Barić, G., and Wagner, T., 2004, Integrated depositional model for the Cenomanian–Turonian organic-rich strata in North Africa: Earth-Science Reviews, v. 64, p. 51-117.

Lugmair, G.W., and Marti, K., 1978, Lunar initial 143Nd/144Nd: Differential evolution of the lunar crust and mantle: Earth and Planetary Science Letters, v. 39, p. 349-357.

Macgregor, D.S., 1996, The hydrocarbon systems of North Africa: Marine and Petroleum Geology, v. 13, p. 329-340.

—, 1998, Introduction: Geological Society, London, Special Publications, v. 132, p. 1-6.

Macgregor, D.S., and Moody, R.T.J., 1998, Mesozoic and Cenozoic petroleum systems of North Africa: Geological Society, London, Special Publications, v. 132, p. 201-216.

Malusà, M.G., Polino, R., Feroni, A.C., Ellero, A., Ottria, G., Baidder, L., and Musumeci, G., 2007, Post-Variscan tectonics in eastern Anti-Atlas (Morocco): Terra Nova, v. 19, p. 481-489.

Margoum, A., 2001, Le Précambrian de l'Anti-Atlas occidental. La boutonnière du Kerdous. Etude microstructurale et géochronologique, Mémoire T.E.R., Université de Bretagne occidentale, inédit, p. 32.

Marzoli, A., Bertrand, H., Knight, K.B., Cirilli, S., Buratti, N., Vérati, C., Nomade, S., Renne, P.R., Youbi, N., Martini, R., Allenbach, K., Neuwerth, R., Rapaille, C., Zaninetti, L., and Bellieni, G., 2004, Synchrony of the Central Atlantic magmatic province and the Triassic-Jurassic boundary climatic and biotic crisis: Geology, v. 32, p. 973-976.

McHone, J.G., 2000, Non-plume magmatism and rifting during the opening of the central Atlantic Ocean: Tectonophysics, v. 316, p. 287-296.

Michard, A., 1976, Eléments de Géologie Marocaine. Notes et Mémoires du Service Géologique du Maroc 252, Rabat, 420 pp.

Michard, A., Frizon de Lamotte, D., Saddiqi, O., and Chalouan, A., 2008a, An Outline of the Geology of Morocco, *in* Michard, A., Saddiqi, O., Chalouan, A., and Frizon de Lamotte, D., eds., Continental Evolution: The Geology of Morocco: Berlin, Heidelberg, Springer-Verlag, p. 1-32.

Michard, A., Hoepffner, C., Soulaimani, A., and Baidder, L., 2008b, The Variscan Belt, *in* Michard, A., Saddiqi, O., Chalouan, A., and Frizon de Lamotte, D., eds., Continental Evolution: The Geology of Morocco: Lecture Notes in Earth Sciences: Berlin, Heidelberg, Springer-Verlag, p. 65-132.

Michard, A., Soulaimani, A., Hoepffner, C., Ouanaimi, H., Baidder, L., Rjimati, E.C., and Saddiqi, O., 2010, The South-Western Branch of the Variscan Belt: Evidence from Morocco: Tectonophysics, v. 492, p. 1-24.

Michard, A., Yazidi, A., Benziane, F., Hollard, H., and Willefert, S., 1982, Foreland thrusts and olistromes on the pre-Sahara margin of the Variscan orogen, Morocco: Geology, v. 10, p. 253-256.

Miller, D.S., and Duddy, I.R., 1989, Early Cretaceous uplift and erosion of the northern Appalachian Basin, New York, based on apatite fission track analysis: Earth and Planetary Science Letters, v. 93, p. 35-49.

Ministére de l'Energie et des Mines, D.d.l.G., 1985, Carte Géologique du Maroc: Paris.

Missenard, Y., Saddiqi, O., Barbarand, J., Leturmy, P., Ruiz, G., El Haimer, F.Z., and Frizon de Lamotte, D., 2008, Cenozoic denudation in the Marrakech High Atlas, Morocco: insight from apatite fission-track thermochronology: Terra Nova, v. 20, p. 221-228.

Missenard, Y., Zeyen, H., Frizon de Lamotte, D., Leturmy, P., Petit, C., Sébrier, M., and Saddiqi, O., 2006, Crustal versus asthenospheric origin of relief of the Atlas Mountains of Morocco: J. Geophys. Res., v. 111, p. B03401.

Mitchell, S.G., and Reiners, P.W., 2003, Influence of wildfires on apatite and zircon (U-Th)/He ages: Geology, v. 31, p. 1025-1028.

Morabet, A.M., Bouchta, R., and Jabour, H., 1998, An overview of the petroleum systems of Morocco: Geological Society London, Special Publications, v. 132, p. 283-296.

Morel, J.-L., Zouine, E.-M., Andrieux, J., and Faure-Muret, A., 2000, Déformations néogènes et quaternaires de la bordure nord haut atlasique (Maroc): rôle du socle et consequences structurales: Journal of African Earth Sciences, v. 30, p. 119-131.

Mustaphi, H., Medina, F., Jabour, H., and Hoepffner, C., 1997, Le bassin du Souss (Zone de

Faille du Tizi n'Test, Haut Atlas occidental, Maroc): résultat d'une inversion tectonique contrlée par une faille de détachement profonde: Journal of African Earth Sciences, v. 24, p. 153-168.

Naeser, C.W., 1979, Thermal history of sedimentary basins in fission track dating of subsurface rocks: SEPM Special Publication, v. 26, p. 109-112.

Nasdala, L., 2009, Pb^{+} irradiation of synthetic zircon (ZrSiO4): Infrared spectroscopic investigation—Discussion: American Mineralogist, v. 94, p. 853-855.

Nasdala, L., Reiners, P.W., Garver, J.I., Kennedy, A.K., Stern, R.A., Balan, E., and Wirth, R., 2004, Incomplete retention of radiation damage in zircon from Sri Lanka: American Mineralogist, v. 89, p. 219-231.

Nasdala, L., Wenzel, M., Vavra, G., Irmer, G., Wenzel, T., and Kober, B., 2001, Metamictisation of natural zircon: accumulation versus thermal annealing of radioactivity-induced damage: Contributions to Mineralogy and Petrology, v. 141, p. 125-144.

Nzoussi-Mbassani, P., Disnar, J.R., and Laggoun-Défarge, F., 2003, Organic matter characteristics of Cenomanian–Turonian source rocks: implications for petroleum and gas exploration onshore Senegal: Marine and Petroleum Geology, v. 20, p. 411-427.

Nzoussi-Mbassani, P., Khamli, N., Disnar, J.R., Laggoun-Défarge, F., and Boussafir, M., 2005, Cenomanian-Turonian organic sedimentation in North-West Africa: A comparison between the Tarfaya (Morocco) and Senegal Basins: Sedimentary Geology, v. 177, p. 271-295.

Olsen, P.E., Kent, D.V., Et-Touhami, M., and Puffer, J.H., 2003, Cyclo-, Magneto-, and Bio-Stratigraphic Constraints on the Duration of the CAMP Event and its Relationship to the Triassic-Jurassic Boundary, *in* Hames, W.E., McHone, J.G., Renne, P.R., and Ruppel, C., eds., The Central Atlantic Magmatic Province: Insights from fragments of Pangea: Washington DC, American Geophysical Union Monograph 136, p. 7-32.

ONAREP, 2002, Rabat-Safi segment Hydrocarbon Exploration Play Summary, Publicity Brochure.

—, 2003, Opportunities for Hydrocarbon Exploration and Production in Morocco. Publicity Brochure.

Pique, A., Bouabdelli, M., Soulaimani, A., Youbi, N., and Iliani, M., 1999, The Late Proterozoic PIII conglomerates of the Anti Atlas (southern Morocco). Their relationships with the Panafrican orogeny or a Late Proterozoic rifting episode: Comptes Rendus de l'Academie des Sciences Series IIA Earth and Planetary Science, v. 328, p. 409-414.

Piqué, A., and Laville, E., 1996, The central Atlantic rifting: Reactivation of Palaeozoic structures?: Journal of Geodynamics, v. 21, p. 235-255.

Pique, A., and Michard, A., 1989, Moroccan Hercynides; a synopsis; the Paleozoic sedimentary and tectonic evolution at the northern margin of West Africa: Am J Sci, v. 289, p. 286-330.

Rahn, M.K., Brandon, M.T., Batt, G.E., and Garver, J.I., 2004, A zero-damage model for fission-track annealing in zircon: American Mineralogist, v. 89, p. 473-484.

Ranke, U., von Rad, U., and Wissmann, G., 1982, Stratigraphy, facies and tectonic development of the onshore and offshore Aaiun-Tarfaya Basin - a review, *in* von Rad, U., Hinz, K., Sarnthein, M., and Seibold, E., eds., Geology of the northwest African continental margin, Springer Verlag, p. 86-105.

Ravenhurst, C.E., and Donelick, R.A., 1992, Fission track thermochronology, *in* Zentilli, M., and Reynolds, P.H., eds., Short course on low temperature thermochronology Mineralogical Association of Canada Short Course Handbook 20, p. 21-42.

Reiners, P.W., 2005, Zircon (U-Th)/He Thermochronometry: Reviews in Mineralogy and Geochemistry, v. 58, p. 151-179.

Reiners, P.W., and Brandon, M.T., 2006, Using thermochronology to understand orogenic erosion: Annual Review of Earth and Planetary Sciences, v. 34, p. 419-466.

Reiners, P.W., and Farley, K.A., 2001, Influence of crystal size on apatite (U–Th)/He thermochronology: an example from the Bighorn

Mountains, Wyoming: Earth and Planetary Science Letters, v. 188, p. 413-420.

Reiners, P.W., Farley, K.A., and Hickes, H.J., 2002, He diffusion and (U-Th)/He thermochronometry of zircon: initial results from Fish Canyon Tuff and Gold Butte: Tectonophysics, v. 349, p. 297-308.

Reiners, P.W., Spell, T.L., Nicolescu, S., and Zanetti, K.A., 2004, Zircon (U-Th)/He thermochronometry: He diffusion and comparisons with $^{40}Ar/^{39}Ar$ dating: Geochimica et Cosmochimica Acta, v. 68, p. 1857-1887.

Rimi, A., 1990, Geothermal gradients and heat flow trends in Morocco: Geothermics, v. 19, p. 443-454.

—, 1999, Mantle heat flow and geotherms for the main geologic domains in Morocco: International Journal of Earth Sciences, v. 88, p. 458-466.

—, 2000, First assessment of geothermal ressources in Morocco, World Geothermal Congress: Kyushu-Tohoku, Japan, p. 397-402.

—, 2001, Carte du gradient géothermique au Maroc: Bulletin de l'Institut scientifique, Rabat, Section Sciences de la Terre, v. 23, p. 1-6.

Rimi, A., Chalouan, A., and Bahi, L., 1998, Heat flow in the westernmost part of the Alpine Mediterranean system (the Rif, Morocco): Tectonophysics, v. 285, p. 135-146.

Rimi, A., and Lucazeau, F., 1987, Heat flow density measurements in northern Morocco: Journal of African Earth Sciences, v. 6, p. 835-843.

Rodgers, J.J.W., and Santosh, M., 2002, Configuration of Columbia, a Mesoproterozoic supercontinent, *in* Rodgers, J.J.W., and Santosh, M., eds., Mesoproterozoic supercontinent, International Association for Gondwana Research 5, p. 5-22.

Rosenbaum, G., Lister, G.S., and Duboz, C., 2002, Relative motions of Africa, Iberia and Europe during Alpine orogeny: Tectonophysics, v. 359, p. 117-129.

Ruiz, G., Helg, U., Negro, F., Adatte, T., and Burkhard, M., 2008, Illite crystallinity patterns in the Anti-Atlas of Morocco: Swiss Journal of Geosciences, v. 101, p. 387-395.

Ruiz, G.M.H., Sebti, S., Negro, F., Saddiqi, O., Frizon de Lamotte, D., Stockli, D., Foeken, J., Stuart, F., Barbarand, J., and Schaer, J.P., 2011, From central Atlantic continental rift to Neogene uplift – western Anti-Atlas (Morocco): Terra Nova, v. 23, p. 35-41.

Sachse, V.F., 2011, Petroleum source rocks of western and central Africa: the examples of the marine Tarfaya Basin, Morocco and the continental Congo Basin, Democratic Republic of Congo, Dissertation thesis, RWTH Aachen University.

Sachse, V.F., Heim, S., Jabour, H., Kluth, O., Schümann, T., Aquit, M., and Littke, R., 2014, Organic geochemical characterization of Santonian to Early Campanian organic matter-rich marls (Sondage No 1 cores) as related to OAE3 from the Tarfaya Basin, Morocco: Marine and Petroleum Geology.

Sachse, V.F., Littke, R., Heim, S., Kluth, O., Schober, J., Boutib, L., Jabour, H., Perssen, F., and Sindern, S., 2011, Petroleum source rocks of the Tarfaya Basin and adjacent areas, Morocco: Organic Geochemistry, v. 42, p. 209-227.

Sachse, V.F., Littke, R., Jabour, H., Schümann, T., and Kluth, O., 2012, Late Cretaceous (Late Turonian, Coniacian and Santonian) petroleum source rocks as part of an OAE, Tarfaya Basin, Morocco: Marine and Petroleum Geology, v. 29, p. 35-49.

Saddiqi, O., El Haimer, F.Z., Michard, A., Barbarand, J., Ruiz, G.M.H., Mansour, E.M., Leturmy, P., and Frizon de Lamotte, D., 2009, Apatite fission-track analyses on basement granites from south-western Meseta, Morocco: Paleogeographic implications and interpretation of AFT age discrepancies: Tectonophysics, v. 475, p. 29-37.

Sahabi, M., Aslanian, D., and Olivet, J.-L., 2004, Un nouveau point de départ pour l'histoire de l'Atlantique central: Comptes Rendus Geosciences, v. 336, p. 1041-1052.

Saquaque, A., Admou, H., Karson, J., Hefferan, K., and Reuber, I., 1989, Precambrian accretionary tectonics in the Bou Azzer-El Graara region, Anti-Atlas, Morocco: Geology, v. 17, p. 1107-1110.

Sebai, A., Feraud, G., Bertrand, H., and Hanes, J., 1991, $^{40}Ar/^{39}Ar$ dating and geochemistry of tholeiitic magmatism related to the early opening

of the Central Atlantic rift: Earth and Planetary Science Letters, v. 104, p. 455-472.

Sebti, S., Saddiqi, O., El Haimer, F.Z., Michard, A., Ruiz, G., Bousquet, R., Baidder, L., and Frizon de Lamotte, D., 2009, Vertical movements at the fringe of the West African Craton: First zircon fission track datings from the Anti-Atlas Precambrian basement, Morocco: Comptes Rendus Geosciences, v. 341, p. 71-77.

Shuster, D.L., and Farley, K.A., 2009, The influence of artificial radiation damage and thermal annealing on helium diffusion kinetics in apatite: Geochimica et Cosmochimica Acta, v. 73, p. 183-196.

Shuster, D.L., Flowers, R.M., and Farley, K.A., 2006, The influence of natural radiation damage on helium diffusion kinetics in apatite: Earth and Planetary Science Letters, v. 249, p. 148-161.

Sobel, E.R., and Seward, D., 2010, Influence of etching conditions on apatite fission-track etch pit diameter: Chemical Geology, v. 271, p. 59-69.

Soulaimani, A., and Burkhard, M., 2008, The Anti-Atlas chain (Morocco): the southern margin of the Variscan belt along the edge of the West African craton: Geological Society, London, Special Publications, v. 297, p. 433-452.

Soulaimani, A., Essaifi, A., Youbi, N., and Hafid, A., 2004, Les marqueurs structuraux et magmatiques de l'extension crustale au Protérozoïque terminal-Cambrien basal autour du massif de Kerdous (Anti-Atlas occidental, Maroc): Comptes Rendus Geosciences, v. 336, p. 1433-1441.

Soulaimani, A., and Piqué, A., 2004, The Tasrirt structure (Kerdous inlier, Western Anti-Atlas, Morocco): a late Pan-African transtensive dome: Journal of African Earth Sciences, v. 39, p. 247-255.

Spiegel, C., Kohn, B., Belton, D., Berner, Z., and Gleadow, A., 2009, Apatite (U–Th–Sm)/He thermochronology of rapidly cooled samples: The effect of He implantation: Earth and Planetary Science Letters, v. 285, p. 105-114.

Steiner, C., Hobson, A., Favre, P., Stampfli, G.M., and Hernandez, J., 1998, Mesozoic sequence of Fuerteventura (Canary Islands): Witness of Early Jurassic sea-floor spreading in the central Atlantic: Geological Society of America Bulletin, v. 110, p. 1304-1317.

Stockli, D.F., 2005, Application of Low-Temperature Thermochronometry to Extensional Tectonic Settings: Reviews in Mineralogy and Geochemistry, v. 58, p. 411-448.

Stockli, D.F., Dumitru, T.A., McWilliams, M.O., and Farley, K.A., 2003, Cenozoic tectonic evolution of the White Mountains, California and Nevada: Geological Society of America Bulletin, v. 115, p. 788-816.

Tagami, T., Carter, A., and Hurford, A.J., 1996, Natural long-term annealing of the zircon fission-track system in Vienna Basin deep borehole samples: constraints upon the partial annealing zone and closure temperature: Chemical Geology, v. 130, p. 147-157.

Teixell, A., Arboleya, M.-L., Julivert, M., and Charroud, M., 2003, Tectonic shortening and topography in the central High Atlas (Morocco): Tectonics, v. 22, p. 1051.

Teixell, A., Ayarza, P., Zeyen, H., Fernàndez, M., and Arboleya, M.L., 2005, Effects of mantle upwelling in a compressional setting: the Atlas Mountains of Morocco: Terra Nova, v. 17, p. 456-461.

Tesón, E., Pueyo, E.L., Teixell, A., Barnolas, A., Agustí, J., and Furió, M., 2010, Magnetostratigraphy of the Ouarzazate Basin: Implications for the timing of deformation and mountain building in the High Atlas Mountains of Morocco: Geodinamica Acta, v. 23, p. 151-165.

Thomas, R.J., Chevallier, L.P., Gresse, P.G., Harmer, R.E., Eglington, B.M., Armstrong, R.A., de Beer, C.H., Martini, J.E.J., de Kock, G.S., Macey, P.H., and Ingram, B.A., 2002, Precambrian evolution of the Sirwa Window, Anti-Atlas Orogen, Morocco: Precambrian Research, v. 118, p. 1-57.

Tissot, B., Demaison, G., Masson, P., Delteil, J.R., and Combaz, A., 1980, Paleoenvironment and petroleum potential of Middle Cretaceous black shales in Atlantic basins: AAPG Bulletin, v. 64, p. 2051-2063.

Vance, E.R., 1975, α-Recoil damage in zircon: Radiation Effects, v. 24, p. 1-6.

Verati, C., Rapaille, C., Féraud, G., Marzoli, A., Bertrand, H., and Youbi, N., 2007, 40Ar/39Ar ages

and duration of the Central Atlantic Magmatic Province volcanism in Morocco and Portugal and its relation to the Triassic-Jurassic boundary: Palaeogeography, Palaeoclimatology, Palaeoecology, v. 244, p. 308-325.

Vermeesch, P., Seward, D., Latkoczy, C., Wipf, M., Günther, D., and Baur, H., 2007, [alpha]-Emitting mineral inclusions in apatite, their effect on (U-Th)/He ages, and how to reduce it: Geochimica et Cosmochimica Acta, v. 71, p. 1737-1746.

von Rad, U., and Einsele, G., 1980, Mesozoic-Cainozoic Subsidence History and Palaeobathymetry of the Northwest African Continental Margin (Aaiun Basin to D. S. D. P. Site 397): Philosophical Transactions of the Royal Society of London. Series A, Mathematical and Physical Sciences, v. 294, p. 37-50.

von Rad, U., and Sarti, M., 1986, Early Cretaceous »events« in the evolution of the eastern and western North Atlantic continental margins: Geologische Rundschau, v. 75, p. 139-158.

von Rad, U., and Wissmann, G., 1982, Cretaceous-Cenozoic history of the West Saharan continental margin (NW Africa): development, destruction and gravitational sedimentation, *in* von Rad, U., Hinz, K., Sarnthein, M., and Seibold, E., eds., Geology of the northwest African continental margin, Springer Verlag, p. 106-131.

Wagner, G.A., 1972, Spaltspurenalter von Mineralen und natürlichen Gläsern: eine Übersicht: Fortschritte der Mineralogie, v. 49, p. 114-145.

Wagner, G.A., and Van den Haute, P., 1992, Fission-track dating: Stuttgart, Enke Verlag - Kluwer Academic Publishers.

Walsh, G.J., Aleinikoff, J.N., Benziane, F., Yazidi, A., and Armstrong, T.R., 2002, U–Pb zircon geochronology of the Paleoproterozoic Tagragra de Tata inlier and its Neoproterozoic cover, western Anti-Atlas, Morocco: Precambrian Research, v. 117, p. 1-20.

Wendt, J., 1985, Disintegration of the continental margin of northwestern Gondwana: Late Devonian of the eastern Anti-Atlas (Morocco): Geology, v. 13, p. 815-818.

Wenke, A., Zühlke, R., Jabour, H., and Kluth, O., 2011, High-resolution sequence stratigraphy in basin reconnaissance: example from the Tarfaya Basin, Morocco: First Break, v. 29, p. 85-96.

—, 2013, Quantitative subsidence analysis and sediment flux history of the Tarfaya-Laayoune Basins, North West African passive continental margin (submitted).

Wiedmann, J., Butt, A., and Einsele, G., 1982, Cretaceous stratigraphy, environment, and subsidence history at the Moroccan continental margin, *in* von Rad, U., Hinz, K., Sarnthein, M., and Seibold, E., eds., Geology of the northwest African continental margin, Springer Verlag, p. 366-395.

Wilson, M., 1997, Thermal evolution of the Central Atlantic passive margins: continental break-up above a Mesozoic super-plume: Journal of the Geological Society, v. 154, p. 491-495.

Wipf, M., 2006, Evolution of the Western Cordillera and costal margin of Peru: Evidence from low-temperature thermochronology and geomorphology, Dissertation thesis, ETH Zürich.

Wipf, M., Glasmacher, U., Stockli, D., Emmerich, A., Bechstädt, T., and Baur, H., 2010, Reconstruction of the differentiated long-term exhumation history of Fuerteventura, Canary Islands, Spain, through fission-track and (U-Th–Sm)/He data: International Journal of Earth Sciences, v. 99, p. 675-686.

Withjack, M.O., Schlische, R.W., and Olsen, P.E., 2012, 13 - Development of the passive margin of Eastern North America: Mesozoic rifting, igneous activity, and breakup, Regional Geology and Tectonics: Phanerozoic Rift Systems and Sedimentary Basins: Boston, Elsevier, p. 300-335.

Wolf, R.A., Farley, K.A., and Kass, D.M., 1998, Modeling of the temperature sensitivity of the apatite (U-Th)/He thermochronometer: Chemical Geology, v. 148, p. 105-114.

Wolf, R.A., Farley, K.A., and Silver, L.T., 1996, Helium diffusion and low-temperature thermochronometry of apatite: Geochimica et Cosmochimica Acta, v. 60, p. 4231-4240.

Yamada, K., Tagami, T., and Shimobayashi, N., 2003, Experimental study on hydrothermal annealing of fission tracks in zircon: Chemical Geology, v. 201, p. 351-357.

Yamada, R., Murakami, M., and Tagami, T., 2007, Statistical modelling of annealing kinetics of fission tracks in zircon; Reassessment of laboratory experiments: Chemical Geology, v. 236, p. 75-91.

Yamada, R., Tagami, T., Nishimura, S., and Ito, H., 1995, Annealing kinetics of fission tracks in zircon: an experimental study: Chemical Geology, v. 122, p. 249-258.

Zarhloule, Y., Bouri, S., Lahrach, A., Boughriba, M., El Mandour, A., and Ben Dhia, H., 2005, Hydrostratigraphical Study, Geochemistry of Thermal Springs, Shallow and Deep Geothermal Exploration in Morocco: Hydrogeothermal Potentialities, Proceedings World Geothermal Congress: Antalya, Turkey, p. 13.

Zeyen, H., Ayarza, P., Fernàndez, M., and Rimi, A., 2005, Lithospheric structure under the western African-European plate boundary: A transect across the Atlas Mountains and the Gulf of Cadiz: Tectonics, v. 24, p. TC2001.

Zhang, M., Boatner, L.A., Salje, E.K.H., Honda, S., and Ewing, R.C., 2008, Pb^{+} irradiation of synthetic zircon (ZrSiO4): Infrared spectroscopic investigation: American Mineralogist, v. 93, p. 1418-1423.

Zhang, M., Ewing, R.C., Boatner, L.A., Salje, E.K.H., Weber, W.J., Daniel, P., Zhang, Y., and Farnan, I., 2009, Pb+ irradiation of synthetic zircon (ZrSiO4): Infrared spectroscopic investigation—Reply: American Mineralogist, v. 94, p. 856-858.

Zouhri, S., Kchikach, A., Saddiqi, O., El Haimer, F.Z., Baidder, L., and Michard, A., 2008, The Cretaceous-Tertiary Plateaus, *in* Michard, A., Saddiqi, O., Chalouan, A., and Frizon de Lamotte, D., eds., Continental Evolution: The Geology of Morocco: Berlin, Heidelberg, Springer-Verlag, p. 331-358.

Zühlke, R., Bouaouda, M.-S., Ouajhain, B., Bechstädt, T., and Leinfelder, R., 2004, Quantitative Meso-/Cenozoic development of the eastern Central Atlantic continental shelf, western High Atlas, Morocco: Marine and Petroleum Geology, v. 21, p. 225-276.

Eidesstattliche Versicherung gemäß §8 der Promotionsordnung der Naturwissenschaftlich-Mathematischen Gesamtfakultät der Universität Heidelberg

1. Bei der eingereichten Dissertation zu dem Thema

   Variscan to Neogene long-term landscape evolution at the Moroccan passive continental margin (Tarfaya Basin and western Anti-Atlas)

   handelt sich um eine eigenständig erbrachte Leistung.

2. Ich habe nur die angegebenen Quellen und Hilfsmittel benutzt und mich keiner unzulässigen Hilfe Dritter bedient.

3. Ich erkläre weiterhin, dass ich an keiner anderen Stelle ein Prüfungsverfahren beantragt bzw. die Dissertation in dieser oder anderer Form bereits anderweitig als Prüfungsarbeit verwendet oder einer anderen Fakultät als Dissertation vorgelegt habe.

4. Die Bedeutung der eidesstattlichen Versicherung und die strafrechtlichen Folgen einer unrichtigen oder unvollständigen eidesstattlichen Versicherung sind mir bekannt.

Heidelberg, den 15. Mai 2014

Ort und Datum

Unterschrift